

ИЗВЕСТИЯ ВЫСШИХ УЧЕБНЫХ ЗАВЕДЕНИЙ ЧЕРНАЯ МЕТАЛЛУРГИЯ

IZVESTIYA. FERROUS METALLURGY

fermet.misis.ru

2025 Том 68 № 1
Vol. No.

МЕТАЛЛУРГИЧЕСКИЕ ТЕХНОЛОГИИ

Разработка технологии производства профильных труб, обеспечивающей более высокую точность геометрических параметров по сравнению с зарубежными производителями

МАТЕРИАЛОВЕДЕНИЕ

Исследование влияния режимов термической обработки на свойства сплава 56ДГНХ

ФИЗИКО-ХИМИЧЕСКИЕ ОСНОВЫ МЕТАЛЛУРГИЧЕСКИХ ПРОЦЕССОВ

Развитие исследований физико-химических свойств оксидных и металлических расплавов

ИЗВЕСТИЯ ВЫСШИХ УЧЕБНЫХ ЗАВЕДЕНИЙ ЧЕРНАЯ МЕТАЛЛУРГИЯ

Научно-технический журнал

Издается с января 1958 г. Выпускается 6 раз в год

2025 Том 68 № 1
Vol. No.

IZVESTIYA FERROUS METALLURGY

Scientific and Technical Journal

Published since January 1958. Issued 6 times a year

IZVESTIYA FERROUS METALLURGY

www.fermet.misis.ru

ISSN 0368-0797 (Print) ISSN 2410-2091 (Online)

Alternative title:

Izvestiya vuzov. Chernaya metallurgiya

Founders:



Editor-in-Chief:

Leopol'd I. Leont'ev, Academician, Adviser of the Russian Academy of Sciences; Dr. Sci. (Eng.), Prof., NUST "MISIS"; Chief Researcher, Institute of Metallurgy UB RAS, Moscow
4 Leninskii Ave., Moscow 119049, Russian Federation
National University of Science and Technology "MISIS"

Deputy Editor-in-Chief:

Evgenii V. Protopopov, Dr. Sci. (Eng.), Prof., Siberian State Industrial University, Novokuznetsk

Publisher:

National University of Science and Technology "MISIS"

Editorial Office Address:

in Moscow

4 Leninskii Ave., Moscow 119049, Russian Federation
National University of Science and Technology "MISIS"
Tel.: +7 (495) 638-44-11
E-mail: fermet.misis@mail.ru, ferrous@sis.ru

in Novokuznetsk

42 Kirova Str., Novokuznetsk, Kemerovo Region – Kuzbass
654007, Russian Federation
Siberian State Industrial University
Tel.: +7 (3843) 74-86-28 E-mail: redjizvz@sibsiu.ru

Editorial Board:

Sailaubai O. Baisanov, Dr. Sci. (Eng.), Prof., Abishev Chemical-Metallurgical Institute, Karaganda, Republic of Kazakhstan
Vladimir D. Belov, Dr. Sci. (Eng.), Prof., NUST MISIS, Moscow
Anatolii A. Brodov, Cand. Sci. (Econ.), Bardin Central Research Institute for Ferrous Metallurgy, Moscow
Il'ya V. Chumanov, Dr. Sci. (Eng.), Prof., South Ural State Research University, Chelyabinsk
Andrei N. Dmitriev, Dr. Sci. (Eng.), Prof., Academician, RANS, A.M. Prokhorov Academy of Engineering Sciences, Institute of Metallurgy, Ural Branch of RAS, Ural Federal University, Yekaterinburg
Aleksei V. Dub, Dr. Sci. (Eng.), Prof., JSC "Science and Innovations", Moscow
Mikhail R. Filonov, Dr. Sci. (Eng.), Prof., NUST MISIS, Moscow
Sergei M. Gorbatyuk, Dr. Sci. (Eng.), Prof., NUST MISIS, Moscow
Konstantin V. Grigorovich, Academician of RAS, Dr. Sci. (Eng.), Baikov Institute of Metallurgy and Materials Science of RAS, Moscow
Victor E. Gromov, Dr. Sci. (Eng.), Prof., Siberian State Industrial University, Novokuznetsk
Aleksei G. Kolmakov, Dr. Sci. (Eng.), Corresponding Member of RAS, Baikov Institute of Metallurgy and Materials Science of RAS, Moscow
Valerii M. Kolokol'tsev, Dr. Sci. (Eng.), Prof., Magnitogorsk State Technical University, Magnitogorsk
Mariya V. Kostina, Dr. Sci. (Eng.), Baikov Institute of Metallurgy and Materials Science of RAS, Moscow
Konstantin L. Kosyrev, Dr. Sci. (Eng.), Academician of RANS, Electrosteel Heavy Engineering Works JSC, Moscow
Yuliya A. Kurganova, Dr. Sci. (Eng.), Prof., Bauman Moscow State Technical University, Moscow
Linn Horst, Linn High Therm GmbH, Hirschbach, Germany
Vladimir I. Lysak, Academician of RAS, Dr. Sci. (Eng.), Prof., Rector, Volgograd State Technical University, Volgograd
Valerii P. Meshalkin, Dr. Sci. (Eng.), Academician of RAS, Prof., D.I. Mendeleyev Russian Chemical-Technological University, Moscow
Radik R. Mulyukov, Dr. Sci. (Phys.-Chem.), Prof., Corresponding Member of RAS, Institute of Metals Superplasticity Problems of RAS, Ufa

Sergei A. Nikulin, Dr. Sci. (Eng.), Prof., Corresponding Member of RANS, NUST MISIS, Moscow
Asylbek Kh. Nurumgaliev, Dr. Sci. (Eng.), Prof., Karaganda State Industrial University, Karaganda, Republic of Kazakhstan
Oleg I. Ostrovski, Dr. Sci. (Eng.), Prof., University of New South Wales, Sydney, Australia
Loris Pietrelli, Dr., Scientist, Italian National Agency for New Technologies, Energy and Sustainable Economic Development, Rome, Italy
Igor' Yu. Pyshmintsev, Dr. Sci. (Eng.), Russian Research Institute of the Pipe Industry, Chelyabinsk
Andrei I. Rudskoi, Academician of RAS, Dr. Sci. (Eng.), Prof., Rector, Peter the Great Saint-Petersburg Polytechnic University, Saint-Petersburg
Oleg Yu. Sheshukov, Dr. Sci. (Eng.), Prof., Ural Federal University, Yekaterinburg
Laura M. Simonyan, Dr. Sci. (Eng.), Prof., NUST MISIS, Moscow
Robert F. Singer, Dr. Sci. (Eng.), Prof., Friedrich-Alexander University, Germany
Boris A. Sivak, Cand. Sci. (Eng.), Prof., VNIIMETMASH Holding Company, Moscow
Leonid A. Smirnov, Dr. Sci. (Eng.), Prof., Academician of RAS, OJSC "Ural Institute of Metals", Yekaterinburg
Sergei V. Solodov, Cand. Sci. (Eng.), NUST MISIS, Moscow
Marcus Speidel, Dr. Natur. Sci., Prof., Swiss Academy of Materials, Switzerland
Nikolai A. Spirin, Dr. Sci. (Eng.), Prof., Ural Federal University, Yekaterinburg
Guoi Tang, Institute of Advanced Materials of Tsinghua University, Shenzhen, China
Mikhail V. Temlyantsev, Dr. Sci. (Eng.), Prof., Siberian State Industrial University, Novokuznetsk
Ekaterina P. Volynkina, Dr. Sci. (Eng.), Advisor, ALE "Kuzbass Association of Waste Processors", Novokuznetsk
Aleksei B. Yur'ev, Dr. Sci. (Eng.), Prof., Rector, Siberian State Industrial University, Novokuznetsk
Vladimir S. Yusupov, Dr. Sci. (Eng.), Prof., Baikov Institute of Metallurgy and Materials Science of RAS, Moscow
Vladimir I. Zhuchkov, Dr. Sci. (Eng.), Prof., Institute of Metallurgy, Ural Branch of RAS, Ural Federal University, Yekaterinburg
Michael Zinigrad, Dr. Sci. (Physical Chemistry), Prof., Rector, Ariel University, Israel
Vladimir I. Zolotukhin, Dr. Sci. (Eng.), Prof., Tula State University, Tula

In accordance with paragraph 5 of the Rules for the formation of the Higher Attestation Commission list journal "Izvestiya. Ferrous metallurgy" is included in the list of leading peer-reviewed scientific journals, publication in which is taken into account in the defense of candidate and doctoral dissertations, as indexed in international data bases.

Indexed: Scopus, Russian Science Citation Index (RSCI), Research Bible, Chemical Abstracts, OCLC and Google Scholar
Registered in Federal Service for Supervision in the Sphere of Mass Communications **PI number FS77-35456.**



Articles are available under Creative Commons Attribution 4.0 License.

ИЗВЕСТИЯ ВЫСШИХ УЧЕБНЫХ ЗАВЕДЕНИЙ ЧЕРНАЯ МЕТАЛЛУРГИЯ

www.fermet.misis.ru

ISSN 0368-0797 (Print) ISSN 2410-2091 (Online)

Варианты названия:

Известия вузов. Черная металлургия

Izvestiya. Ferrous Metallurgy

Учредители:



Редакционная коллегия:

С. О. Байсанов, д.т.н., профессор, ХМИ им. Ж.Абишева, г. Караганда, Республика Казахстан

В. Д. Белов, д.т.н., профессор, НИТУ МИСИС, г. Москва

А. А. Бродов, к.экон.н., ФГУП «ЦНИИчермет им. И.П. Бардина», г. Москва

Е. П. Волынкина, д.т.н., советник, ОЮЛ «Кузбасская Ассоциация переработчиков отходов», г. Новокузнецк

С. М. Горбатько, д.т.н., профессор, НИТУ МИСИС, г. Москва

К. В. Григорович, академик РАН, д.т.н., ИМЕТ им. А.А. Байкова РАН, г. Москва

В. Е. Громов, д.ф.-м.н., профессор, СибГИУ, г. Новокузнецк

А. Н. Дмитриев, д.т.н., профессор, академик РАЕН, академик АИН РФ, г. Екатеринбург

А. В. Дуб, д.т.н., профессор, ЗАО «Наука и инновации», г. Москва

В. И. Жучков, д.т.н., профессор, ИМЕТ УрО РАН, г. Екатеринбург

Р. Ф. Зингер, д.т.н., профессор, Институт Фридриха-Александра, Германия

М. Зиниград, д.т.н., профессор, Институт Ариэля, Израиль

В. И. Золотухин, д.т.н., профессор, ТулГУ, г. Тула

А. Г. Колмаков, д.т.н., чл.-корр. РАН, ИМЕТ им. А.А. Байкова РАН, г. Москва

В. М. Колокольцев, д.т.н., профессор, МГТУ им. Г.И. Носова, г. Магнитогорск

М. В. Костина, д.т.н., ИМЕТ им. А.А. Байкова РАН, г. Москва

К. Л. Косырев, д.т.н., академик РАЕН, ОАО «Электростальский завод тяжелого машиностроения», г. Москва

Ю. А. Курганова, д.т.н., профессор, МГТУ им. Н.Э. Баумана, г. Москва

Х. Линн, ООО «Линн Хай Терм», Германия

В. И. Лысак, академик РАН, д.т.н., профессор, ВолГТУ, г. Волгоград

В. П. Мешалкин, академик РАН, д.т.н., профессор, РХТУ им. Д.И. Менделеева, г. Москва

В соответствии п. 5 Правил формирования перечня ВАК журнал «Известия вузов. Черная металлургия» входит в перечень ведущих рецензируемых научных журналов и изданий, публикация в которых учитывается при защитах кандидатских и докторских диссертаций как индексируемый в МБД.

Главный редактор:

Леопольд Игоревич Леонтьев, академик РАН, советник, Президиум РАН; д.т.н., профессор, НИТУ «МИСИС»; главный научный сотрудник, Институт металлургии УрО РАН
Россия, 119049, Москва, Ленинский просп., д. 4, стр. 1, Национальный исследовательский технологический университет «МИСИС»

Заместитель главного редактора:

Евгений Валентинович Протопопов, д.т.н., профессор, Сибирский государственный индустриальный университет г. Новокузнецк

Издатель:

Национальный исследовательский технологический университет «МИСИС»

Адреса подразделений редакции:

в Москве

Россия, 119049, Москва, Ленинский просп., д. 4, стр. 1
Национальный исследовательский технологический университет «МИСИС»

Тел.: +7 (495) 638-44-11 E-mail: ferrous@isis.ru

в Новокузнецке

Россия, 654007, Новокузнецк,
Кемеровская обл. – Кузбасс, ул. Кирова, зд. 42
Сибирский государственный индустриальный университет
Тел.: +7 (3843) 74-86-28 E-mail: redjizvz@sibsiu.ru

Р. Р. Мулюков, д.ф.м.-н., профессор, чл.-корр. ФГБУН ИПСМ РАН, г. Уфа
С. А. Никулин, д.т.н., профессор, чл.-корр. РАЕН, НИТУ МИСИС, г. Москва
А. Х. Нурумгалиев, д.т.н., профессор, КГИУ, г. Караганда, Республика Казахстан
О. И. Островский, д.т.н., профессор, Университет Нового Южного Уэльса, Сидней, Австралия
Л. Пиетрелли, д.т.н., Итальянское национальное агентство по новым технологиям, энергетике и устойчивому экономическому развитию, Рим, Италия
И. Ю. Пышминцев, д.т.н., РосНИТИ, г. Челябинск
А. И. Рудской, академик РАН, д.т.н., профессор, СПбПУ Петра Великого, г. Санкт-Петербург
Б. А. Сивак, к.т.н., профессор, АО АХК «ВНИИМТМАШ», г. Москва
Л. М. Симонян, д.т.н., профессор, НИТУ МИСИС, г. Москва
Л. А. Смирнов, академик РАН, д.т.н., профессор, ОАО «Уральский институт металлов», г. Екатеринбург
С. В. Солодов, к.т.н., НИТУ МИСИС, г. Москва
Н. А. Спирин, д.т.н., профессор, УрФУ, г. Екатеринбург
Г. Танг, Институт перспективных материалов университета Циньхуа, г. Шеньжень, Китай
М. В. Темлянецев, д.т.н., профессор, СибГИУ, г. Новокузнецк
М. Р. Филонов, д.т.н., профессор, НИТУ МИСИС, г. Москва
И. В. Чуманов, д.т.н., профессор, ЮУрГУ, г. Челябинск
О. Ю. Шешуков, д.т.н., профессор УрФУ, г. Екатеринбург
М. О. Шпайдель, д.ест.н., профессор, Швейцарская академия материаловедения, Швейцария
А. Б. Юрьев, д.т.н., профессор, ректор, СибГИУ, г. Новокузнецк
В. С. Юсупов, д.т.н., профессор, ИМЕТ им. А.А. Байкова РАН, г. Москва

Индексирование: Scopus, Russian Science Citation Index (RSCI), Research Bible, Chemical Abstracts, OCLC и Google Scholar

Зарегистрирован Федеральной службой по надзору в сфере связи и массовых коммуникаций ПИ № ФС77-35456.



Статьи доступны под лицензией Creative Commons Attribution 4.0 License.

СОДЕРЖАНИЕ

CONTENTS

METALLURGICAL TECHNOLOGIES

- Mozzhegorov M.N., Mashentseva M.S.** Development of profile pipes production technology, providing higher accuracy of geometric parameters compared to foreign manufactures 8
- Pospelov I.D.** Stiffness modulus of stands in finishing group of continuous wide-strip hot rolling mill 14
- Teplyakova L.A., Kunitsyna T.S., Pechkovskii V.A., Kashin A.D.** Tensile fracture of tempered martensitic steel 21
- Nevskii S.A., Bashchenko L.P., Sarychev V.D., Granovskii A.Yu., Shamsutdinova D.V.** Influence of inclined electric field on decay of a liquid jet during heat treatment and surfacing 30
- Gromov V.E., Kononov S.V., Polevoi E.V.** Anthology of rails produced by JSC EVRAZ United West Siberian Metallurgical Plant in the 21st century 40

MATERIALS SCIENCE

- Belomyttsev M.Yu., Mikhailov M.A., Kozlov D.A., Mikhailov A.M., Karavatskii I.I.** Influence of heat treatment modes on the properties of 56DGNKh (Cu20Ni20Mn2Cr) alloy 44
- Vlasov I.V., Gordienko A.I., Semenchuk V.M.** Effect of thermal cycles on formation of pearlitic heat-resistant steel structure under wire arc additive manufacturing 51
- Koltygin A.V., Bazhenov V.E., Belova A.A., Sannikov A.V., Lyskovich A.A., Belov V.D., Shchedrin E.Yu.** Influence of heat treatment on structure, phase composition, hardness and electrical conductivity of VZhL14N-VI nickel superalloy 60

PHYSICO-CHEMICAL BASICS
OF METALLURGICAL PROCESSES

- Kazakevich G.A., Popov A.Yu.** Construction of liquidus surface of Fe–B–Mn–C–Cr five-component diagram .. 69
- Sheshukov O.Yu., Nevidimov V.N., Nekrasov I.V., Metelkin A.A., Tsepelev V.S.** Development of research on the physico-chemical properties of oxide and metal melts 76

МЕТАЛЛУРГИЧЕСКИЕ ТЕХНОЛОГИИ

- Мозжегоров М.Н., Машенцева М.С.** Разработка технологии производства профильных труб, обеспечивающей более высокую точность геометрических параметров по сравнению с зарубежными производителями 8
- Поспелов И.Д.** Исследование модуля жесткости клетей чистовой группы непрерывного широкополосного стана горячей прокатки 14
- Теплякова Л.А., Куницына Т.С., Печковский В.А., Кашин А.Д.** Разрушение отпущенной мартенситной стали при растяжении 21
- Невский С.А., Башченко Л.П., Сарычев В.Д., Грановский А.Ю., Шамсутдинова Д.В.** Влияние наклонного электрического поля на распад струи жидкости в процессах термообработки и наплавки 30
- Громов В.Е., Коновалов С.В., Полевой Е.В.** Антология рельсов производства «ЕВРАЗ Объединенный Западно-Сибирский металлургический комбинат» XXI века 40

МАТЕРИАЛОВЕДЕНИЕ

- Беломятцев М.Ю., Михайлов М.А., Козлов Д.А., Михайлов А.М., Каравацкий И.И.** Исследование влияния режимов термической обработки на свойства сплава 56ДГНХ 44
- Власов И.В., Гордиенко А.И., Семенчук В.М.** Влияние термических циклов на формирование структуры жаропрочной стали перлитного класса в условиях проволочного электродугового аддитивного производства 51
- Колтыгин А.В., Баженов В.Е., Белова А.А., Саников А.В., Лыскович А.А., Белов В.Д., Щедрин Е.Ю.** Влияние термической обработки на фазовый состав, структуру, твердость и электропроводность никелевого жаропрочного сплава ВЖЛ14Н-ВИ 60

ФИЗИКО-ХИМИЧЕСКИЕ ОСНОВЫ
МЕТАЛЛУРГИЧЕСКИХ ПРОЦЕССОВ

- Казакевич Г.А., Попов А.Ю.** Построение поверхности ликвидус пятикомпонентной схемы диаграммы Fe–B–Mn–C–Cr 69
- Шешуков О.Ю., Невидимов В.Н., Некрасов И.В., Метелкин А.А., Цепелев В.С.** Развитие исследований физико-химических свойств оксидных и металлических расплавов 76

СОДЕРЖАНИЕ (продолжение)

CONTENTS (Continuation)

**ECONOMIC EFFICIENCY
OF METALLURGICAL PRODUCTION**

Fastykovskii A.R., Musatova A.I., Martyshev N.V. Development of models for functioning of drawing equipment for multi-mill servicing 84

Chernikova O.P., Afanas'eva O.V., Afanas'ev E.G. Directions of decarbonization of Russian ferrous metallurgy ... 90

IN THE ORDER OF DISCUSSION

Murashov V.A., Strogonov K.V., Bastynets A.K., Lvov D.D. Development of a continuous extra-furnace steel processing unit 98

**ЭКОНОМИЧЕСКАЯ ЭФФЕКТИВНОСТЬ
МЕТАЛЛУРГИЧЕСКОГО ПРОИЗВОДСТВА**

Фастыковский А.Р., Мусатова А.И., Мартюшев Н.В. Разработка моделей функционирования волочильного оборудования при многостановом обслуживании 84

Черникова О.П., Афанасьева О.В., Афанасьев Е.Г. Направления декарбонизации Российской черной металлургии 90

В ПОРЯДКЕ ДИСКУССИИ

Мурашов В.А., Строгонов К.В., Бастынец А.К., Львов Д.Д. Разработка агрегата внепечной обработки стали непрерывного действия 98



UDC 621.774

DOI 10.17073/0368-0797-2025-1-8-13



Original article

Оригинальная статья

DEVELOPMENT OF PROFILE PIPES PRODUCTION TECHNOLOGY, PROVIDING HIGHER ACCURACY OF GEOMETRIC PARAMETERS COMPARED TO FOREIGN MANUFACTURES

M. N. Mozzhegorov, M. S. Mashentseva

LLC “TMK Research Center” (30 Novorossiiskaya Str., Chelyabinsk 454139, Russian Federation)

mashentseva@rosniti.ru

Abstract. The method of profiling circular pipes is used in the lines of pipe-electric welding and profiling units in order to master the production of pipe products of non-circular cross-section from corrosion-resistant steel grades. Tubular products used in nuclear power generation facilities have higher requirements to mechanical properties and geometrical parameters. In particular, the most difficult aspect of manufacturing profile pipes-windings for turbo-generator stators with a rectangular cross-section is ensuring the flatness of flanges and achieving the radius of the outer corner rounding within a tolerance of ± 0.10 mm relative to the nominal value. In order to successfully master the production of this type of product, a synthesis of the circular pipe profiling scheme was carried out. The authors developed the technology of profiling in drive rolls forming box gauges and in non-driven four-roll stands. Computer modeling of the profiling process was carried out in the Marc Mentat 2021 program. After experimental rolling, the profiles' geometric parameters were analyzed using an optical microscope and special software. Acceptance tests were performed in accordance with the requirements to profile pipes for windings of turbogenerator stators.

Keywords: shaping mill, pipe-electric welding unit (PEWU), profiling technology, outer contour corner radius, concavity of profile flanges, roll-pass design, computer modeling

For citation: Mozzhegorov M.N., Mashentseva M.S. Development of profile pipes production technology, providing higher accuracy of geometric parameters compared to foreign manufactures. *Izvestiya. Ferrous Metallurgy*. 2025;68(1):8–13.

<https://doi.org/10.17073/0368-0797-2025-1-8-13>

РАЗРАБОТКА ТЕХНОЛОГИИ ПРОИЗВОДСТВА ПРОФИЛЬНЫХ ТРУБ, ОБЕСПЕЧИВАЮЩЕЙ БОЛЕЕ ВЫСОКУЮ ТОЧНОСТЬ ГЕОМЕТРИЧЕСКИХ ПАРАМЕТРОВ ПО СРАВНЕНИЮ С ЗАРУБЕЖНЫМИ ПРОИЗВОДИТЕЛЯМИ

М. Н. Мозжегоров, М. С. Машенцева

ООО «Исследовательский центр ТМК» (Россия, 454139, Челябинск, Новороссийская ул., 30)

mashentseva@rosniti.ru

Аннотация. Для освоения производства трубной продукции некруглого поперечного сечения из коррозионностойких марок сталей широко используется метод профилирования круглых труб в линиях трубоэлектросварочных и профилировочных агрегатов. К трубной продукции, применяемой в установках генерации атомной энергии, предъявляются повышенные требования к механическим свойствам и геометрическим параметрам. В частности, для профильных труб-обмоток статоров турбогенераторов прямоугольного поперечного сечения наиболее труднодостижимыми являются обеспечение плоскостности полок и получение радиусов наружного закругления углов в допуске $\pm 0,10$ мм по отношению к номиналу. Для успешного освоения производства данного вида продукции проведен синтез схемы профилирования круглой трубы. Разработана технология профилирования в приводных валках, образующих ящичные калибры, и не приводных четырехвалковых клетях. Компьютерное моделирование процесса профилирования было выполнено в программе Marc Mentat 2021. После проведения комплекса опытных прокаток авторы проанализировали геометрические параметры профилей с применением оптического микроскопа и специального программного обеспечения. Приемочно-сдаточные испытания прошли в соответствии с требованиями к профильным трубам для обмоток статоров турбогенераторов.

Ключевые слова: профилировочный стан, трубоэлектросварочный агрегат (ТЭСА), технология профилирования, радиус угла наружного контура, вогнутость полок профиля, ящичный калибр, калибровка валкового инструмента, компьютерное моделирование

Для цитирования: Можжегоров М.Н., Машенцева М.С. Разработка технологии производства профильных труб, обеспечивающей более высокую точность геометрических параметров по сравнению с зарубежными производителями. *Известия вузов. Черная металлургия*. 2025;68(1):8–13. <https://doi.org/10.17073/0368-0797-2025-1-8-13>

RESEARCH OBJECTIVE

The rapid development of industry is driving continuous increases in the requirements for the performance characteristics of products used in power generation facilities, including nuclear power plants [1]. Today, the uninterrupted operation of many enterprises in the nuclear industry depends on the availability of specific components – profile pipes with defined cross-sections for turbo-generator stators.

To meet the demand for profile pipes from power engineering companies in Russia, specialists at the Pipe Metallurgical Company (TMK) have explored the feasibility of manufacturing the required products.

During the preparatory phase for the production of profile pipes with dimensions of $10.0 \times 3.8 \times 0.9$ mm, several challenges arose that prevented the consistent achievement of key quality characteristics [1] when using the drawing method, namely:

- concavity of the profile flanges exceeded the specified technical requirements (Fig. 1, a);
- surface defects formed during profiling (Fig. 1, b);
- effective radii of the outer corner rounding (measured in accordance with ASTM A554 [2]) exceeded the geometric tolerance requirements.

As part of the study, an analysis of the equipment available at the production site for manufacturing the required products was carried out, and the feasibility of producing welded profile pipes was assessed. Based on the analysis, a fundamental technological scheme for the production process of profile pipes

on the PEWU T 30/35 line was developed, and a list of tools and equipment required for upgrading the PEWU was compiled to enable continuous production [3; 4]. The most technologically advanced solution for producing the required range of products is the continuous production of profile pipes from coil stock using the argon-arc welding method for circular pipe billets, followed by heat treatment and profiling to the specified dimensions on the PEWU T 30/35 line.

A preliminary analysis indicated that the successful implementation of continuous welded profile pipe production requires the following additional equipment and tools for the TESA T 30/35 line:

- a bright annealing furnace;
- two non-driven four-roll stands [5];
- roll forming, calibrating, and profiling tools.

SCIENTIFIC RESEARCH AND TECHNOLOGICAL SOLUTIONS

To improve the technology under import substitution conditions, it was decided to organize pilot production of profile pipes with dimensions of $10.0 \times 3.8 \times 0.9 \times 4000$ mm from circular pipe billets using a semi-continuous process at the existing shaping mill.

To implement the proposed solution, a profiling scheme was designed, the roll-pass design was calculated [6; 7], and computer modeling of the circular pipe billet profiling process was performed [8 – 10]. To assess the performance of the new roll-pass design at the mode-

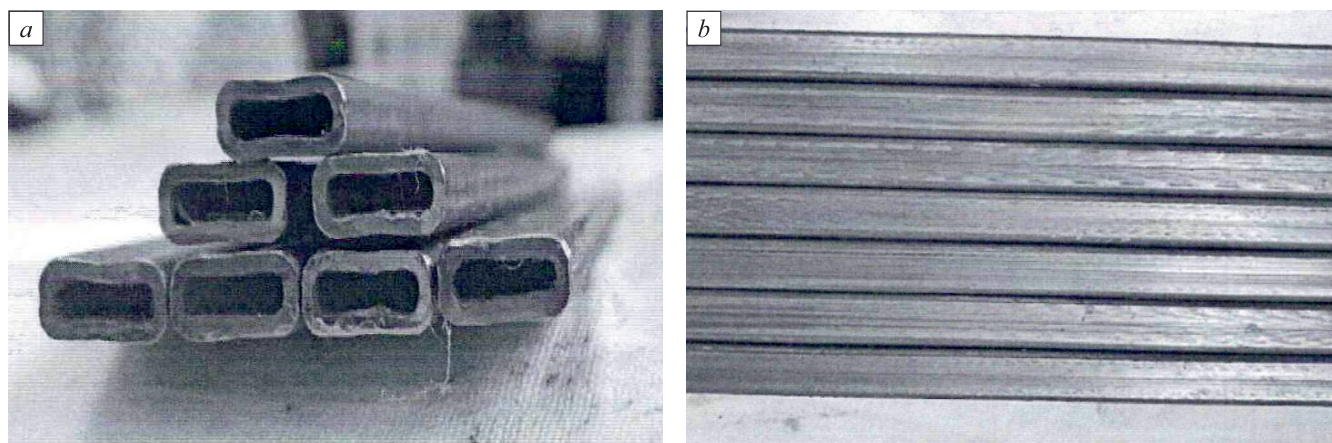


Fig. 1. Profile pipes made by drawing: cross-section (a); backfins on the outer surface (b)

Рис. 1. Профильные трубы, изготовленные методом волочения: поперечное сечение (a); задиры на наружной поверхности (b)

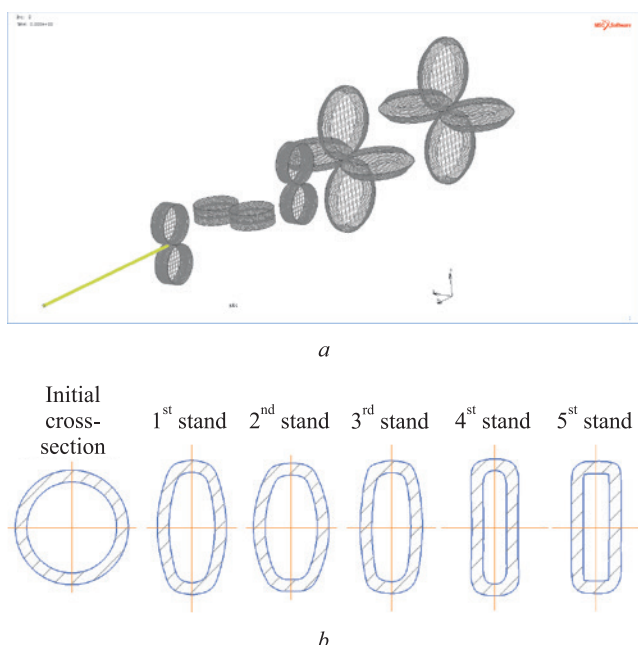


Fig. 2. Finite element modeling:
finite element model of rolling a pipe from a circle to a square (a);
cross-section of finite element model of a profile pipe (b)

Рис. 2. Конечно-элементное моделирование:

конечно-элементная модель прокатки трубы из круга в квадрат (a);
поперечное сечение конечно-элементной-модели
профильной трубы (b)

ling stage, a pipe billet with a diameter of 8.75 mm and a wall thickness of 0.9 mm was selected as the test object. The pipe model was divided into 3600 finite elements of the Shell 7¹ type [11]. Various bending simulation methods using the Marc (CAD/CAE) system were extensively studied by Zharkov A.V. The author [12 – 18] applied this type of element for thin-walled pipes where the wall thickness is significantly smaller than the diameter. To achieve high accuracy and reduce computational costs, mesh refinement was applied in areas of intense deformation [19]. The roll models were defined as perfectly rigid bodies [20], a common assumption in simulations of continuous pipe forming processes, which is considered acceptable given the small wall thickness. The finite element model of the profile rolling process is shown in Fig. 2, a.

The analysis of the simulation results assessed the stress-strain state of the pipe in the interstand space based on the distribution of plastic deformations, as well as the geometric parameters of the pipe. The cross-section after each stand is shown in Fig. 2, b.

The maximum plastic deformations occur in the regions where the future “corners” of the square pro-

file are formed. These areas experience the highest tensile stresses on the outer diameter and compressive stresses on the inner diameter [21]. In the second and third stands, the primary deformation zone forms at the contact point between the roll tooling and the pipe. The pipe undergoes sequential deformation of its vertical and horizontal dimensions – height in the second stand and width in the third stand [22]. The final rolling stage is carried out in two identical stands: the fourth stand performs the final shape adjustments, while the fifth stand completes the profile calibration.

The geometric parameters of the finite element modeling are summarized in Table 1. To verify compliance with the specified requirements and evaluate the performance of the developed calibration, measurements were taken from the finite element model of the pipe profile, including height (*A*), width (*B*), and wall thickness at the front end (FE), center, and rear end (RE) of the pipe after each stand.

Based on the research findings, the following technological scheme for profile pipe production was approved:

- formation and welding of round-section tubes with dimensions 9.0×0.9 mm, lengths of 5 – 6 m, made of 08Kh18N10T stainless steel on the PEWU, using an argon-hydrogen gas mixture;
- heat treatment;
- straightening;
- profiling in a mill with two driven two-roll stands with box gauges and two non-driven four-roll stands to achieve the final dimensions of 10.0×3.8×0.9 mm, with pipe movement ensured by six driven two-roll stands equipped with rolls from the calibration set designed for 9 mm diameter pipes;
- secondary heat treatment;
- final acceptance tests.

Table 1. Geometric parameters of pipe samples after modeling

Таблица 1. Геометрические параметры образцов труб после моделирования

Stand number	Overall dimensions, mm					
	<i>A</i>			<i>B</i>		
	FE	center	RE	FE	center	RE
1	10.27	10.27	10.25	5.31	5.34	5.31
2	9.73	9.78	9.82	5.86	5.83	5.81
3	10.14	10.13	10.14	4.84	4.82	4.84
4	10.08	10.08	10.09	3.88	3.86	3.82
5	10.06	10.08	10.07	3.86	3.85	3.82
Quality requirements	10.00 ± 0.10			3.80 ± 0.10		

¹ Korneev A.B., Morgulets S.V., Klimov M.A., Devyatov S.V. Experience in Using the MSC Marc System to Solve Complex Problems. URL: https://www.cadmater.ru/magazin/articles/cm_29_msc.html (accessed on December 12, 2024).

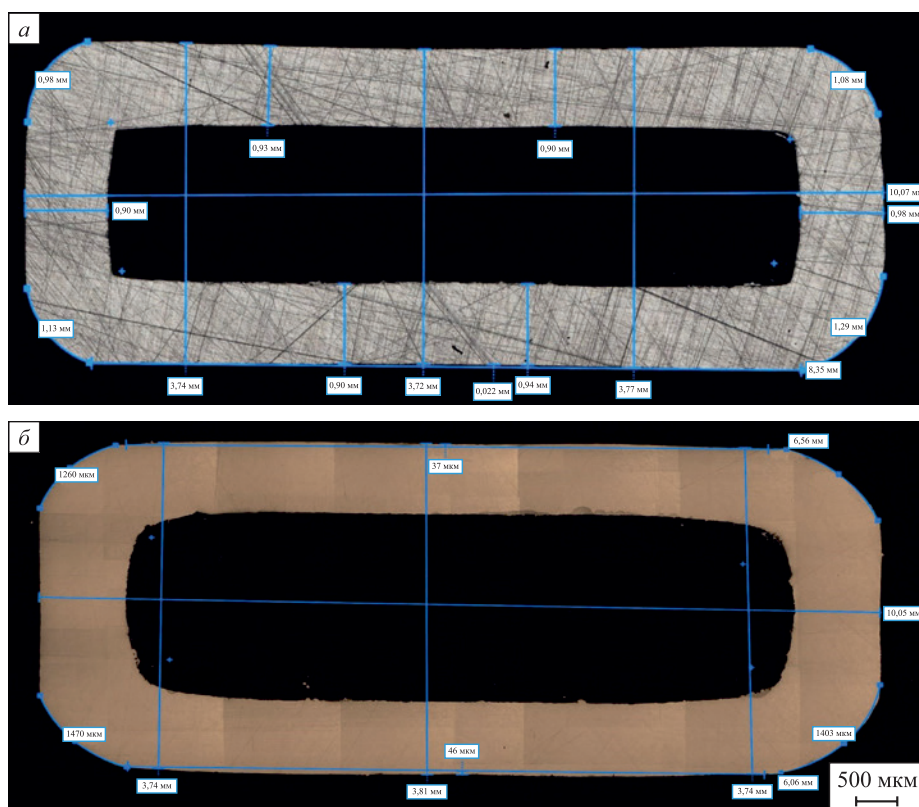


Fig. 3. Geometric parameters of pipes manufactured by: a Russian (a), and foreign enterprise (b)

Рис. 3. Геометрические параметры труб, произведенных на российском (a) и зарубежном (b) предприятиях

The shaping mill was upgraded and equipped with an additional motor to ensure the stable operation of the drive system and increased pulling capacity.

The next stage involved a series of pilot industrial rolling tests to refine the pipe profiling technology. Seamless pipes with diameters ranging from 8.40 to 8.75 mm and wall thicknesses from 0.88 to 1.05 mm were used as billets. Profiling modes were tested at speeds ranging from 0.5 to 1.5 m/min [23].

To ensure proper corner filling, sequential deformation of the billet in vertical and horizontal planes was applied, with minimal compression of the cross-sectional perimeter [24; 25].

As a result of the experimental rolling, a trial industrial batch of profile pipes with a total weight of 50 kg was produced. The geometric characteristics of the pipes

were examined using an optical microscope and specialized software.

The measurement results are shown in Fig. 3, a.

For comparison of geometric parameters, similar studies were conducted on pipe samples supplied by a foreign manufacturer (Fig. 3, b).

RESEARCH RESULTS

Based on the results of the research and experiments, the developed profiling technology was approved as the standard for producing pipes with dimensions of 10.0×3.8×0.9 mm on the profiling mill.

The results of geometric parameter measurements for pipes produced at Russian and foreign facilities are summarized in Table 2.

Table 2. Geometric parameters of pipe samples

Таблица 2. Геометрические параметры образцов труб

Manufacturer	Overall dimensions, mm		Radius of corners' outer rounding, mm				Convexity/ concavity of flanges, mm
	<i>A</i>	<i>B</i>					
Russian enterprise	10.07	3.72 – 3.77	0.98	1.08	1.13	1.29	(–0.022) – (–0.030)
Foreign enterprise	10.05	3.74 – 3.81	1.26	1.56	1.40	1.47	(+0.037) – (+0.046)
Quality requirements	10.00 ± 0.10	3.80 ± 0.10	0.90 – 1.20				0.10

CONCLUSIONS

The developed profiling technology enables the production of profile pipes that outperform foreign counterparts in geometric characteristics, particularly in the radius of the corners' outer rounding.

The adoption of this technology has contributed to strengthening the technological sovereignty of the Russian Federation's economy, as outlined in Direction No. 13.1.3 of Government Decree No. 603, dated April 15, 2023.

Implementing the continuous profile production scheme, which includes heat treatment and profiling within the pipe-electric welding unit (PEWU) line, ensures full compliance with the requirements for profile pipes used in turbo-generator stator windings. This is achieved through significantly reduced variations in wall thickness in pipe billets produced by welding from coil stock.

REFERENCES / СПИСОК ЛИТЕРАТУРЫ

1. Berezovskii S.F., Kropylev F.M. Rollforming. Moscow: Metallurgiya; 1978:152. (In Russ.).
Березовский С.Ф., Кропылев Ф.М. Производство гнутых профилей. Москва: Металлургия; 1978:152.
2. ASTM A554 Standard Specification for Welded Stainless Steel Mechanical Tubing. Copyright © ASTM International, West Conshohocken, PA, United States.
3. Akopyan K.E., Yusupov V.S., Koryakovskii E.D., Kontievskii I.L., Bolobanova N.L. Concerning the profiling of electrowelded steel pipes with a triangular cross section. *Steel in Translation*. 2023;53(11):1050–1055.
<https://doi.org/10.3103/S0967091223110037>
4. Blagodartsev I.V., Shemshurova N.G. About process modeling of molding of triangular cross-section pipes from the round ones. *Izvestiya. Ferrous Metallurgy*. 2014; 57(2):65–66. (In Russ.).
<https://doi.org/10.17073/0368-0797-2014-2-65-66>
Благодарцев И.В., Шемшурова Н.Г. О моделировании процесса формовки трубы треугольного поперечного сечения из круглой. *Известия вузов. Черная металлургия*. 2014;(2):65–66.
<https://doi.org/10.17073/0368-0797-2014-2-65-66>
5. Parshin S.V. Processes and Machines for the Manufacture of Profile Pipes: Scientific and Practical Ed. Yekaterinburg: USTU-UPI; 2006:356. (In Russ.).
Паршин С.В. Процессы и машины для изготовления профильных труб: научно-практическое издание. Екатеринбург: УГТУ–УПИ; 2006:356.
6. Suvorov V.I. Method for manufacturing longitudinally welded pipes of rectangular and square cross-section. Patent 2568804 RU. *Bulleten' izobretenii*. 2015:32.
Пат. 2568804 RU. Способ изготовления прямошовных труб прямоугольного и квадратного сечения / Суворов В.И.; заявлено 30.04.2014; опубликовано 20.11.2015. Бюллетень № 32.
7. Suvorov V.I., Mozzhegorov M.N., Pyatkov V.L., Pluzhnikov N.S. Optimizing the continuous production of electrowelded pipe. *Steel in Translation*. 2011;(2):135–139.
<https://doi.org/10.3103/S0967091211020173>
8. Zienkiewicz O.C., Taylor R.L., Zhu J.Z. Finite Element Method: Its Basis and Fundamentals. Seventh Edition. Elsevier Ltd; 2013:756.
<https://doi.org/10.1016/C2009-0-24909-9>
9. Fleissner F., Gaugele T., Eberhard P. Applications of the discrete element method in mechanical engineering. *Multibody System Dynamics*. 2007;18:81–94.
<https://doi.org/10.1007/s11044-007-9066-2>
10. Okulov R.A., Semenova N.V. Modeling the effect of billet diameter deviations on dimensional accuracy when profiling shaped tubes to improve the process. *Inzhenernyi vestnik Dona*. 2019;(5(56)):21–29. (In Russ.).
Окулов Р.А., Семенова Н.В. Моделирование влияния отклонений диаметра заготовки на точность размеров при изготовлении профильных труб с целью совершенствования процесса. *Инженерный вестник Дона*. 2019;(5(56)):21–29.
11. Shatrov B.V. Theoretical foundations of the analysis of structures using the finite element method. MAI; 1998:101. (In Russ.).
Шатров Б.В. Теоретические основы анализа конструкций с применением метода конечных элементов. МАИ; 1998:101.
12. Zharkov A.V. Modeling in the Marc system of processing the materials in mechanical engineering. Part 1. One-angular bending. *Vestnik mashinostroeniya*. 2012;(8):67–72. (In Russ.).
Жарков А.В. Моделирование в системе Marc обработки материалов в машиностроении. Часть 1. Одноугловая гибка. *Вестник машиностроения*. 2012;(8):67–72.
13. Zharkov A.V. Marc (CAD/CAE) system model analysis of materials processing. Part 2. Double-angle bending in absence of blank holder. *Vestnik mashinostroeniya*. 2012;(9):61–67. (In Russ.).
Жарков А.В. Моделирование в системе Marc обработки материалов в машиностроении. Часть 2. Двухугловая гибка без прижима заготовки. *Вестник машиностроения*. 2012;(9):61–67.
14. Zharkov A.V. Marc (CAD/CAE) system model analysis of materials processing. Part 3. Double-angle bending with blank holding. *Vestnik mashinostroeniya*. 2012;(10):60–65. (In Russ.).
Жарков А.В. Моделирование в системе Marc обработки материалов в машиностроении. Часть 3. Двухугловая гибка с прижимом заготовки. *Вестник машиностроения*. 2012;(10):60–65.
15. Zharkov A.V. Marc system modeling materials processing in engineering. Part 4. Extension of axisymmetric part without wall necking. *Vestnik mashinostroeniya*. 2012;(11):58–64. (In Russ.).
Жарков А.В. Моделирование в системе Marc обработки материалов в машиностроении. Часть 4. Вытяжка осесимметричной детали без утонения стенки. *Вестник машиностроения*. 2012;(11):58–64.
16. Zharkov A.V. Marc system modeling materials processing in engineering. Part 5. Extension of axisymmetric part with wall necking. *Vestnik mashinostroeniya*. 2012;(12):54–61. (In Russ.).

- Жарков А.В. Моделирование в системе Marc обработки материалов в машиностроении. Часть 5. Вытяжка осесимметричной детали с утонением стенки. *Вестник машиностроения*. 2012;(12):54–61.
17. Zharkov A.V. Material processing model analysis in Marc system in engineering. Part 6. Draw-forming complex part. *Vestnik mashinostroeniya*. 2013;(2):67–73. (In Russ.).
- Жарков А.В. Моделирование в системе Marc обработки материалов в машиностроении. Часть 6. Вытяжка детали сложной формы. *Вестник машиностроения*. 2013;(2):67–73.
18. Zharkov A.V. Material processing model analysis in Marc system in engineering. Part 7. Test and editing by stretching. *Vestnik mashinostroeniya*. 2013;(3):43–47. (In Russ.).
- Жарков А.В. Моделирование в системе Marc обработки материалов в машиностроении. Часть 7. Испытания и правка растяжением. *Вестник машиностроения*. 2013;(3):43–47.
19. Lepestov A.E., Sokolova O.V., Skripkin A.Yu. Effect of deformation of a stand with an open gauge profile on accuracy of continuous pipe forming. *Proizvodstvo prokata*. 2011;(5):32–34. (In Russ.).
- Лепестов А.Е., Соколова О.В., Скрипкин А.Ю. Исследование влияния деформации клетки с открытым профилем калибра на точность непрерывной формовки труб. *Производство проката*. 2011;(5):32–34.
20. Ji-ying L.I.U., Seldmair A. Computer aided design for roll-forming shaped tube. In: *Proceedings of the 5th Tube Tech China. Wuzhen, Jiaxing city, Zhejiang province: Lecture Notes in Electrical Engineering*. 2022:87–92.
21. Shevakin Yu.V. Machines and Units for Production of Steel Pipes. Moscow: Inetermet Inzhiniring; 2007:388. (In Russ.).
- Шевакин Ю.В. Машины и агрегаты для производства стальных труб. Москва: Интермет Инжиниринг; 2007:388.
22. Matveev Yu.M., Vatin Ya.L. Calibration of Pipe Mill Tools. Moscow: Metallurgiya; 1970:480. (In Russ.).
- Матвеев Ю.М., Ваткин Я.Л. Калибровка инструмента трубных станов. Москва: Металлургия; 1970:480.
23. Vydrin A.V., Shirokov V.V. Speed simulation of continuous pipe rolling. *Steel in Translation*. 2011;41:140–142. <https://doi.org/10.3103/S0967091211020215>
24. Suvorov V.I., Varnak A.G., Mozzhegorov M.N. Calculation of perimeter and weight of currently produced profile pipes of. In: *Pipes – 2011: Proceedings of the Int. Sci.-Pract. Conf. 27–28, 2011, Chelyabinsk. Vol. 2. Chelyabinsk: Truby-2011; 2011:77–89. (In Russ.).*
- Суворов В.И., Варнак А.Г., Мозжегоров М.Н. Расчет периметра и веса профильных труб текущего производства. В кн.: *Трубы – 2011: Труды Международной научно-практической конференции 27–28 сентября 2011, Челябинск. Том 2. Челябинск: Издательство «Трубы-2011»; 2011:77–89.*
25. Farahmad H.R., Abrinia K. An upper bound analysis for reshaping thick tubes to polygonal cross section tubes through multistage roll forming process. *International Journal of Mechanical Science*. 2015;100:90–98. <https://doi.org/10.1016/j.ijmecsci.2015.06.012>

Information about the Authors

Сведения об авторах

Mikhail N. Mozzhegorov, Senior Researcher of the Laboratory of Pipe Strength and Welding, LLC "TMK Research Center", Chelyabinsk
ORCID: 0009-0007-6400-1634
E-mail: mozzhegorov@rosniti.ru

Mariya S. Mashentseva, Research Associate in the Pipe Forming Sector, LLC "TMK Research Center", Chelyabinsk
ORCID: 0000-0001-7856-3266
E-mail: mashentseva@rosniti.ru

Михаил Николаевич Мозжегоров, старший научный сотрудник лаборатории прочности и сварки труб, ООО «Исследовательский центр ТМК» в г. Челябинск
ORCID: 0009-0007-6400-1634
E-mail: mozzhegorov@rosniti.ru

Мария Сергеевна Машенцева, научный сотрудник сектора формовки труб, ООО «Исследовательский центр ТМК» в г. Челябинск
ORCID: 0000-0001-7856-3266
E-mail: mashentseva@rosniti.ru

Received 08.05.2024
 Revised 23.09.2024
 Accepted 12.11.2024

Поступила в редакцию 08.05.2024
 После доработки 23.09.2024
 Принята к публикации 12.11.2024



UDC 621.771.06

DOI 10.17073/0368-0797-2025-1-14-20



Original article

Оригинальная статья

STIFFNESS MODULUS OF STANDS IN FINISHING GROUP OF CONTINUOUS WIDE-STRIP HOT ROLLING MILL

I. D. Pospelov[✉]

■ Cherepovets State University (5 Lunacharskogo Ave., Cherepovets, Vologda Region 162600, Russian Federation)

✉ idpospelov@chsu.ru

Abstract. Stiffness modulus is an important technical parameter of each four-high stand of continuous wide-strip hot rolling mill and characterizes the roll force that causes elastic deformation of all structural elements of the working stand in the assembly. Accuracy of deviations of longitudinal and widthwise profile of hot-rolled strips and quality of sheet products directly depends on reliability of determination of such parameter at the design stage of efficient technological rolling schedule. After review of classical methods for calculating elastic deformations of four-high stands based on the laws of the elasticity theory and modern publications, it was concluded that it is necessary to take into account the dynamic component when determining the stiffness modulus of the working stands of hot and cold rolling mills. Lack of record-keeping above the specified component entails significant errors in the alignment of the roll gaps at the stage of mill setting for rolling the strips of the required final thickness. In this work, we studied the stiffness modulus of the finishing stands of the operating continuous wide-strip mill, taking into account their constructional features in the production of hot-rolled strips of various sheet gauge of low-carbon steels, mainly intended for further cold rolling. When analyzing experimental data, reliable regression equations were obtained that allow taking into account the effect of the rolled strip width on the stiffness modulus of stands. The results of investigations are presented in graphical and tabular form, demonstrating the change in the stiffness modulus for different mill stands. The results allow us to design and make changes to the existing hot rolling modes in order to ensure the required accuracy of the longitudinal and widthwise profile of hot-rolled strips.

Keywords: stiffness modulus of four-high stand, continuous wide-strip hot rolling mill, rolling force, rolling gap, strip width, regression equations, rolling schedule

For citation: Pospelov I.D. Stiffness modulus of stands in finishing group of continuous wide-strip hot rolling mill. *Izvestiya. Ferrous Metallurgy*. 2025;68(1):14–20. <https://doi.org/10.17073/0368-0797-2025-1-14-20>

ИССЛЕДОВАНИЕ МОДУЛЯ ЖЕСТКОСТИ КЛЕТЕЙ ЧИСТОВОЙ ГРУППЫ НЕПРЕРЫВНОГО ШИРОКОПОЛОСНОГО СТАНА ГОРЯЧЕЙ ПРОКАТКИ

И. Д. Поспелов[✉]

■ Череповецкий государственный университет (Россия, 162600, Вологодская обл., Череповец, пр. Луначарского, 5)

✉ idpospelov@chsu.ru

Аннотация. Модуль жесткости является важным техническим параметром каждой клетки «кварто» непрерывного широкополосного стана горячей прокатки и характеризует величину усилия прокатки, вызывающую упругую деформацию всех конструктивных элементов рабочей клетки в сборе. От достоверности определения такого параметра на этапе проектирования эффективных технологических режимов прокатки напрямую зависит точность отклонений продольного и поперечного профиля горячекатаных полос и качество листового проката. При обзоре классических методов расчета упругих деформаций рабочих четырехвалковых клеток, основанных на законах теории упругости, и современных публикаций сделан вывод, что необходимо учитывать динамическую составляющую при определении модуля жесткости рабочих клеток станов горячей и холодной прокатки. Отсутствие учета вышеуказанной составляющей влечет за собой существенные ошибки в выставлении межвалковых зазоров на этапе настройки стана под прокатку полос требуемой конечной толщины. В данной работе выполнено исследование модуля жесткости клеток чистовой группы действующего непрерывного широкополосного стана с учетом их конструктивных особенностей при производстве горячекатаных полос различного листового сортамента низкоуглеродистых сталей, преимущественно предназначенных для дальнейшей холодной прокатки. При анализе экспериментальных данных получены достоверные уравнения регрессии, позволяющие учитывать влияние ширины прокатываемой полосы на модуль жесткости клеток. Исследование представлено в графической и табличной форме, демонстрирующей изменение значений модуля жесткости для различных клеток стана. Результаты исследования позволяют проектировать и вносить изменения в существующие технологические режимы горячей прокатки с целью обеспечения требуемой точности продольного и поперечного профиля горячекатаных полос.

Ключевые слова: модуль жесткости четырехвалковой клетки, непрерывный широкополосный стан горячей прокатки, усилие прокатки, межвалковый зазор, ширина полосы, уравнения регрессии, режимы прокатки

Для цитирования: Поспелов И.Д. Исследование модуля жесткости клеток чистовой группы непрерывного широкополосного стана горячей прокатки. *Известия вузов. Черная металлургия*. 2025;68(1):14–20. <https://doi.org/10.17073/0368-0797-2025-1-14-20>

INTRODUCTION

In recent decades, global production standards have tightened tolerances for deviations in the longitudinal and widthwise profile of hot-rolled strips made of low-carbon steels. This trend is driven by the increasing requirements for the quality of sheet products. These requirements apply both to the thinnest hot-rolled strips (0.8 – 1.5 mm thick), which are directly used in mechanical engineering and construction, and to strips with a thickness of 1.8 – 5.5 mm, which serve as semifinished rolled stock for cold rolling mills, where they undergo further processing to meet strict geometric tolerances for longitudinal and widthwise profiles.

The accuracy requirements for hot-rolled steel sheets supplied in stacks and coils are regulated by GOST 19903–74, which classifies sheets into two accuracy groups: high accuracy (Group A) and normal accuracy (Group B). Depending on their thickness and width, these sheets are subject to different thickness tolerances. For example, sheets with a thickness of 1.8 – 2.0 mm and a width of 1500 – 1820 mm have a thickness tolerance of ± 0.17 mm for high accuracy and ± 0.20 mm for normal accuracy. However, even stricter requirements apply to hot-rolled strips intended for cold rolling mills for the production of autobody sheet. In such cases, thickness deviations across the entire surface must not exceed $\pm(2 - 5)$ % of the nominal thickness of the semifinished rolled stock [1].

Reducing deviations in the standardized characteristics of the longitudinal profile of hot-rolled strips within the specified tolerances has driven the development of thin-strip hot rolling theory [2 – 4]. Based on this theory, models have been developed to control longitudinal and widthwise thickness deviation, considering all significant technological parameters of the rolling schedule [5 – 7].

A review of international publications reveals a direct correlation between the accuracy parameters of the longitudinal and widthwise profile of hot-rolled [8 – 10] and cold-rolled strips [11; 12] and the stiffness parameters of both individual structural elements and the assembled four-high stands. Similar studies are widely represented in classical domestic textbooks [13 – 15]. Of particular interest is the stiffness modulus of each stand in the continuous rolling mill, as the accuracy of determining this characteristic directly affects the proper setting of the rolling gap [16; 17]. This, in turn, influences the precision of the initial mill setup and the effectiveness of control

actions for adjusting strip thickness accuracy during rolling [18 – 20].

The objective of this study is to investigate changes in the stiffness modulus of finishing stands in continuous hot rolling mills for various strip gauges by analyzing experimental data obtained from an operating wide-strip rolling mill.

MATERIALS AND METHODS

The equation describing the direct linear relationship between the elastic deformation of the four-high stand and the rolling force P_i acting on the rolls can be expressed as follows:

$$P_i = M_{st}(h_i - S_i), \quad (1)$$

where M_{st} is the stiffness modulus of the four-high stand, MN/mm; h_i is the strip thickness after rolling in the i -th stand, mm; S_i is the initially set roll gap in the i -th working stand, mm.

As previously noted, the accuracy of determining M_{st} in equation (1), given a specified strip thickness h_i , directly affects the correct initial setting of the roll gap S_i and, consequently, the overall rolling precision.

During metal reduction to the required thickness h_i , the working rolls experience a rolling force P_i , which can be assumed to act vertically. This force is transmitted through all structural elements of the assembled stand, including the four-high roll system, thrust bearings with pressure capsules, back-up chocks, thrust bearings of mill screws, mill screws, packing nuts of mill screws, and close-top roll housings (Fig. 1). Classical methods for calculating elastic deformations in four-high working stands [13 – 15] are based on the assumption that all structural components deform according to the laws of elasticity. Using this assumption, the stiffness modulus of each four-high working stand in a continuous mill is determined through well-established theoretical formulas for the elastic deformation of all the aforementioned components that bear the vertical rolling force during operation. However, as noted in [13 – 15], these formulas apply only to the static stiffness modulus and do not account for key dynamic factors, such as the influence of back-up roll rotational speed on deformation within hydrodynamic bearings, the horizontal displacement of vertical axial planes of back-up and working rolls relative to each other [21], and other rolling dynamics [10 – 12] affecting all assembled stand components.

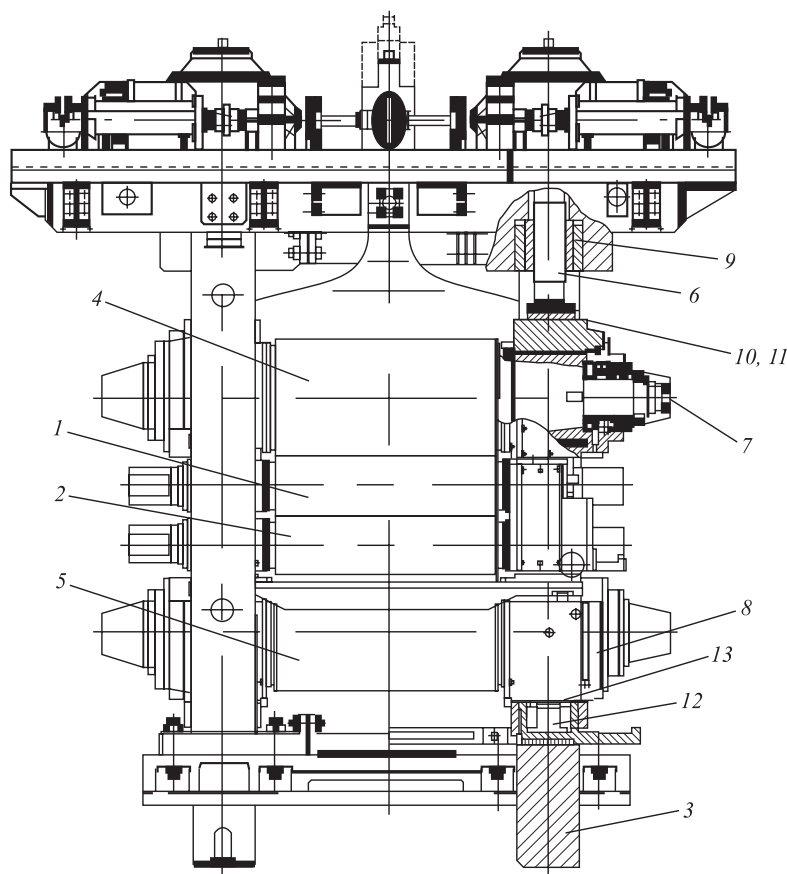


Fig. 1. Construction of four-high stand of hot rolling mill:

1, 2 – working rolls; 3 – close-top roll housing; 4, 5 – back-up rolls; 6 – mill screw; 7, 8 – back-up chocks;
9 – packing nut; 10 – thrust bearing of mill screw; 11 – pressure capsule of mill screw;
12 – bearing part of lower back-up chocks; 13 – pressure capsule of lower back-up chocks

Рис. 1. Конструкция четырехвалковой клетки стана горячей прокатки:

1, 2 – рабочие валки; 3 – станина закрытого типа; 4, 5 – опорные валки; 6 – нажимной винт;
7, 8 – подушки опорных валков; 9 – гайка нажимная; 10 – подпятник нажимного винта; 11 – месдоза нажимного винта;
12 – опора подушки нижнего опорного валка; 13 – месдоза нижней подушки

Under modern operating conditions, assessing the stiffness modulus of mill stands is most efficiently conducted using loading curves obtained by pre-stressing the rotating working rolls into the pre-stressed stand position. This method was applied to evaluate the stiffness modulus of the four-high stands in the finishing group of hot rolling mill 2000 at PAO Severstal. The loading force during the assessment was varied within the actual operating rolling force range: from 0 to 30 MN for stands 6–9 and from 0 to 20 MN for stands 10–12, while maintaining a constant working roll rotation speed equal to the average strip rolling speed in the i -th stand. To minimize the additional measurement errors, a coolant was applied to the rolls during loading before the start of measurements.

The experimental data on loading force $P_{ld,i}$ and total elastic deformations in the i -th finishing stand $S_{st,i}$ were recorded by the automated process control system (APCS) of the finishing group of hot rolling mill 2000. The processed data were then presented graphically in

Fig. 2, showing the relationship between the total loading force $P_{ld,i}$ of each stand and the elastic deformation of all structural elements of the stand $S_{st,i}$. The material properties and nominal diameters of the working and back-up rolls are listed in Table 1.

The stiffness modulus of the pre-stressed stand in the i -th stand $M_{st,i}^0$ was determined based on the linear portion of the curves in Fig. 2, using the ratio of the loading force $P_{ld,i}$ to the elastic deformation of the stand $S_{st,i}$:

$$M_{st,i}^0 = \frac{P_{ld,i}}{S_{st,i}}. \quad (2)$$

Analysis of the curves in Fig. 2 showed that for all mill stands, the onset of the linear deformation region occurs at a loading force of 6.484–3.041 MN, with higher values corresponding to the first stands. As the loading force increases further, the stand deformation follows a strictly linear trend, remaining fully compliant with elasticity laws across the entire operating force range.

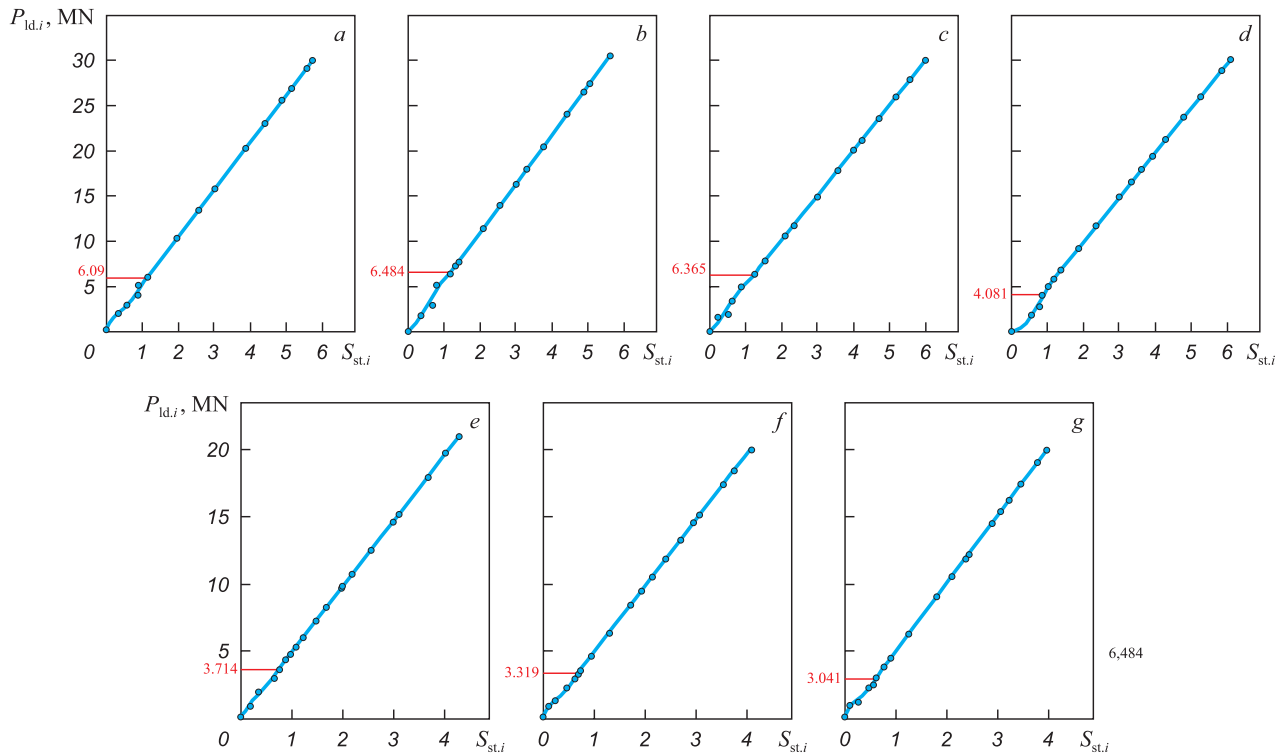


Fig. 2. Graphics of loading pre-stressed stands of rotating work rolls:
a – stand 6; b – stand 7; c – stand 8; d – stand 9; e – stand 10; f – stand 11; g – stand 12

Рис. 2. Графические схемы нагружения клетей стана методом предварительного сжатия вращающихся рабочих валков:
a – клеть 6; b – клеть 7; c – клеть 8; d – клеть 9; e – клеть 10; f – клеть 11; g – клеть 12

Determining the stiffness modulus of the pre-stressed stand $M_{st,i}^0$ using equation (2), based on the data from Fig. 2, and its subsequent application without significant error is valid for rolling strips in the finishing group of hot rolling mill 2000 at a maximum width of $b_i = 1820$ mm.

The dependence of the stiffness modulus of the four-high stands in the finishing group of hot rolling mill 2000 on the width of the rolled strip b_i was investigated using

the following methodology. During steady-state rolling, all stands operate under conditions of constant positioning of the screw-down mechanisms. As the strip undergoes deformation in the i -th stand, the APCS of the finishing group records the average strip thickness h_i , the rolling force P_i and the average elastic deformation of the stand $S_{st,i}$. The averaged stiffness modulus of the i -th stand $M_{st,i}^b$, considering the variation in strip width b_i can be calculated using equation

Table 1. Elastic material characteristics and nominal diameters of working and back-up rolls in finishing group of mill 2000

Таблица 1. Упругие свойства материала и номинальные диаметры рабочих и опорных валков клетей чистовой группы стана 2000

Stand No.	D_w , mm	E_w , MPa	ν_w	Working roll material	D_b , mm	E_b , MPa	ν_b
6	930	200,000	0.29	High-chromium hardened cast iron	1600	219,000	0.35
7	890	205,000					
8	800	215,000	0.32	High-chromium heat-resistant cast iron			
9, 10	800	175,000	0.28	Indefinite chill cast iron			
11, 12	825						

N o t e: D_w – nominal diameter of working rolls; E_w – elastic modulus of working roll material; ν_w – Poisson’s ratio of working roll material; D_b – nominal diameter of back-up rolls; E_b – elastic modulus of back-up roll material; ν_b – Poisson’s ratio of back-up roll material.

$$M_{st,i}^b = \frac{P_i}{S_{st,i}}. \quad (3)$$

The physical meaning of this parameter $M_{st,i}^b$ reflects the change in the stand's elastic deformation due to the deflection of the roll system under the rolled strip of width b_i . The difference between the stiffness modulus of the stand without a strip $M_{st,i}^0$ and the calculated value obtained using equation (3) is denoted as $\Delta M_{st,i}^b$. Upon completion of the study, databases were compiled to record the following rolling parameters for the i -th stand:

- average strip width b_i and average strip thickness h_i of the rolled strip;
- value of the change in elastic deformation of the stand $S_{st,i}$;
- calculated value of the correction factor $\Delta M_{st,i}^b$.

Thus, the stiffness modulus of the stand for a strip width b_i less than 1820 mm, accounting for the correction factor $\Delta M_{st,i}^b$, can be determined using the following equation

$$M_{st,i} = M_{st,i}^0 - \Delta M_{st,i}^b, \quad (4)$$

where $M_{st,i}^0$ is represents the stiffness modulus of the pre-stressed stand, MN/mm; $\Delta M_{st,i}^b$ is the correction factor for assessing the stiffness modulus of the i -th stand, considering the variation in rolled strip width b_i , MN/mm.

RESULTS AND DISCUSSION

The dataset prepared for regression analysis was obtained from 46 rolling schedules in the finishing group of hot rolling mill 2000, covering low-carbon steel strips with thicknesses ranging from 1.2 to 5.5 mm and widths from 1005 to 1625 mm. These strips were primarily intended for further cold rolling and were processed using different sets of working and back-up rolls. During the regression analysis, linear equations (Table 2), were derived, which accurately describe the correction factor $\Delta M_{st,i}^b$ for the stiffness modulus of the pre-stressed stand $M_{st,i}^0$ as a function of the rolled strip width b_i .

Since the actual values of Fisher's criterion F in Table 3 significantly exceed the critical value $F_{cr}(1; 44) = 4$ at degrees of freedom $k_1 = 1$ and $k_2 = 44$, the determination coefficients R^2 are statistically significant, confir-

Table 2. Values of stiffness modulus of pre-stressed stand $M_{st,i}^0$, regression equations for $\Delta M_{st,i}^b$ calculation and their reliability

Таблица 2. Значения модуля жесткости клетки «забоя» $M_{st,i}^0$, регрессионные уравнения расчета $\Delta M_{st,i}^b$ и их достоверность

Stand No.	$M_{st,i}^0$, MN/mm	Regression equation for calculating $\Delta M_{st,i}^b$, MN/mm	R^2	F
6	5.25	$0.6136 - 0.000300b_i$	0.8928	183.22
7	5.45	$0.8247 - 0.000410b_i$	0.8349	111.25
8	5.00	$0.9884 - 0.000494b_i$	0.9552	469.07
9	4.95	$1.0474 - 0.000524b_i$	0.9140	233.81
10	4.89	$1.0409 - 0.000520b_i$	0.9540	456.26
11	4.93	$0.8574 - 0.000428b_i$	0.9194	205.95
12	5.055	$0.9173 - 0.000458b_i$	0.9417	355.36

Table 3. Calculated values of rolling stands stiffness modulus and verification thereof by force calculation

Таблица 3. Расчетные значения модуля жесткости клетки и проверка их достоверности путем расчета усилия

Stand No.	$\Delta M_{st,i}^b$, MN/mm	$M_{st,i}$, MN/mm	h_i , mm	S_i , mm	P_i , MN		ΔP_i , %
					calculated	measured	
6	0.386	5.0264	18.55	13.260	26.590	25.070	6.06
7	0.297	5.1583	10.02	4.510	28.422	27.588	3.02
8	0.353	4.6538	5.63	1.303	20.137	20.682	2.64
9	0.373	4.5838	3.95	0.620	15.264	15.786	3.31
10	0.372	4.5251	2.89	−0.464	15.177	15.547	2.38
11	0.306	4.6290	2.28	−0.797	14.243	14.292	0.34
12	0.328	4.7331	2.00	0.151	8.7515	8.787	0.40

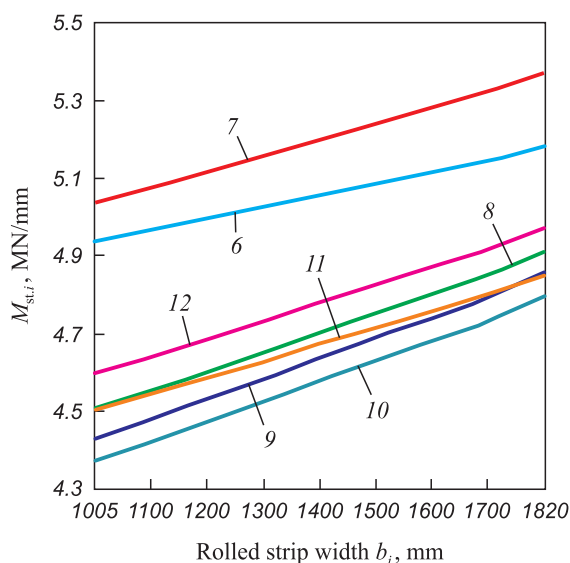


Fig. 3. Graphics of change in stiffness modulus $M_{st,i}$ depending on width of rolled strip b_i : (numbers of curves – numbers of stands)

Рис. 3. Графики изменения модуля жесткости $M_{st,i}$ в зависимости от ширины прокатываемой полосы b_i : (цифры кривых – номер клетки)

ming the reliability of the regression equations for $\Delta M_{st,i}^b$ in Table 2. These equations are valid within the following parameter ranges:

- working roll crown profiles from -0.5 to -0.15 mm;
- working roll diameters from 930 to 800 mm;
- back-up roll diameters from 1616 to 1488 mm;
- back-up roll chamfer depth of 0.8 mm and chamfer length of 300 mm.

Based on the Table 3 data, graphs were plotted (Fig. 3) to illustrate the variation in the stiffness modulus $M_{st,i}$ for each stand in the finishing continuous group of hot rolling mill 2000, depending on the rolled strip width b_i .

The accuracy of determining the stiffness modulus $M_{st,i}$ considering the correction factor $\Delta M_{st,i}^b$ for strip width variation b_i , was verified by solving equation (1) and comparing the measured rolling force P_i in the i -th stand during the rolling of a 2.0 mm-thick, 1300 mm-wide strip of 08Yu steel. The initial roll gap S_i was recorded by the APCS of the finishing group of hot rolling mill 2000, as shown in Table 3. The calculated and measured rolling forces, along with their comparison results, are also provided in Table 3.

Since the maximum comparison error ΔP_i in Table 3 does not exceed 6.06 %, the findings of this study can be effectively applied in designing hot rolling schedules for hot rolling mill 2000. These results ensure the required longitudinal and widthwise profile accuracy of hot-rolled strips while incorporating control models for longitudinal and widthwise thickness deviations [5 – 7].

CONCLUSIONS

Based on the analysis of experimental data, reliable dependencies have been established that describe the effect of rolled strip width on the variation of the stiffness modulus of four-high stands in the finishing group of the operating hot rolling mill.

It has been determined that rolling within the finishing group, from the first to the last stand, with rolling forces below 6.484 – 3.041 MN is undesirable, as under such conditions, the stands experience nonlinear deformation, leading to additional fluctuations in the roll gap.

The research findings can be applied in the development of optimized rolling schedules for the finishing group of mill stands, ensuring the production of hot-rolled strips with minimal deviations in the longitudinal and widthwise geometric profile characteristics.

REFERENCES / СПИСОК ЛИТЕРАТУРЫ

1. Garber E.A. Cold Rolling Mills. Moscow: Chermetinformat-sia; 2004:416. (In Russ.).
Гарбер Э.А. Станы холодной прокатки. Москва: Чермет-информация; 2004:416.
2. Garber E.A., Kozhevnikova I.A., Tarasov P.A. Calculation of hot rolling forces of thin strips taking into account the stress-strain state in adhesion region of deformation zone. *Proizvodstvo prokata*. 2007;(4):7–15. (In Russ.).
Гарбер Э.А., Кожевникова И.А., Тарасов П.А. Расчет усилий горячей прокатки тонких полос с учетом напряженно-деформированного состояния в зоне прилипания очага деформации. *Производство проката*. 2007;(4):7–15.
3. Garber E.A., Kozhevnikova I.A., Tarasov P.A., Zavrazh-nov A.A., Traino A.I. Simulation of contact stresses and forces during hot rolling of thin wide strips with allowance for a stick zone and elastic regions in the deformation zone. *Russian Metallurgy (Metally)*. 2007;(2):112–119.
<https://doi.org/10.1134/S003602950702005X>
Гарбер Э.А., Кожевникова И.А., Тарасов П.А., Завраж-нов А.А., Трайно А.И. Моделирование контактных на-пряжений и усилий горячей прокатки тонких широких полос с учетом зоны прилипания и упругих участков очага деформации. *Металлы*. 2007;(2):26–35.
4. Garber E.A., Pospelov I.D., Kozhevnikova I.A. Influence of chemical compositions and elastic properties of strip and rolls on energy and force parameters in wide-strip hot rolling mills. *Proizvodstvo prokata*. 2011;(8):2–7. (In Russ.).
Гарбер Э.А., Пospelov И.Д., Кожевникова И.А. Влияние химического состава и упругих свойств полосы и валков на энергосиловые параметры широкополосных станов горячей прокатки. *Производство проката*. 2011;(8):2–7.
5. Garber E.A., Kozhevnikova I.A., Tarasov P.A. Effective hot rolling modes of thin strips at wide-strip mills. *Proizvodstvo prokata*. 2007;(4):7–15. (In Russ.).
Гарбер Э.А., Кожевникова И.А., Тарасов П.А. Эффек-тивные режимы горячей прокатки тонких полос на широкополосных станах. *Производство проката*. 2009;(1):10–16.

6. Garber E.A., Pospelov I.D., Traino A.I., Savinykh A.F., Nikolaev N.Yu., Mishnev P.A. Simulation of the longitudinal thickness deviation of the steel strips hot rolled in the continuous group of a broad-strip mill. *Russian Metallurgy (Metally)*. 2012;(9):831–836.
<https://doi.org/10.1134/S0036029512090042>
Гарбер Э.А., Поспелов И.Д., Траино А.И., Савиных А.Ф., Николаев Н.Ю., Мишнев П.А. Моделирование продольной разнотолщинности горячекатаных стальных полос в непрерывной группе клетей широкополосного стана. *Металлы*. 2012;(4):47–53.
7. Pospelov I.D., Rumyantsev V.V. Joint regulation of longitudinal and transverse gage variations during hot rolling in finishing group of stands of continuous broadband mill. *Rolling Production. Appendix to Journal "Technology of Metals"*. 2024;(20):10–19. (In Russ.).
<https://doi.org/10.31044/1684-2499-2024-0-20-10-19>
Поспелов И.Д., Румянцев В.В. Совместное регулирование продольной и поперечной разнотолщинности при горячей прокатке в чистовой группе клетей непрерывного широкополосного стана. *Прокатное производство. Приложение к журналу «Технология металлов»*. 2024;(20):10–19.
<https://doi.org/10.31044/1684-2499-2024-0-20-10-19>
8. Wu J., Yan X. Coupling vibration model for hot rolling mills and its application. *Journal of Vibroengineering*. 2019;21(7):1795–1809.
<https://doi.org/10.21595/jve.2019.20226>
9. Qi J.B., Wang X.X., Yan X.Q. Influence of mill modulus control gain on vibration in hot rolling mills. *Journal of Iron and Steel Research International*. 2020;27:528–536.
<https://doi.org/10.1007/s42243-020-00375-3>
10. Wang L., Hou P., Wang S., Wang C., Yan X., Wang X. Study on the effect of rolling mill dynamic stiffness on coupled vibration of hydraulic machine. *Journal of Vibroengineering*. 2024;26(3):455–468.
<https://doi.org/10.21595/jve.2023.23524>
11. Jia X.D., Wang S., Yan X.Q., Wang L.D., Wang H.P. Research on dynamic response of cold rolling mill with dynamic stiffness compensation. *Electronics*. 2023;12(3):0599.
<https://doi.org/10.3390/electronics12030599>
12. Gong D.Y., Xu J.Z., Yuan F.C. Study on roll elastic deformation asymmetrical 4-high mill stiffness. *Journal of Northeastern University (Natural Science)*. 2012; 33(11):1586–1590.
13. Tselikov A.I., Polukhin P.I., Grebenik V.M., etc. *Machines and Aggregates of Metallurgical Plants: Textbook: in 3 vols.* Moscow: Al'yans; 2018. (In Russ.).
Целиков А.И., Полухин П.И., Гребеник В.М. и др. *Машины и агрегаты металлургических заводов: Учеб-*
- ник для студентов металлургических и машиностроительных специальностей вузов: в 3-х томах. Москва: Альянс; 2018:679.
14. Korolev A.A. *Mechanical Equipment of Rolling and Pipe Shops: Textbook for Universities.* Moscow: Metallurgiya; 1987:480. (In Russ.).
Королев А.А. *Механическое оборудование прокатных и трубных цехов: Учебник для вузов.* Москва: Металлургия; 1987:480.
15. Grigoryan G.G., Zhelezov Yu.D., Chernyi V.A., Kuznetsov L.A., Zhuravskii A.G. *Adjustment, Stabilization and Control of Thin-Sheet Rolling.* Moscow: Metallurgiya; 1975. (In Russ.).
Григорян Г.Г., Железнов Ю.Д., Черный В.А., Кузнецов Л.А., Журавский А.Г. *Настройка, стабилизация и контроль процесса тонколистовой прокатки.* Москва: Металлургия; 1975:368.
16. Wenyu M., Fenqin W., Xibang Z., Wei G., Ziyang L., Lin T. Influence of rolling force and roll gap on thickness of strip. *IOP Conf. Series: Materials Science and Engineering*. 2017;239:012012.
<https://doi.org/10.1088/1757-899X/239/1/012012>
17. Laihua T., Qiaoyi W., Huajie W. Establishment and numerical analysis of rolling force model based on dynamic roll gap. *Applied Sciences*. 2023;13(13):7394.
<https://doi.org/10.3390/app13137394>
18. Zhenhua W., Yu H., Yuanming L., Tao W. Prediction model of strip crown in hot rolling process based on machine learning and industrial data. *Metals*. 2023;13(5):900.
<https://doi.org/10.3390/met13050900>
19. Haibo X., Xingsheng L., Tao Z. Numerical analysis of the effect of work roll bending on strip crown during tandem hot rolling. *International Journal of Applied Mechanics*. 2022;14(07):2250052.
<https://doi.org/10.1142/S1758825122500521>
20. Liu G.M., Li Y.G., Huang Q.X., Yang X. Axial force analysis and roll contour configuration of four-high CVC mill. *Mathematical Problems in Engineering*. 2018;(2):7527402.
<https://doi.org/10.1155/2018/7527402>
21. Garber E.A., Kozhevnikova I.A., Tarasov P.A., Traino A.I. Effect of sliding and rolling friction on the energy-force parameters during hot rolling in four-high stands. *Russian Metallurgy (Metally)*. 2007;(6):484–491.
<https://doi.org/10.1134/S0036029507060080>
Гарбер Э.А., Кожевникова И.А., Тарасов П.А., Траино А.И. К вопросу о влиянии трения первого и второго рода на энергосиловые параметры горячей прокатки в клетях кварто. *Металлы*. 2007;(6):47–56.

Information about the Author

Ivan D. Pospelov, Cand. Sci. (Eng.), Assist. Prof., Cherepovets State University
ORCID: 0009-0000-5974-5718
E-mail: idpospelov@chsu.ru

Сведения об авторе

Иван Дмитриевич Поспелов, к.т.н., доцент, Череповецкий государственный университет
ORCID: 0009-0000-5974-5718
E-mail: idpospelov@chsu.ru

Received 24.07.2024
 Revised 18.09.2024
 Accepted 29.10.2024

Поступила в редакцию 24.07.2024
 После доработки 18.09.2024
 Принята к публикации 29.10.2024



UDC 669.15-194.55:539.374

DOI 10.17073/0368-0797-2025-1-21-29



Оригинальная статья

Original article

TENSILE FRACTURE OF TEMPERED MARTENSITIC STEEL

L. A. Teplyakova¹✉, T. S. Kunitsyna¹, V. A. Pechkovskii¹, A. D. Kashin²

¹ Tomsk State University of Architecture and Building (2 Solyanaya Sqr., Tomsk 634003, Russian Federation)

² Institute of Strength Physics and Materials Science, Siberian Branch of the Russian Academy of Sciences (2/4 Akademicheskii Ave., Tomsk 634055, Russian Federation)

✉ lat168@mail.ru

Abstract. The work is devoted to the study of development regularities of plastic deformation and destruction of medium-alloy steel with a tempered martensite structure (0.34C–Cr–Ni–3Mo–V–Fe steel) under active tension. This steel is characterized by a multi-scale defect structure and contains cementite precipitates and special carbides. An experimental study of the evolution of defect and carbide subsystems during plastic deformation required the use of different methods: optical and electron (scanning and transmission) microscopy; X-ray structural analysis; measurements of quantitative characteristics of the microstructure and pattern of microcracks and their statistical processing. The research revealed that the places of significant localization of plastic deformation at the pre-destruction stage are the boundary areas of grains (former austenitic and real martensitic); all structural components of tempered martensite (plates, packets, blocks of laths, laths). A comparison of nature of the deformation relief and the fine structure formed before destruction with the pattern of fractures at various structural-scale levels indicates that the destruction of the steel under study, as well as the plastic deformation preceding it, bears the features of heredity of the original internal structure. Thus, the fracture of the studied steel has a multi-level nature, caused by: hierarchy of the initial internal microstructure; evolution of carbide phases; localization of plastic deformation developing at all stages of plastic deformation and, as a consequence, preparing the paths for microcracks propagation.

Keywords: tempered lath martensite, dislocation structure, deformation relief, fracture surface, scale-structural levels of fracture

For citation: Teplyakova L.A., Kunitsyna T.S., Pechkovskii V.A., Kashin A.D. Tensile fracture of tempered martensitic steel. *Izvestiya. Ferrous Metallurgy*. 2025;68(1):21–29. <https://doi.org/10.17073/0368-0797-2025-1-21-29>

РАЗРУШЕНИЕ ОТПУЩЕННОЙ МАРТЕНСИТНОЙ СТАЛИ ПРИ РАСТЯЖЕНИИ

Л. А. Теплякова¹✉, Т. С. Куницына¹, В. А. Печковский¹, А. Д. Кашин²

¹ Томский государственный архитектурно-строительный университет (Россия, 634003, Томск, пл. Соляная, 2)

² Институт физики прочности и материаловедения Сибирского Отделения РАН (Россия, 634055, Томск, пр. Академический, 2/4)

✉ lat168@mail.ru

Аннотация. Настоящая работа посвящена изучению закономерностей развития пластической деформации и разрушения среднелегированной стали со структурой отпущенного мартенсита (сталь 34ХНЗМФА) при активном растяжении. Данная сталь отличается многомасштабной дефектной структурой и содержит выделения цементита и специальные карбиды. Экспериментальное исследование эволюции дефектной и карбидной подсистем при пластической деформации потребовало применения комплекса методов: оптическая и электронная (сканирующая и просвечивающая) микроскопия, рентгеноструктурный анализ; измерения количественных характеристик микроструктуры и картины микротрещин и их статистическая обработка. В работе выявлено, что местами существенной локализации пластической деформации на стадии предразрушения являются приграничные области: зерен (бывшего аустенитного и реального мартенситного); всех структурных составляющих отпущенного мартенсита (пластины, пакеты, блоки реек, рейки). Сопоставление характера деформационного рельефа и тонкой структуры, формирующейся перед разрушением, с картиной изломов на различных структурно-масштабных уровнях свидетельствует о том, что разрушение исследованной стали, также как и пластическая деформация, ей предшествующая, несет в себе черты наследственности исходной внутренней структуры. Таким образом, разрушение исследованной стали имеет многоуровневый характер, обусловленный: иерархией исходной внутренней микроструктуры; эволюцией карбидных фаз; локализацией пластической деформации, развивающейся на всех стадиях пластической деформации и, как следствие, подготавливающей пути распространения микротрещин.

Ключевые слова: пакетный отпущенный мартенсит, дислокационная структура, деформационный рельеф, поверхность разрушения, масштабно-структурные уровни разрушения

Для цитирования: Теплякова Л.А., Куницына Т.С., Печковский В.А., Кашин А.Д. Разрушение отпущенной мартенситной стали при растяжении. *Известия вузов. Черная металлургия*. 2025;68(1):21–29. <https://doi.org/10.17073/0368-0797-2025-1-21-29>

INTRODUCTION

Steel with a tempered martensite structure exhibits good plastic properties combined with high strength both at the initial stages of deformation [1 – 3] and under significant degrees of plastic deformation [4 – 6]. The optimal mechanical properties of martensitic steel are the reason for its wide industrial application [7], particularly in the automotive industry [8]. It is known that the internal structure of steel with a tempered martensite structure is hierarchically organized within a range of scales differing by three orders of magnitude [8 – 11]. The main morphological component of martensite is tempered lath martensite [9; 10]. The basic element of this microstructure is a lath with a width ranging from 0.2 to 0.5 μm . Laths tend to align parallel to each other within large regions of the parent austenitic grain in which they form. A group of laths with the same orientation is referred to as a block, and a group of several blocks sharing the same habit plane is called a packet. The boundaries of both blocks and packets are effective barriers to dislocation motion, providing the strength and impact toughness of martensitic steels [2; 3]. It should be noted that the mechanisms of plastic deformation in steels with such a complex defect structure are still insufficiently studied [7; 12]. Previous studies [13; 14] have shown that for medium-alloy steel with a tempered martensite structure under active tension, there is pronounced localization of deformation associated with the boundaries of misorientation between inherited austenitic grains and real martensitic grains. These studies revealed that during active loading, plastic deformation undergoes self-organization within groups of real grains. The linear dimensions of martensitic grain groups that self-organize during deformation are comparable to the sizes of the inherited austenitic grains. In other words, during plastic deformation, deformation localization occurs in close relation to the grain subsystem.

The development of shear deformation in the packet component of martensite is also accompanied by shear localization, which is related to the hierarchical structure of packet martensite. In [15], it was established that within packets of martensitic crystals (laths), localization occurs through the formation of two subsystems of shear traces: fine and coarse. The fine shear trace subsystem forms from the very beginning of plastic deformation under conditions of homogeneous sample deformation. The emergence and evolution of the coarse shear trace subsystem correlate with the formation of the first

(elongated) neck in the sample, representing the main micromechanism leading to the localization of plastic deformation at the sample scale (macrolocalization). The sites of coarse shear localization are the boundary areas of laths and packet fragments. The appearance of coarse shear trace subsystems correlates with the formation of a fragmented (isotropic) dislocation structure within the packet. In other words, shear plastic deformation in steel with a tempered martensite structure is closely linked to its hierarchically organized localization throughout all stages of deformation, including those preceding fracture. According to the results of these studies, it is logical to assume that the fracture of this class of steel should also be hierarchically conditioned by the preceding deformation.

The present study aims to establish the development regularities of the fracture process in medium-alloy steel with a tempered martensite structure within a physically justified range of scales and to identify its relation to the preceding plastic deformation.

MATERIAL AND METHODS

For this study, 0.34C–Cr–Ni–3Mo–V–Fe steel was used. Following rolling, the steel underwent quenching from 950 °C in water, followed by tempering at 600 °C for 4 h and subsequent water cooling as the final stage of heat treatment. After thermomechanical processing, the steel developed a structure of highly tempered mixed packet-lath martensite. Most of the carbon is present in the form of carbide precipitates, including cementite and special carbides, predominantly Me_2C , Me_6C and Me_{23}C . Tensile testing was performed on an Instron machine at a strain rate of $6 \cdot 10^{-4} \text{ s}^{-1}$ at room temperature. The fracture surface was analyzed using optical microscopy, scanning electron microscopy (SEM), and transmission electron microscopy (TEM) on samples cut parallel and perpendicular to the rolling direction, referred to as longitudinal and transverse samples, respectively. Measurements were taken for the microcrack density, their length, and the orientation angles relative to the tensile axis. The measurement results were subjected to statistical processing, and the corresponding average values were determined.

RESEARCH RESULTS AND DISCUSSION

Initial structure (before deformation). The internal structure of the studied 0.34C–Cr–Ni–3Mo–V–Fe steel before loading represents a complex system.

It includes: boundaries of misorientation between grains and all structural components of martensite (plates, packets, packet fragments – blocks, and laths); a developed dislocation structure with an average scalar dislocation density of approximately 10^{10} cm^{-2} ; a subsystem of carbide phases, consisting of cementite and special carbides. The structural and phase analyses conducted in this study, combined with the assessment of quantitative characteristics, made it possible to create, in effect, a “passport” for the investigated steel. This passport provides a detailed representation of the hierarchical organization of the internal structure across the entire physically justified range of scales. The results of this analysis are summarized in Table 1. The dislocation structure within packets and plates is diverse, including network, cellular, and fragmented substructures [1; 16]. Cementite precipitates are predominantly located along the boundaries of martensitic structural components, while the distribution of special carbides is closely associated with the dislocation substructure. In the network structure, special carbides are found at the nodes of dislocation networks, whereas in the cellular and fragmented substructures,

they are located at the junctions of cell boundaries and fragment interfaces, respectively [11; 16].

During plastic deformation, both the defect and carbide subsystems undergo significant evolution, accompanied by multi-level deformation localization [13 – 15] and transformations of carbide phases [17]. In steel with a tempered martensite structure, crack initiation is generally not a critical concern. However, potential sites for microcrack initiation include non-metallic inclusions, various misorientation boundaries and their intersections, as well as carbide particles. Understanding the conditions that enable initiated cracks to propagate is therefore of great importance. It is noteworthy that most of the current knowledge regarding the structure of microcracks and the fracture surface has been obtained using optical microscopy and scanning electron microscopy [18 – 21]. In contrast, the application of transmission electron microscopy on foils remains relatively uncommon in studies of fracture processes [22; 23].

In this study, an extensive electron microscopy investigation was conducted to examine

Table 1. Classification of structural levels by scale

Таблица 1. Классификация структурных уровней по масштабу

Scale level number	Structural level number	Structural element		Average size, μm
1	1	Entire sample		$(4 \times 4 \times 6) \cdot 1000$
2	2	Segregation bands		50×5000
	3	Non-metallic inclusions (sulfides)		20×30
	4	Inherited grain (group of real grains)		140
	5	Real grain		20
3	6	Packet		4×6
	7	Plate		2.5×4.0
	8	Packet fragment (block)		0.8×4.0
4	9	Packet martensite crystal (lath)		0.19×4.0
	10	Lath fragment		0.6×4.0
5	11	Cementite particles	At plate boundaries	$(0.6 \times 4) \cdot 10^{-2}$
			At lath boundaries	$(3 \times 25) \cdot 10^{-2}$
			In plate matrix	$(2 \times 14) \cdot 10^{-2}$
			In lath matrix	$(1.7 \times 10) \cdot 10^{-2}$
	12	Special carbide particles	At plate boundaries	$8 \cdot 10^{-2}$
			At lath boundaries	$1.6 \cdot 10^{-2}$
			In plate matrix	$1.1 \cdot 10^{-2}$
			In lath matrix	$1.4 \cdot 10^{-2}$
	13	Dislocation cell		$4 \cdot 10^{-2} - 5 \cdot 10^{-2}$
	14	Dislocation cell link		$1 \cdot 10^{-2} - 15 \cdot 10^{-2}$

the fine structure at various stages of plastic flow in 0.34C–Cr–Ni–3Mo–V–Fe steel, covering deformation levels up to those preceding fracture (in the region of the second neck [13]).

Microcracks and interface boundaries. Fig. 1 presents typical examples of the fine structure of the steel, highlighting microcracks propagating along interface boundaries. These boundaries were formed both as a result of prior thermomechanical treatment – including grain boundaries (Fig. 1, *a*), the boundaries of martensitic structural components such as packets and plates (Figs. 1, *b*, *c*), and lath boundaries (Fig. 1, *d*) – as well as along boundaries of dislocation fragments generated during plastic deformation (Figs. 1, *e*, *f*).

Analysis of numerous micrographs obtained in this study reveals that microcracks tend to propagate along surfaces where highly localized shear deformation has occurred. This phenomenon represents the natural outcome of localized deformation, arising from the insufficient relaxation of internal stresses through mechanisms other than microcrack formation. This observation is consistent with the fact that, in steel with a tempered martensite structure, local stress concentrations in specific regions can reach values comparable to the material's theoretical strength, even though the average stress levels correspond to the actual ultimate strength, typically achieved during the later stages of plastic deformation [16]. Moreover, it is noteworthy that microcrack

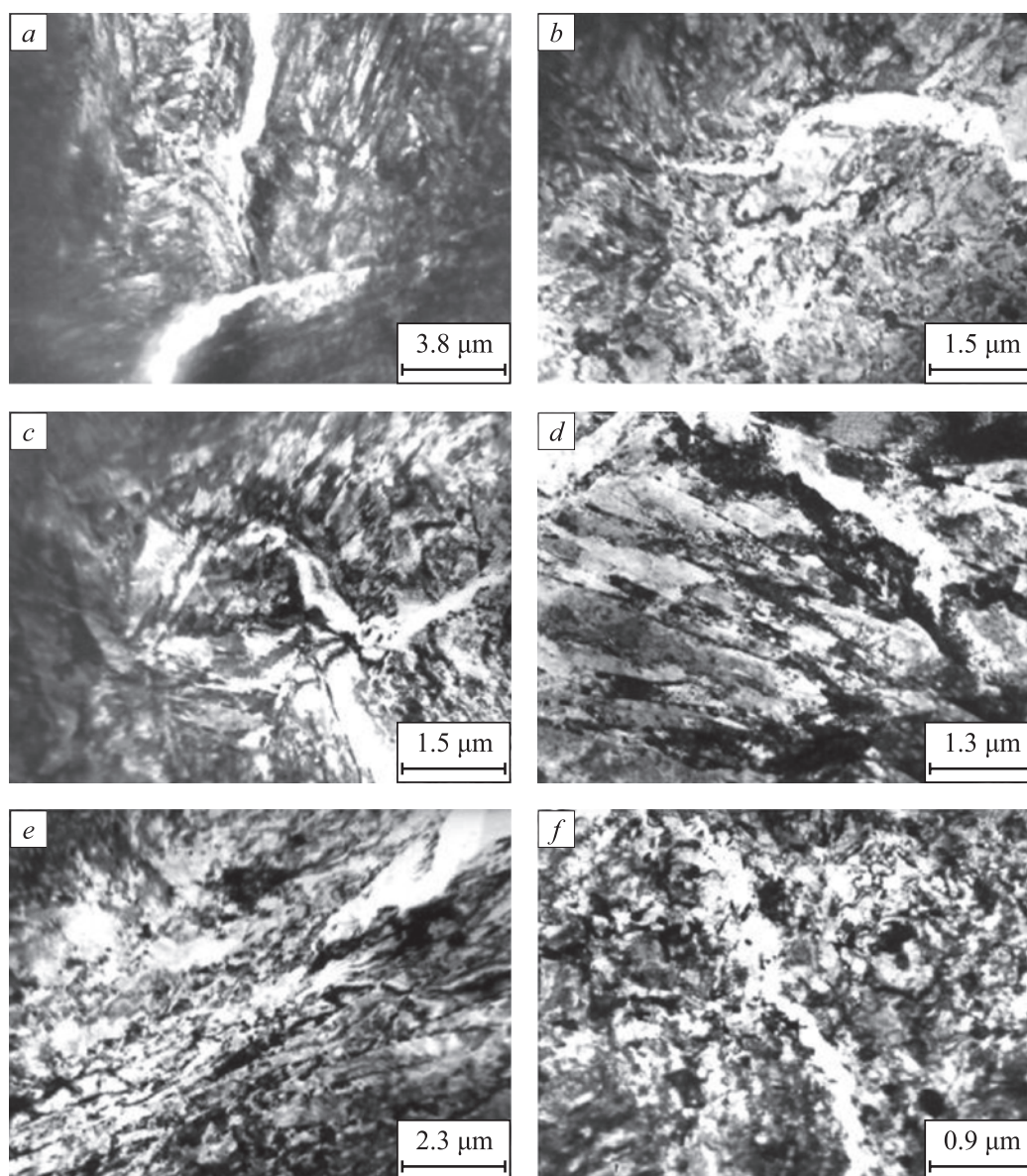


Fig. 1. Cracks propagating along grain boundaries (*a*, *b*), structural components of martensite (*c*, *d*) and fragments (*e*, *f*)

Рис. 1. Трещины, распространяющиеся по границам зерен (*a*, *b*), структурных составляющих мартенсита (*c*, *d*) и фрагментов (*e*, *f*)

propagation paths frequently pass through regions characterized by an isotropic fragmented substructure. This substructure represents the final stage in the sequence of substructural transformations observed in this steel, progressing from network to cellular, then to anisotropic fragments, and finally to the isotropic fragmented substructure [24]. This sequence of transformations occurs earlier at interface boundaries than in the surrounding matrix, indicating that these boundary regions exhaust their available mechanisms for relaxing localized long-range stress amplitudes – induced during deformation – sooner than the matrix itself.

Microcracks. In the studied steel with a mixed tempered martensite structure, which contains a subsystem of sub-boundaries formed during thermomechanical treatment, microcracks appear from the very onset of plastic deformation. As noted earlier, deformation leads to the formation of new misorientation boundaries (boundaries of dislocation fragments within martensite crystals), with their misorientation angles increasing

as the degree of deformation grows [17; 24]. Simultaneously, there is an increase in the microcrack density and a decrease in their average length (Fig. 2, *a*), which correlates with the rising overall density of misorientation boundaries in martensite and their intersections.

The average length of microcracks prior to fracture is approximately 1 μm , which is comparable to the typical linear dimensions of a lath block (Table 1). This indicates that microcracks in this steel cross lath boundaries but are impeded by block boundaries, which exhibit larger misorientation angles than lath boundaries [14; 19].

In this study, the proportions of microcracks oriented at various angles relative to the tensile axis were measured, and the results are presented in Fig. 2, *b*. At higher degrees of deformation, microcracks oriented at 45° to the tensile axis become predominant, while the proportion of cracks oriented parallel to the tensile axis decreases significantly. This indicates the dominance of cleavage cracks at advanced deformation stages [22].

Scale-structural levels of fracture. As previously discussed, the internal structure of steel with a tempered martensite structure consists of three hierarchically organized subsystems: misorientation boundaries, a developed dislocation structure, and carbide phase precipitates. During plastic deformation, each of these subsystems evolves within its corresponding scale range, with their evolutionary patterns being interconnected and mutually dependent (for more details, see [17; 24]). Given this hierarchical organization, it was expected that the ductile fracture of this steel would also display a multi-level character. In this study, the fracture surfaces of the samples were examined across a range of scales differing by three orders of magnitude. Table 2 presents micrographs alongside quantitative characteristics of the fracture patterns observed in both longitudinal and transverse samples of 0.34C–Cr–Ni–3Mo–V–Fe steel with a tempered martensite structure, reflecting distinct structural scale levels.

The longitudinal samples predominantly exhibit a cup-and-cone fracture, whereas the transverse samples display a combination of cup-and-cone and brittle fracture features. The linear dimensions of the dimples at various scale levels were measured, their average values determined, and these measurements were compared with the average sizes of structural elements listed in Table 1. This comparison revealed a clear correlation between the fracture surface characteristics and the average sizes of key structural components, including inherited grains, real grains, plates, packets, and finer elements such as dislocation fragments formed during plastic deformation at strain levels preceding fracture (Table 1, Level 4). The identified correlation is consistent with previously established patterns [13 – 15] of multi-level, hierarchically organized localization of plastic deformation.

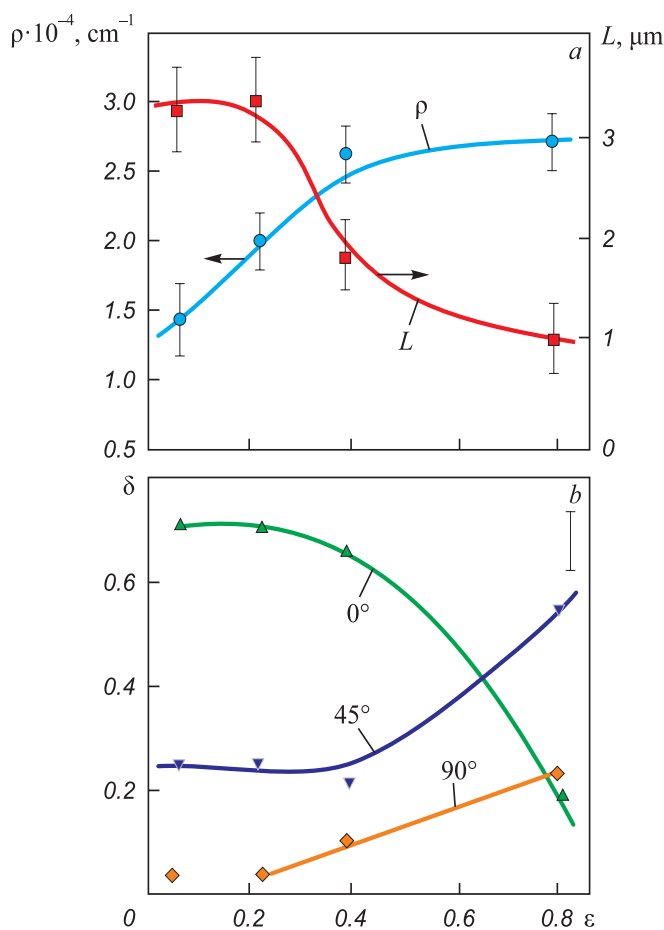
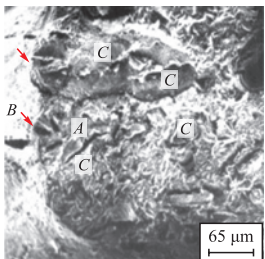
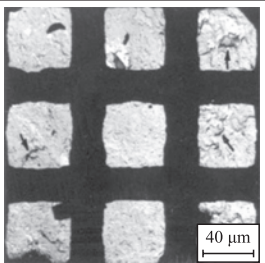
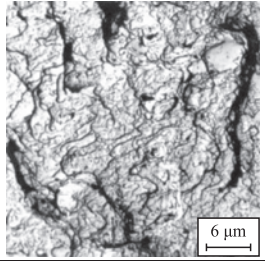
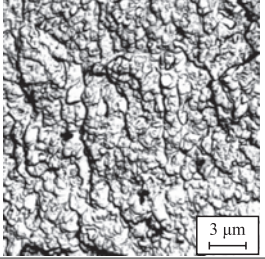
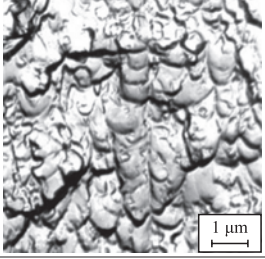
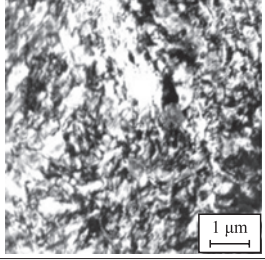


Fig. 2. Relationship between crack density ρ , their length L (a) and proportion of cracks δ parallel (0°), perpendicular (90°) and running at an angle of 45° to the tensile axis (b) with deformation degree

Рис. 2. Связь плотности трещин ρ , их длины L (a) и доли трещин δ , параллельных (0°), перпендикулярных (90°) и идущих под углом 45° к оси растяжения (b) со степенью деформации

Table 2. Characteristics of the fracture pattern

Таблица 2. Характеристики картины изломов

Structural-scale level	Observed fracture feature	Micrograph of the fracture feature	Characteristic size of the fracture feature, μm	Average spacing between fracture features, μm	Corresponding microstructural element
Entire sample (Level 1)	Cracks (A) Pits (B) Quasi-brittle fracture zones (C)		Average crack length ~150 Pit diameter 50 – 100 Quasi-brittle zone diameter 200 – 500	~100	Grain groups. Non-metallic inclusions
Grain group (Level 2)	Bands of localized plastic deformation	 	Band width 0.5 – 1.5	50 – 300	Result of plastic deformation near grain boundaries
Grain (Level 3)	Bands of localized deformation Regions with uniform dimple morphology Dimples within these regions Elongated dimples		Band width ~0.3	6,5	Packet groups
			6×10	6×10	Packets
			0.64	0.56	Lath or lath groups within packets
			1.5×9.0	–	Plates
Packet, plate (Level 4)	Internal structure of dimples		0.5 – 0.6		Fragments within laths and plates
	Fragmented substructure		Fragment size: In plates – 0.35×0.08 in laths – 0.18×0.07		

tion along misorientation boundaries. Notably, as shown in [15], the average shear intensity in the boundary regions of tempered martensite crystals (blocks and laths) is approximately three times higher than in the crystal matrix. In other words, the intense localization of plastic deformation facilitates the formation of preferential pathways for microcrack propagation.

In conclusion, the comparison of the deformation relief and the fine structure formed prior to fracture with the fracture patterns observed at different structural-scale levels demonstrates that the fracture of the studied steel, much like the plastic deformation that precedes it, reflects the inherited characteristics of the original internal structure.

CONCLUSIONS

The initiation and propagation of microcracks in steel with a tempered martensite structure at the later stages of plastic deformation were investigated using various analytical methods. The results showed that almost all observed microcracks propagate along interface boundaries, specifically: grain boundaries and the boundaries of coherently deforming grain groups, the boundaries of plates, packets, and lath blocks, and the boundaries of dislocation substructure fragments, which represent the final stage in the sequence of substructural transformations in the studied steel.

It was found that during plastic deformation, the length of microcracks decreases, and in the deformation stage preceding fracture, microcracks can cross lath boundaries but are typically arrested at block boundaries. Notably, the majority of these microcracks form through the cleavage mechanism.

The fracture process in the studied steel exhibits a multi-level nature, determined by: the hierarchical structure of the original internal microstructure, the localization of plastic deformation, which evolves throughout all stages of plastic deformation, and, as a result, the formation of preferential pathways for microcrack propagation.

REFERENCES / СПИСОК ЛИТЕРАТУРЫ

- Ivanov Yu.F., Gromov V.E., Popova N.A., Konovalov S.V., Koneva N.A. Structural and Phase States and Mechanisms of Hardening of Deformed Steel. Novokuznetsk: Polygraphist; 2016:510. (In Russ.).
Структурно-фазовые состояния и механизмы упрочнения деформированной стали / Ю.Ф. Иванов, В.Е. Громов, Н.А. Попова, С.В. Коновалов, Н.А. Конева. Новокузнецк: Полиграфист; 2016:510.
- Harjo S., Kawasaki T., Tomota Y., Gong W., Aizawa K., Tichy G., Shi Z., Ungár T. Work hardening, dislocation structure, and load partitioning in lath martensite determined by in situ neutron diffraction line profile analysis. *Metallurgical and Materials Transactions A*. 2017;48(9):4080–4092. <https://doi.org/10.1007/s11661-017-4172-0>
- Kwak K., Mayama T., Mine Y., Takashima K. Anisotropy of strength and plasticity in lath martensite steel. *Materials Science and Engineering: A*. 2016;674:104–116. <https://doi.org/10.1016/j.msea.2016.07.047>
- Jo K.-R., Seo E.-J., Sulistiyo D.H., Kim J.-K., Kim S.-W., De Cooman B.C. On the plasticity mechanisms of lath martensitic steel. *Materials Science and Engineering: A*. 2017;704:252–261. <https://doi.org/10.1016/j.msea.2017.08.024>
- Jafarian H.R., Tarazkouhi M.F. Significant enhancement of tensile properties through combination of severe plastic deformation and reverse transformation in an ultrafine/nano grain lath martensitic steel. *Materials Science and Engineering: A*. 2017;686:113–120. <https://doi.org/10.1016/j.msea.2017.01.034>
- Shamsujjoha M. Evolution of microstructures, dislocation density and arrangement during deformation of low carbon lath martensitic steels. *Materials Science and Engineering: A*. 2020;776:139039. <https://doi.org/10.1016/j.msea.2020.139039>
- Inoue J., Sadeghi A., Koseki T. Slip band formation at free surface of lath martensite in low carbon steel. *Acta Materialia*. 2019;165:129–141. <https://doi.org/10.1016/j.actamat.2018.11.026>
- Chen T., Chiba T., Koyama M., Shibata A., Akiyama E., Takai K. Hierarchical characteristics of hydrogen-assisted crack growth and microstructural strain evolution in tempered martensitic steels: Case of quasi-cleavage fracture. *Metallurgical and Materials Transactions A*. 2021;52(10):4703–4713. <https://doi.org/10.1007/s11661-021-06423-1>
- Krauss G., Marder A.R. The morphology of martensite in iron alloys. *Metallurgical Transactions*. 1971;2(9):2343–2357. <https://doi.org/10.1007/BF02814873>
- Morito S., Tanaka H., Konishi R., Furuhashi T., Maki T. The morphology and crystallography of lath martensite in Fe–C alloys. *Acta Materialia*. 2003;51(6):1789–1799. [https://doi.org/10.1016/S1359-6454\(02\)00577-3](https://doi.org/10.1016/S1359-6454(02)00577-3)
- Teplyakova L., Gershteyn G., Popova N., Kozlov E., Ignatenko L., Springer R., Schaper M., Bach Fr.-W. Scale-dependent hierarchy of structural elements in the microstructure of thermomechanical treated ferritic steels with residual austenite. *Materialwissenschaft und Werkstofftechnik*. 2009;40(9):704–712. <https://doi.org/10.1002/mawe.200900503>
- Morsdorf L., Jeannin O., Barbier D., Mitsuhara M., Raabe D., Tasan C.C. Multiple mechanisms of lath martensite plasticity. *Acta Materialia*. 2016;121:202–214. <https://doi.org/10.1016/j.actamat.2016.09.006>
- Teplyakova L.A., Popova N.A., Kozlov E.V. Localization of plastic deformation in tempered martensitic steels at large-scale levels. *Fundamental'nye problemy sovremenogo materialovedeniya (Basic Problems of Material Science (BPMS))*. 2012;9(4-2):659–663. (In Russ.).
Теплякова Л.А., Попова Н.А., Козлов Э.В. Локализация пластической деформации в отпущенных мартенситных сталях на крупномасштабных уровнях. *Фундаментальные проблемы современного материаловедения*. 2012;9(4-2):659–663.
- Teplyakova L.A., Popova N.A., Kunitsyna T.S. Localization of deformation in martensitic steels at the struc-

tural and scale level: Grain. Bands of localized deformation. *Fundamental'nye problemy sovremennogo materialovedeniya (Basic Problems of Material Science (BPMS))*. 2018;15(4):331–338. (In Russ.).

Теплякова Л.А., Попова Н.А., Куницына Т.С. Локализация деформации в мартенситных сталях на структурно-масштабном уровне: зерно. Полосы локализованной деформации. *Фундаментальные проблемы современного материаловедения*. 2018;15(4):331–338.

15. Teplyakova L.A., Kashin A.D., Kunitsyna T.S. Development of shear deformation in lath martensite of medium-alloy steels under tension. *Izvestiya. Ferrous Metallurgy*. 2023;66(2):154–161.
<https://doi.org/10.17073/0368-0797-2023-2-154-161>

Теплякова Л.А., Кашин А.Д., Куницына Т.С. Развитие сдвиговой деформации в пакетном мартенсите средне-легированных сталей при растяжении. *Известия вузов. Черная металлургия*. 2023;66(2):154–161.
<https://doi.org/10.17073/0368-0797-2023-2-154-161>

16. Kozlov E.V., Popova N.A., Ignatenko L.N., Grigorieva N.A., Kovalevskaya T.A., Teplyakova L.A., Chukhin B.D. Stages of plastic deformation, evolution of structure and sliding pattern in alloys with dispersed hardening. *Izvestiya vuzov. Physics*. 1991;34(3):112–128. (In Russ.).

Козлов Э.В., Попова Н.А., Игнатенко Л.Н., Григорьева Н.А., Ковалевская Т.А., Теплякова Л.А., Чухин Б.Д. Стадии пластической деформации, эволюция структуры и картина скольжения в сплавах с дисперсным упрочнением. *Известия вузов. Физика*. 1991;34(3):112–128.

17. Kozlov E.V., Popova N.A., Ignatenko L.N., Teplyakova L.A., Klopotov A.A. Patterns of substructural-phase transformations during plastic deformation of martensitic steel. *Izvestiya vuzov. Physics*. 1994;37(4):76–82. (In Russ.).

Козлов Э.В., Попова Н.А., Игнатенко Л.Н., Теплякова Л.А., Клопотов А.А. Закономерности субструктурно-фазовых превращений при пластической деформации мартенситной стали. *Известия вузов. Физика*. 1994;37(4):76–82.

18. Abdollah-Zadeh A., Jafari-Pirlari A., Barzegari M. Tempered martensite embrittlement in a 32NiCrMoV125 steel. *Journal of Materials Engineering and Performance*. 2005;14(5):569–573. <https://doi.org/10.1361/105994905X64657>

19. Du C., Hoefnagels J.P.M., Vaes R., Geers M.G.D. Plasticity of lath martensite by sliding of substructure boundaries. *Scripta Materialia*. 2016;120:37–40.

<https://doi.org/10.1016/j.scriptamat.2016.04.006>

20. Kadkhodapour J., Butz A., Ziaei-Rad S., Schmauder S. A micro mechanical study on failure initiation of dual tension using single crystal plasticity model. *International Journal of Plasticity*. 2011;27(7):1103–1125.

<https://doi.org/10.1016/j.ijplas.2010.12.001>

21. Shibata A., Gutierrez-Urrutia I., Nakamura A., Okada K., Miyamoto G., Madi Y., Besson J., Hara T., Tsuzaki K. Three-dimensional propagation behavior of hydrogen-related intergranular cracks in high strength martensitic steel. *International Journal of Hydrogen Energy*. 2023;48(88):34565–34574.

<https://doi.org/10.1016/j.ijhydene.2023.05.211>

22. Li S., Zhu G., Kang Y. Effect of substructure on mechanical properties and fracture behavior of lath martensite in 0.1C–1.1Si–1.7Mn steel. *Journal of Alloys and Compounds*. 2016;675:104–115.

<https://doi.org/10.1016/j.jallcom.2016.03.100>

23. Trishkina L.I., Klopotov A.A., Potekaev A.I., Cherkasova T.V., Borodin V.I., Kulagina V.V. Regularities of micro-crack propagation in substructures. *Russian Physics Journal*. 2023;66(1):416–430.

<https://doi.org/10.1007/s11182-023-02956-7>

24. Kozlov E.V., Teplyakova L.A., Popova N.A., Ignatenko L.N., Klopotov A.A., Koneva N.A. Influence of substructure type on carbon redistribution in martensitic steel during plastic deformation. *Izvestiya vuzov. Physics*. 2002;45(3):72–86. (In Russ.).

Козлов Э.В., Теплякова Л.А., Попова Н.А., Игнатенко Л.Н., Клопотов А.А., Конева Н.А. Влияние типа субструктур на перераспределение углерода в стали мартенситного класса в ходе пластической деформации. *Известия вузов. Физика*. 2002;45(3):72–86.

Information about the Authors

Сведения об авторах

Lyudmila A. Teplyakova, Dr. Sci. (Phys.–Math.), Prof. of the Chair of Physics, Tomsk State University of Architecture and Building

ORCID: 0000-0001-5038-7379

E-mail: lat168@mail.ru

Tat'yana S. Kunitsyna, Cand. Sci. (Phys.–Math.), Assist. Prof. of the Chair of Advanced Mathematics, Tomsk State University of Architecture and Building

ORCID: 0000-0001-6801-4909

E-mail: kma11061990@mail.ru

Vladislav A. Pechkovskii, Postgraduate, Tomsk State University of Architecture and Building

E-mail: Poits16@yandex.ru

Aleksandr D. Kashin, Postgraduate, Institute of Strength Physics and Materials Science, Siberian Branch of Russian Academy of Sciences

ORCID: 0000-0003-1860-3654

E-mail: kash@mail.ru

Людмила Алексеевна Теплякова, д.ф.-м.н., профессор кафедры физики, Томский государственный архитектурно-строительный университет

ORCID: 0000-0001-5038-7379

E-mail: lat168@mail.ru

Татьяна Семеновна Куницына, к.ф.-м.н., доцент кафедры высшей математики, Томский государственный архитектурно-строительный университет

ORCID: 0000-0001-6801-4909

E-mail: kma11061990@mail.ru

Владислав Андреевич Печковский, аспирант, Томский государственный архитектурно-строительный университет

E-mail: Poits16@yandex.ru

Александр Данилович Кашин, аспирант, Институт физики прочности и материаловедения СО РАН

ORCID: 0000-0003-1860-3654

E-mail: kash@mail.ru

Contribution of the Authors

Вклад авторов

L. A. Teplyakova – problem statement, analysis of research results, formulation of conclusions.

T. S. Kunitsyna – complex metallographic and electron microscopic analysis.

V. A. Pechkovskii – measurement of quantitative characteristics of deformation relief.

A. D. Kashin – statistical processing of the data obtained.

Л. А. Теплякова – постановка задачи, анализ результатов исследований, формулировка выводов.

Т. С. Куницына – комплексное металлографическое и электронно-микроскопическое исследование.

В. А. Печковский – измерение количественных характеристик деформационного рельефа

А. Д. Кашин – статистическая обработка полученных данных.

Received 20.09.2024

Revised 23.10.2024

Accepted 17.12.2024

Поступила в редакцию 20.09.2024

После доработки 23.10.2024

Принята к публикации 17.12.2024



UDC 536.425:539.25:539.351

DOI 10.17073/0368-0797-2025-1-30-39



Original article

Оригинальная статья

INFLUENCE OF INCLINED ELECTRIC FIELD ON DECAY OF A LIQUID JET DURING HEAT TREATMENT AND SURFACING

S. A. Nevskii , L. P. Bashchenko, V. D. Sarychev,
A. Yu. Granovskii, D. V. Shamsutdinova

■ Siberian State Industrial University (42 Kirova Str., Novokuznetsk, Kemerovo Region – Kuzbass 654007, Russian Federation)

✉ nevskiy.sergei@yandex.ru

Abstract. The combined effect of inclined electric fields and a transverse acoustic field on the Kelvin–Helmholtz instability of the interface of viscous electrically conductive liquids is studied using the example of air–water and argon–iron systems. An inclined electric field, regardless of the effect of sound vibrations, leads to the increased Kelvin–Helmholtz instability in the micrometer wavelength range. The most intense increase in the disturbances of the interface is observed at the angle of inclination of the electric field $\pi/3$. This opens up new opportunities for the development of technologies for accelerated cooling of rolled products and surfacing materials by regulating the drop transfer of material. The combined effect of acoustic and electric fields has an ambiguous effect on the Kelvin–Helmholtz instability. In the case of an air–water system, sound vibrations lead to suppression of the Kelvin–Helmholtz instability, while a tangential electric field with a strength of $3 \cdot 10^6$ V/m enhances this effect, and a normal field, on the contrary, weakens it. For the argon–iron system, sound vibrations lead to the complete disappearance of the viscosity-conditioned maximum and to a significant decrease in the growth rate of disturbances at the interface, which corresponds to the first maximum. Application of a horizontal electric field with a strength of $3 \cdot 10^7$ V/m significantly weakens the effect of suppressing the Kelvin–Helmholtz instability, while in a vertical field, on the contrary, increases it. It was established that the restoration of the first hydrodynamic maximum in a normal electric field is possible with a ratio of specific electrical conductivities σ greater than 0.012, regardless of the presence of a sound field. A change in the influence of the vertical electric field from a stabilizing to a destabilizing one is possible with a ratio of σ from 0.015 or more.

Keywords: electric field, acoustic field, heat treatment, air–water system, argon–iron system, Kelvin–Helmholtz instability, viscous potential approximation

Acknowledgements: The work was supported by the Russian Science Foundation (grant No. 22-79-10229, <https://rscf.ru/project/22-79-10229/>).

For citation: Nevskii S.A., Bashchenko L.P., Sarychev V.D., Granovskii A.Yu., Shamsutdinova D.V. Influence of inclined electric field on decay of a liquid jet during heat treatment and surfacing. *Izvestiya. Ferrous Metallurgy*. 2025;68(1):30–39.

<https://doi.org/10.17073/0368-0797-2025-1-30-39>

ВЛИЯНИЕ НАКЛОННОГО ЭЛЕКТРИЧЕСКОГО ПОЛЯ НА РАСПАД СТРУИ ЖИДКОСТИ В ПРОЦЕССАХ ТЕРМООБРАБОТКИ И НАПЛАВКИ

С. А. Невский , Л. П. Башченко, В. Д. Сарычев,
А. Ю. Грановский, Д. В. Шамсутдинова

■ Сибирский государственный индустриальный университет (Россия, 654007, Кемеровская обл. – Кузбасс, Новокузнецк, ул. Кирова, 42)

✉ nevskiy.sergei@yandex.ru

Аннотация. Изучено совместное воздействие наклонных электрических полей и поперечного акустического поля на неустойчивость Кельвина–Гельмгольца границы раздела вязких электропроводных жидкостей на примере систем воздух–вода и аргон–железо. Наклонное электрическое поле вне зависимости от воздействия звуковых колебаний приводит к усилению неустойчивости Кельвина–Гельмгольца в микрометровом диапазоне длин волн. Наиболее интенсивный рост возмущений поверхности раздела наблюдается при угле наклона электрического поля $\pi/3$. Это открывает новые возможности для разработки технологий ускоренного охлаждения проката и наплавки материалов путем регулирования капельного переноса материала. Совместное воздействие акустических и электрических полей оказывает неоднозначное влияние на неустойчивость Кельвина–Гельмгольца. В случае системы воздух–вода звуковые колебания приводят к подавлению неустойчивости Кельвина–Гельмгольца, при этом тангенциальное электрическое поле напряженностью $3 \cdot 10^6$ В/м усили-

вает данный эффект, а нормальное поле, наоборот, ослабляет его. Для системы аргон–железо звуковые колебания приводят к полному исчезновению вязкостно-обусловленного максимума и к значительному снижению скорости роста возмущений поверхности раздела, которая соответствует первому максимуму. Приложение горизонтального электрического поля напряженностью $3 \cdot 10^7$ В/м значительно ослабляет эффект подавления неустойчивости Кельвина–Гельмгольца, а в вертикальном поле он, наоборот, усиливается. Установлено, что восстановление первого гидродинамического максимума в нормальном электрическом поле возможно при соотношении удельных электрических проводимостей σ более 0,012 вне зависимости от наличия звукового поля. Смена знака влияния вертикального электрического поля со стабилизирующего на дестабилизирующее возможно при соотношении σ от 0,015 и более.

Ключевые слова: электрическое поле, акустическое поле, термообработка, система воздух – вода, система аргон – железо, неустойчивость Кельвина–Гельмгольца, вязко-потенциальное приближение

Благодарности: Исследование выполнено за счет гранта Российского научного фонда № 22-79-10229, <https://rscf.ru/project/22-79-10229/>.

Для цитирования: Невский С.А., Башенко Л.П., Сарычев В.Д., Грановский А.Ю., Шамсутдинова Д.В. Влияние наклонного электрического поля на распад струи жидкости в процессах термообработки и наплавки. *Известия вузов. Черная металлургия*. 2025;68(1):30–39.

<https://doi.org/10.17073/0368-0797-2025-1-30-39>

INTRODUCTION

The Kelvin–Helmholtz instability occurs in various research fields, ranging from terrestrial magnetohydrodynamics [1] and turbulent liquid mixing [2] to processes such as coating deposition by electrical explosion [3] and astrophysical phenomena like the solar wind [4]. This instability serves as a powerful trigger that disrupts the stability of systems involving the mixing of two or more liquids with different properties. Some of the most notable applications of this instability include acoustic modes in air-consuming systems such as boilers, jet engines, and gas turbines [5]. Another significant application of this instability is the breakup of a liquid jet into droplets in an electric field [6; 7]. This phenomenon underlies the operation of precision devices that are integral to various technological processes, such as electric arc welding and the production of ultrafine refractory powders [6; 7]. In [8], the influence of an inclined electric field on the Kelvin–Helmholtz instability of two ideal dielectric liquids was studied, revealing the conditions under which the liquid transitions to a stable mode under a horizontal electric field. It was also demonstrated that the vertical component of the electric field exerts a destabilizing effect. Another promising application of this instability is the accelerated cooling of rolled products. In [9], it was shown that by controlling the velocity of the air–water system, it is possible to achieve the formation of droplets in the nanometer range. Upon impacting rolled products, these droplets induce a thermoelastic wave, thereby increasing their impact toughness.

The origin and development of the Kelvin–Helmholtz instability of two viscous liquids were investigated in [10; 11]. A key feature of these studies is the use of the viscous potential approximation. This approach assumes the absence of shear stress components of the stress tensor at the interface, while the viscosity of the liquid is taken into account only in the condition of continuity of normal stresses at the interface [10]. In the general case, the situation is complicated by the need to determine the velocity profile of the fluid, and

as shown in [11; 12], there is no analytical solution for the stability of a flow with a complex velocity profile. However, at high wavenumbers (short wavelengths), this approximation is justified, as demonstrated in [13].

The interaction of the Kelvin–Helmholtz instability with ultrasonic vibrations in the case of a problem with planar geometry under the viscous potential flow approximation was studied in [14; 15]. The interaction of the Kelvin–Helmholtz instability with ultrasonic vibrations in a planar geometry under the viscous potential approximation was studied in [14; 15]. It was assumed that the effect of acoustic vibrations is equivalent to an effective oscillating gravitational field. It was found that acoustic influence shifts the maximum growth rate toward higher wavenumbers [15], and a stability region was identified between weak acoustic excitation and parametric resonance.

The objective of this study was to investigate the combined influence of an inclined electric field and a transverse acoustic field on the stability of the planar surface of an electrically conductive liquid using the example of the iron–argon and air–water systems under the viscous potential flow approximation. The simultaneous application of these two factors enables the creation of micro- and nanodroplet flow patterns, which is crucial for the development of new technologies in welding, surfacing, and accelerated cooling of rolled products.

PROBLEM STATEMENT

Consider the instability of the planar interface between two viscous electrically conductive fluids. The first fluid is characterized by density ρ_1 , kinematic viscosity ν_1 , electrical conductivity σ_1 , and dielectric permittivity ε_1 (Fig. 1). It occupies the region $(-\infty \leq x \leq +\infty$ and $-h_1 \leq z \leq 0)$ and moves with a horizontal velocity U_1 . The second fluid occupies the region $(-\infty \leq x \leq +\infty$ and $0 \leq z \leq h_2)$ and is characterized by density ρ_2 , kinematic viscosity ν_2 , electrical conductivity σ_2 , and dielectric permittivity ε_2 . The horizontal velocity of the second fluid

is U_2 . The variable ξ represents the deviation of the interface from its equilibrium position (Fig. 1).

The flow velocities of the first and second fluids are much lower than the speed of sound; therefore, they can be considered incompressible. The kinematics of the interface motion is described by the function $F(x, z, t) = z - \xi(x, t)$. Thus $\vec{n} = \frac{\nabla F}{|\nabla F|} = \frac{-\frac{\partial \xi}{\partial x} \vec{e}_x + \vec{e}_z}{\sqrt{1 + \left(\frac{\partial \xi}{\partial x}\right)^2}}$ the normal

vector is defined as (where ∇ is the gradient operator. In the linear approximation, the normal vector $\vec{n} = -\frac{\partial \xi}{\partial x} \vec{e}_x + \vec{e}_z$ takes the form. The system under consideration is placed in an external transverse acoustic field and an inclined electric field relative to the planar interface of the fluid (Fig. 1). The electric field vector, taking into account the disturbances of the interface, is given by $\vec{E} = E_{0x} \vec{e}_x - E_{0z} \vec{e}_z - \nabla \psi$ (where ψ is the disturbance of the electric potential, and E_{0x} and E_{0z} are the normal and tangential components of the unperturbed electric field, respectively). The inclination angle of the electric field (Fig. 1) relative to the unperturbed surface β is defined as $\arctg\left(\frac{E_{0z}}{E_{0x}}\right)$.

The fundamental linearized equations of the viscous potential flow model for relatively small disturbances, taking into account the electric field, according to [10; 15], are given as:

$$\begin{aligned} \Delta \Phi_1 &= 0; \quad -h_1 < z < 0; \\ \Delta \Phi_2 &= 0; \quad 0 < z < h_2; \\ \Delta \psi_1 &= 0; \quad -h_1 < z < 0; \\ \Delta \psi_2 &= 0; \quad 0 < z < h_2, \end{aligned} \quad (1)$$

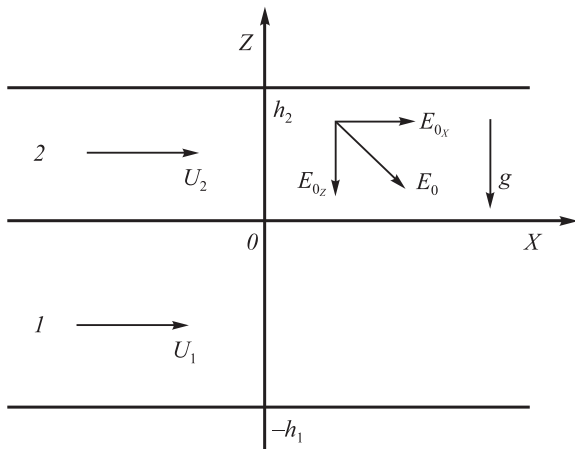


Fig. 1. On formulation of the problem of origin and development of the Kelvin–Helmholtz instability

Рис. 1. К постановке задачи о возникновении и развитии неустойчивости Кельвина–Гельмгольца

where Φ is represents the velocity potential disturbance.

When deriving the first and second equations of system (1), the terms associated with the electric field were neglected, which is valid for electrically conductive liquids [16 – 18], in the absence of a volumetric charge. Therefore, the electric field component will only be considered in the boundary conditions at the liquid–gas interface. At the boundaries h_2 and h_1 , we impose conditions ensuring the absence of disturbances in the flow velocity and the electric field:

$$\begin{aligned} z = -h_1: \quad \frac{\partial \Phi_1}{\partial z} &= 0; \quad \frac{\partial \psi_1}{\partial x} = 0; \\ z = h_2: \quad \frac{\partial \Phi_2}{\partial z} &= 0; \quad \frac{\partial \psi_2}{\partial x} = 0. \end{aligned} \quad (2)$$

The boundary conditions for the disturbances of the flow potential of the liquid at the interface, taking into account the electric field, are given by:

$$\begin{aligned} z = 0: \quad \frac{\partial \Phi_1}{\partial z} &= \frac{\partial \xi}{\partial t} + U_1 \frac{\partial \xi}{\partial x}; \quad \frac{\partial \Phi_2}{\partial z} = \frac{\partial \xi}{\partial t} + U_2 \frac{\partial \xi}{\partial x}; \\ -p_1 + 2\rho_1 \nu_1 \frac{\partial^2 \Phi_1}{\partial z^2} + p_{s1} - \frac{1}{2} \varepsilon_1 \varepsilon_0 (E_{1n}^2 - E_{1\tau}^2) + \\ + p_2 - 2\rho_2 \nu_2 \frac{\partial^2 \Phi_2}{\partial z^2} - p_{s2} + \frac{1}{2} \varepsilon_2 \varepsilon_0 (E_{2n}^2 - E_{2\tau}^2) &= \gamma \frac{\partial^2 \xi}{\partial x^2}, \end{aligned} \quad (3)$$

where U_i is the velocity of the i -th fluid; $p_i = -\rho_i \times \left(\frac{\partial \Phi_i}{\partial t} + U_i \frac{\partial \Phi_i}{\partial x} \right)$ is the pressure disturbance in the i -th fluid; p_{si} is the disturbance of the pressure of the acoustic field; $i = 1, 2$ is the fluid index; γ is the surface tension; E_{in} and $E_{i\tau}$ are the normal and tangential components of the field, respectively.

The boundary conditions for the electric field at the interface are defined as [19]:

$$\vec{n} \cdot \vec{E}_1 = \vec{n} \cdot \vec{E}_2; \quad \sigma_1 (\vec{n} \cdot \vec{E}_1) = \sigma_2 (\vec{n} \cdot \vec{E}_2). \quad (4)$$

Substituting the above values of the normal vector and the electric field into equation (4) and subsequently linearizing, taking into account that at the interface of two conductors $\sigma_1 E_{01z} = \sigma_2 E_{02z}$, and $E_{01x} = E_{02x}$, leads to the following:

$$\begin{aligned} E_{10z} \frac{\partial \xi}{\partial x} + \frac{\partial \psi_1}{\partial x} &= E_{20z} \frac{\partial \xi}{\partial x} + \frac{\partial \psi_2}{\partial x}; \\ \sigma_1 \left(E_{10x} \frac{\partial \xi}{\partial x} + \frac{\partial \psi_1}{\partial z} \right) &= \sigma_2 \left(E_{20x} \frac{\partial \xi}{\partial x} + \frac{\partial \psi_2}{\partial z} \right). \end{aligned} \quad (5)$$

The solution to equations (1) will be sought in the form:

$$\begin{aligned}
 \Phi_1(x, z, t) &= A_1 \cosh[k(z + h_1)] \exp(\omega t + ikx); \\
 \Phi_2(x, z, t) &= A_2 \cosh[k(z - h_2)] \exp(\omega t + ikx); \\
 \Psi_1(x, z, t) &= A_3 \sinh[k(z + h_1)] \exp(\omega t + ikx); \\
 \Psi_2(x, z, t) &= A_4 \sinh[k(z - h_2)] \exp(\omega t + ikx); \\
 \xi(x, t) &= \xi_0 \exp(\omega t + ikx).
 \end{aligned} \quad (6)$$

Substituting the third, fourth, and fifth equations of (6) into equation (5) leads to the following system of equations for the constants A_3 and A_4 :

$$\begin{aligned}
 A_3 \sinh(kh_1) + A_4 \sinh(kh_2) &= (E_{20z} - E_{10z}) \xi_0; \\
 A_3 \sigma_1 \cosh(kh_1) - A_4 \sigma_2 \cosh(kh_2) &= \\
 &= i \xi_0 (\sigma_2 E_{20x} - \sigma_1 E_{10x}).
 \end{aligned} \quad (7)$$

The solution to system (7) after transformation takes the form:

$$\begin{aligned}
 A_3 &= - \left\{ \left[i (\sigma_1 E_{10x} - \sigma_2 E_{20x}) + (\sigma_2 E_{10z} - \sigma_1 E_{20z}) \times \right. \right. \\
 &\quad \left. \times \coth(kh_2) \right] \xi_0 \} \times \\
 &\quad \times \left\{ \sinh(kh_1) [\coth(kh_1) \sigma_1 + \coth(kh_2) \sigma_2] \right\}^{-1}; \\
 A_4 &= - \left\{ \left[i (\sigma_1 E_{10x} - \sigma_2 E_{20x}) + (\sigma_1 E_{20z} - \sigma_2 E_{10z}) \times \right. \right. \\
 &\quad \left. \times \coth(kh_1) \right] \xi_0 \} \times \\
 &\quad \times \left\{ \sinh(kh_2) [\coth(kh_1) \sigma_1 + \coth(kh_2) \sigma_2] \right\}^{-1}.
 \end{aligned} \quad (8)$$

Then, the disturbances of the electric potential will take the following form:

$$\begin{aligned}
 \Psi_1(x, z, t) &= - \left\{ \left[i (\sigma_1 E_{10x} - \sigma_2 E_{20x}) + \right. \right. \\
 &\quad \left. \left. + (\sigma_2 E_{10z} - \sigma_1 E_{20z}) \coth(kh_2) \right] \sinh[k(z + h_1)] / \right. \\
 &\quad \left. / \left\{ \sinh(kh_1) [\coth(kh_1) \sigma_1 + \coth(kh_2) \sigma_2] \right\}; \right. \\
 &\quad \left. \xi_0 \exp(\omega t + ikx); \right. \\
 \Psi_2(x, z, t) &= \left\{ \left[i (\sigma_1 E_{10x} - \sigma_2 E_{20x}) + \right. \right. \\
 &\quad \left. \left. + (\sigma_1 E_{20z} - \sigma_2 E_{10z}) \coth(kh_1) \right] \sinh[k(z - h_2)] / \right. \\
 &\quad \left. / \left\{ \sinh(kh_2) [\coth(kh_1) \sigma_1 + \coth(kh_2) \sigma_2] \right\}; \right. \\
 &\quad \left. \xi_0 \exp(\omega t - ikx). \right.
 \end{aligned} \quad (9)$$

To derive the disturbances of the flow potential, we substitute the first, second, and fifth equations of system (6) into the kinematic boundary conditions (3). As a result, we obtain:

$$\begin{aligned}
 \Phi_1(x, z, t) &= \frac{\omega + ikU_1}{k \sinh(kh_1)} \times \\
 &\quad \times \cosh[k(z + h_1)] \xi_0 \exp(\omega t + ikx); \\
 \Phi_2(x, z, t) &= - \frac{\omega + ikU_2}{k \sinh(kh_2)} \times \\
 &\quad \times \cosh[k(z - h_2)] \xi_0 \exp(\omega t + ikx).
 \end{aligned} \quad (10)$$

The contribution of the acoustic field to the pressure is determined in the same way as in [14; 15]: $p_{si} = \rho_i g_{eff} \xi_0 \times \exp(\omega t + ikx)$ (where $g_{eff} = g - \Omega U_a \cos(\Omega t)$ is the effective acceleration; Ω and U_a are the frequency and amplitude of the acoustic excitation. Substituting (9) and (10) into the dynamic boundary condition (3) and performing subsequent transformations, taking into account that at $z = 0$: $\sigma_1 E_{01z} = \sigma_2 E_{02z}$, $E_{01x} = E_{02x}$, leads to the following dispersion equation:

$$\begin{aligned}
 a_0 \omega^2 + 2(a_1 + ib_1) \omega + a_2 + ib_2 &= 0; \\
 a_0 &= \rho_1 \coth(kh_1) + \rho_2 \coth(kh_2); \\
 a_1 &= \rho_1 v_1 k^2 \coth(kh_1) + \rho_2 v_2 k^2 \coth(kh_2); \\
 b_1 &= \rho_1 U_1 k \coth(kh_1) + \rho_2 U_2 k \coth(kh_2); \\
 a_2 &= -k^2 \left[\rho_1 U_1^2 \coth(kh_1) + \rho_2 U_2^2 \coth(kh_2) \right] + \\
 &\quad + \gamma k^3 + (\rho_1 - \rho_2) g_{eff} k + \\
 &\quad + \varepsilon_1 \varepsilon_0 k^2 \left[\frac{(\sigma_1 - \sigma_2) E_{20x}^2}{\coth(kh_1) \sigma_1 + \coth(kh_2) \sigma_2} - \right. \\
 &\quad \left. - \frac{\sigma_2^2 (\sigma_1 - \sigma_2) \coth(kh_1) \coth(kh_2) E_{20z}^2}{\sigma_1^2 [\coth(kh_1) \sigma_1 + \coth(kh_2) \sigma_2]} \right] + \\
 &\quad + \varepsilon_2 \varepsilon_0 k^2 \left[\frac{(\sigma_1 - \sigma_2) \coth(kh_1) \coth(kh_2) E_{20z}^2}{\coth(kh_1) \sigma_1 + \coth(kh_2) \sigma_2} - \right. \\
 &\quad \left. - \frac{(\sigma_1 - \sigma_2) E_{20x}^2}{\coth(kh_1) \sigma_1 + \coth(kh_2) \sigma_2} \right]; \\
 b_2 &= \left\{ \varepsilon_1 \varepsilon_0 k^2 \sigma_2 (\sigma_1 - \sigma_2) [\coth(kh_1) + \coth(kh_2)] \times \right. \\
 &\quad \times E_{20x} E_{20z} \} / \left\{ \sigma_1 [\coth(kh_1) \sigma_1 + \coth(kh_2) \sigma_2] \right\} + \\
 &\quad + \left\{ \varepsilon_2 \varepsilon_0 k^2 (\sigma_1 - \sigma_2) [\coth(kh_1) + \coth(kh_2)] \times \right. \\
 &\quad \times E_{20x} E_{20z} \} / \left\{ \coth(kh_1) \sigma_1 + \coth(kh_2) \sigma_2 \right\} + \\
 &\quad + 2k^3 [\rho_1 v_1 U_1 \coth(kh_1) + \rho_2 v_2 U_2 \coth(kh_2)].
 \end{aligned} \quad (11)$$

To analyze equation (11) while considering the influence of weak acoustic fields, we adopt the approach used in [14; 15]. According to this method:

$$\begin{aligned}
 a_0 \frac{d^2 f}{dt^2} + 2(a_1 + ib_1) \frac{df}{dt} + (a_2 + ib_2) f &= 0; \\
 a_2 &= c - C_{ac} \cos(\Omega t); \quad C_{ac} = (\rho_2 - \rho_1) \Omega k U_a; \\
 c &= -k^2 \left[\rho_1 U_1^2 \coth(kh_1) + \rho_2 U_2^2 \coth(kh_2) \right] + \gamma k^3 + \\
 &\quad + (\rho_1 - \rho_2) g k + \varepsilon_1 \varepsilon_0 k^2 \left[\frac{(\sigma_1 - \sigma_2) E_{20x}^2}{\coth(kh_1) \sigma_1 + \coth(kh_2) \sigma_2} - \right. \\
 &\quad \left. - \frac{\sigma_2^2 (\sigma_1 - \sigma_2) \coth(kh_1) \coth(kh_2) E_{20z}^2}{\sigma_1^2 [\coth(kh_1) \sigma_1 + \coth(kh_2) \sigma_2]} \right] + \\
 &\quad + \varepsilon_2 \varepsilon_0 k^2 \left[\frac{(\sigma_1 - \sigma_2) \coth(kh_1) \coth(kh_2) E_{20z}^2}{\coth(kh_1) \sigma_1 + \coth(kh_2) \sigma_2} - \right. \\
 &\quad \left. - \frac{(\sigma_1 - \sigma_2) E_{20x}^2}{\coth(kh_1) \sigma_1 + \coth(kh_2) \sigma_2} \right],
 \end{aligned} \quad (12)$$

where f is a time-dependent function and represents the sum of a “slow” disturbance component $A_1(t) = f_1 \exp(\omega t)$, and a “fast” disturbance component, $A_2(t) = f_2 \cos(\Omega t)$, which corresponds to acoustic vibrations. Here Ω is the frequency of the acoustic influence [14; 15]. Substituting this sum into equation (7) and discarding the cosine and sine terms, considering that $f_2 = -C_{ac} A_1 / (a_0 \Omega^2)$ [14], we obtain:

$$a_0 \omega^2 + 2(a_1 + ib_1)\omega + c + ib_2 + \frac{C_{ac}^2}{2a_0 \Omega^2} = 0. \quad (13)$$

The solution of equation (7) takes the form:

$$\begin{aligned} \omega_1 &= -\frac{a_1 + ib_1}{a_0} + \\ &+ \frac{\sqrt{(a_1 + ib_1)^2 - a_0 \left(c + \frac{C_{ac}^2}{2a_0 \Omega^2} + ib_2 \right)}}{a_0}; \\ \omega_2 &= -\frac{a_1 + ib_1}{a_0} - \\ &- \frac{\sqrt{(a_1 + ib_1)^2 - a_0 \left(c + \frac{C_{ac}^2}{2a_0 \Omega^2} + ib_2 \right)}}{a_0}. \end{aligned} \quad (14)$$

The second root of equation (8) has no physical significance and is therefore not considered. The growth rate of disturbances at the liquid interface is determined as $\alpha = \text{Re}(\omega_1)$. Consequently, we obtain:

$$\begin{aligned} \alpha &= -\frac{a_1}{a_0} + \frac{1}{2a_0} \left[2(a_1^2 + b_1^2 - a_0) - \frac{C_{ac}^2}{\Omega^2} + \right. \\ &+ \left. 2\sqrt{\left(a_1^2 + b_1^2 - a_0 c - \frac{C_{ac}^2}{2\Omega^2} \right)^2 + (2a_1 b_1 - b_2 a_0)^2} \right]^{1/2}. \end{aligned} \quad (15)$$

The data for calculations using equation (9) are presented in the Table.

RESEARCH RESULTS AND DISCUSSION

Air-water system

In Fig. 2, *a*, the dependencies of the growth rate of disturbances at the air–water interface on the wave-number in the absence of an acoustic field under the influence of electric fields are shown. The velocity difference between the horizontal layers was 15 m/s. This function has only one maximum, regardless of the presence of an electric field (curves 1–3). A tangential electric field ($\beta = 0$) with a strength of approximately $3 \cdot 10^6$ V/m stabilizes the Kelvin–Helmholtz instability, which is expressed in a decrease in α_m and a shift of the maximum mode k_m toward lower values (curve 2). A normal electric field ($\beta = \pi/2$) of the same strength, on the contrary, enhances this instability (curve 3), which is consistent with widely accepted concepts [8; 19]. At inclination angles of the electric field vector $\beta \pi/6, \pi/4, \pi/3$ (Fig. 2, *b*), an increase in k_m is observed from $59,170 \text{ m}^{-1}$ ($\lambda_m = 106.19 \text{ }\mu\text{m}$) at $\beta = \pi/6$ to $119,709 \text{ m}^{-1}$ ($\lambda_m = 52.48 \text{ }\mu\text{m}$) at $\beta = \pi/3$. The analysis of neutral curves (Fig. 2, *c*) showed that the presence of a vertical component of the electric field significantly narrows the range of relative velocity differences between the fluids, within which capillary forces and the tangential electric field suppress the Kelvin–Helmholtz instability. It should be noted that a similar effect was observed in [8] for the case of inviscid dielectric liquids.

Let us consider the combined influence of weak acoustic and inclined electric fields on the Kelvin–Helmholtz instability. Fig. 3, *a* shows the dependencies of the disturbance growth rate at an amplitude value of the acoustic oscillation velocity $U_a = 5 \text{ m/s}$. These dependencies indicate that acoustic vibrations suppress the Kelvin–Helm-

Characteristics of the materials and parameters of external influence

Характеристики материалов и параметры внешнего воздействия

Characteristic	Characteristic values			
	Water	Air	Iron	Argon
Density, kg/m ³	997	1.1308	6700	0.2434
Viscosity, μ , Pa·s	$8.94 \cdot 10^{-4}$	$1.7798 \cdot 10^{-5}$	$4.4 \cdot 10^{-3}$	$8.07 \cdot 10^{-5}$
Surface tension, σ , N/m	0.059		1.2	
Specific electrical conductivity, S/m	0.01	0.001	$7.52 \cdot 10^5$	10^3
Dielectric permittivity	81	1	4640	1
Velocity of the first fluid, U_1 , m/s	1	–	1	–
Velocity of the second fluid, U_2 , m/s	–	16	–	101
Thickness of the first fluid, h_1 , m	10^{-3}	10^{-3}	10^{-3}	10^{-3}
Thickness of the second fluid, h_2 , m	$3 \cdot 10^{-3}$	$3 \cdot 10^{-3}$	$3 \cdot 10^{-3}$	$3 \cdot 10^{-3}$

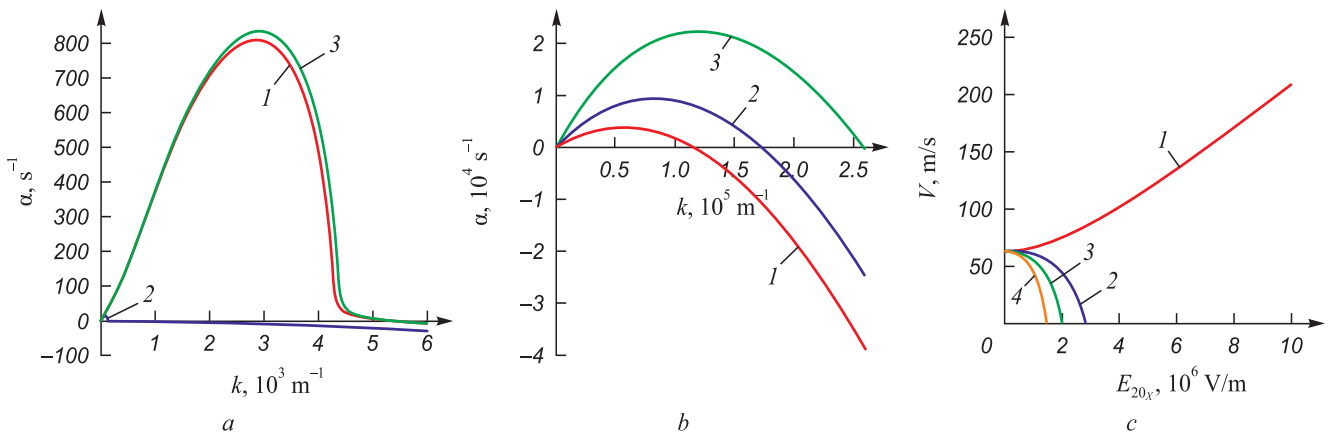


Fig. 2. Dependences of growth rate of perturbations of the air–water interface (a, b)

and neutral curves (c) under the influence of electric fields (notation here and in Fig. 3):

a: 1 – without field action; 2 – at $E_{20x} = 3 \cdot 10^6$ V/m and $E_{20z} = 0$ V/m; 3 – at $E_{20x} = 0$ V/m and $E_{20z} = 3 \cdot 10^6$ V/m;

b: 1 – 3 – angle of inclination of the electric field $\pi/6$, $\pi/4$, and $\pi/3$, respectively;

c: 1 – 4 – angle of inclination of the electric field $\pi/6$, $\pi/4$, and $\pi/3$, respectively

Рис. 2. Зависимости скорости роста возмущений поверхности раздела воздух – вода (a, b)

и нейтральные кривые (c) при воздействии электрических полей (обозначения здесь и на рис. 3):

a: 1 – без воздействия поля; 2 – при $E_{20x} = 3 \cdot 10^6$ В/м и $E_{20z} = 0$ В/м; 3 – при $E_{20x} = 0$ В/м и $E_{20z} = 3 \cdot 10^6$ В/м;

b: 1 – 3 – угол наклона электрического поля $\pi/6$, $\pi/4$ и $\pi/3$ соответственно;

c: 1 – 4 – угол наклона электрического поля 0 , $\pi/6$, $\pi/4$ и $\pi/3$ соответственно

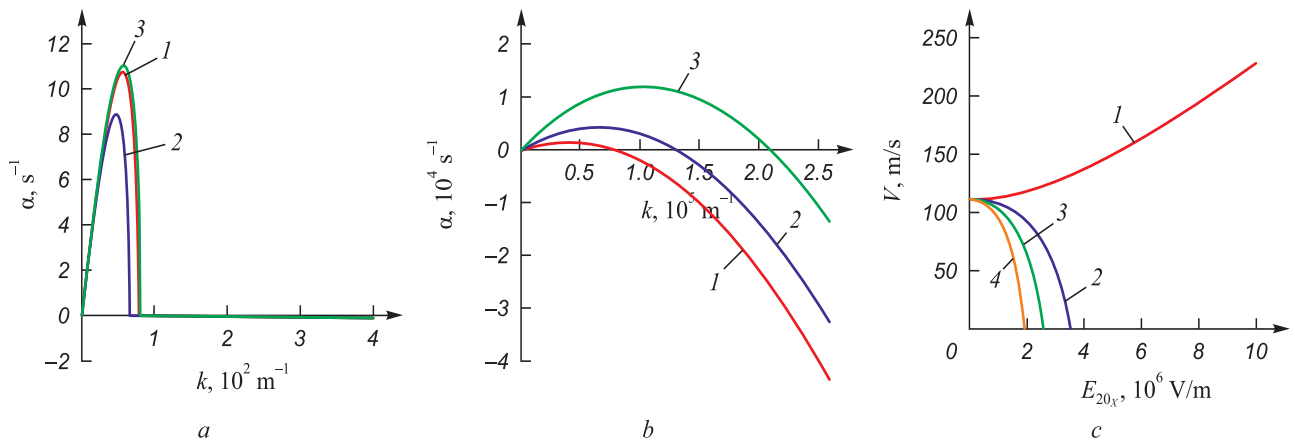


Fig. 3. Dependences of the growth rate of disturbances of the air–water interface (a, b)

and neutral curves (c) under the combined action of electric fields and acoustic vibrations with a velocity amplitude of 5 m/s

Рис. 3. Зависимости скорости роста возмущений поверхности раздела воздух – вода (a, b)

и нейтральные кривые (c) при совместном воздействии электрических полей и акустических колебаний с амплитудой скорости 5 м/с

holtz instability (curves 1 – 3), with the tangential electric field amplifying this effect (curve 2), while the normal electric field, on the contrary, weakens it. A weakening of the suppression effect is also observed at electric field inclination angles $\beta \pi/6$, $\pi/4$, $\pi/3$ (Fig. 3, b), which is confirmed by the analysis of neutral curves (Fig. 3, c). Notably, similar suppression phenomena of the Kelvin–Helmholtz instability were identified in [14]. However, in that study, the application of acoustic fields resulted in a rightward shift of k_m , while the maximum growth rate increased, indicating an enhancement of the Kelvin–Helmholtz instability. The discrepancy between the results of [14] and the present study may be explained

by the fact that in [14], the ratio $\frac{C_{ac}^2}{2a_0\Omega^2}$ in equation (8) was taken with a negative sign, whereas in this study, it was taken with a positive sign.

Argon-iron system

Now, let us consider a different situation that arises in surfacing or welding processes. In these processes, when the electrode melts in an argon shielding gas environment, a jet of liquid metal forms, which, under certain conditions, breaks up into droplets [20]. The mode of material transfer determines the quality of the formed coating,

making the development of methods for controlling this process an important task. In this system, the mutual flow of gas and liquid gives rise to the Kelvin–Helmholtz instability [20]. Fig. 4, *a* presents dispersion curves, showing that they exhibit two maxima. According to [13], the first maximum is hydrodynamic, while the second is viscosity-induced (curve 1). The application of a tangential electric field with a strength of $3 \cdot 10^7$ V/m leads to the near-complete suppression of the hydrodynamic maximum (curve 2), whereas in a normal electric field, this effect is weaker (curve 3). As results of [19] show, the change in the sign of the influence of the transverse electric field on capillary instability is associated with the ratio of the specific electrical conductivities $\sigma = \sigma_2/\sigma_1$ and the dielectric

permittivities of the fluids $\varepsilon = \varepsilon_2/\varepsilon_1$. If $\varepsilon > \sigma$, the electric field has a stabilizing effect; otherwise, when ($\varepsilon < \sigma$) the electric field has a destabilizing effect [19]. In the case under consideration (see Table), for the argon–iron system $\sigma \sim 0.00133$, and $\varepsilon \sim 0.0002$, which should indicate a destabilizing effect of the normal field. However, this is not observed (Fig. 4, *a*). This discrepancy with capillary instability can be explained by the fact that, in this case, the relative velocity of the flowing layers becomes significant, altering the condition for the occurrence of Kelvin–Helmholtz instability maxima [21]. A further increase in the specific electrical conductivity ratio σ beyond 0.012 leads to the restoration of the hydrodynamic maximum and the complete suppression of the viscosity-induced

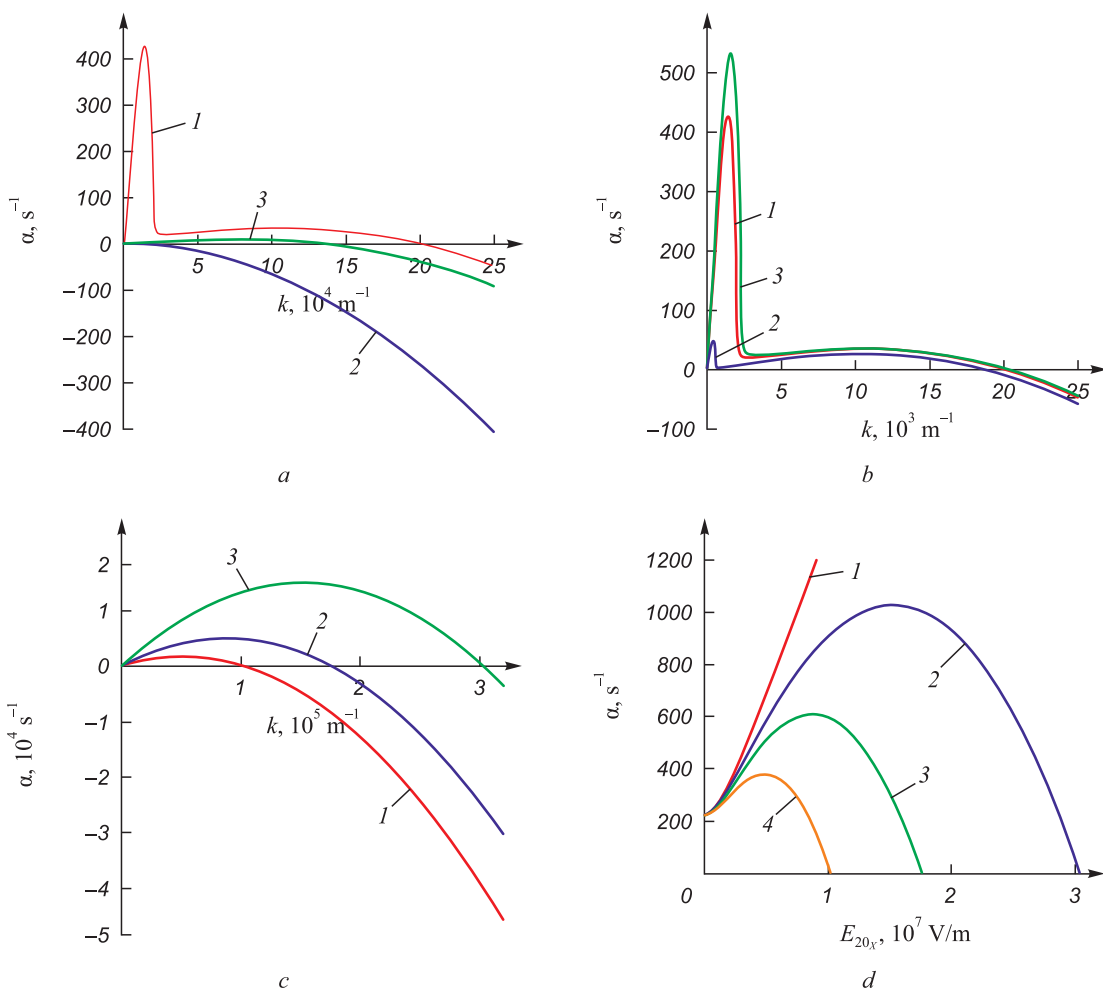


Fig. 4. Dependences of the growth rate of disturbances of the argon–iron interface (*a–c*)

and neutral curves (*d*) under the combined action of electric fields (notation here and in Fig. 5):

a: 1 – without field action; 2 – at $E_{20x} = 3 \cdot 10^7$ V/m and $E_{20z} = 0$ V/m; 3 – at $E_{20x} = 0$ B/m V/m and $E_{20z} = 3 \cdot 10^7$ V/m;

b: 1–3 – angle of inclination of the electric field $\pi/6$, $\pi/4$, and $\pi/3$, respectively;

c: at $\sigma \geq 0.012$: 1 – without field action; 2 – at $E_{20z} = 3 \cdot 10^7$ V/m and $\sigma = 0.013$, $E_{20x} = 0$ V/m; 3 – at $E_{20z} = 3 \cdot 10^7$ V/m and $\sigma = 0.015$, $E_{20x} = 0$ V/m;

d: 1–4 – angle of inclination of the electric field 0, $\pi/6$, $\pi/4$ and $\pi/3$, respectively

Рис. 4. Зависимости скорости роста возмущений поверхности раздела аргон–железо (*a–c*)

и нейтральные кривые (*d*) при совместном воздействии электрических полей (обозначения здесь и на рис. 5):

a: 1 – без воздействия поля; 2 – при $E_{20x} = 3 \cdot 10^7$ В/м и $E_{20z} = 0$ В/м; 3 – при $E_{20x} = 0$ В/м и $E_{20z} = 3 \cdot 10^7$ В/м;

b: 1–3 – угол наклона электрического поля $\pi/6$, $\pi/4$ и $\pi/3$ соответственно;

c: при $\sigma \geq 0,012$: 1 – без воздействия поля; 2 – при $E_{20z} = 3 \cdot 10^7$ В/м и $\sigma = 0,013$, $E_{20x} = 0$ В/м; 3 – при $E_{20z} = 3 \cdot 10^7$ В/м и $\sigma = 0,015$, $E_{20x} = 0$ В/м;

d: 1–4 – угол наклона электрического поля 0, $\pi/6$, $\pi/4$ и $\pi/3$ соответственно

maximum. When $\sigma \geq 0.015$, the effect changes from stabilizing to destabilizing (Fig. 4, *b*). The results of studying the effect of inclined electric fields (Fig. 4, *c*) showed that these fields enhance the Kelvin–Helmholtz instability regardless of the values of σ and ε . In this case, the maximum growth rate is viscosity-induced. At field strengths $E_{20x} < 3 \cdot 10^7$ V/m, a weakly pronounced hydrodynamic maximum is observed. The neutral stability curves indicate that, as in the air–water system, a reduction in the stability region of interface disturbances is observed (Fig. 4, *d*).

The combined effect of acoustic vibrations with a velocity amplitude of 10 m/s and an electric field with a strength of $3 \cdot 10^7$ V/m at $\sigma \sim 0.00133$, and $\varepsilon \sim 0.0002$, on the contrary, leads to the complete suppression of the viscosity-induced instability maximum (Fig. 5, *a*, curve 1) and a sharp reduction in the maximum growth rate α_m of disturbances of hydrodynamic origin. The application of a horizontal electric field significantly weakens this

effect (Fig. 5, *a*, curve 2), while in a vertical field, this effect, on the contrary, is amplified (Fig. 5, *a*, curve 3), despite the fact that at $E_{20x} = 0$ and $E_{20z} = 3 \cdot 10^7$ V/m, the value of k_m is greater than $E_{20x} = 3 \cdot 10^7$ V/m and $E_{20z} = 0$. A change in the sign of the effect to destabilizing also occurs at $\sigma \geq 0.015$ (Fig. 5, *b*). The application of an inclined electric field, as in the absence of sound, enhances the Kelvin–Helmholtz instability, but α_m is somewhat lower (Fig. 5, *c*). The neutral curves (Fig. 5, *d*) show an increase in the range of fluid velocities in which capillary forces and tangential fields suppress the Kelvin–Helmholtz instability under the influence of an acoustic field.

CONCLUSIONS

Inclined electric fields contribute to the enhancement of the Kelvin–Helmholtz instability at the interfaces of conducting fluids, regardless of the ratio of their den-

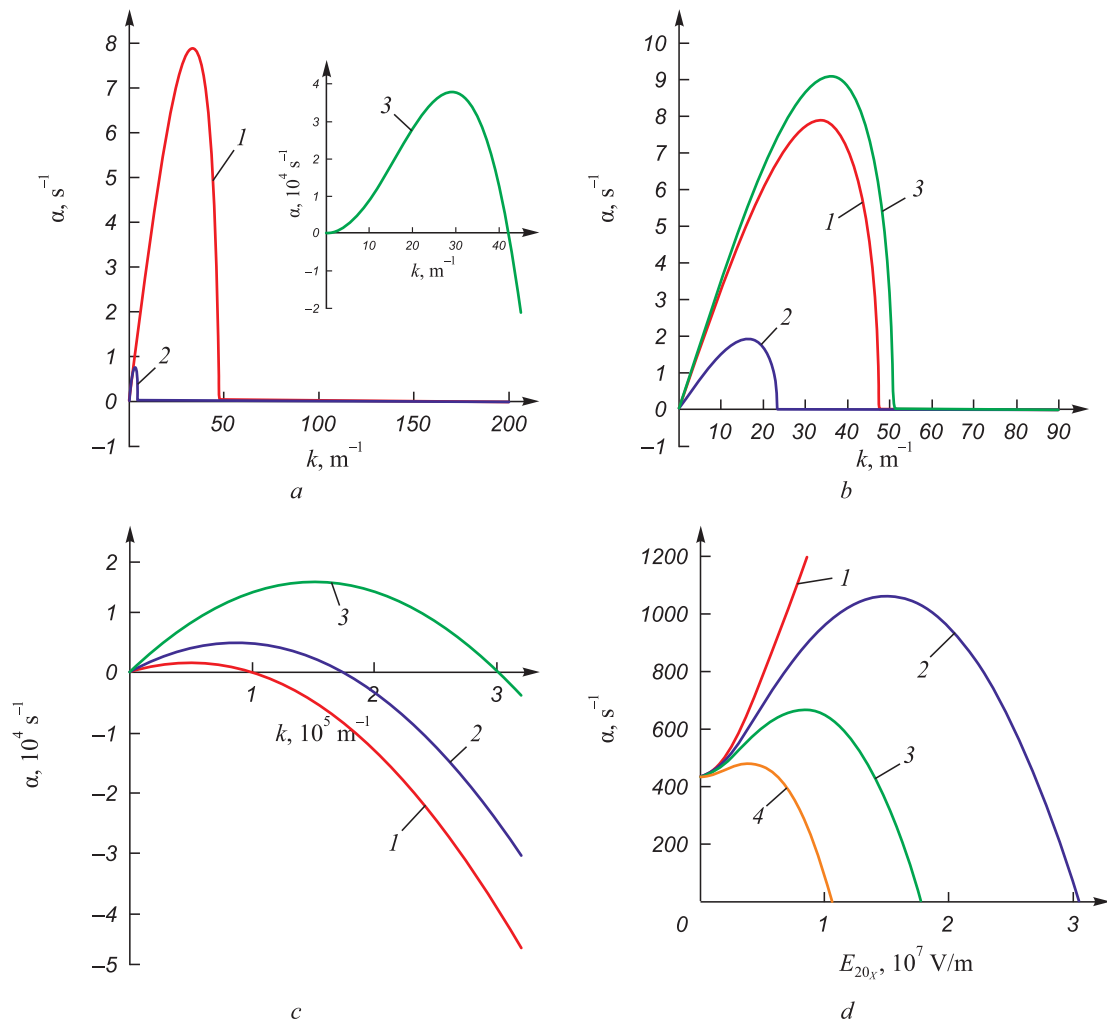


Fig. 5. Dependences of the growth rate of disturbances of the argon–iron interface (*a–c*) and neutral curves (*d*) under the combined action of electric fields and acoustic vibrations with a velocity amplitude of 10 m/s

Рис. 5. Зависимости скорости роста возмущений поверхности раздела аргон–железо (*a–c*) и нейтральные кривые (*d*) при совместном воздействии электрических полей и акустических колебаний с амплитудой скорости 10 м/с

sities, specific electrical conductivities, and the presence of acoustic fields.

It has been established that the combined application of inclined electric fields and acoustic vibrations in the air–water system allows the formation of liquid droplets in the range of 10 to 100 μm , even at low gas flow velocities. This opens up new prospects for the development of accelerated cooling technologies for rolled products to achieve high hardness and impact toughness.

For the argon–iron system, it has been shown that a vertical electric field at $\sigma \sim 10^{-3}$ and $\varepsilon \sim 10^{-4}$ practically suppresses the hydrodynamic maximum. An increase in the specific electrical conductivity ratio σ beyond 0.012, on the contrary, leads to the restoration of the hydrodynamic maximum and the complete suppression of the viscosity-induced one. At $\sigma \geq 0.015$, the effect changes from stabilizing to destabilizing, regardless of the number of maxima in the dependence of the growth rate on the wavelength. The application of a tangential electric field completely suppresses the Kelvin–Helmholtz instability.

The combined effect of acoustic vibrations and a normal electric field leads to the complete suppression of the viscosity-induced instability maximum and a sharp reduction in the maximum growth rate of disturbances of hydrodynamic origin, while in a horizontal electric field, this effect is significantly weaker.

REFERENCES / СПИСОК ЛИТЕРАТУРЫ

1. Praturi D.S., Girimaji S.S. Mechanisms of canonical Kelvin–Helmholtz instability suppression in magnetohydrodynamic flows. *Physics of Fluids*. 2019;31(2):024108. <https://doi.org/10.1063/1.5083857>
 2. Rahmani M., Seymour B.R., Lawrence G.A. The effect of Prandtl number on mixing in low Reynolds number Kelvin–Helmholtz billows. *Physics of Fluids*. 2016;28(5):054107. <https://doi.org/10.1063/1.4949267>
 3. Panin V.E., Gromov V.E., Romanov D.A., Budovskikh E.A., Panin S.V. The physical basics of structure formation in electroexplosive coatings. *Doklady Physics*. 2017;62:67–70. <https://doi.org/10.1134/S1028335817020112>
 4. Mishin V.V., Tomozov V.M. Kelvin–Helmholtz instability in the solar atmosphere, solar wind and geomagnetosphere. *Solar Physics*. 2016;291:3165–3184. <https://doi.org/10.1007/s11207-016-0891-4>
 5. Petrarolo A., Kobald M., Schlechtriem S. Understanding Kelvin–Helmholtz instability in paraffin-based hybrid rocket fuels. *Experiments in Fluids*. 2018;59:62. <https://doi.org/10.1007/s00348-018-2516-1>
 6. Grigor'ev A.I., Shiryayev A.A., Shiryayeva S.O. Instability of a charged droplet in an inhomogeneous electrostatic field of a rod of finite thickness. *Fluid Dynamics*. 2018;53(1):34–48. <https://doi.org/10.1134/S0015462818010081>
- Григорьев А.И., Ширяев А.А., Ширяева С.О. Неустойчивость заряженной капли в неоднородном электростатическом поле стержня конечной толщины. *Известия РАН. Механика жидкости и газа*. 2018;(1):36–50. <https://doi.org/10.7868/S0568528118010048>

7. Saraev Yu.N., Chinakhov D.A., Ilyashchenko D.I., Kiselev A.S., Gordynets A.S. Investigation of the stability of melting and electrode metal transfer in consumable electrode arc welding using power sources with different dynamic characteristics. *Welding International*. 2017;31(10):784–790. <https://doi.org/10.1080/09507116.2017.1343977>
 8. Korovin V.M. Effect of tilted electrostatic field on the Kelvin–Helmholtz instability in a liquid dielectric and gas flow. *Technical Physics*. 2017;62:1316–321. <https://doi.org/10.1134/S1063784217090134>
 9. Sarychev V.D., Khaimzon B.B., Nevskii S.A., Il'yashchenko A.V., Grishunin V.A. Mathematical models of mechanisms for rolled products accelerated cooling. *Izvestiya. Ferrous Metallurgy*. 2018;61(4):326–332. (In Russ.). <https://doi.org/10.17073/0368-0797-2018-4-326-332>
- Сарычев В.Д., Хаимзон Б.Б., Невский С.А., Ильященко А.В., Гришунин В.А. Математические модели механизмов ускоренного охлаждения проката. *Известия вузов. Черная металлургия*. 2018;61(4):326–332. <https://doi.org/10.17073/0368-0797-2018-4-326-332>
10. Awasthi M.K., Asthana R., Agrawal G.S. Viscous correction for the viscous potential flow analysis of Kelvin–Helmholtz instability of cylindrical flow with heat and mass transfer. *International Journal of Heat and Mass Trans.* 2014;78:251–259. <https://doi.org/10.1016/j.ijheatmasstransfer.2014.06.082>
 11. Barreras F., Lozano A., Dopazo C. Linear instability analysis of the viscous longitudinal perturbation on an air-blasted liquid sheet. *Atomization and Sprays*. 2001;11(2):139–154. <https://doi.org/10.1615/ATOMIZSPR.V11.I2.30>
 12. Logvinov O.A. Linear stability of stratified flow of two viscous fluids. *Moscow University Mechanics Bulletin*. 2022;77:117–126. <https://doi.org/10.3103/S0027133022040021>
 13. Sarychev V.D., Granovskii A.Yu., Gromov V.E. Model of formation of inner nanolayers in shear flows of material. *Technical Physics*. 2013;58(10):1544–157. <https://doi.org/10.1134/S1063784213100113>
 14. Bychkov V. Analytical scalings for flame interaction with sound waves. *Physics of Fluids*. 1999;11(10):3168–3173. <https://doi.org/10.1063/1.870173>
 15. Bilgili S., Ugarte O., Akkerman V. Interplay of Kelvin–Helmholtz instability with acoustics in a viscous potential flow. *Physics of Fluids*. 2020;32(8):084108. <https://doi.org/10.1063/5.0017448>
 16. Awasthi M.K., Dutt N., Kumar A., Kumar S. Electrohydrodynamic capillary instability of Rivlin–Ericksen viscoelastic fluid film with mass and heat transfer. *Heat Transfer*. 2024;53(1):115–133. <https://doi.org/10.1002/hjt.22944>
 17. Saville D.A. Electrohydrodynamic stability: effects of charge relaxation at the interface of a liquid jet. *Journal of Fluid Mechanics*. 1971;48(4):815–827. <https://doi.org/10.1017/S0022112071001873>
 18. Shkadov V.Ya., Shutov A.A. Stability of a surface-charged viscous jet in an electric field. *Fluid Dynamics*. 1998;33(2):176–185. <https://doi.org/10.1007/BF02698699>
 19. Awasthi M.K. Study on electrohydrodynamic capillary instability of viscoelastic fluids with radial electric field. *Inter-*

- national Journal of Applied Mechanics*. 2014;6(4):1450037.
<https://doi.org/10.1142/S1758825114500379>
20. Zhao Y., Chung H. Numerical simulation of droplet transfer behavior in variable polarity gas metal arc welding. *International Journal of Heat and Mass Transfer*. 2017;111:1129–1141.
<https://doi.org/10.1016/j.ijheatmasstransfer.2017.04.090>
21. Nevskii S.A., Sarychev V.D., Granovsky A.Yu., Bashchenko L.P., Gromov V.E. Formation of micro- and nano- in electroexplosive carboborization of titanium alloys by the mechanism hydrodynamic instabilities. *Fundamental'nye problemy sovremennogo materialovedeniya (Basic Problems of Material Science (BPMS))*. 2023;20(3):317–328. (In Russ.).
<https://doi.org/10.25712/ASTU.1811-1416.2023.03.004>
- Невский С.А., Сарычев В.Д., Грановский А.Ю., Башенко Л.П., Громов В.Е. Формирование микро- и наноструктур при электровзрывном карбоборировании титановых сплавов по механизму гидродинамических неустойчивостей. *Фундаментальные проблемы современного материаловедения*. 2023;20(3):317–328.
<https://doi.org/10.25712/ASTU.1811-1416.2023.03.004>

Information about the Authors

Сведения об авторах

Sergei A. Nevskii, Dr. Sci. (Eng.), Assist. Prof. of the Chair of Science named after V.M. Finkel', Siberian State Industrial University
ORCID: 0000-0001-7032-9029
E-mail: nevskiy_sa@physics.sibsiu.ru

Сергей Андреевич Невский, д.т.н., доцент кафедры естественно-научных дисциплин им. профессора В.М. Финкеля, Сибирский государственный индустриальный университет
ORCID: 0000-0001-7032-9029
E-mail: nevskiy_sa@physics.sibsiu.ru

Lyudmila P. Bashchenko, Cand. Sci. (Eng.), Assist. Prof. of the Chair "Thermal Power and Ecology", Siberian State Industrial University
ORCID: 0000-0003-1878-909X
E-mail: luda.baschenko@gmail.com

Людмила Петровна Башенко, к.т.н., доцент кафедры тепло-энергетики и экологии, Сибирский государственный индустриальный университет
ORCID: 0000-0003-1878-909X
E-mail: luda.baschenko@gmail.com

Vladimir D. Sarychev, Cand. Sci. (Eng.), Assist. Prof. of the Chair of Sciences named after V.M. Finkel', Siberian State Industrial University
ORCID: 0000-0002-4861-0778
E-mail: sarychev_vd@mail.ru

Владимир Дмитриевич Сарычев, к.т.н., доцент кафедры естественнонаучных дисциплин им. профессора В.М. Финкеля, Сибирский государственный индустриальный университет
ORCID: 0000-0002-4861-0778
E-mail: sarychev_vd@mail.ru

Aleksei Yu. Granovskii, Cand. Sci. (Eng.), Senior Researcher of the Department of Scientific Research, Siberian State Industrial University
ORCID: 0009-0006-4583-8431
E-mail: legatokun@gmail.com

Алексей Юрьевич Грановский, к.т.н., старший научный сотрудник Управления научных исследований, Сибирский государственный индустриальный университет
ORCID: 0009-0006-4583-8431
E-mail: legatokun@gmail.com

Diana V. Shamsutdinova, Student of Institute of Pedagogical Education, Siberian State Industrial University
E-mail: dianas1009hamsutdinova@gmail.com

Диана Витальевна Шамсутдинова, студент Института педагогического образования, Сибирский государственный индустриальный университет
E-mail: dianas1009hamsutdinova@gmail.com

Contribution of the Authors

Вклад авторов

S. A. Nevskii – problem statement, obtaining and analyzing the dispersion equation, discussion and verification of modeling results.

С. А. Невский – постановка задачи, получение и анализ дисперсионного уравнения, обсуждение и верификация результатов моделирования.

L. P. Baschenko – calculations, discussion of results, design of the article.

Л. П. Башенко – проведение расчетов, обсуждение результатов, оформление статьи.

V. D. Sarychev – formulation of the work idea, analysis and discussion of research results, verification of modeling results.

В. Д. Сарычев – идея работы, анализ и обсуждение результатов исследования, верификация результатов моделирования.

A. Yu. Granovskii – analysis and discussion of research results, verification.

А. Ю. Грановский – анализ и обсуждение результатов исследования, верификация результатов моделирования.

D. V. Shamsutdinova – discussion of results, analysis of literary sources on the Kelvin–Helmholtz instability.

Д. В. Шамсутдинова – обсуждение результатов, анализ литературных источников по неустойчивости Кельвина–Гельмгольца.

Received 09.04.2024
Revised 09.06.2024
Accepted 17.12.2024

Поступила в редакцию 09.04.2024
После доработки 09.06.2024
Принята к публикации 17.12.2024



UDC 669.539.382:669.17

DOI 10.17073/0368-0797-2025-1-40-43



Short report

Краткое сообщение

ANTHOLOGY OF RAILS PRODUCED BY JSC EVRAZ UNITED WEST SIBERIAN METALLURGICAL PLANT IN THE 21ST CENTURY

V. E. Gromov¹, S. V. Konovalov¹, E. V. Polevoi²¹ Siberian State Industrial University (42 Kirova Str., Novokuznetsk, Kemerovo Region – Kuzbass 654007, Russian Federation)² JSC EVRAZ United West Siberian Metallurgical Plant (16 Kosmicheskoe Route, Novokuznetsk, Kemerovo Region – Kuzbass 654043, Russian Federation)

✉ gromov@physics.sibsui.ru

Abstract. JSC EVRAZ United West Siberian Metallurgical Plant is the main manufacturer of rails in the Russian Federation. The work traces the evolution of the plant's rail assortment over the past quarter century. A brief review of publications on modern concepts of the formation of structural and phase states of defective substructure and properties of volumetrically and differentially hardened pre-eutectoid, trans-eutectoid and bainite rails during production and subsequent long-term operation was performed. The service life of rails is determined by many factors: metal purity, structure, phase composition, operating conditions, heat treatment technology, etc. Special attention is paid to a new type of rail products – rails of the DT400IK category with increased wear resistance and contact endurance made of eutectoid steel, designed for use in difficult conditions. The paper considers the promising areas of rail assortment expansion.

Keywords: rails, volumetric quenching, differential quenching, structure, properties, operation

For citation: Gromov V.E., Konovalov S.V., Polevoi E.V. Anthology of rails produced by JSC EVRAZ United West Siberian Metallurgical Plant in the 21st century. *Izvestiya. Ferrous Metallurgy*. 2025;68(1):40–43. <https://doi.org/10.17073/0368-0797-2025-1-40-43>

АНТОЛОГИЯ РЕЛЬСОВ ПРОИЗВОДСТВА «ЕВРАЗ ОБЪЕДИНЕННЫЙ ЗАПАДНО-СИБИРСКИЙ МЕТАЛЛУРГИЧЕСКИЙ КОМБИНАТ» XXI ВЕКА

В. Е. Громов¹, С. В. Коновалов¹, Е. В. Полевой²¹ Сибирский государственный индустриальный университет (Россия, 654007, Кемеровская обл. – Кузбасс, Новокузнецк, ул. Кирова, 42)² АО «ЕВРАЗ Объединенный Западно-Сибирский металлургический комбинат» (Россия, 654043, Кемеровская обл. – Кузбасс, Новокузнецк, шоссе Космическое, 16)

✉ gromov@physics.sibsui.ru

Аннотация. АО «ЕВРАЗ Объединенный Западно-Сибирский металлургический комбинат» является основным производителем рельсов в Российской Федерации. В работе прослежена эволюция рельсового сортамента комбината за последнюю четверть века. Выполнен краткий обзор публикаций по современным представлениям формирования структурно-фазовых состояний, дефектной субструктуры и свойств объемно и дифференцированно закаленных доэвтектоидных, заэвтектоидных и бейнитных рельсов при производстве и последующей длительной эксплуатации. Срок службы рельсов определяют многие факторы: чистота металла, структура, фазовый состав, условия эксплуатации, технология термообработки и др. Особое внимание уделено новому виду рельсовой продукции – рельсам категории ДТ400ИК повышенной износостойкости и контактной выносливости из заэвтектоидной стали, предназначенных для эксплуатации в сложных условиях. Рассмотрены перспективные направления расширения рельсового сортамента.

Ключевые слова: рельсы, объемная закалка, дифференцированная закалка, структура, свойства, эксплуатация

Для цитирования: Громов В.Е., Коновалов С.В., Полевой Е.В. Антология рельсов производства «ЕВРАЗ Объединенный Западно-Сибирский металлургический комбинат» XXI века. *Известия вузов. Черная металлургия*. 2025;68(1):40–43.

<https://doi.org/10.17073/0368-0797-2025-1-40-43>

Currently, railways account for up to 85 % of global freight turnover and more than 50 % of passenger transportation. In recent years, there has been a significant increase in the intensity of railway transport operations and traffic load, which necessitates high service durability of rails. To address these challenges, technologies for volumetric and differential quenching of 100-meter rails have been implemented, with production in Russia commencing in 2013 [1]. The processes of formation and evolution of the structural and phase states, as well as the properties of rail surface layers during long-term operation, constitute a complex set of interrelated scientific and technical issues. The importance of research in this area lies both in the depth of understanding it provides of fundamental issues in physical metallurgy and heat treatment, and in its practical significance [2].

A review of the literature [3 – 5] shows that the service life of rails is influenced by a range of factors, including metal purity, structure, phase composition, operating conditions, and heat treatment technology. In modern high-speed railway systems, high contact pressures cause significant structural changes in the surface layers of rails, even after relatively low accumulated tonnage. These changes are characterized by abnormally high microhardness and the decomposition of cementite. Over prolonged periods of operation, various defects accumulate in the rails, triggering processes such as segregation, relaxation, homogenization, recrystallization, and phase transitions. These processes can lead to the deterioration of the rails' physical and mechanical properties, ultimately resulting in rail failure.

Research aimed at understanding the physical mechanisms of hardening and the development of structural and phase states in rails during long-term operation highlights that this remains one of the key challenges in the fields of physical metallurgy, heat treatment, and condensed matter physics.

In 2018, JSC EVRAZ United West Siberian Metallurgical Plant (EVRAZ ZSMK) launched the production of a new type of rails made from trans-eutectoid steel of the DT400IK category. These rails are characterized by enhanced wear resistance and contact endurance, specifically designed for use on straight railway sections at speeds of up to 200 km/h and on curved sections without restrictions on load intensity [6].

At EVRAZ ZSMK, considerable attention is devoted to researching the wear resistance of rail steel under abrasive conditions [7] and in rolling contact conditions using specialized equipment, including to meet the requirements of international customers. The influence of microstructure and chemical composition on tribological properties has been thoroughly studied while maintaining comparable levels of mechanical properties and hardness. Based on the results of these studies, a new

generation of general-purpose rails with a higher hardness category – DT370 – has been developed, offering a combination of superior physical, mechanical, and performance characteristics.

The study presented in [8] examines the evolution of approaches to the formation of structure and properties in rails of various structural classes produced by EVRAZ ZSMK over the past 25 years, covering all stages from rolling and heat treatment to long-term operation. Using modern methods of physical metallurgy, particularly transmission electron microscopy, a detailed layer-by-layer analysis was conducted. This analysis identified quantitative parameters of the dislocation substructure, internal stress fields, and structural-phase states formed in the rail head along the central axis and gage corner after volumetric and differential quenching, as well as their evolution during long-term service. A comparative assessment of the tribological properties of rails after volumetric and differential quenching and extended operation was carried out. The physical mechanisms responsible for rail metal hardening during prolonged service were identified, along with their quantitative characteristics.

Another study focused on methods for improving the fatigue life of rails through magnetic and plasma hardening, as well as electron beam treatment. Resource-efficient technologies, along with heat treatment and rolling modes for EVRAZ ZSMK rail production, were analyzed. Additionally, studies on the kinetics of austenite transformation were conducted to optimize the chemical composition and heat treatment processes of rail steels, including for the production of butt-welded joints [9].

The production of rails from bainitic steel remains a relevant challenge. Studies of promising bainitic steels have demonstrated the advantages of rails made from these steels in terms of a comprehensive set of physical and mechanical properties compared to rails made from traditional pearlitic steel. Based on the results of computational modeling, a new R71 rail profile has been developed, featuring an increased mass per meter to support heavy-haul freight operations in the Russia's Eastern Railway Network. These new rails are designed to meet the growing demands of modern rail transport, including higher railway capacity, increased load intensity, and enhanced reliability of rail track superstructure components. The introduction of R71 rails marks an important step towards creating a reliable, low-maintenance railway track in Russia for heavy-haul applications. In collaboration with representatives from JSC Russian Railways (RZD), an acceptance commission was held, and technical specifications were developed and approved. Field tests at the experimental ring of Railway Research Institute (JSC VNIIZHT), along with the certification process for these rails, are scheduled for the third quarter of 2025 [10].

The plant manufactures various types of switch rails and continuously expands its product line. A certificate

has been issued for a new type of switch rail – OR65 of the NT320VS category. These special-purpose rails are designed with enhanced strength and are intended for use in the construction of track superstructures on high-speed and mixed-traffic railway lines.

Key areas of development include the rolling of 800-meter-long rail strings with differential hardening, as well as improving the mechanical properties of differentially heat-hardened rails through the addition of modifying elements, particularly rare-earth metals. These technological innovations are expected to make railway tracks significantly quieter and reduce maintenance costs.

As part of the Strategy for the Development of the Metallurgical Industry of the Russian Federation through 2030, approved by the Russian Government at the end of 2022, a key objective has been set: to develop and implement technology for producing differentially heat-hardened rail strings 800 meters in length. These rails are expected to maintain uniform properties along their entire length and support an accumulated traffic tonnage of 2.5 billion gross tons, along with rail fastenings designed to offer comparable durability. The development of these advanced rails is already underway at EVRAZ ZSMK, with heavy-duty rails likely to be used in the production of the 800-meter-long rail strings at the plant.

As railway infrastructure continues to develop and expand, the demand for rail products is steadily rising. With each passing year, the speed and weight of rolling stock increase, resulting in greater load intensity on railway networks. EVRAZ ZSMK's rail production is well-equipped to meet the growing demands of 21st-century rail transport.

REFERENCES / СПИСОК ЛИТЕРАТУРЫ

1. Yur'ev A.B., Yunin G.N., Golovatenko A.V., Dorofeev V.V., Polevoi E.V. Development and implementation of the first in Russia technology for the production of differentially heat-strengthened rails using the heat of rolling heating. *Stal'*. 2016;(11):33–35. (In Russ.).
Юрьев А.Б., Юнин Г.Н., Головатенко А.В., Дорофеев В.В., Полевой Е.В. Разработка и внедрение первой в России технологии производства дифференцированно-термоупрочненных рельсов с использованием тепла прокатного нагрева. *Сталь*. 2016;(11):33–35.
2. Gromov V.E., Yuriev A.B., Morozov K.V., Ivanov Yu.F. Microstructure of Quenched Rails. Cambridge: CISP Ltd.; 2016:195.
3. Yuryev A.A., Kuznetsov R.V., Gromov V.E., Ivanov Yu.F., Shlyarova Yu.A. Long Rails: Structure and Properties after Ultra-Long Operation: Monograph. 2nd ed. Novokuznetsk: Poligrafist; 2022:311. (In Russ.).
Yuriev A.B., Gromov V.E., Ivanov Yu.F., Rubannikova Yu.A., Starostenkov M.D., Tabakov P.Y. Structure and Properties of Lengthy Rails after Extreme Long-Term Operation. Materials Research Society LLC USA; 2021:190.
4. Длинномерные рельсы: структура и свойства после сверхдлительной эксплуатации: Монография. Издание 2-е, доп. и переработанное / А.А. Юрьев, Р.В. Кузнецов, В.Е. Громов, Ю.Ф. Иванов, Ю.А. Шлярова. Новокузнецк: Полиграфист; 2022:311.
5. Gromov V.E., Nevskii S.A., Porfir'ev M.A., Kryukov R.E. Electron Microscopy of Rails Made of Transeutectoid Steel after Operation. Novokuznetsk: Poligrafist; 2024:212. (In Russ.).
Электронная микроскопия рельсов из заэвтектоидной стали после эксплуатации / В.Е. Громов, С.А. Невский, М.А. Порфирьев, Р.Е. Крюков. Новокузнецк: Полиграфист; 2024:212.
6. Polevoy E.V., Yunin G.N., Golovatenko A.V., Temlian-tsev M.V. Recent developments of rail steel products at the “EVRAZ West Siberian Iron & Steel Works”. *Stal'*. 2019;(7):55–58. (In Russ.).
Полевой Е.В., Юнин Г.Н., Головатенко А.В., Темлянцев М.В. Новейшие разработки рельсовой продукции в АО «ЕВРАЗ ЗСМК». *Сталь*. 2019;(7):55–58.
7. Polevoi E.V., Molokanov R.N., Borisov A.S., Yunusov A.M., Bessonova O.V. Experience of EVRAZ ZSMK in the production of rails for heavy-haul traffic for export. *Railway Track and Facilities*. 2024;(6):18–20. (In Russ.).
Полевой Е.В., Молоканов Р.Н., Борисов А.С., Юнусов А.М., Бессонова О.В. Опыт ЕВРАЗ ЗСМК по производству рельсов для тяжеловесного движения на экспорт. *Путь и путевое хозяйство*. 2024;(6):18–20.
8. Gromov V.E., Yur'ev A.B., Yur'ev A.A., Konovalev S.V., Porfir'ev M.A., Serebryakova A.A. Anthology of Structural and Phase States and Properties of Russian Rails of the XXI Century. Novokuznetsk: Poligrafist; 2024:181. (In Russ.).
Антология структурно-фазовых состояний и свойств российских рельсов XXI века / В.Е. Громов, А.Б. Юрьев, А.А. Юрьев, С.В. Коновалов, М.А. Порфирьев, А.А. Серебрякова. Новокузнецк: Полиграфист; 2024:181.
9. Polevoi E.V., Simonov Yu.N., Kozyrev N.A., Shevchenko R.A., Mikhno A.R. Phase and structural transformations when forming a welded joint from rail steel. Report 3. The use of thermokinetic and isothermal diagrams of austenite decomposition for selection of optimal modes of electric contact welding. *Izvestiya. Ferrous Metallurgy*. 2021;64(6): 420–426. (In Russ.).
<https://doi.org/10.17073/0368-0797-2021-6-420-426>
Полевой Е.В., Симонов Ю.Н., Козырев Н.А., Шевченко Р.А., Михно А.Р. Исследование фазовых и структурных превращений при формировании сварного соединения из рельсовой стали. Сообщение 3. Использование термокинетической и изотермической диаграмм распада аустенита для выбора оптимальных режимов электроконтактной сварки. *Известия вузов. Черная металлургия*. 2021;64(6):420–426.
<https://doi.org/10.17073/0368-0797-2021-6-420-426>
10. Dorofeev V.V., Dobryansky A.V., Yunin G.N., Golovatenko A.V., Molokanov R.N., Ovchinnikov D.V. Utility model patent 224546U1 RU. Railway rail. Application no. 12/18/2023, publ. 03/28/2024. Byul. no. 10. (In Russ.).
Патент на полезную модель 224546U1 RU. Железнодорожный рельс / В.В. Дорофеев, А.В. Добрянский, Г.Н. Юнин, А.В. Головатенко, Р.Н. Молоканов, Д.В. Овчинников. Заявл. 18.12.2023, опубл. 28.03.2024. Бюл. № 10.

Сведения об авторах

Information about the Authors

Viktor E. Gromov, Dr. Sci. (Phys.-Math.), Prof, Head of the Chair of Science named after V.M. Finkel', Siberian State Industrial University

ORCID: 0000-0002-5147-5343

E-mail: gromov@physics.sibsiu.ru

Sergei V. Konovalov, Dr. Sci. (Eng.), Prof., Vice-Rector for Research and Innovation, Siberian State Industrial University

ORCID: 0000-0003-4809-8660

E-mail: konovalov@sibsiu.ru

Egor V. Polevoi, Cand. Sci. (Eng.), Head of Bureau of Metal Science and Heat Treatment of Technical Department of the Rail Site, JSC EVRAZ United West Siberian Metallurgical Plant

E-mail: egor.polevoj@evraz.com

Виктор Евгеньевич Громов, д.ф.-м.н., профессор, заведующий кафедрой естественнонаучных дисциплин им. профессора В.М. Финкеля, Сибирский государственный индустриальный университет

ORCID: 0000-0002-5147-5343

E-mail: gromov@physics.sibsiu.ru

Сергей Валерьевич Коновалов, д.т.н., профессор, проректор по научной и инновационной деятельности, Сибирский государственный индустриальный университет

ORCID: 0000-0003-4809-8660

E-mail: konovalov@sibsiu.ru

Егор Владимирович Полевой, к.т.н., начальник бюро металловедения и термической обработки технического отдела рельсовой площадки, АО «ЕВРАЗ Объединенный Западно-Сибирский металлургический комбинат»

E-mail: egor.polevoj@evraz.com

Contribution of the Authors

Вклад авторов

V. E. Gromov – conceptualization, analysis of literary data on the influence of various factors on rails service life.

S. V. Konovalov – analysis of researches on the mechanisms of metal strengthening of rails during long-term operation.

E. V. Polevoi – analysis of developments of JSC EVRAZ United West Siberian Metallurgical Plant rail production in the 21st century.

В. Е. Громов – общая концепция работы, анализ литературных данных по влиянию различных факторов на срок службы рельсов.

С. В. Коновалов – анализ работ по механизмам упрочнения металла рельсов при длительной эксплуатации.

Е. В. Полевой – анализ разработок ЕВРАЗ ЗСМК по производству рельсов в XXI веке.

Received 10.09.2024

Revised 10.11.2024

Accepted 17.11.2024

Поступила в редакцию 10.09.2024

После доработки 10.11.2024

Принята к публикации 17.11.2024



UDC 621.78:669.15

DOI 10.17073/0368-0797-2025-1-44-50



Original article

Оригинальная статья

INFLUENCE OF HEAT TREATMENT MODES ON THE PROPERTIES OF 56DGNKH (Cu₂₀Ni₂₀Mn₂Cr) ALLOY

M. Yu. Belomytsev¹, M. A. Mikhailov², D. A. Kozlov¹,
A. M. Mikhailov², I. I. Karavatskii¹

¹ National University of Science and Technology “MISIS” (4 Leninskii Ave., Moscow 119049, Russian Federation)

² LLC Scientific and Technical Centre “Technologies of Special Metallurgy” (Office 181, 2 Institutskii Drive, Mosrentgen Village, Moscow 108820, Russian Federation)

✉ myubelom@yandex.ru

Abstract. Alloys of the Cu–Ni–Mn system are used in many areas, and for some applications (watchmaking, dentistry, precision mechanics) they must have high hardness. A state of high hardness can be achieved by two-stage heat treatment – quenching and subsequent aging. To obtain a good set of performance characteristics, decomposition of the solid solution must proceed through a continuous mechanism, which can be regulated by additional alloying (for example, chromium) and aging parameters. In this work, we studied the influence of quenching and aging modes on microhardness of 56DGNKh (Cu₂₀Ni₂₀Mn₂Cr) alloy. It was shown that quenching from temperatures of 700 – 750 °C provides higher microhardness values than quenching from 800 °C. By varying the temperature and duration of aging, it was found that the maximum microhardness is observed at aging temperatures of 475 – 500 °C. Metallographic analysis shows that in this case, the supersaturated solid solution of Mn, Ni and Cr in copper decomposes into a less supersaturated solid solution and the precipitation of MnNi intermetallic particles occurs according to a continuous mechanism. The change in microhardness of 56DGNKh alloy depending on the aging time is multi-stage: its increase at short exposures is replaced by a subsequent decrease at increasing exposure with a clearly defined maximum or “plateau” between these two parts of the graph, and this type of dependence is observed at all aging temperatures. X-ray diffraction phase analysis shows that during the aging process, concentration of the solid solution decreases and MnNi particles are formed, the crystal lattice period of which differs from the period of the solid solution by 50 pm. The observed patterns of changes in hardness during the aging process are explained from the standpoint of the general theory of decomposition of supersaturated solid solutions. The maximum increase in microhardness (up to 450 kgf/mm² versus 130 – 160 kgf/mm² in the state after quenching) is achieved at a coherent or semi-coherent interface between MnNi particles and a Ni-based solid solution. This is observed after quenching from 750 °C and aging at 475 °C for 10 h.

Keywords: copper alloy, heat treatment, quenching, aging, microhardness, structure, X-ray phase analysis, decomposition of solid solution

For citation: Belomytsev M.Yu., Mikhailov M.A., Kozlov D.A., Mikhailov A.M., Karavatskii I.I. Influence of heat treatment modes on the properties of 56DGNKh (Cu₂₀Ni₂₀Mn₂Cr) alloy. *Izvestiya. Ferrous Metallurgy*. 2025;68(1):44–50. <https://doi.org/10.17073/0368-0797-2025-1-44-50>

ИССЛЕДОВАНИЕ ВЛИЯНИЯ РЕЖИМОВ ТЕРМИЧЕСКОЙ ОБРАБОТКИ НА СВОЙСТВА СПЛАВА 56ДГНХ

М. Ю. Беломытцев¹, М. А. Михайлов², Д. А. Козлов¹,
А. М. Михайлов², И. И. Каравацкий¹

¹ Национальный исследовательский технологический университет «МИСИС» (Россия, 119049, Москва, Ленинский пр., 4)

² ООО Научно-технический центр «Технологии Специальной Металлургии» (Россия, 108820, Москва, п. Мосрентген, Институтский проезд, 2, офис 181)

✉ myubelom@yandex.ru

Аннотация. Сплавы системы Cu–Ni–Mn находят применение во многих областях и для некоторых из них (часовое производство, стоматология, точная механика) должны обладать высокой твердостью. Состояние с высокой твердостью достигается двухстадийной термической обработкой – закалкой и последующим старением. Для получения хорошего комплекса эксплуатационных характеристик распад твердого раствора должен идти по механизму непрерывного распада, что можно регулировать дополнительным легированием (например, хромом) и параметрами режима старения. В работе изучено влияние режимов закалки и старения на микротвердость сплава 56ДГНХ. Показано, что закалка от температур 700 – 750 °C обеспечивает большие значения микротвердости, чем закалка от 800 °C. Варьированием температуры и длительности старения найдено, что максимум микротвердости наблюдается при температурах старения

475 – 500 °С. Металлографический анализ показывает, что при этом происходит распад пересыщенного твердого раствора Mn, Ni и Cr в меди на менее пересыщенный твердый раствор и выделение частиц интерметаллида MnNi идет по механизму непрерывного распада. Изменение микротвердости сплава 56ДГНХ в зависимости от времени старения многостадийно. Ее рост при небольших выдержках сменяется последующим снижением при увеличении выдержки с отчетливо выраженным максимумом либо «плато» между этими двумя частями графика. Такой характер зависимости наблюдается при всех температурах старения. Рентгеноструктурный фазовый анализ показывает, что в процессе старения происходит уменьшение концентрации твердого раствора и образование частиц MnNi, период кристаллической решетки которых отличается от периода твердого раствора на 50 пм. Наблюдаемые закономерности изменения микротвердости в процессе старения объяснены с позиций общей теории распада пересыщенных твердых растворов. Максимум прироста микротвердости (до HV 0,5 = 45 кгс/мм² против HV 0,5 = 130 – 160 кгс/мм² в закаленном состоянии) достигается при когерентной или полукогерентной границе раздела частиц MnNi и твердого раствора на основе никеля. Это наблюдается после закалки от 750 °С и старения при 475 °С в течение 10 ч.

Ключевые слова: сплавы меди, термическая обработка, закалка, старение, микротвердость, структура, рентгеновский фазовый анализ, распад твердых растворов

Для цитирования: Беломятцев М.Ю., Михайлов М.А., Козлов Д.А., Михайлов А.М., Каравацкий И.И. Исследование влияния режимов термической обработки на свойства сплава 56ДГНХ. *Известия вузов. Черная металлургия*. 2025;68(1):44–50.

<https://doi.org/10.17073/0368-0797-2025-1-44-50>

INTRODUCTION

Alloys of the Cu–Ni–Mn ternary system are used in watchmaking for the manufacture of high-precision, small-sized components. They are also employed as high-temperature brazing alloys for brazing components with a high coefficient of linear expansion (CLE), such as glass. Additionally, they are used as dental materials for crowns and bridges due to the similarity of their CLE to that of tooth tissues. For application in some of these fields, they must possess sufficiently high hardness [1].

Despite the existing research on the Cu–Ni–Mn ternary system, some of its alloys remain insufficiently studied. At present, they are considered promising for applications in precision mechanics, electronics, and medicine due to their excellent corrosion resistance, stable coefficient of linear expansion (CLE), adequate elasticity, and valuable aesthetic properties.

The aim of this study is to investigate the effect of various heat treatment modes on the mechanical properties of 56DGNKh alloy.

Alloys of the Cu–Ni–Mn system can exist in two states: metastable and stable [2; 3]. After rapid cooling from temperatures not exceeding 910 °С they exhibit the structure of a supersaturated solid solution of nickel and manganese in copper and remain in a metastable state. Heating the metastable state leads to the formation of a stable two-phase structure, consisting of a solid solution of nickel and manganese in the copper lattice and a θ -phase, which is a homogeneous ordered solid solution that can be represented by the general formula MnNi [4; 5].

Fig. 1 shows a segment of the isothermal section of the Cu–Ni–Mn ternary phase diagram at 450 °С. The line of equal mass fractions of nickel and manganese also represents the line of minimal copper solubility in the MnNi compound. In alloys with compositions lying on this line, the amount of θ -phase is at its maximum. Based on this, alloys with equal nickel and manganese

contents, specifically 60 % Cu – 20 % Ni – 20 % Mn, are considered technically promising [6; 7].

An important factor influencing the structural strength of the 56DGNKh alloy (i.e., the favorable combination of strength, ductility, and hardness) is the structure of the θ -phase. Depending on the temperature at which it forms, the θ -phase may develop either through a discontinuous decomposition mechanism or a continuous decomposition mechanism of the supersaturated solid solution [8]. Continuous decomposition results in a fine-dispersed structure uniformly distributed throughout the original copper grain, whereas discontinuous decomposition promotes the growth of θ -phase precipitates from the grain boundaries, which reduces the mechanical properties of 56DGNKh alloy [9 – 12].

All processes based on the phenomenon of diffusion-driven decomposition of a solid solution are governed by the rate of this phase transformation. Proper alloying enables the acceleration of these processes without

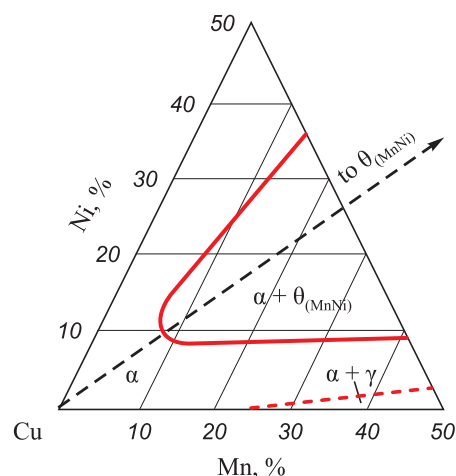


Fig. 1. Isothermal section of phase diagram of the Cu – Ni – Mn system at 450 °С [7]

Рис. 1. Изотермический разрез диаграммы состояния системы Cu – Ni – Mn при 450 °С [7]

degrading the structural characteristics of the precipitated particles. As calorimetric studies have shown [13], additional alloying of the Cu–Ni–Mn system with chromium in an amount of 1.8 – 2.2 wt. % allows for the highest rate of initial decomposition of the supersaturated solid solution and promotes the continuous decomposition mechanism. During continuous decomposition, a large number of MnNi particles exceeding 5 nm in size forms within the grain at the initial stage of the process, effectively preventing the growth of discontinuous decomposition regions from the grain boundaries [14; 15]. It should also be noted that regardless of the type of decomposition occurring, equilibrium is not fully reached even after prolonged aging treatments of more than 100 h [13; 16].

The aim of this study is to determine the optimal aging parameters for 56DGNKh alloy to maximize hardness under conditions that promote the continuous decomposition of its supersaturated solid solution.

EXPERIMENTAL METHODOLOGY

This study examined samples of 56DGNKh alloy, whose chemical composition is presented in the Table. The alloy was produced by induction melting in a protective atmosphere. The material was not subjected to homogenization annealing. Rods with a diameter of approximately 40 mm were obtained by hot forging of the ingot.

The samples used for testing measured approximately 5×5×7 mm. Their heat treatment was conducted in two stages: quenching and aging, both performed in vacuum inside an evacuated quartz ampoule. Quenching was carried out from temperatures ranging from 700 to 800 °C, with a 30-min holding time under a vacuum of approximately 10⁻² mmHg. Cooling involved removing the ampoule from the furnace and allowing it to cool without air admission. Under these conditions, the samples cooled from the heating temperature to approximately 150 °C in 2.5 min, followed by further cooling in air. The effect of quenching on the formation of a homogeneous solid solution was confirmed by the low hardness of the samples and the microstructure, which corresponded to a solid solution with approximately equiaxed grains ranging from 25 to 45 μm, with some annealing twins, this was also supported by X-ray phase analysis results. The decomposition of the metastable supersaturated solid solution was achieved through the thermal aging process. Aging was performed in a muffle furnace in air for 2, 7, 10, 12, and 25 h at temperatures ranging

from 375 to 525 °C. After aging, the samples were cooled in air. Three samples were tested for each aging mode.

Microhardness measurements and microstructural analysis using metallographic methods were conducted on sections located at least 1 mm from the sample surface. The polished samples, prepared using standard surface preparation techniques, were etched with *aqua regia* [17] for 30 – 60 s. Microhardness (*HV*, in kgf/mm²) was measured using a PMT-3 microhardness tester following the Vickers method under a 500 g load. Variations in microhardness values between samples (up to 90 HV) due to liquation heterogeneity significantly exceeded the measurement error for an individual sample (maximum 11 HV). Therefore, the graphs present the average microhardness values obtained for each sample, without indicating the measurement spread.

The phase composition of the alloy was analyzed by X-ray phase analysis using a DRON-3M diffractometer with CoK_α radiation.

RESEARCH RESULTS

The microhardness of the 56DGNKh alloy samples after quenching is relatively low, measuring HV 0.5 = 100 – 130 kgf/mm². The microstructure at this stage does not contain any second-phase inclusions (Fig. 2, a).

During aging, the change in microhardness follows a multi-stage pattern: an initial increase at short aging times is followed by a subsequent decrease with increasing aging time, with a clearly defined maximum or a plateau between these two stages of the graph.

Fig. 3 presents data on the microhardness values obtained after different heat treatment modes.

Analysis of these dependencies reveals the following.

The maximum microhardness of 56DGNKh alloy achieved through aging is HV 0.5 = 456 kgf/mm², which is 3.5 – 4.5 times higher than the initial value.

When quenching temperatures are in the range of 700 – 750 °C, the microhardness attained after aging is at its highest. Increasing the quenching temperature to 800 °C leads to a reduction in maximum microhardness (Fig. 3, a). Therefore, the optimal quenching temperature should be considered 750 °C.

The maximum microhardness is observed at aging temperatures of 475 – 500 °C for aging durations of 7 to 12 h. This temperature and time range should be used for the aging process.

With varying aging times, the pattern of microhardness changes remains the same for all aging temperatures, but the degree of hardening achieved differs. The common characteristic of these dependencies is that microhardness increases with aging time up to a certain point, after

Chemical composition of 56DGNKh alloy, wt. %

Химический состав сплава 56ДГНХ, мас. %

Cu	Ni	Mn	Cr
55 – 57	20 – 22	20 – 22	1.8 – 2.2

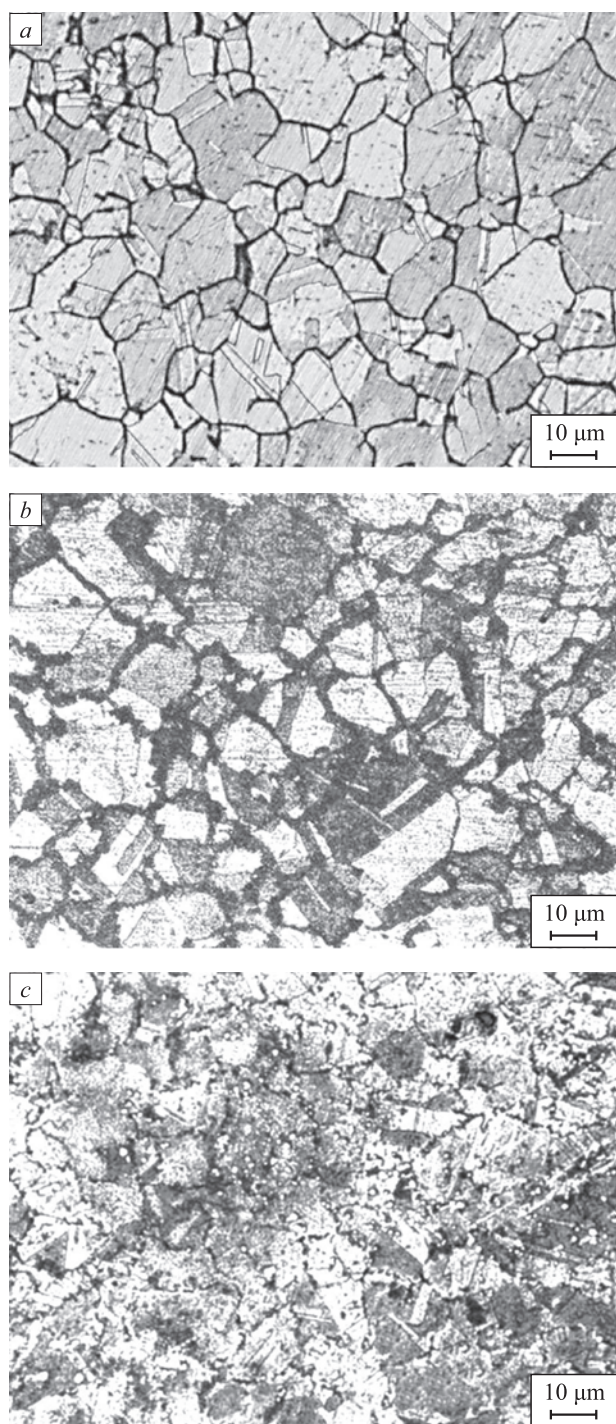


Fig. 2. Microstructure of 56DGNKh alloy after quenching (a), aging by intermittent decomposition at 525 °C for 2 h (b) and aging by continuous decomposition at 475 °C for 10 h (c)

Рис. 2. Микроструктура сплава 56ДГНХ в состоянии после закалки (a), старения по механизму прерывистого распада при 525 °C в течение 2 ч (b) и старения по механизму непрерывного распада при 475 °C в течение 10 ч (c)

which it begins to decrease. The rate of decrease is higher at higher aging temperatures. The aging time after which microhardness starts to decline shortens as the aging temperature increases (Fig. 3, b). The optimal aging mode for achieving the maximum increase in microhardness in

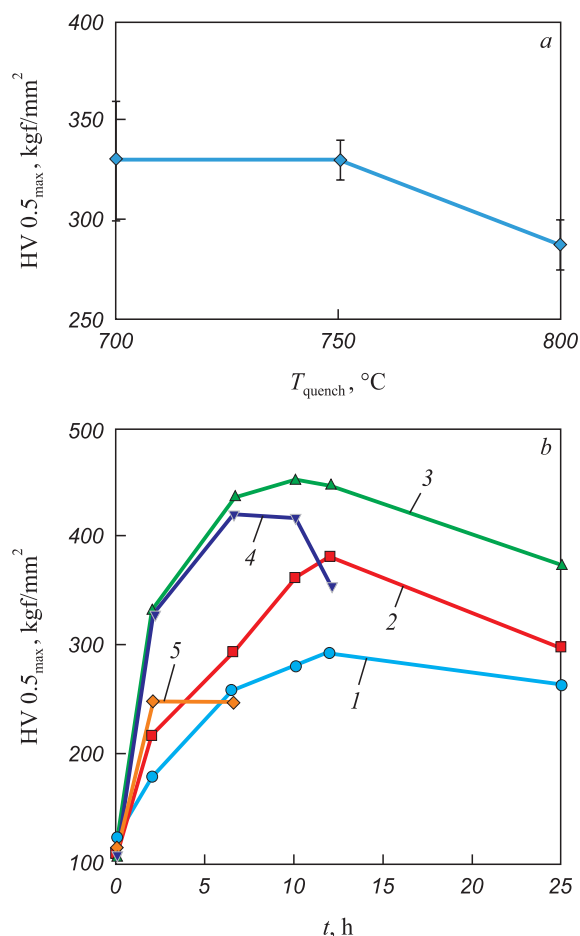


Fig. 3. Dependence of microhardness of 56DGNKh alloy on the quenching temperature (a) and aging duration at temperatures °C:

1 – 475; 2 – 425; 3 – 475; 4 – 500; 5 – 525, quenching from 750 °C (b)

Рис. 3. Зависимость микротвердости сплава 56ДГНХ от температуры закалки (a) и продолжительности старения при температуре старения, °C:

1 – 475; 2 – 425; 3 – 475; 4 – 500; 5 – 525, закалка от 750 °C (b)

56DGNKh alloy is heating to 475 °C with a 10 h holding time. Under these conditions, the microhardness increases to HV 0.5 = 450 kgf/mm².

Phase and structural analysis of 56DGNKh alloy in different states revealed that after quenching, X-ray diffraction (XRD) patterns show only lines corresponding to a solid solution based on copper with an FCC lattice. No effects of isomorphous regions in the matrix with a similar lattice parameter are observed in diffraction lines, even for reflections with large indices (e.g., (220)) (Fig. 4, a), confirming the homogeneity of the quenched solid solution. For this solid solution state, a slight shift in diffraction lines from the tabulated values characteristic of pure copper is observed, which is caused by lattice distortions due to the high concentration of nickel and manganese in the solid solution.

The essence of the aging process is the formation of MnNi compound particles, which leads to a decrease

in the concentration of alloying elements (Mn, Ni, Cr) in the solid solution. The early stages of this process are not detected by X-ray diffraction analysis because the amount of the precipitated hardening phase is still low, and the lattice parameters of the copper-based solid solution and the MnNi compound are very similar. However, this process can be observed metallographically: if the phase transformation follows a discontinuous decomposition mechanism, dark precipitate bands of the MnNi second phase begin to form along the grain boundaries of the α -solid solution present in the alloy after quenching (Fig. 2, *b*). When a sufficient amount of the MnNi phase has precipitated, its formation is indicated by changes in the shape of diffraction lines [18] on X-ray diffraction patterns (Fig. 4, *b*, *c*).

The absence of this effect in the first diffraction lines with low indices is explained by the close lattice parameters of the tetragonal θ -phase and copper. The observed shift of the primary (220) line from $2\theta = 87.5^\circ$ (Fig. 4, *a*) toward higher angles (almost $2\theta = 90^\circ$, Fig. 4, *b*) indicates that the lattice parameter of the solid solution is approaching the equilibrium lattice parameter values characteristic of pure copper (tabulated $2\theta = 88^\circ 54'$).

According to the general theory of supersaturated solid solution decomposition, the two-stage nature of hardness changes during aging can be explained by the structural and crystallographic characteristics of the alloy [10; 19; 20]:

- during the initial hardness increase, the amount of precipitated MnNi phase is small, but the particles remain coherent with the matrix, leading to a gradual hardness increase as their volume fraction grows;
- as the number of precipitated particles increases, they begin to lose coherence with the matrix, but their increasing volume fraction results in maximum hardening;
- at later aging stages, as the particle size continues to grow and coherence with the matrix is lost, their hardening effect diminishes due to an increased interparticle distance, despite their continuing increase in volume fraction.

With increasing aging temperature, the described sequence of transformations exhibits a wave-like pattern. At higher aging temperatures, MnNi intermetallic particles precipitate rapidly and quickly lose coherence with the matrix. As a result, the maximum microhardness is reached sooner, but the overall hardening effect is lower. At lower aging temperatures, the precipitation process occurs more slowly, and the number of MnNi particles increases at a slower rate. The loss of coherence also progresses gradually, shifting the hardness peak to longer aging times while allowing for a higher overall strengthening effect. Based on this analysis, the optimal aging conditions are those that provide the longest possible coexistence of coherent copper-based α -solid solu-

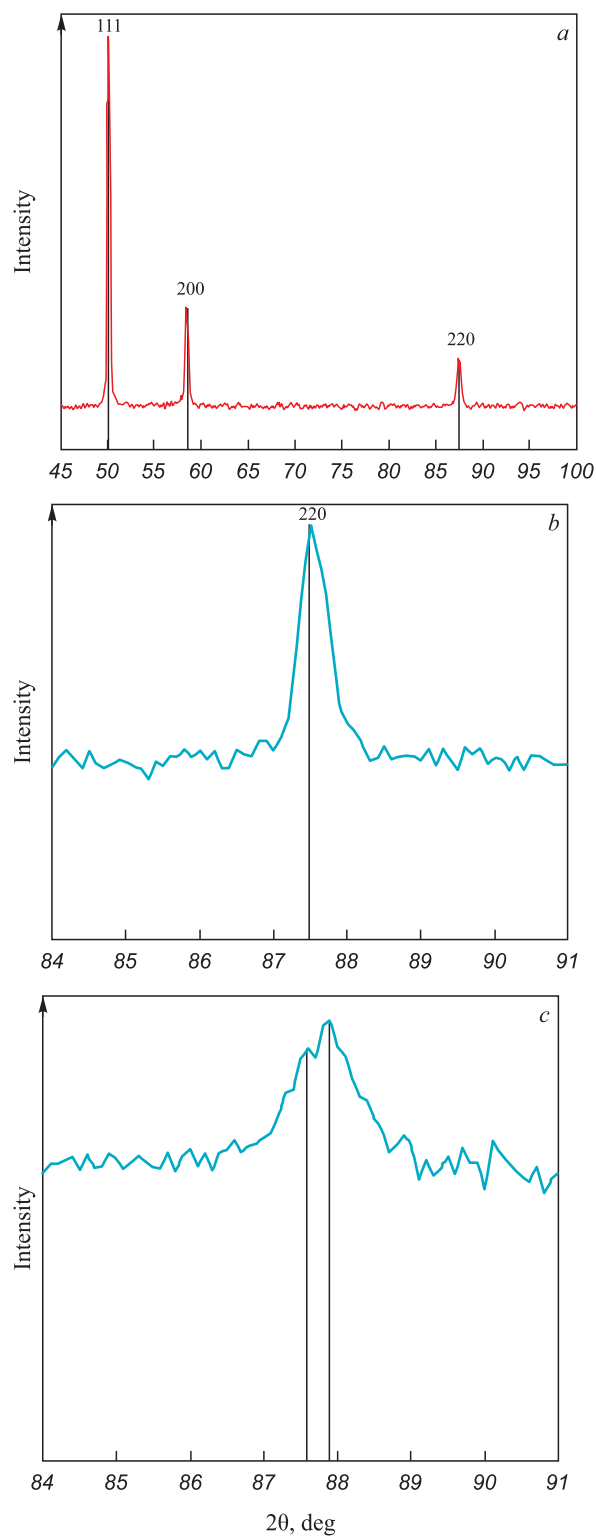


Fig. 4. X-ray diffraction pattern of 56DGNKh alloy after quenching from 800 °C for 30 min (*a*); the third diffraction maximum of this pattern, corresponding to the $\langle 220 \rangle$ line of the copper lattice (*b*) and the same line for the alloy after quenching and aging at 475 °C for 25 h (*c*)

Рис. 4. Рентгенограмма сплава 56ДГНХ после закалки с 800 °C в течение 30 мин (*a*); третий дифракционный максимум рентгенограммы сплава 56ДГНХ после закалки от 800 °C с выдержкой в течение 30 мин, соответствующий линии (220) решетки меди (*b*); та же линия для сплава после закалки и старения при 475 °C в течение 25 ч (*c*)

tion regions and MnNi hardening phase particles. This is achieved at aging temperatures of 475 – 500 °C.

CONCLUSIONS

In the quenched state, the microhardness of 56DGNKh alloy ranges from 100 to 130 kgf/mm², which is characteristic of a homogeneous copper-based solid solution.

As the aging temperature increases from 375 to 475 °C, the microhardness exhibits a monotonic increase from HV 0.5 = 156 – 190 kgf/mm² to HV 0.5 = 440 – 456 kgf/mm², with higher temperatures leading to a faster attainment of peak hardness; however, the ultimate hardness value depends on the specific aging temperature.

At 500 – 525 °C, a sharp drop in maximum attainable microhardness is observed, reducing it to HV 0.5 = 250 – 290 kgf/mm², indicating overaging of the alloy. The microhardness dependence on aging time follows a curve with a distinct peak across all quenching and aging temperatures.

The optimal two-stage heat treatment for this alloy consists of quenching, which involves heating to 750 °C, holding for 30 min, and cooling at a rate of no less than 300 °C/min, followed by aging by reheating to 475 °C, holding for 10 h, and subsequent cooling in air. After this treatment, the microhardness reaches HV 0.5 = 450 kgf/mm².

REFERENCES / СПИСОК ЛИТЕРАТУРЫ

1. Molotilov B.V. Precision Alloys. Moscow: Metallurgiya; 1974:315. (In Russ.).
Молотиллов Б.В. Прецизионные сплавы. Москва: Металлургия; 1974:315.
2. Kolachev B.A., Elagin V.I., Livanov V.A. Metal Science and Heat Treatment of Non-Ferrous Metals and Alloys. Moscow: NUST MISIS; 1999:416. (In Russ.).
Колачев Б.А., Елагин В.И., Ливанов В.А. Металловедение и термическая обработка цветных металлов и сплавов. Москва: МИСИС; 1999:416.
3. Pastukhova Zh.P., Rakhstadt A.G. Spring Copper Alloys. Moscow: Metallurgiya; 1979:336. (In Russ.).
Пастухова Ж.П., Рахштадт А.Г. Пружинные сплавы меди. Москва: Металлургия; 1979:336.
4. Shapiro S., Tyler O.K., Laham R. Phenomenology of precipitation in copper-20 pct nickel-20 pct manganese. *Metalurgical Transactions*. 1974;5(11):2457–2469.
<http://doi.org/10.1007/BF02644029>
5. Miki M., Hori S. Thermodynamics of Ni – Mn solid solution lattice. *Journal of Japan Institute of Metals*. 1982;46(3): 301–306.
6. Osintsev O.E., Fedorov V.N. Copper and Copper Alloys. Moscow: Mashinostroenie; 2004:420. (In Russ.).
Осинцев О.Е., Федоров В.Н. Медь и медные сплавы. Москва: Машиностроение; 2004:420.
7. Bazhenov V.E. Phase diagram of the Cu – Ni – Mn system. *Tsvetnaya metallurgiya*. 2013;(1):49–55. (In Russ.).
Баженов В.Е. Фазовая диаграмма системы Cu – Ni – Mn. *Цветная металлургия*. 2013;(1):49–55.
8. Rolland J., Whitwham D. Discontinuous precipitation kinetics in Cu – Ni – Mn alloys. *Comptes Rendus de l'Académie des Sciences*. 1970;269:1265–1268.
9. Novikov I.I. Theory of Metals Heat Treatment. Moscow: Metallurgiya; 1986:480. (In Russ.).
Новиков И.И. Теория термической обработки металлов. Москва: Металлургия; 1986:480.
10. Martin J.W. Micromechanisms in Particle-Hardened Alloys. Cambridge University Press; 1980:84.
11. Xie W., Wang Q., Xie G., Liu D., Mi X., Gau X. Research of interaction between continuous and discontinuous precipitation in Cu-20Ni-20Mn alloy. *Rare Metal Materials and Engineering*. 2017;46(12):3799–3804.
12. Xie W.-B., Wang Q.-S., Mi X.-J., Xie G.-L., Liu D.-M., Gao X.-C., Li Y. Microstructure evolution and properties of Cu-20Ni-20Mn alloy during aging process. *Transactions of Nonferrous Metals Society of China*. 2015;25(10): 3247–3251.
[https://doi.org/10.1016/S1003-6326\(15\)63960-7](https://doi.org/10.1016/S1003-6326(15)63960-7)
13. Rad'kov A.I., Tretyakova S.M., Potapov A.A. The influence of chromium on the strength properties of the 56DGNX alloy. In: *Thermal and Elastic Properties of Precision Alloys*. Moscow: Metallurgiya; 1986:82–86.
Радьков А.И., Третьякова С.М., Потапов А.А. Влияние хрома на прочностные свойства сплава 56ДГНХ. В кн.: *Тепловые и упругие свойства прецизионных сплавов. Тематический сборник научных трудов*. Москва: Металлургия; 1986:82–86. (In Russ.).
14. Sukhovarov V.F. Discontinuous Precipitation of Phases in Alloys. Novosibirsk: Nauka; 1983:312. (In Russ.).
Суховаров В.Ф. Прерывистое выделение фаз в сплавах. Новосибирск: Наука; 1983:312.
15. Xie W.-B., Wang Q.-S., Xie G.-L., Mi X.-J., Liu D.-M., Gao X.-C. Kinetics of discontinuous precipitation in Cu-20Ni-20Mn alloy. *International Journal of Minerals, Metallurgy and Materials*. 2016;23(3):323.
<https://doi.org/10.1007/s12613-016-1241-0>
16. Mhaede M., Altenberger I., Kuhn H.-A., Wollmann M., Wagner L. Enhancing mechanical properties of high strength Cu-20Mn-20Ni. In: *4th Int. Conf. on Laser Peening, May, 2013, Madrid, Spain*.
17. Kovalenko V.S. Metallographic Reagents. Ref. ed. Moscow: Metallurgiya; 1981:120. (In Russ.).
Коваленко В.С. Металлографические реактивы: Справочное издание Москва: Металлургия; 1981:120.
18. Gorelik S.S., Rastorguev L.N., Skakov Yu.A. X-ray and Electron-Optical Analysis. Moscow: Metallurgiya; 1970:366. (In Russ.).
Горелик С.С., Расторгуев Л.Н., Скаков Ю.А. Рентгенографический и электроннооптический анализ. Москва: Металлургия; 1970:366.
19. Shtremel' M.A. Strength of Alloys. Part 2. Deformation. Moscow: NUST MISIS; 1997:527. (In Russ.).
Штремель М.А. Прочность сплавов. Часть 2. Деформация. Москва: ИД МИСИС; 1997:527.
20. Cockinson D., Dick K. Prediction and observation of hardening mechanisms. *Theoretical Interchange Journal*. 1969;14:88.

Information about the Authors

Сведения об авторах

Mikhail Yu. Belomyttsev, Dr. Sci. (Eng.), Prof. of the Chair "Metallography and Physics of Strength", National University of Science and Technology "MISIS"

E-mail: myubelom@yandex.ru

Mikhail A. Mikhailov, Chief Engineer, LLC Scientific and Technical Centre "Technologies of Special Metallurgy"

E-mail: mikhailovma@mail.ru

Dmitrii A. Kozlov, Cand. Sci. (Eng.), Senior Researcher of the Chair "Metallography and Physics of Strength", National University of Science and Technology "MISIS"

E-mail: rostnab.kda@mail.com

Aleksandr M. Mikhailov, General Director, LLC Scientific and Technical Centre "Technologies of Special Metallurgy"

E-mail: alex.alloys@gmail.com

Il'ya I. Karavatskii, Student, National University of Science and Technology "MISIS"

E-mail: ikaravatskiy@gmail.com

Михаил Юрьевич Беломытцев, д.т.н., профессор кафедры металловедения и физики прочности, Национальный исследовательский технологический университет «МИСИС»

E-mail: myubelom@yandex.ru

Михаил Александрович Михайлов, главный инженер, ООО Научно-технический центр «Технологии Специальной Металлургии»

E-mail: mikhailovma@mail.ru

Дмитрий Александрович Козлов, к.т.н., старший научный сотрудник кафедры металловедения и физики прочности, Национальный исследовательский технологический университет «МИСИС»

E-mail: rostnab.kda@mail.com

Александр Михайлович Михайлов, генеральный директор, ООО Научно-технический центр «Технологии Специальной Металлургии»

E-mail: alex.alloys@gmail.com

Илья Иванович Каравацкий, студент, Национальный исследовательский технологический университет «МИСИС»

E-mail: ikaravatskiy@gmail.com

Contribution of the Authors

Вклад авторов

M. Yu. Belomyttsev – article conceptualization, rationale for the study, writing the final version of the article.

M. A. Mikhailov – providing the metallurgical part of the work (preparation and smelting of the alloy).

D. A. Kozlov – providing the radiographic part of the work (recording, interpretation, analysis of spectra).

A. M. Mikhailov – providing part of the work related to pressure treatment, sample manufacturing, and heat treatments.

I. I. Karavatskii – literary analysis, provision of metallographic and X-ray structural parts of the work, writing a draft version of the article.

М. Ю. Беломытцев – концепция статьи, обоснование проведения исследования, написание окончательного варианта статьи.

М. А. Михайлов – обеспечение металлургической части работы (подготовка и проведение выплавки сплава).

Д. А. Козлов – обеспечение рентгенографической части работы (съемка, расшифровка, анализ спектров).

А. М. Михайлов – обеспечение части работы, связанной с обработкой давлением, изготовлением образцов, проведением термических обработок.

И. И. Каравацкий – анализ состояния вопроса по литературным источникам, обеспечение металлогической и рентгеноструктурной части работы, написание чернового варианта статьи.

Received 19.04.2024

Revised 14.06.2024

Accepted 29.10.2024

Поступила в редакцию 19.04.2024

После доработки 14.06.2024

Принята к публикации 29.10.2024



UDC 621.791.927.5

DOI 10.17073/0368-0797-2025-1-51-59



Original article

Оригинальная статья

EFFECT OF THERMAL CYCLES ON FORMATION OF PEARLITIC HEAT-RESISTANT STEEL STRUCTURE UNDER WIRE ARC ADDITIVE MANUFACTURING

I. V. Vlasov[✉], A. I. Gordienko, V. M. Semenchuk

Institute of Strength Physics and Materials Science, Siberian Branch of Russian Academy of Sciences (2/4 Akademicheskii Ave., Tomsk 634055, Russian Federation)

✉ viv@ispms.ru

Abstract. The authors investigated the microstructure and mechanical properties of a model wall manufactured by arc wire 3D printing. 3D printing was performed using heat-resistant pearlitic steel wire in coldArc reduced heat input mode. Stationary thermal imager was employed to analyze the thermal cycles during layer deposition. Compressed air cooling to 200 °C was applied before each layer deposition to reduce heat accumulation. The high temperature gradients between the molten metal and the cooled layer resulted in areas with non-uniform structure, typical of welded joints after arc welding. Such areas with non-uniform structure were formed during the printing of each new layer and repeated throughout the wall height. It was observed that each solidified layer undergoes cyclic thermal effects during the deposition of subsequent ten layers. Intensive heating from deposition of two to three new layers leads to partial structural-phase transformations in the underlying layer. Deposition of the next 7 – 8 layers leads to heating similar to the “tempering” thermal operation. Microstructure analysis across different areas of the wall revealed acicular bainite with a small proportion of lath ferrite, bainitic ferrite, and martensitic-austenitic constituents. A slight increase in the width dimensions of acicular structure laths was observed with increasing wall height compared to the lower layers. The highest microhardness values were observed at the wall and substrate fusion zone (320 ± 7 kgf/mm²) due to rapid heat conduction and high cooling rates during the initial stages of printing. In the wall bulk, microhardness values ranged from 260 to 300 kgf/mm². The scatter of values and the periodic nature of the microhardness curve are associated with the formation of areas with non-uniform structure within each deposited layer of the wall. The wall material exhibits high strength characteristics (up to 800 MPa) and relative elongation (9 – 12 %).

Keywords: additive technology, WAAM, GMAW, pearlitic heat-resistant steel, microstructure, mechanical properties, thermal cycling

Acknowledgements: The work was performed within the framework of the Russian Science Foundation project No. 24-29-00827.

For citation: Vlasov I.V., Gordienko A.I., Semenchuk V.M. Effect of thermal cycles on formation of pearlitic heat-resistant steel structure under wire arc additive manufacturing. *Izvestiya. Ferrous Metallurgy*. 2025;68(1):51–59. <https://doi.org/10.17073/0368-0797-2025-1-51-59>

ВЛИЯНИЕ ТЕРМИЧЕСКИХ ЦИКЛОВ НА ФОРМИРОВАНИЕ СТРУКТУРЫ ЖАРОПРОЧНОЙ СТАЛИ ПЕРЛИТНОГО КЛАССА В УСЛОВИЯХ ПРОВОЛОЧНОГО ЭЛЕКТРОДУГОВОГО АДДИТИВНОГО ПРОИЗВОДСТВА

И. В. Власов[✉], А. И. Гордиенко, В. М. Семенчук

Институт физики прочности и материаловедения Сибирского отделения РАН (Россия, 634055, Томск, Академический пр., 2/4)

✉ viv@ispms.ru

Аннотация. В работе исследованы микроструктура и механические свойства модельной стенки из жаропрочной стали перлитного класса, изготовленной с использованием электродуговой проволочной 3D-печати в режиме сниженного тепловложения coldArc. Для анализа тепловых циклов при нанесении слоев использовался стационарный тепловизор. Перед нанесением каждого слоя применялось охлаждение сжатым воздухом до 200 °C, чтобы уменьшить накопление тепла. Высокие градиенты температур между расплавленным металлом и охлажденным слоем привели к образованию участков с неоднородной структурой, строение которых типично для сварного шва после электродуговой сварки. Такие участки с неоднородной структурой формируются при печати каждого нового слоя и повторяются по всей высоте стенки. Обнаружено, что каждый закристаллизовавшийся слой подвергается циклическому термическому воздействию при нанесении последующих десяти слоев. Высокий нагрев от нанесения двух-трех новых слоев приводит к частичным структурно-фазовым превращениям в нижележащем слое. Нанесение последующих семи – восьми слоев приводит к нагреву, аналогичному термической

операции отпуск. При анализе микроструктуры в разных участках стенки выявлен игольчатый бейнит с небольшой долей реечного и бейнитного феррита и мартенситно-аустенитной составляющей. По мере увеличения высоты стенки наблюдалось незначительное увеличение ширины реек игольчатых структур по сравнению с нижними слоями стенки. Наиболее высокие значения микротвердости наблюдались в месте сплавления стенки и подложки (320 ± 7 кгс/мм²) в результате быстрого теплоотвода и высокой скорости охлаждения на начальных этапах печати. В основном объеме стенки значения микротвердости изменялись в диапазоне 260 – 300 кгс/мм². Разброс значений и периодический характер кривой микротвердости связан с формированием участков с неоднородной структурой в пределах каждого нанесенного слоя стенки. Материал стенки характеризуется высокими значениями прочностных характеристик (до 800 МПа) и относительного удлинения (9 – 12 %).

Ключевые слова: аддитивная технология, WAAM, GMAW, жаропрочная сталь перлитного класса, микроструктура, механические свойства, термоциклирование

Благодарности: Исследование выполнено за счет гранта Российского научного фонда № 24-29-00827.

Для цитирования: Власов И.В., Гордиенко А.И., Семенчук В.М. Влияние термических циклов на формирование структуры жаропрочной стали перлитного класса в условиях проволочного электродугового аддитивного производства. *Известия вузов. Черная металлургия*. 2025;68(1):51–59. <https://doi.org/10.17073/0368-0797-2025-1-51-59>

INTRODUCTION

Additive manufacturing technologies are categorized into three main groups based on the energy source used: laser-based, electron beam-based, and arc-based methods [1]. Compared to laser- and electron beam-based processes, the use of an electric arc provides higher energy efficiency and greater 3D printing speeds, with material deposition rates reaching approximately 4 – 9 kg/h [2]. A key advantage of wire arc additive manufacturing (WAAM) in a shielding gas environment, based on the *Gas Metal Arc Welding* (GMAW) process, is the ability to produce large-scale components [3]. However, a major disadvantage of WAAM technologies is excessive heat accumulation within the manufactured part [4; 5]. This occurs because heat dissipation becomes more difficult as the number of deposited layers increases [6]. The reduction in cooling rate leads to more complex thermal history during layer deposition, changes in bead width and geometry [7 – 9], and, consequently, results in non-uniform microstructure and property variations across different sections of the part, along with reduced dimensional accuracy.

One approach to mitigating heat accumulation in WAAM is the application of reduced heat input technologies, such as *Cold Metal Transfer* (CMT) (developed by Fronius) and *coldArc* (developed by EWM) [10]. These techniques involve short arc welding, characterized by alternating cycles of short circuiting and arc burning. In [11], it was demonstrated that walls manufactured under reduced heat input conditions exhibit improved mechanical properties and reduced surface roughness. B.P. Nagasai and co-authors [12] identified that components fabricated using CMT technology exhibit a finer-grained microstructure and higher mechanical characteristics compared to those produced under standard arc welding modes in shielding gases.

Monitoring and controlling interlayer temperature (the temperature of the top layer before the next layer is deposited) is another method for managing heat accu-

mulation in the manufactured part. Studies [6; 13] have shown that interlayer temperature increases up to 550 °C as the number of deposited layers grows. To monitor temperature during 3D printing, thermographic infrared cameras [6] or thermocouples [8] are commonly used. To maintain consistent interlayer temperature, the introduction of pauses between layer depositions has been proposed [13; 14]. However, extending the time intervals reduces productivity, as achieving the required interlayer temperature through passive cooling significantly increases the overall manufacturing time. Therefore, active cooling methods are employed to minimize pauses between layers while maintaining geometric accuracy. The simplest and most versatile approach is CO₂ jet cooling, which was investigated in [15] for the production of a titanium alloy wall. However, more complex yet highly efficient cooling systems also exist. In [16], a thermoelectric cooling system was proposed for 3D printing of walls. Its operating principle involves direct heat removal through contact plates that move as the wall grows.

Low-alloy pearlitic heat-resistant steels are an important class of structural steels [17]. These steels are widely used in heat exchangers and steam heaters [18]. The correlation between thermal cycling and microstructural changes (grain morphology and size, phase composition) in pearlitic heat-resistant steels during wire arc additive manufacturing remains insufficiently studied.

Thus, this study aims to investigate the effect of cyclic heating during wire arc additive manufacturing of pearlitic heat-resistant steel on the formation of microstructure and mechanical properties. To minimize heat accumulation in the printed wall and prevent excessive bead spreading during printing, the *coldArc* reduced heat input mode and forced air cooling were applied.

RESEARCH MATERIALS AND METHODS

For 3D printing of the model wall, a 1.2 mm diameter OK Autrod 13.14 welding wire (ESAB Corporation, USA) with a carbon content of 0.06 – 0.10 % was

used. A 10 mm thick plate of 12Kh1MF steel served as the substrate. According to the quality certificate, the carbon content in 12Kh1MF steel was 0.12 %. This steel has a chemical composition similar to that of the wire and is commonly used for components operating at 540 – 580 °C. The main alloying elements in this steel are chromium, molybdenum, and vanadium.

The 3D printing process was performed using the Gas Metal Arc Welding (GMAW) arc deposition method in a shielding gas environment. The shielding gas consisted of a mixture of 82 % Ar and 18 % CO₂. The movement of the welding torch was controlled using a FANUC AM-100iD robotic arc welding system (FANUC, Japan) with an R-30iB Plus controller. A stationary FLIR A305sc thermal imager was used for temperature monitoring and control.

The manipulator operated in conjunction with an EWM Titan XQ R 400 power source (EWM, Germany). Layer deposition was carried out in the *coldArc* reduced heat input mode, a modification of the GMAW process. The *coldArc* mode allows for reduced heat input by employing short arc welding.

The torch angle relative to the substrate was 10° (Fig. 1, a). The 3D printing parameters were as follows: current – 118 A, voltage – 16.9 V, wire feed rate – 3000 mm/min, torch travel speed – 350 mm/min. The wall had a height of approximately 70 mm and consisted of 42 layers (Fig. 1, b).

In a previous study [19], the authors investigated the microstructure and mechanical properties of model walls printed using the same wire without additional cooling. It was shown that heat accumulation negatively affects the mechanical properties of the printed walls. In the present study, to reduce heat buildup, each layer was cooled to 200 °C after deposition. Compressed air cooling was applied using a compressor. Additionally, the substrate was preheated to 100 – 150 °C to reduce the temperature gradient and improve fusion zone uniformity.

Samples for mechanical testing and microstructural analysis were extracted from the bulk of the wall. All samples had identical geometry and were polished using abrasive papers of varying grit sizes (80 – 2000) to achieve a mirror-like surface finish. A cross-section of the wall was prepared for microstructural examination and microhardness measurements (Fig. 1, c). Microstructure analysis was conducted using a Carl Zeiss Axiovert 25 optical microscope and a LEO EVO 50 scanning electron microscope (Carl Zeiss, Germany) at the NANOTECH Shared Research Facility of the Institute of Strength Physics and Materials Science, Siberian Branch of the Russian Academy of Sciences. Microhardness measurements were taken along the entire height of the cross-section using a PMT-3 microhardness tester with a Vickers pyramid load of 0.98 N (100 g).

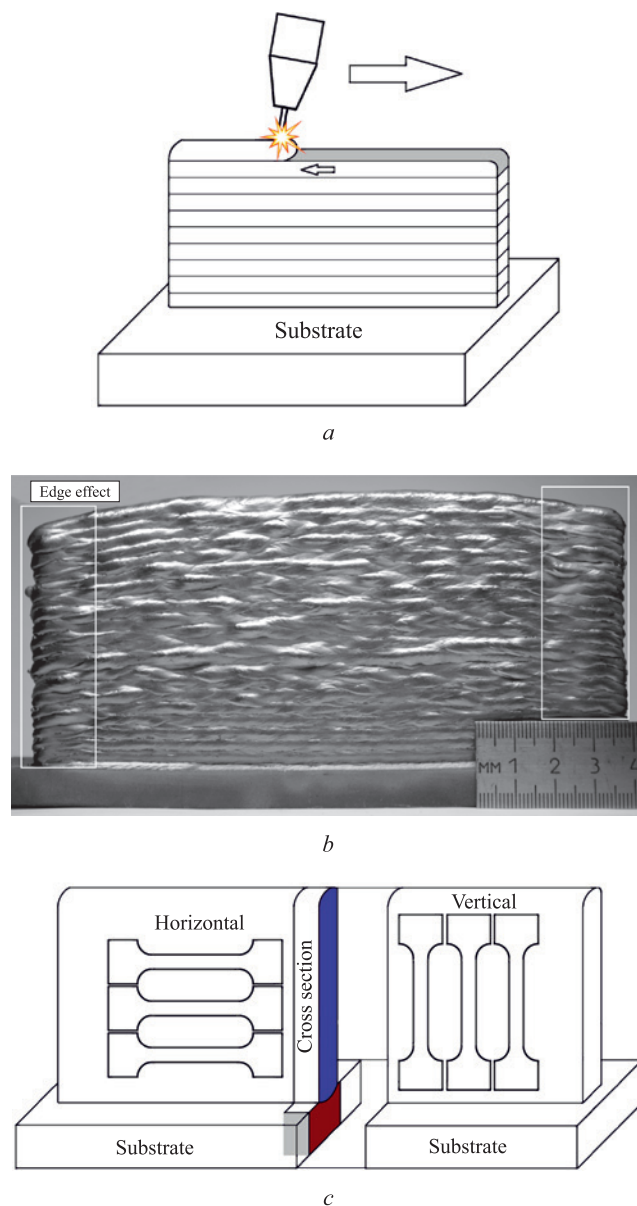


Fig. 1. Schematic representation of layer-by-layer deposition (a), appearance of the printed wall (b), sample cutting scheme (c)

Рис. 1. Схема нанесения слоев (a), внешний вид напечатанной стенки (b), схема вырезки образцов (c)

Tensile test samples had a dog-bone shape (Fig. 1, c) with a gauge section of 5×1×30 mm³. Tensile testing was performed on an Instron 5582 electromechanical testing machine at a crosshead speed of 1 mm/min.

EXPERIMENT RESULTS

Thermal cycle analysis

Thermal radiation intensity was measured immediately after the deposition of a new layer until the hottest region of the wall cooled down to 200 °C. The measurement results, presented in Fig. 2, a, b, reflect the thermal evolution following layer deposition and do not

represent the maximum heating values occurring during the 3D printing process.

Thermal imaging was conducted across the entire visible surface of the wall. For ease of data interpretation, two reference points were selected for analyzing temperature variations during wall formation. The locations of these points corresponded to the areas of maximum heating – one at the edges of the lower section of the wall (5th layer), where heat dissipation to the substrate and welding table was high, and another in the middle section of the wall (21st layer). Monitoring the temperature at these points allowed for an assessment of the attenuation of cyclic thermal heating within an individual layer as new layers were deposited on top of it.

At the completion of the fifth layer, the maximum recorded temperature reached ~900 °C (Fig. 2, *a*). The cooling rate of this layer reached 85 °C/s (Fig. 2, *b*).

As subsequent layers were deposited, the peak reheating temperature and cooling rate of the fifth layer gradually decreased. The temperature range necessary for polymorphic transformations (above 700 °C) was reached during the deposition of the sixth and seventh layers (Fig. 2, *a*). The cooling rate at these elevated temperatures decreased to 40 – 50 °C/s. Further layer deposition resulted in heating of the fifth layer to temperatures below 700 °C, which could lead to tempering of the material.

When the layer was heated below 700 °C, the cooling rate varied between 10 and 1 °C/s (Fig. 2, *b*).

A similar pattern was observed when analyzing the thermal history of the 21st layer. Heating above 700 °C was achieved during the deposition of the next three layers. Thus, it can be concluded that only the top two to three layers exert a significant thermal effect on the underlying layer, leading to ($\alpha \rightarrow \gamma$) phase transformations.

Metallographic examination

The wall surface exhibits waviness (Fig. 1, *b*), which becomes more pronounced after the deposition of four to six layers. This effect is caused by the spreading behavior of each deposited layer during printing and is characteristic of this manufacturing technology.

Microstructural analysis was performed on a cross-section of the wall (Fig. 1, *c*). At the wall and substrate fusion zone, the fusion boundary and the heat-affected zone (HAZ) are clearly distinguished. A bainitic-martensitic structure formed at the fusion boundary. Moving away from the fusion boundary, the substrate structure within the HAZ transitions from bainitic to ferritic-bainitic, and finally to a ferritic-pearlitic structure in the substrate material.

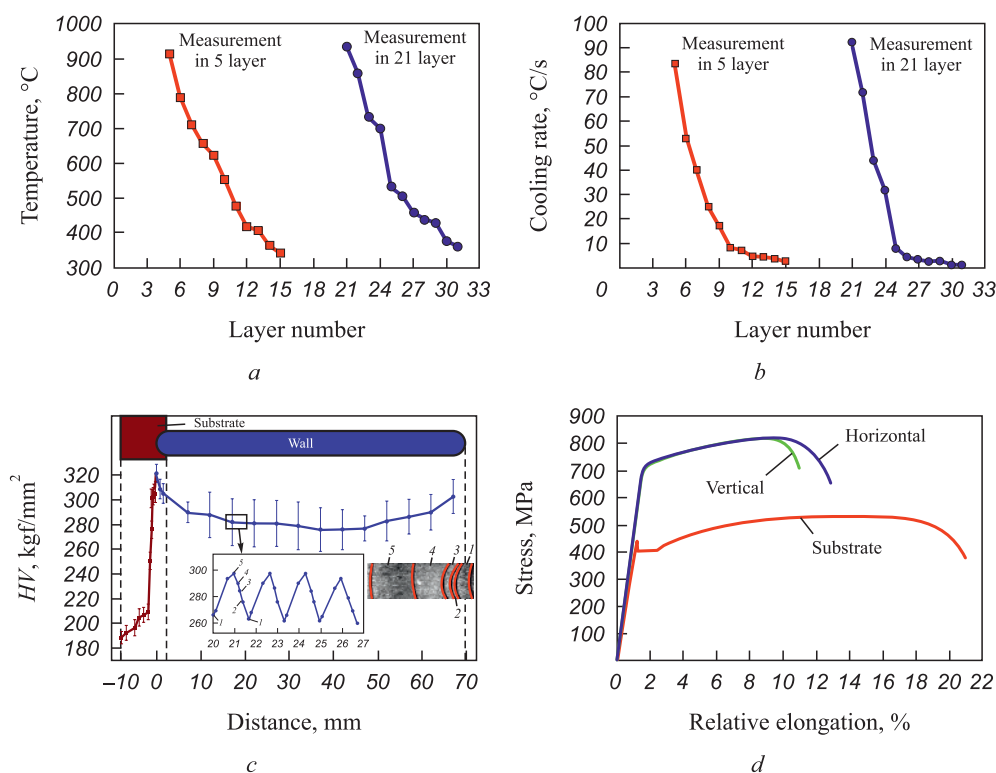


Fig. 2. Changes in temperature (*a*) and cooling rate (*b*) in separate layers during the wall printing, microhardness of the wall cross-section (*c*), graphs of static tension (*d*)

Рис. 2. Изменение температуры (*a*) и скорости охлаждения (*b*) в выбранных слоях в процессе печати стенки, график распределения микротвердости (*c*), диаграммы статического растяжения (*d*)

The wall consists of regions with a non-uniform microstructure (Fig. 3, *a*), which form due to new layer deposition and phase transformations occurring during heating and cooling. Owing to arc oscillation and layer spreading, the height of these regions varies between 1.3 and 2.2 mm. Each region can be divided into five distinct structural zones.

Zone 1 consists of large elongated grains (Fig. 3, *b*), with widths reaching 100 – 150 μm . The grain boundaries correspond to those of the former austenite grains. Within

these large grains, a predominantly acicular ferrite (AF) structure is observed. The average width of acicular ferrite laths was $1.78 \pm 0.2 \mu\text{m}$. In SEM-images, dark interlayers can be observed at grain boundaries, consisting of a matrix with dispersed inclusions ranging in size from 0.18 to 0.70 μm (Fig. 3, *i*).

The microstructure of Zone 2 also contains large grains (Fig. 3, *c*), but they exhibit a quasi-equiaxed shape. In Zone 3, the grain size with distinct boundaries is significantly smaller, ranging from 17 to 40 μm ,

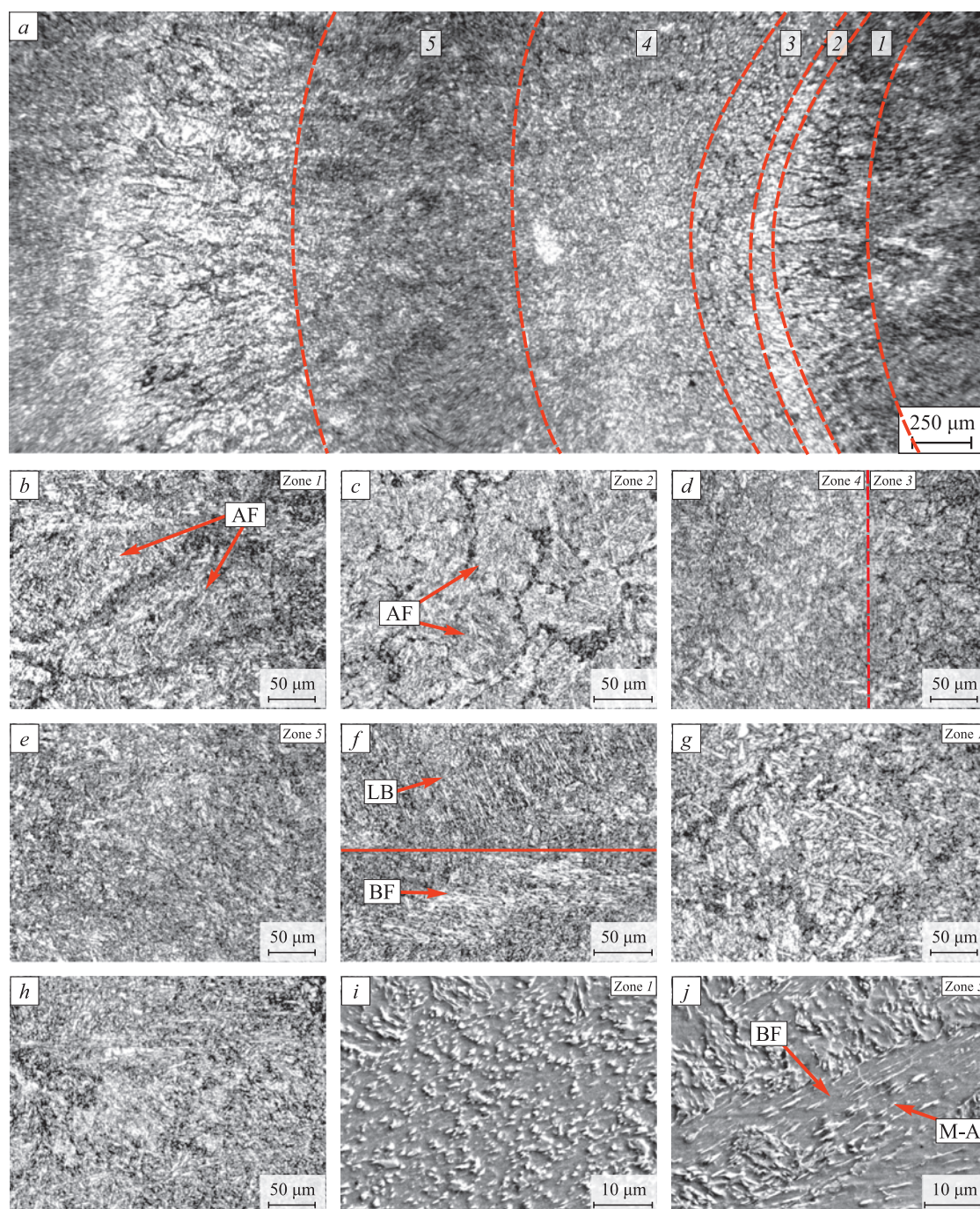


Fig. 3. Optical images of microstructures obtained from the wall cross-section (*a – h*), SEM-images (*i, j*)

Рис. 3. Оптические изображения микроструктур, полученных с поперечного сечения стенки (*a – h*), РЭМ-изображения (*i, j*)

and the interlayers at the grain boundaries become thinner (Fig. 3, *d*) compared to Zones 1 and 2. It appears that the layer boundary is located within Zones 1 and 2.

Zone 4 consists of a fine-grained ferritic-bainitic structure (Fig. 3, *d*). The size of the quasi-polygonal ferrite grains is $4.41 \pm 1.1 \mu\text{m}$. The bainitic structure in this zone is represented by acicular ferrite. The prior austenite grain boundaries are no longer distinguishable in Zone 4.

Zone 5 exhibits the highest refinement of the microstructure and is primarily composed of acicular ferrite (Fig. 3, *e*), with a small proportion of lath bainite (LB) and bainitic ferrite (BF) (Fig. 3, *f*). The average width of acicular ferrite laths in Zone 5 is lower than in Zone 1, measuring $1.69 \pm 0.22 \mu\text{m}$. Within bainitic ferrite grains, elongated interlayers are observed, which may correspond to martensitic-austenitic (M–A) constituents (Fig. 3, *j*). Studies [20; 21] indicate that the martensitic-austenitic constituent is a product of incomplete austenite decomposition during bainitic transformation [20; 21]. The width of the martensitic-austenitic interlayers is $0.25 \pm 0.11 \mu\text{m}$.

As the wall height increases, a slight increase in the width of acicular structure laths is observed, reaching $1.86 \pm 0.3 \mu\text{m}$ in Zone 1 (Fig. 3, *g*) and $1.81 \pm 0.44 \mu\text{m}$ in Zone 5, compared to the lower layers of the wall (Fig. 3, *b*).

In the upper section of the wall (~5 mm from the top), no distinct regions with characteristic zones are observed. The structure is more uniform and consists of acicular ferrite (Fig. 3, *h*).

Microhardness measurements

The orientation scheme of the wall cross-section for microhardness measurements and the microhardness distribution graphs are presented in Fig. 2, *c*. The fusion boundary between the wall and the substrate is taken as the zero reference point on the *x*-axis. The microhardness curve corresponding to the measurements in the wall lies in the positive range of the *x*-axis, while the microhardness values of the substrate, including the weld-fusion area, fall within the –8 to 2 mm range.

Moving away from the flat surface of the substrate (in contact with the welding table), the microhardness initially increases gradually and then rises sharply. This increase is associated with the thermal effect on the substrate during the deposition of the first layers of the wall. Therefore, the region of sharp microhardness increase corresponds to the HAZ. At the wall and substrate fusion zone, microhardness increases to $320 \pm 7 \text{ kgf/mm}^2$ (Fig. 2, *c*). As the number of deposited layers increases, the average microhardness values gradually decrease up to a wall height of ~47 mm (down to ~275 kgf/mm²), and then increase again to 300 kgf/mm² at the top of the wall.

A significant scatter in microhardness values was observed. This variation is attributed to differences in microhardness across regions with non-uniform microstructure (Fig. 3, *a*). A more detailed graph of microhardness variations measured at a distance of 20 mm from the base of the wall is shown in the inset of Fig. 2, *c*. The microhardness values were correlated with corresponding microstructural zones. The highest microhardness values (up to 300 kgf/mm²) were recorded in Zone 5, which corresponds to a region with non-uniform microstructure (Fig. 3, *a*). The lowest microhardness values (down to 260 kgf/mm²) were found in Zone 1, which is characterized by coarse grains. Zones 2 – 4 exhibit intermediate microhardness values. Since such structurally non-uniform regions are repeated throughout the wall, the microhardness distribution curve exhibits periodicity (Fig. 2, *c*, inset).

Static tensile testing

Fig. 2, *d* presents the loading diagrams for samples extracted from the substrate (12Kh1MF steel) and the printed wall. The loading curve of the substrate samples exhibits a yield plateau, whereas no such plateau is observed in the wall samples. The yield strength and ultimate tensile strength of the wall samples are ~40 and ~34 % higher, respectively, compared to the substrate material, while their ductility is reduced by a factor of two (see Table). The strength characteristics of the wall samples also exceed the mechanical properties of the wire specified in GOST 2246–70 (see Table). The ductility of samples extracted in the vertical direction is ~20 % lower compared to those cut in the horizontal direction.

DISCUSSION OF RESULTS

The study of thermal cycling during 3D printing of the model wall allowed for an investigation of the effects of diminishing cyclic heating with successive layer deposition and its influence on the microstructure and mechanical properties of the material.

Forced cooling of the wall before depositing a new layer prevented excessive heat accumulation and ensured a high cooling rate for the deposited and underlying layers (Fig. 2, *b*). As a result, regions with a non-uniform structure are present throughout the entire height of the wall (Fig. 3, *a*). While underlying layers undergo reheating, the lower peak temperatures and accelerated cooling limit diffusion processes and recrystallization.

The zones observed within the wall regions (Fig. 3, *a*) correspond to typical zones formed in welded steels. Zone 1 represents the rapid solidification zone from the molten state, as indicated by the presence of large grains elongated in the crystallization direction (Fig. 3, *b*). Zone 2 corresponds to the coarse-grained heat-affected

Results of static tensile test

Результаты испытаний на статическое растяжение

Sample type	Cutting direction	$\sigma_{0.2}$, MPa	σ_v , MPa	ε , %
Substrate	–	$410 \pm 20^*$	530 ± 30	20 ± 2
OK Autrod 13.14 Wire (GOST 2246–70)	–	600	700	16
Wall	Horizontal	700 ± 30	800 ± 40	12 ± 2
	Vertical	700 ± 30	810 ± 40	9.5 ± 2
* Yield plateau observed				

zone, where the previous layer was reheated above the austenite recrystallization temperature.

The broad interlayers with internal particles at the boundaries of large grains in Zones 1 and 2 indicate that during thermal cycling, heating reached ($\alpha \rightarrow \gamma$) phase transformation temperatures, allowing for partial diffusion-driven redistribution of carbon at grain boundaries. Due to the lack of prolonged holding time and rapid cooling, intermediate/bainitic structures formed at the grain boundaries.

The reduction in grain size in Zone 3 (Fig. 3, *d*) suggests that this region (fine-grained HAZ) experienced heating above the A_{c3} temperature. In Zone 4, prior austenite grain boundaries are no longer visible, and a higher proportion of a bright phase with a quasi-equiaxed shape is observed (Fig. 3, *d*). This suggests that heating in this region occurred within the ($\alpha + \gamma$) phase temperature range [22]. Zone 5 experienced the least thermal exposure, both in terms of heating temperature and duration. As a result, this zone retains a microstructure most similar to that formed during the initial solidification of a deposited layer (Fig. 3, *h*).

Thus, during cooling after layer deposition, Zone 1 with large elongated grains forms in the lower portion of the layer, followed by the formation of an acicular ferrite structure in the remaining volume of the layer due to a decrease in cooling rate. Zones 2 – 5 (Fig. 3, *a*) represent heat-affected regions in the previously deposited layer. With the deposition of additional layers, the underlying layers undergo cyclic thermal exposure at varying temperatures (Fig. 2, *a*).

Cooling the wall to 200 °C before depositing a new layer led to higher microhardness values (up to 305 kgf/mm², Fig. 2, *c*) compared to air cooling (210 kgf/mm²), as previously shown in [19]. The decrease in microhardness along the wall height (Fig. 2, *c*) is attributed to thermal cycling and structural “tempering” effects. At the initial stages of printing, the substrate and welding table acted as additional heat sinks, but their influence diminished as the number of layers increased. The formation of a non-uniform structure in the wall resulted in significant microhardness variation. The higher microhardness

values in the upper section of the wall are associated with the absence of thermal cycling from subsequently deposited layers (Fig. 2, *c*).

Potential approaches to improving structural uniformity include increasing the preheating temperature before depositing a new layer and optimizing cooling rate ranges to allow sufficient time for recrystallization processes to occur.

CONCLUSIONS

The microstructure and mechanical properties of a model wall fabricated using wire arc additive manufacturing in a shielding gas environment under *coldArc* reduced heat input mode were studied.

The use of forced cooling between layer depositions to 200 °C effectively limited heat accumulation in the wall during 3D printing. Due to the high temperature gradient, the cooling rate of the deposited layer reached 85 – 90 °C/s. It was shown that each solidified layer undergoes cyclic thermal exposure during the deposition of the subsequent ten layers. Heating from the deposition of two to three new layers leads to structural-phase transformations in the underlying layer. The next seven to eight layers result in heating comparable to an “tempering” thermal operation.

As a result of rapid cooling after printing, combined with recurrent thermal exposure, regions with non-uniform microstructure formed throughout the entire height of the wall. These regions include: a rapid solidification zone with large elongated grains, a coarse-grained zone, a fine-grained zone, intercritical heat-affected zones.

The microstructure across different areas of the wall consisted primarily of acicular bainite, with a small fraction of lath bainite, bainitic ferrite, and martensitic-austenitic constituents.

A significant scatter in microhardness values was observed along the wall height, ranging from 275 to 320 ± 7 kgf/mm², which is attributed to the non-uniform microstructure. The strength properties of the wall material reached 800 MPa, with relative elongation ranging from 9 to 12 %.

REFERENCES / СПИСОК ЛИТЕРАТУРЫ

- Ding D., Pan Z., Cuiuri D. Wire-feed additive manufacturing of metal components: technologies, developments and future interests. *The International Journal of Advanced Manufacturing Technology*. 2015;81(1–4):465–481. <https://doi.org/10.1007/s00170-015-7077-3>
- Buchanan C., Gardner L. Metal 3D printing in construction: A review of methods, research, applications, opportunities and challenges. *Engineering Structures*. 2019;180:332–348. <https://doi.org/10.1016/j.engstruct.2018.11.045>
- Jafari D., Vaneker T.H.J., Gibson I. Wire and arc additive manufacturing: Opportunities and challenges to control the quality and accuracy of manufactured parts. *Materials & Design*. 2021;202:109471. <https://doi.org/10.1016/j.matdes.2021.109471>
- Chernovol N., Marefat F., Lauwers B., Rymenant P.V. Effect of welding parameters on microstructure and mechanical properties of mild steel components produced by WAAM. *Welding in the World*. 2023;67(4):1021–1036. <https://doi.org/10.1007/s40194-022-01422-1>
- Munusamy S., Jerald J. Effect of in-situ intrinsic heat treatment in metal additive manufacturing: A comprehensive review. *Metals and Materials International*. 2023;29:3423–3441. <https://doi.org/10.1007/s12540-023-01462-2>
- Rodrigues T.A., Duarte V., Avila J.A., Santos T.G., Miranda R.M., Oliveira J.P. Wire and arc additive manufacturing of HSLA steel: Effect of thermal cycles on microstructure and mechanical properties. *Additive Manufacturing*. 2019;27:440–450. <https://doi.org/10.1016/j.addma.2019.03.029>
- Pobol I.L., Bakinovskii A.A., Stepankova M.K., Burin A.N., Gubko A.D. Influence of heat cycling conditions in the additive manufacturing of stainless steel and Al–Si alloy raw parts on their microstructure. *Foundry Production and Metallurgy*. 2018;(4):133–138. (In Russ.). <https://doi.org/10.21122/1683-6065-2018-4-133-138>
Поболь И.Л., Бакиновский А.А., Степанкова М.К., Бурин А.Н., Губко А.Д. Влияние условий термоциклирования в процессе аддитивного производства заготовок из нержавеющей стали и силумина на их микроструктуру. *Литье и металлургия*. 2018;(4):133–138. <https://doi.org/10.21122/1683-6065-2018-4-133-138>
- Zhang T., Li H., Gong H., Wu Y., Chen X., Zhang X. Study on location-related thermal cycles and microstructure variation of additively manufactured inconel 718. *Journal of Materials Research and Technology*. 2022;18:3056–3072. <https://doi.org/10.1016/j.jmrt.2022.03.178>
- Vlasov I.V., Gordienko A.I., Kuznetsova A.E., Semenchuk V.M. Structure and mechanical properties anisotropy of a steel product manufactured by layer-by-layer electric arc wire 3D printing. *Izvestiya. Ferrous Metallurgy*. 2023;66(6):709–717. <https://doi.org/10.17073/0368-0797-2023-6-709-717>
Власов И.В., Гордиенко А.И., Кузнецова А.Е., Семенчук В.М. Исследование структуры и анизотропии механических свойств стального изделия, полученного методом послойной электродуговой проволоочной 3D-печати. *Известия вузов. Черная Металлургия*. 2023;66(6):709–717. <https://doi.org/10.17073/0368-0797-2023-6-709-717>
- Cunningham C.R., Flynn J.M., Shokrani A., Dhokia V., Newman S.T. Invited review article: Strategies and processes for high quality wire arc additive manufacturing. *Additive Manufacturing*. 2018;22:672–686. <https://doi.org/10.1016/j.addma.2018.06.020>
- Le V.T., Bui M.C., Nguyen T.D., Nguyen V.A., Nguyen V.C. On the connection of the heat input to the forming quality in wire-and-arc additive manufacturing of stainless steels. *Vacuum*. 2023;209:111807. <https://doi.org/10.1016/j.vacuum.2023.111807>
- Nagasai B.P., Malarvizhi S., Balasubramanian V. Mechanical properties and microstructural characteristics of wire arc additive manufactured 308 L stainless steel cylindrical components made by gas metal arc and cold metal transfer arc welding processes. *Journal of Materials Processing Technology*. 2022;307:117655. <https://doi.org/10.1016/j.jmatprotec.2022.117655>
- Wang T., Zhang Y., Wu Z., Shi C. Microstructure and properties of die steel fabricated by WAAM using H13 wire. *Vacuum*. 2018;149:185–189. <https://doi.org/10.1016/j.vacuum.2017.12.034>
- Montevecchi F., Venturini G., Grossi N., Scippa A., Campatelli G. Idle time selection for wire-arc additive manufacturing: A finite element-based technique. *Additive Manufacturing*. 2018;21:479–486. <https://doi.org/10.1016/j.addma.2018.01.007>
- Wu B., Pan Z., Ding D., Cuiuri D., Li H., Fei Z. The effects of forced interpass cooling on the material properties of wire arc additively manufactured Ti6Al4V alloy. *Journal of Materials Processing Technology*. 2018;258:97–105. <https://doi.org/10.1016/j.jmatprotec.2018.03.024>
- Li F., Chen S., Shi J., Zhao Y., Tian H. Thermoelectric cooling-aided bead geometry regulation in wire and arc-based additive manufacturing of thin-walled structures. *Applied Sciences*. 2018;8(2):207. <https://doi.org/10.3390/app8020207>
- Jakubowska M., Wrobel A., Manaj W., Sypien A. Degradation of microstructure and strength properties of heat-resistant steels operating under variable loads. *International Journal of Pressure Vessels and Piping*. 2023;202:104916. <https://doi.org/10.1016/j.ijpvp.2023.104916>
- Zhang J., Chen H., Fan D., Huang J., Yu X., Feng W., Xu K. Effects of phosphorus impurity on the microstructure and impact toughness of weld joint for the 12Cr2Mo1R heat resistant steel. *Journal of Manufacturing Processes*. 2019;38:453–461. <https://doi.org/10.1016/j.jmapro.2019.01.026>
- Vlasov I.V., Gordienko A.I., Eremin A.V., Semenchuk V.M., Kuznetsova A.E. Structure and mechanical behavior of heat-resistant steel manufactured by multilayer arc deposition. *Metals*. 2023;13(8):1375. <https://doi.org/10.3390/met13081375>
- Sridharan N., Noakes M.W., Nycz A., Love L.J., Dehoff R.R., Babu S.S. On the toughness scatter in low alloy C–Mn steel samples fabricated using wire arc additive manufacturing. *Materials Science and Engineering: A*. 2018;713:18–27. <https://doi.org/10.1016/j.msea.2017.11.101>
- Shi Y., Han Z. Effect of weld thermal cycle on microstructure and fracture toughness of simulated heat-affected zone for a 800 MPa grade high strength low alloy steel. *Journal of Materials Processing Technology*. 2008;207(1–3):30–39. <https://doi.org/10.1016/j.jmatprotec.2007.12.049>

22. Poletskov P.P., Denisov S.V., Nikitenko O.A., Chukin D.M., Gushchina M.S. Decay of supercooled austenite of low-carbon pipe steel with the use of Gleeble 3500 complex. *Izvestiya. Ferrous Metallurgy*. 2019;62(3):235–240. (In Russ.).
<https://doi.org/10.17073/0368-0797-2019-3-235-240>

Полецков П.П., Денисов С.В., Никитенко О.А., Чукин Д.М., Гущина М.С. Исследование распада переохлажденного аустенита низкоуглеродистой трубной стали с использованием комплекса Gleeble 3500. *Известия вузов. Черная металлургия*. 2019;62(3):235–240.
<https://doi.org/10.17073/0368-0797-2019-3-235-240>

Information about the Authors

Сведения об авторах

Il'ya V. Vlasov, Cand. Sci. (Eng.), Research Associate of the Laboratory of Physical Mesomechanics and Non-Destructive Testing, Institute of Strength Physics and Materials Science, Siberian Branch Russian Academy of Sciences

ORCID: 0000-0001-9110-8313

E-mail: viv@ispms.ru

Antonina I. Gordienko, Cand. Sci. (Eng.), Research Associate of the Laboratory of Physical Mesomechanics and Non-Destructive Testing, Institute of Strength Physics and Materials Science, Siberian Branch Russian Academy of Sciences

ORCID: 0000-0002-4361-8906

E-mail: mirantil@ispms.ru

Vyacheslav M. Semenchuk, Junior Researcher of the Laboratory of Local Metallurgy in Additive Manufacturing Technologies, Institute of Strength Physics and Materials Science, Siberian Branch Russian Academy of Sciences

ORCID: 0000-0002-7215-0505

E-mail: svm_70@ispms.ru

Илья Викторович Власов, к.т.н., научный сотрудник лаборатории физической мезомеханики и неразрушающих методов контроля, Институт физики прочности и материаловедения Сибирского отделения РАН

ORCID: 0000-0001-9110-8313

E-mail: viv@ispms.ru

Антонина Ильдаровна Гордиенко, к.т.н., научный сотрудник лаборатории физической мезомеханики и неразрушающих методов контроля, Институт физики прочности и материаловедения Сибирского отделения РАН

ORCID: 0000-0002-4361-8906

E-mail: mirantil@ispms.ru

Вячеслав Максимович Семенчук, младший научный сотрудник лаборатории локальной металлургии в аддитивных технологиях, Институт физики прочности и материаловедения Сибирского отделения РАН

ORCID: 0000-0002-7215-0505

E-mail: svm_70@ispms.ru

Contribution of the Authors

Вклад авторов

I. V. Vlasov – formation of the main concept, goals and objectives; writing the text, literary review, conducting mechanical tests, data analysis.

A. I. Gordienko – performing microstructural studies, results processing, data analysis, revising the text.

V. M. Semenchuk – selection of additive manufacturing modes, preparation of the samples, results discussion.

И. В. Власов – формирование основной концепции, цели и задач исследования; написание текста статьи, литературный обзор публикаций по теме, проведение механических испытаний, анализ экспериментальных данных.

А. И. Гордиенко – проведение микроструктурных исследований, обработка результатов и анализ данных, доработка текста.

В. М. Семенчук – подбор режимов проведения аддитивного формирования, подготовка образцов для исследований, обсуждение полученных результатов.

Received 15.05.2024

Revised 05.06.2024

Accepted 12.11.2024

Поступила в редакцию 15.05.2024

После доработки 05.06.2024

Принята к публикации 12.11.2024



UDC 669.245: 621.74.045

DOI 10.17073/0368-0797-2025-1-60-68



Original article

Оригинальная статья

INFLUENCE OF HEAT TREATMENT ON STRUCTURE, PHASE COMPOSITION, HARDNESS AND ELECTRICAL CONDUCTIVITY OF VZhL14N-VI NICKEL SUPERALLOY

A. V. Koltygin¹, V. E. Bazhenov¹, A. A. Belova¹, A. V. Sannikov¹,
A. A. Lyskovich¹, V. D. Belov¹, E. Yu. Shchedrin²

¹ National University of Science and Technology “MISIS” (4 Leninskii Ave., Moscow 119049, Russian Federation)

² PJSC ODK-Kuznetsov (29 Zavodskoe Route, Samara 443009, Russian Federation)

✉ misistlp@mail.ru

Abstract. The phase composition of VZhL14N-VI nickel superalloy was analyzed in a wide temperature range – from room temperature to 1600 °C by means of CALPHAD (CALculation of PHase Diagrams) calculations. In light of the findings, the authors devised potential heat treatment modes for VZhL14N-VI superalloy. The impact of different heat treatment modes on the grain size, hardness, and electrical conductivity of VZhL14N-VI superalloy samples produced by ceramic mold casting was investigated, as well as the effect on the alloy of high-temperature annealing at 1070 – 1170 °C for 1 – 4 h. The alloy heat treatment resulted in a notable increase in grain size and a decrease in hardness. The influence of artificial aging temperature after high-temperature annealing and quenching on the hardness and electrical conductivity of the alloy in the range of 610 – 810 °C was studied. At 810 °C, the alloy exhibits the most pronounced aging effect, accompanied by a rapid increase in hardness, reaching approximately 370 HV. In contrast to the observed changes in hardness, the electrical conductivity of the alloy exhibited minimal variation during the aging process. The proposed heat treatment conditions diverge from those recommended by the OST 1 90126–85 Russian standard for this alloy. The developed heat treatment mode includes the alloy heat treatment at a temperature of 1170 ± 10 °C for 4 h, followed by air cooling and aging at a temperature of 810 ± 10 °C for 10 – 14 h, followed by air cooling. The proposed heat treatment mode is expected to result in an increase in hardness of VZhL14N-VI superalloy castings by 10 – 20 HV in comparison to the samples subjected to the standard heat treatment mode.

Keywords: VZhL14N-VI nickel superalloy, investment casting, heat treatment, castings

Acknowledgements: The work was supported by the Ministry of Science and Higher Education of the Russian Federation within the framework of the Government Resolution No. 218, Agreement No. 075-11-2022-023 dated 06.04.2022 “Creation of a technology for the production of unique large-sized castings from heat-resistant alloys for gas turbine engines, focused on the use of domestic equipment and organization of a modern resource-efficient, computer-oriented foundry production”.

For citation: Koltygin A.V., Bazhenov V.E., Belova A.A., Sannikov A.V., Lyskovich A.A., Belov V.D., Shchedrin E.Yu. Influence of heat treatment on structure, phase composition, hardness and electrical conductivity of VZhL14N-VI nickel superalloy. *Izvestiya. Ferrous Metallurgy*. 2025;68(1):60–68. <https://doi.org/10.17073/0368-0797-2025-1-60-68>

ВЛИЯНИЕ ТЕРМИЧЕСКОЙ ОБРАБОТКИ НА ФАЗОВЫЙ СОСТАВ, СТРУКТУРУ, ТВЕРДОСТЬ И ЭЛЕКТРОПРОВОДНОСТЬ НИКЕЛЕВОГО ЖАРОПРОЧНОГО СПЛАВА ВЖЛ14Н-ВИ

А. В. Колтыгин¹, В. Е. Баженов¹, А. А. Белова¹, А. В. Санников¹,

А. А. Лыскович¹, В. Д. Белов¹, Е. Ю. Щедрин²

¹ Национальный исследовательский технологический университет «МИСИС» (Россия, 119049, Москва, Ленинский пр., 4)

² ПАО «ОДК-Кузнецов» (443009, Россия, Самара, Заводское шоссе, 29)

✉ misistlp@mail.ru

Аннотация. В работе проанализирован фазовый состав никелевого жаропрочного сплава ВЖЛ14Н-ВИ в широком температурном диапазоне – от комнатной температуры до 1600 °С с помощью расчетов по программе Thermo-Calc. На основании полученных данных авторы разработали возможные режимы термообработки жаропрочного сплава ВЖЛ14Н-ВИ. Исследовано влияние различных режимов термообработки на размер зерна, твердость и электропроводность образцов жаропрочного сплава ВЖЛ14Н-ВИ, полученных методом литья в керамические формы, а также влияние на сплав высокотемпературного отжига при температуре 1070 – 1170 °С в течение 1 – 4 ч. Термическая обработка сплава привела к заметному увеличению размера зерен и снижению твердости. Было изучено влияние температуры искусственного старения после высокотемпературного отжига и закалки на твердость и электропроводность сплава в диапазоне температур 610 – 810 °С. При температуре 810 °С сплав проявляет наиболее выраженный эффект старения, сопровождающийся быстрым повышением твердости, достигающим приблизительно 370 HV. В отличие от твердости, электропроводность сплава в процессе старения изменялась незначительно. Предлагаемый режим термической обработки отличается от рекомендованного стандартом ОСТ 1 90126–85 для этого сплава. Он включает отжиг при температуре 1170 ± 10 °С в течение 4 ч с последующим охлаждением на воздухе и старением при температуре 810 ± 10 °С в течение 10 – 14 ч с последующим охлаждением на воздухе. Предложенная термообработка позволяет повысить твердость отливок из сплава ВЖЛ14Н-ВИ на 10 – 20 HV по сравнению с образцами, подвергнутыми термообработке по стандартному режиму.

Ключевые слова: никелевый жаропрочный сплав ВЖЛ14Н-ВИ, литье по выплавляемым моделям, термическая обработка, отливки

Благодарности: Работа выполнена при финансовой поддержке Министерства науки и высшего образования Российской Федерации в рамках Постановления Правительства № 218 по соглашению о предоставлении субсидии № 075-11-2022-023 от 06.04.2022 г. «Создание технологии изготовления уникальных крупногабаритных отливок из жаропрочных сплавов для газотурбинных двигателей, ориентированной на использование отечественного оборудования и организацию современного ресурсоэффективного, компьютероориентированного литейного производства».

Для цитирования: Колтыгин А.В., Баженов В.Е., Белова А.А., Санников А.В., Лыскович А.А., Белов В.Д., Щедрин Е.Ю. Влияние термической обработки на фазовый состав, структуру, твердость и электропроводность никелевого жаропрочного сплава ВЖЛ14Н-ВИ. *Известия вузов. Черная металлургия*. 2025;68(1):60–68. <https://doi.org/10.17073/0368-0797-2025-1-60-68>

INTRODUCTION

Currently, a wide range of nickel-based heat-resistant cast superalloys have been developed and successfully applied for the production of heat-resistant structural components in aircraft engines [1; 2]. In Russian aircraft engineering, VZhL14N-VI alloy (OST 1 90126–85; base – Ni; up to 0.08 % C¹; up to 20.0 % Cr; up to 5.0 % Mo; up to 1.5 % Al; up to 2.9 % Ti; up to 2.8 % Nb; up to 10 % Fe) is widely used for large-scale structural castings, particularly in combustion chamber components. This alloy primarily contains chromium and iron as major alloying elements and has no direct foreign equivalents. The closest in composition are Inconel 718 (ASTM Ni B670) and Inconel 718Plus (UNS N07818) alloys. These belong to the second generation of superalloys, characterized by a high chromium content, often with cobalt, as well as refractory elements such as tungsten,

molybdenum, and niobium. A key feature of these alloys is their substantial γ' phase content (a face-centered cubic ordered Ni₃(Al, Ti) phase) [1; 3; 4]. The primary requirement for combustion chamber structural components, which operate at moderate temperatures of 500 – 900 °C and pressures up to 45 atm, is high strength combined with good ductility across the entire temperature range [5]. This is achieved through the complex alloying of the Fe–Ni alloy with solid-solution strengthening and carbide-forming elements. Chromium is a component of the Ni-based solid solution, contributing to its strengthening, while also being involved in carbide formation. This significantly enhances the oxidation resistance of the Ni–Fe alloy at operating temperatures [4 – 6]. Aluminum and titanium promote the formation of the γ' phase and strengthen the alloy during heat treatment. Molybdenum, tungsten, and niobium are added as carbide-forming elements responsible for the formation of fine-dispersed carbides, which enhance the alloy's high-temperature strength. They also strengthen the solid solution, while niobium, in addition, participates in the formation of strengthening

¹ Here and throughout the text, unless otherwise stated, element contents are given in wt. %.

precipitates in the nickel-based solid solution slightly reducing the processability of the alloy by impairing the weldability and machinability of castings [7; 8]. The addition of iron reduces the overall cost of the alloy due to the lower cost of iron compared to nickel, replacing part of the nickel content. At a moderate iron content, as in VZhL14N-VI alloy, its long-term strength at the operating temperatures of combustion chamber components remains at an acceptable level.

The operational properties of VZhL14N-VI alloy castings are strongly influenced by the quantity of alloying elements, the carbide and strengthening phases they form, and their distribution within the alloy structure. While the impact of individual alloying elements and structural components on the operational properties of VZhL14N-VI alloy has been well studied [1 – 5], the effect of structure and phase composition formation conditions on the mechanical properties of castings remains insufficiently explored. This often results in deviations of the alloy's properties from expected values [9; 10]. It is crucial to consider both the formation of the as-cast structure and the structure obtained after heat treatment [1; 10; 11]. The operational properties of cast components are determined by the combination of grain size and metal structure. The hardening of VZhL14N-VI-type alloys is primarily governed by the formation of γ' strengthening precipitates within the γ matrix phase. These precipitates exhibit greater thermal stability compared to γ'' (a body-centered tetragonal ordered Ni_3Nb phase), which forms in other heat-resistant nickel alloys. Additionally, the hardening of the alloy is influenced by the precipitation of δ (orthorhombic Ni_3Nb), η (hexagonal Ni_3Ti), and σ (hexagonal CrFeMoNi , CrMoNi , $(\text{Cr}, \text{Mo})_3\text{Ni}$) phases, along with carbide phases such as MeC , Me_{23}C_6 , and Me_6C (Me_7C_3 is rarely observed). These phases have a face-centered cubic lattice and limit grain growth in the alloy [11 – 14]. By adjusting the heat treatment modes to control the formation of these phases, the mechanical properties of cast components can be modified within a relatively broad range.

This study examines the effect of heat treatment modes on the macro- and microstructure, phase composition, and hardness of VZhL14N-VI alloy samples produced by ceramic mold casting to determine their influence on alloy hardening.

MATERIALS AND METHODS

The test samples were cut from cast plates measuring $100 \times 100 \times 10$ mm. The castings were produced using ceramic mold casting technology. Fused quartz of various fractions, manufactured by DINUR (Pervouralsk, Russia), was used as the filler for the slurry and stucco coating. To prepare the refractory slurry, Ultracast One+ and Ultracast Prime binders (Technopark LLC, Moscow,

Russia) were used. Pre-alloyed VZhL14N-VI, produced by VIAM (Moscow, Russia), was used as the charge material. The melting and pouring of the alloy were performed in a vacuum induction melting and casting unit (VAKETO, Moscow, Russia) using a mullite-corundum-zirconium crucible manufactured by ELEMET (Elektrogorsk, Russia). From the obtained castings, samples measuring $4 \times 9 \times 56$ mm were cut. The alloy samples were subjected to heat treatment in a muffle furnace in air at temperatures of 1070, 1120, and 1170 °C. The duration of high-temperature treatment ranged from 1 to 4 h, with 1 h increments. The samples were quenched by air blow cooling. For aging, samples quenched after 4 h of high-temperature soaking were used. The aging process was studied under three heat treatment modes, involving soaking at 610, 700, and 810 ± 10 °C for 2 to 14 h.

The microstructure of the alloy was examined using a TESCAN VEGA 3 SBH scanning electron microscope (SEM) equipped with an Oxford energy-dispersive microanalysis system and a Carl Zeiss Axio Observer D1m optical microscope. To reveal the grain structure, metallographic samples were etched using Marble's reagent (20 g Cu_2SO_4 , 100 mL hydrochloric acid, 100 mL ethanol) [15]. To examine the microstructure, an acid mixture (30 mL nitric acid, 0.5 mL hydrochloric acid, 70 mL acetic acid) was also used for etching [16]. The phases present in the microstructure were identified using energy-dispersive X-ray spectroscopy (EDS), based on literature data concerning possible compounds in heat-resistant nickel-based alloys [14; 17] and phase composition calculations.

The electrical conductivity of the alloys was measured using a non-contact eddy current conductometer VE-27NC3 (SIGMA, Russia), with a measurement range of 0.5–2.5 MS/m.

Vickers hardness (HV 10) was determined using a NEMESIS 9001 universal hardness tester (INNOVA-TEST) under a 10 kgf load, with a loading time of 12 s.

The equilibrium phase composition of VZhL14N-VI alloy in the temperature range of 20 to 1600 °C was calculated using the Thermo-Calc software with the TCS Ni-based Superalloys Database (TCNI8).

RESULTS AND DISCUSSION

To achieve a more precise phase identification, the phase composition of the VZhL14N-VI alloy was calculated in the temperature range of 20 to 1600 °C using Thermo-Calc software. The results of the equilibrium phase composition calculation, based on the average composition of VZhL14N-VI alloy in accordance with OST 1 90126–85, are presented in Fig. 1.

It can be observed that from the equilibrium solidus temperature (approximately 1280 °C) down to 1050 °C, the alloy is almost single-phase, consisting primarily

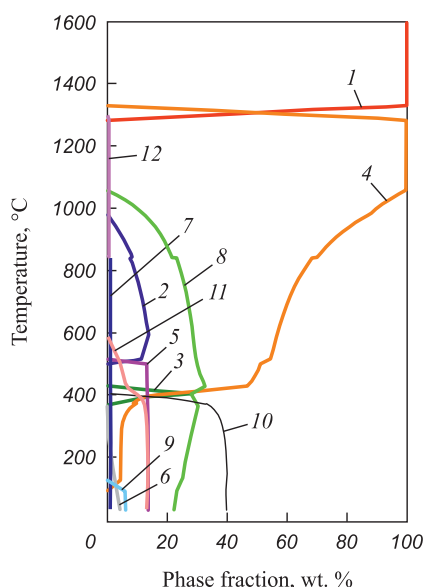


Fig. 1. Calculated phase composition of VZhL14N-VI superalloy (average composition) at temperatures from 20 to 1600 °C:

1 – L; 2 – $\sigma(\text{Cr,Mo})_3\text{Ni}$; 3 – Ni_3Fe ; 4 – γ ; 5 – $\text{P}(\text{NiCrMo})$; 6 – Ni_3Nb ; 7 – Cr_{23}C_6 ; 8 – γ' ; 9 – Ni_3Cr ; 10 – Ni_3Fe ; 11 – (Cr); 12 – (Nb,Ti)C

Рис. 1. Расчетный фазовый состав сплава ВЖЛ14Н-ВИ (средний состав) при температурах от 20 до 1600 °C:

1 – L; 2 – $\sigma(\text{Cr,Mo})_3\text{Ni}$; 3 – Ni_3Fe ; 4 – γ ; 5 – $\text{P}(\text{NiCrMo})$; 6 – Ni_3Nb ; 7 – Cr_{23}C_6 ; 8 – γ' ; 9 – Ni_3Cr ; 10 – Ni_3Fe ; 11 – (Cr); 12 – (Nb,Ti)C

of the γ phase. Below 1050 °C, the main strengthening phase for this alloy, γ' , begins to precipitate [18]. At approximately 980 °C, the σ phase starts to form, which is commonly observed in heat-resistant nickel-based alloys containing iron and typically appears as irregularly shaped globules. With a further decrease in temperature, the volume fractions of γ' and σ phases gradually increase. At approximately 850 °C, carbide inclusions of Me_{23}C_6 start to appear in the structure, where Me is primarily chromium, along with iron and molybdenum.

At 600 °C, the equilibrium content of γ' and σ phases reaches its maximum. When the temperature drops below 600 °C, unwanted particles with a chromium-based solid solution lattice begin to appear in the equilibrium structure. Below 500 °C, the σ phase completely disappears, and other undesirable phases emerge in the structure. Additionally, the equilibrium volume fractions of γ and γ' phases decrease significantly below 400 °C. Thus, within the operating temperature range of combustion chamber cast components in aircraft gas turbine engines made from VZhL14N-VI alloy (750 – 950 °C) [19], the equilibrium phase composition consists of the γ phase, with dispersed γ' and σ phase particles, where the γ' phase predominates. Additionally, a small number of carbide particles are present in the structure, primarily Me_{23}C_6 carbides, with occasional occurrences of MeC carbides.

The as-cast structure of VZhL14N-VI alloy, produced by ceramic mold casting, is shown in Fig. 2, a. The microstructure consists of a nickel-based solid solution matrix (γ phase) with finely dispersed carbide precipitates containing niobium, titanium, and a significant amount of molybdenum, in addition to carbon (Fig. 2, b). According to the calculated phase composition of the alloy (Fig. 1), these carbides begin to precipitate directly from the liquid phase. During heat treatment at temperatures below 850 °C, they are expected to transform into Me_{23}C_6 -type carbides.

Fig. 3 presents the microstructure of VZhL14N-VI alloy after heat treatment following the mode specified in OST 1 90126–85 for this alloy. The treatment includes annealing at 1120 ± 10 °C for 3 h, followed by air cooling, and aging at 700 ± 10 °C for 16 h, with subsequent air cooling.

As seen in Fig. 3, a, heat treatment led to a reduction in dendritic segregation of elements, although complete chemical homogenization was not achieved. Despite ther-

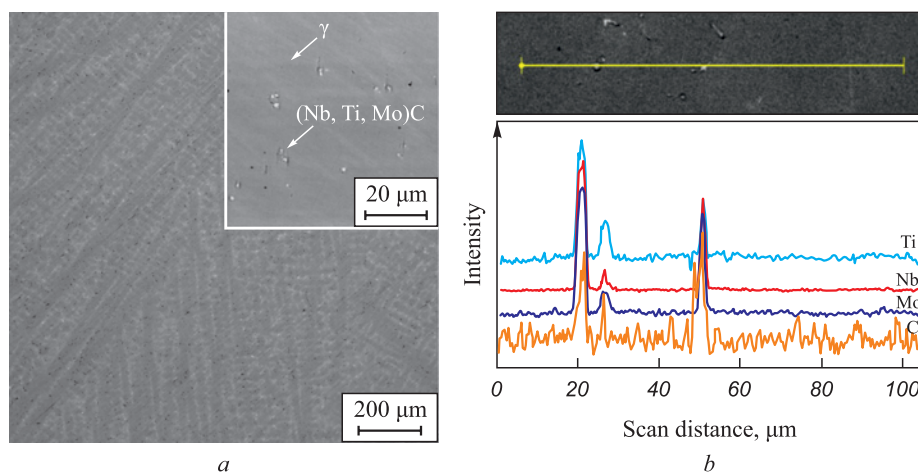


Fig. 2. Microstructure of VZhL14N-VI superalloy obtained by ceramic mold casting (a) and element distribution profile based on EDS results (b)

Рис. 2. Микроструктура сплава ВЖЛ14Н-ВИ, полученного литьем в оболочковую керамическую форму (a), и профиль распределения элементов по результатам микрорентгеноспектрального анализа (b)

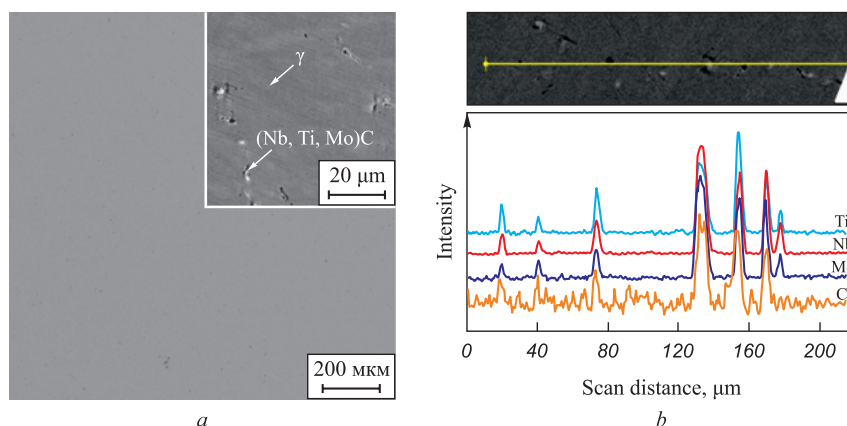


Fig. 3. Microstructure of VZhL14N-VI superalloy after heat treatment including annealing at 1120 ± 10 °C for 3 h followed by air cooling and aging at 700 ± 10 °C for 16 h followed by air cooling (a) and element distribution profile based on EDS results (b)

Рис. 3. Микроструктура сплава ВЖЛ14Н-ВИ после термической обработки по режиму, включающему отжиг при температуре 1120 ± 10 °C в течение 3 ч с последующим охлаждением на воздухе и старением при температуре 700 ± 10 °C в течение 16 ч с последующим охлаждением на воздухе (a), и профиль распределения элементов по результатам микрорентгеноспектрального анализа (b)

modynamic calculations predicting that niobium and titanium carbides should dissolve during high-temperature annealing and be replaced by ultrafine chromium-based $Me_{23}C_6$ carbide precipitates during aging, niobium and titanium carbides were still observed in the alloy structure after heat treatment. Additionally, some carbide particles exhibited increased nitrogen content, which most likely inhibits their dissolution.

It is well known that, according to the Hall–Petch effect, the grain size of polycrystalline nickel-based alloy castings significantly affects their mechanical properties [20]. The influence of various high-temperature heat treatment modes on grain size was studied. Fig. 4, a shows the grain structure of samples solidified under identical cooling conditions in the as-cast state and after heat treat-

ment. Grain coarsening occurs during annealing. Fig. 4, b illustrates the effect of high-temperature heat treatment duration on the grain density on the polished sample surface. During 4 h of annealing, the number of grains per 1 cm^2 in the metallographic section decreased by approximately 2.6 times, regardless of the annealing temperature. Thus, high-temperature annealing significantly increases the grain size of the alloy, which is a negative factor that reduces the mechanical properties of cast components. Therefore, excessive annealing time is undesirable. Changing the annealing temperature within the studied range ($1070 - 1170$ °C) had virtually no effect on the grain size of the alloy (Fig. 4, b).

Fig. 5 presents the effect of heat treatment on the hardness and electrical conductivity of VZhL14N-VI

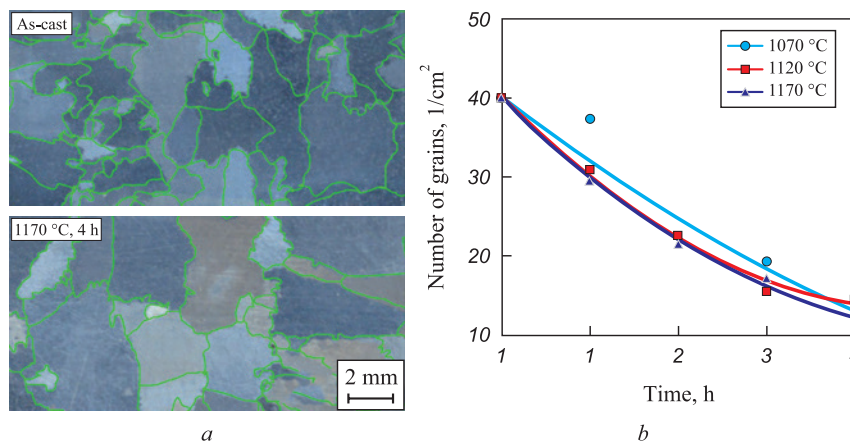


Fig. 4. Grain structure of VZhL14N-VI superalloy in as-cast condition and after high-temperature heat-treatment at 1170 °C for 4 h with following air cooling (a) and dependence of the number of grains per 1 cm^2 in the metallographic section on temperature and time of annealing (b)

Рис. 4. Макроструктура сплава ВЖЛ14Н-ВИ в литом состоянии и после высокотемпературного отжига при 1170 °C в течение 4 ч с последующим охлаждением на воздухе (a) и зависимость количества зерен на 1 cm^2 поверхности шлифа от температуры и времени отжига (b)

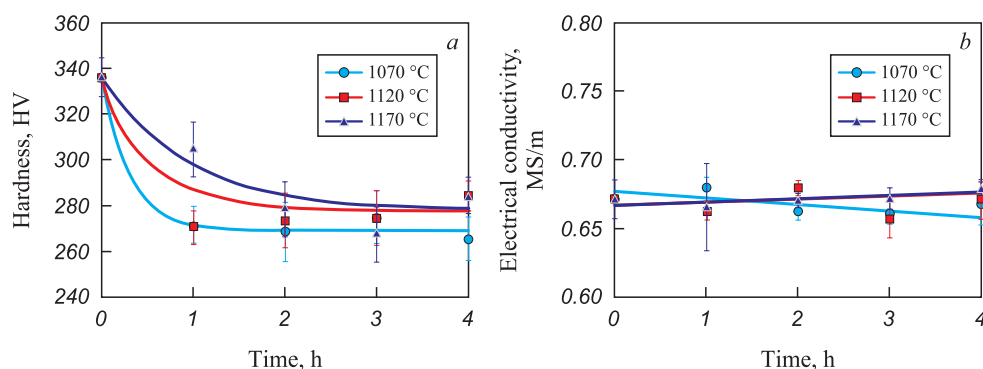


Fig. 5. Influence of temperature and time of holding during high-temperature annealing on hardness (a) and electrical conductivity (b) of VZhL14N-VI superalloy

Рис. 5. Влияние температуры и времени выдержки в процессе высокотемпературного отжига на твердость (a) и электропроводность (b) сплава ВЖЛ14Н-ВИ

alloy samples. The temperature of high-temperature annealing within the examined range had a negligible effect on hardness (Fig. 5, a) after quenching. During high-temperature annealing, the hardness of the alloy rapidly decreased from 336 to ~280 HV for all temperatures used. The influence of high-temperature annealing on the electrical conductivity of the alloy was even smaller (Fig. 5, b). It can be assumed that the electrical conductivity of the alloy remains unchanged during annealing. However, it should be noted that the electrical conductivity measurement method used in this study is relatively crude. Given the small variations in measured electrical conductivity values observed for VZhL14N-VI alloy, the measurement error is relatively high. It is possible that more precise measurement techniques could detect changes in electrical conductivity.

The temperature and duration of artificial aging had a much stronger effect on alloy hardness than the annealing temperature prior to quenching (Fig. 6). The most significant increase in hardness was observed at the maximum aging temperature of 810 °C. At this temperature, the hardness of the alloy reached its near-maximum value of approximately 370 HV within just 2 h of aging. Lower aging temperatures did not result in such significant hardening. The lowest hardness values were observed at 610 °C, where the hardness of the alloy continued to increase throughout the aging process, indicating incomplete decomposition of the supersaturated solid solution. It is evident that this temperature is insufficient for achieving maximum strength through artificial aging. An intermediate hardness level was obtained after aging at 700 °C. The maximum hardening effect, achieved at 810 °C, was practically independent of the annealing temperature before quenching (Fig. 6, d), showing consistent results.

The degree of supersaturated γ -phase decomposition can be indirectly assessed based on changes in electrical conductivity [19]. For the VZhL14N-VI alloy, a weak dependence of electrical conductivity on aging tempera-

ture and duration was observed (Fig. 7). However, while the electrical conductivity of samples aged at 610 and 700 °C was nearly identical, at 810 °C, a significant difference exceeding the measurement uncertainty interval was detected. The electrical conductivity of samples aged at 810 °C was higher than that of samples aged at 610 and 700 °C. This suggests that at 810 °C, γ phase decomposition occurs at a higher rate. At the same time, the electrical conductivity of alloys subjected to high-temperature annealing for solid solution treatment at different temperatures varies insignificantly during aging (Fig. 7, d).

Thus, the highest hardening effect was achieved in VZhL14N-VI alloy samples that were annealed at 1170 °C for 4 h and then artificially aged at 810 °C for 10 – 14 h. The proposed heat treatment mode differs slightly from the current standard specified in OST 1 90126–85 and results in a small hardness increase of 10 – 20 HV in VZhL14N-VI alloy. This mode may be of interest for heat treatment of cast components operating at temperatures above 800 °C.

CONCLUSIONS

The as-cast grain structure of VZhL14N-VI alloy primarily consists of a γ phase solid solution with (Nb, Ti, Mo)C carbide inclusions.

During heat treatment, which includes high-temperature solution annealing followed by artificial aging, a noticeable reduction in coring of alloying elements within the γ phase solid solution is observed. However, the morphology of niobium and molybdenum carbides, identified through X-ray microanalysis, remains unchanged.

Thermodynamic calculations have shown that aging at temperatures below 600 °C may lead to the formation of undesirable phases in the alloy structure, while aging above 850 °C results in a reduction in the volume fraction of hardening γ' and σ particles and inhibits the precipitation of $Me_{23}C_6$ -type carbides.

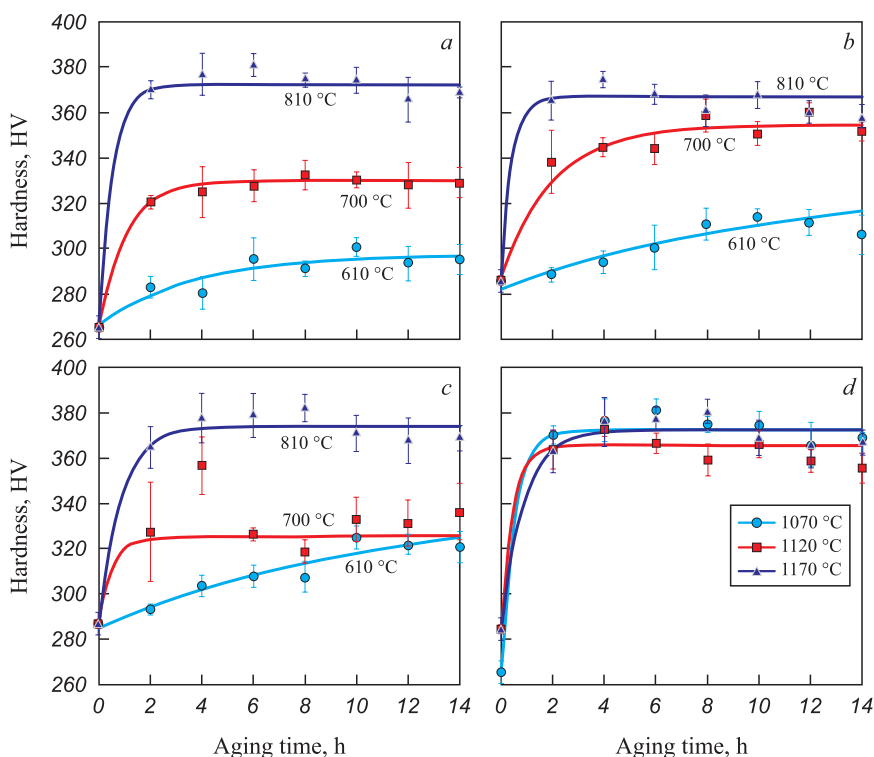


Fig. 6. Influence of high-temperature annealing at 1070 (a), 1120 (b), 1170 °C (c) and aging temperature on hardness of VZhL14N-VI superalloy, and effect of changing the annealing temperature on hardening of the alloy during aging at 810 °C (d)

Рис. 6. Влияние температуры высокотемпературного отжига 1070 (a), 1120 (b), 1170 °C (c) и температуры старения на твердость сплава ВЖЛ14Н-ВИ и изменения температуры отжига на твердый раствор на упрочнение сплава при старении при 810 °C (d)

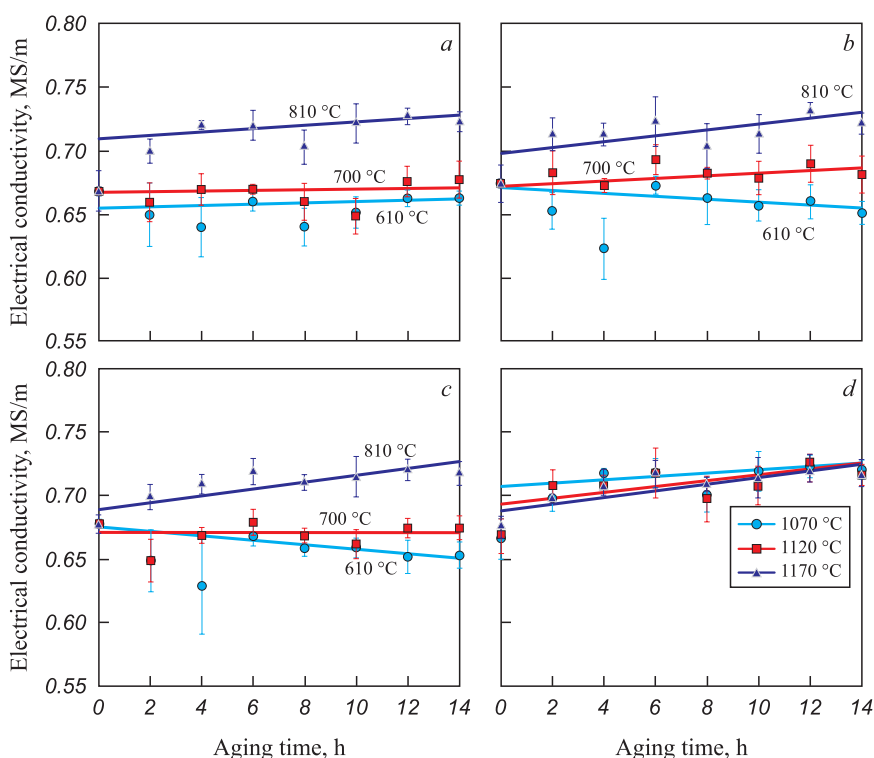


Fig. 7. Influence of high-temperature annealing at 1070 (a), 1120 (b), 1170 °C (c) and aging temperature on electrical conductivity of VZhL14N-VI superalloy, and effect of changing the annealing temperature on electrical conductivity of the alloy during aging at 810 °C (d)

Рис. 7. Влияние температуры высокотемпературного отжига 1070 (a), 1120 (b), 1170 °C (c) и температуры старения на электропроводность сплава ВЖЛ14Н-ВИ и изменения температуры отжига на электропроводность сплава при старении при 810 °C (d)

It has been established that the highest hardening effect is observed in alloys aged at 810 °C, ensuring the most complete decomposition of the supersaturated γ phase solid solution. At the same time, within the studied range of 1070 – 1170 °C, the solution annealing temperature has a significantly smaller effect on the hardening of the alloy compared to the aging temperature. The maximum hardness during aging is reached within 4 – 6 h and remains practically unchanged up to 10 – 14 h.

REFERENCES / СПИСОК ЛИТЕРАТУРЫ

- Logunov A.V., Shmotin Yu.N. Modern Nickel Superalloys for Gas Turbine Disks (Materials and Technologies). Moscow: Nauka i tekhnologii. 2013:264. (In Russ.).
Логунов А.В., Шмотин Ю.Н. Современные жаропрочные никелевые сплавы для дисков газовых турбин (материалы и технологии). Москва: Наука и технологии; 2013:264.
- Sun B., Wang J., Shu D. Precision Forming Technology of Large Superalloy Castings for Aircraft Engines. Singapore: Springer Singapore; 2021:409.
<https://doi.org/10.1007/978-981-33-6220-8>
- Hassan B., Corney J. Grain boundary precipitation in Inconel 718 and ATI 718Plus. *Materials Science and Technology*. 2017;33(16):1879–89.
<https://doi.org/10.1080/02670836.2017.1333222>
- Cemal M., Cevik S., Uzunonut Y., Diltemiz F. ALLVAC 718 Plus™ Superalloy for Aircraft Engine Applications. In: *Recent Advances in Aircraft Technology*. 2012:75–96.
<https://doi.org/10.5772/38433>
- Kablov E.N. History of Aviation Materials Science: VIAM – 75 Years of Search, Creativity, Discoveries. Moscow: Nauka, 2007:343. (In Russ.).
Каблов Е.Н. История авиационного материаловедения: ВИАМ – 75 лет поиска, творчества, открытий. Москва: Наука; 2007:343.
- Lu J., Yang Z., Li Y., Huang J., Zhao X., Yuan Y. Effect of alloying chemistry on fireside corrosion behavior of Ni-Fe-based superalloy for ultra-supercritical boiler applications. *Oxidation of Metals*. 2018;89(5–6):609–621.
<https://doi.org/10.1007/s11085-017-9804-7>
- Dolgoplov V.G. Study of the structure and effect of heat treatment on the mechanical properties of nickel-base alloys. *Инновационные процессы в исследовательской и образовательной деятельности*. 2014;1:60–62.
Dolgoplov V.G. Study of the structure and effect of heat treatment on the mechanical properties of nickel-base alloys. *Innovative Processes in Research and Educational Activities*. 2014;1:60–62.
- Logunov A.V. Problems of Design and Production of High-Temperature Cast Blades for Aircraft Gas Turbine Engines. Vol. 1: Modeling and Digitalization. Moscow: Nauka i tekhnologii; 2023:469. (In Russ.).
Логунов А.В. Проблемы проектирования и производства высокотемпературных литых лопаток авиационных ГТД: в 2-х книгах. Книга 1: Моделирование и цифровизация. Москва: Наука и технологии; 2023:469.
- Oborin L.A., Babitskiy N.A., Zhareb V.P. The thermal transformations of foundry high-temperature oxidation-resistant steels during the melting and the crystallization. *Journal of Siberian Federal University. Engineering & Technologies*. 2012;5(7):724–730. (In Russ.).
Оборин Л.А., Бабицкий Н.А., Жереб В.П. Термические превращения литейных высокопрочных сталей (ВНЛ) и жаропрочных сплавов (ВЖЛ) при плавлении и кристаллизации. *Журнал Сибирского федерального университета. Серия: Техника и технологии*. 2012;5(7):724–730.
- Gadalov V.N., Vornacheva I.V., Pankov D.N., Bugorsky I.A., Zagidullin R.R., Sabitov L.S., Ivanov A.A. Study of the influence of the structure of heat-resistant nickel-chrome alloys on their mechanical properties. *Izvestiya Tula State University. Technical Science*. 2022;(10):463–471.
Гадалов В.Н., Ворначева И.В., Паньков Д.Н., Бугорский И.А., Загидуллин Р.Р., Сабитов Л.С., Иванов А.А. Изучение влияния структуры жаропрочных никельхромовых сплавов на их механические свойства. *Известия Тульского государственного университета. Технические науки*. 2022;(10):463–471.
- Kirchmayer A., Pröbstle M., Huenert D., Neumeier S., Göken M. Influence of grain size and volume fraction of η/δ precipitates on the dwell fatigue crack propagation rate and creep resistance of the nickel-base superalloy ATI 718Plus. *Metallurgical and Materials Transactions A*. 2023;54:2219–2226. <https://doi.org/10.1007/s11661-023-07001-3>
- Donachie M.J., Donachie S.J. Superalloys: A Technical Guide. 2nd ed. Materials Park, Ohio: ASM International; 2002:408.
- Chen Y.T., Yeh A.C., Li M.Y., Kuo S.M. Effects of processing routes on room temperature tensile strength and elongation for Inconel 718. *Materials & Design*. 2017;119: 235–243.
<https://doi.org/10.1016/j.matdes.2017.01.069>
- Geddes B., Leon H., Huang X. Superalloys: Alloying and Performance. Materials Park, Ohio: ASM International; 2010:176.
- Beckert M., Klemm H. Handbuch der metallographischen Ätzverfahren. Leipzig: Deutscher Verlag für Grundstoffindustrie, VEB; 1976:410. (In Germ.).
Беккерт М., Клемм Х. Способы металлографического травления: Справочник: Перевод с немецкого. 2-е издание, переработанное и дополненное. Москва: Металлургия; 1988:400.
- Kovalenko V.S. Metallographic Reagents: Reference Book. 3rd ed. Moscow: Metallurgiya; 1981:120. (In Russ.).
Коваленко В.С. Металлографические реактивы: Справочник. 3-е издание, переработанное и дополненное. Москва: Металлургия; 1981:120.
- Reed R.C. The Superalloys: Fundamentals and Applications. Cambridge: Cambridge University Press; 2006:372.
- Logunov A.V. Nickel Superalloys for Blades and Disks of Gas Turbines. Rybinsk: Gazoturbinnnye tekhnologii; 2017:854. (In Russ.).
Логунов А.В. Жаропрочные никелевые сплавы для лопаток и дисков газовых турбин. Рыбинск: Газотурбинные технологии; 2017:854.
- Lefebvre A. Gas Turbine Combustion. Hemisphere Publishing Corporation; 1983:531.
Лефевр А. Процессы в камерах сгорания ГТД: Перевод с английского. Москва: Мир; 1986:566.
- Lv J. Effect of grain size on mechanical property and corrosion resistance of the Ni-based alloy 690. *Journal of Materials Science & Technology*; 2018;34(9):1685–1691.
<https://doi.org/10.1016/j.jmst.2017.12.017>

Information about the Authors

Сведения об авторах

Andrei V. Koltygin, Cand. Sci. (Eng.), Assist. Prof. of the Chair "Foundry Technology and Art Processing of Materials", National University of Science and Technology "MISIS"

ORCID: 0000-0002-8376-0480

E-mail: misistlp@mail.ru

Vyacheslav E. Bazhenov, Cand. Sci. (Eng.), Assist. Prof. of the Chair "Foundry Technology and Art Processing of Materials", National University of Science and Technology "MISIS"

ORCID: 0000-0003-3214-1935

E-mail: V.E.Bagenov@gmail.com

Anastasiya A. Belova, Postgraduate of the Chair "Foundry Technology and Art Processing of Materials", National University of Science and Technology "MISIS"

ORCID: 0009-0008-4199-8942

E-mail: belova@ic-ltm.ru

Andrei V. Sannikov, Cand. Sci. (Eng.), Junior Researcher of the Chair "Foundry Technology and Art Processing of Materials", National University of Science and Technology "MISIS"

ORCID: 0000-0002-0517-7732

E-mail: sannikov@ic-ltm.ru

Anastasiya A. Lyskovich, Postgraduate of the Chair "Foundry Technology and Art Processing of Materials", National University of Science and Technology "MISIS"

ORCID: 0000-0002-8490-4829

E-mail: nastya719ls999@yandex.ru

Vladimir D. Belov, Dr. Sci. (Eng.), Prof., Head of the Chair "Foundry Technology and Art Processing of Materials", National University of Science and Technology "MISIS"

ORCID: 0000-0003-3607-8144

E-mail: vdbelov@mail.ru

Evgenii Yu. Shchedrin, Chief Metallurgist, PJSC Kuznetsov

E-mail: ogmet@uec-kuznetsov.ru

Андрей Вадимович Колтыгин, к.т.н, доцент кафедры «Литейные технологии и художественная обработка материалов», Национальный исследовательский технологический университет «МИСИС»

ORCID: 0000-0002-8376-0480

E-mail: misistlp@mail.ru

Вячеслав Евгеньевич Баженов, к.т.н, доцент кафедры «Литейные технологии и художественная обработка материалов», Национальный исследовательский технологический университет «МИСИС»

ORCID: 0000-0003-3214-1935

E-mail: V.E.Bagenov@gmail.com

Анастасия Андреевна Белова, аспирант кафедры «Литейные технологии и художественная обработка материалов», Национальный исследовательский технологический университет «МИСИС»

ORCID: 0009-0008-4199-8942

E-mail: belova@ic-ltm.ru

Андрей Владимирович Санников, к.т.н., младший научный сотрудник кафедры «Литейные технологии и художественная обработка материалов», Национальный исследовательский технологический университет «МИСИС»

ORCID: 0000-0002-0517-7732

E-mail: sannikov@ic-ltm.ru

Анастасия Андреевна Лыскович, аспирант кафедры «Литейные технологии и художественная обработка материалов», Национальный исследовательский технологический университет «МИСИС»

ORCID: 0000-0002-8490-4829

E-mail: nastya719ls999@yandex.ru

Владимир Дмитриевич Белов, д.т.н., профессор, заведующий кафедрой «Литейные технологии и художественная обработка материалов», Национальный исследовательский технологический университет «МИСИС»

ORCID: 0000-0003-3607-8144

E-mail: vdbelov@mail.ru

Евгений Юрьевич Щедрин, главный металлург, ПАО «ОДК-Кузнецов»

E-mail: ogmet@uec-kuznetsov.ru

Contribution of the Authors

Вклад авторов

A. V. Koltygin – conceptualization, analysis of results, writing the text.

V. E. Bazhenov – scientific guidance, review and editing of the article.

A. A. Belova – realization of experiment, analysis of results.

A. V. Sannikov – realization of experiment, analysis of results.

A. A. Lyskovich – realization of experiment, analysis of results.

V. D. Belov – supervision, review and editing of the manuscript.

E. Yu. Shchedrin – formulation of the aims and objectives of the study, provision of resources.

А. В. Колтыгин – формирование основной концепции, обработка результатов исследований, написание текста статьи.

В. Е. Баженов – научное руководство, редактирование текста статьи.

А. А. Белова – проведение экспериментов, обработка результатов исследований.

А. В. Санников – проведение экспериментов, обработка результатов исследований.

А. А. Лыскович – проведение экспериментов, обработка результатов исследований.

В. Д. Белов – общее руководство, редактирование текста статьи.

Е. Ю. Щедрин – формулировка цели и задачи исследования, обеспечение ресурсами.

Received 26.06.2024

Revised 14.08.2024

Accepted 29.10.2024

Поступила в редакцию 26.06.2024

После доработки 14.08.2024

Принята к публикации 29.10.2024



UDC 669.017.15

DOI 10.17073/0368-0797-2025-1-69-75



Original article

Оригинальная статья

CONSTRUCTION OF LIQUIDUS SURFACE OF Fe – B – Mn – C – Cr FIVE-COMPONENT DIAGRAM

G. A. Kazakevich , A. Yu. Popov

Russian University of Transport (9, bld. 9 Obraztsova Str., Moscow 127994, Russian Federation)

KazakevichG@mail.ru

Abstract. The authors used the technique of constructing the schemes of multicomponent diagrams ($n > 3$) in traditional coordinates “temperature – concentration”, the basis of which are n – angles with a divergent coordinate grid at $n > 4$, to construct the liquidus surface of the Fe–B–Mn–C–Cr five-component system. Choice of the system was determined by the need to harden the surfaces of parts made from a large number of low-alloy steels by boriding. The critical points of the liquidus surface were melting points of the alloy chemical elements, melting points of borides and melting temperatures of eutectics of the phase diagrams, which are the sides of a pentahedral prism. Individual experimental melting temperatures of the steels and calculated melting temperatures of new eutectics during the interaction of eutectics of double phase diagrams were also taken into account. The latter were determined according to the eutectic reaction rule, which provides for the use of only melting temperatures of the initial eutectics in the calculation. At the same time, phase composition of the multicomponent boride eutectics of the system was determined. The resulting liquidus surface shows the temperature at which crystallization begins and the phase composition of the layer during boriding of casting mold coatings for surface hardening of castings. The calculated melting temperatures of eutectics form the solidus surfaces of the system. In accordance with the concentration values of the elements, especially boron, five solidus surfaces are formed in the system at 1571, 1451, 1394, 1105 and 978 °C. These melting temperatures of eutectics are the boundaries between the diffusion and diffusion-crystallization mechanisms of formation of boronized layer in solid and solidifying states of treated surfaces, therefore, they determine the mechanism of formation of boronized layer, their phase composition, structural morphology and properties.

Keywords: liquidus surface, five-component system, calculation of eutectic temperatures, divergent grid, phase diagram, steel, boriding

For citation: Kazakevich G.A., Popov A.Yu. Construction of liquidus surface of Fe–B–Mn–C–Cr five-component diagram. *Izvestiya. Ferrous Metallurgy*. 2025;68(1):69–75. <https://doi.org/10.17073/0368-0797-2025-1-69-75>

ПОСТРОЕНИЕ ПОВЕРХНОСТИ ЛИКВИДУС ПЯТИКОМПОНЕНТНОЙ СХЕМЫ ДИАГРАММЫ Fe – B – Mn – C – Cr

Г. А. Казакевич , А. Ю. Попов

Российский университет транспорта (Москва, 127994, ул. Образцова, 9, стр. 9)

KazakevichG@mail.ru

Аннотация. Для построения поверхности ликвидус пятикомпонентной системы Fe–B–Mn–C–Cr применялась методика построения в традиционных координатах «температура – концентрация» схем многокомпонентных диаграмм ($n > 3$), основанием которых являются n -угольники с дивергентной координатной сеткой при $n > 4$. Выбор системы обусловлен необходимостью упрочнения поверхностей деталей, изготовленных из большого количества низколегированных сталей борированием. Критическими точками поверхности ликвидус являлись температуры плавления химических элементов сплава, боридов и эвтектик двойных диаграмм состояния, которые являются сторонами пятигранной призмы. Принимались во внимание также отдельные экспериментальные температуры плавления сталей и рассчитанные температуры плавления новых эвтектик, образующихся при взаимодействии эвтектик двойных диаграмм состояния. Последние определялись по правилу эвтектической реакции, предусматривающему использование при расчете только температур плавления исходных эвтектик. Одновременно определялся и фазовый состав многокомпонентных боридных эвтектик системы. Полученная поверхность ликвидус показывает температуру начала кристаллизации и фазовый состав слоя при проведении борирования из обмазок литейных форм для поверхностного упрочнения отливок. Рассчитанные температуры плавления эвтектик образуют поверхности солидус системы. В соответствии с концентрационными значениями элементов, и особенно бора, в системе образуются пять поверхностей ликвидус при 1571, 1451, 1394, 1105 и 978 °C. Данные температуры плавления эвтектик являются границами между диффузионным и диффузионно-кристаллизационным механизмами формирования борированных слоев в твердом и затвердевающем

состояниях обрабатываемых поверхностей. Следовательно, они определяют механизм формирования борированных слоев, их фазовый состав, структурную морфологию и свойства.

Ключевые слова: поверхность ликвидус, пятикомпонентная система, расчет эвтектических температур, дивергентная сетка, диаграммы состояния, стали, борирование

Для цитирования: Казакевич Г.А., Попов А.Ю. Построение поверхности ликвидус пятикомпонентной схемы диаграммы Fe–B–Mn–C–Cr. *Известия вузов. Черная металлургия*. 2025;68(1):69–75. <https://doi.org/10.17073/0368-0797-2025-1-69-75>

INTRODUCTION

Phase diagrams of alloys serve as essential reference tools for both theorists and practitioners in metallurgy, materials science, metal forming, casting, various fields of mechanical engineering, and the operation of technical equipment.

Taking into account that most of the steels and alloys used are multicomponent ($n > 3$), in many cases certain difficulties arise in determining the conditions for performing technological processes, the phase composition and properties of alloys, since there are no constructed state diagrams in the temperature-concentration traditional coordinates [1 – 3]. Typically, binary and ternary diagrams, their isothermal sections, tetrahedral representations for specific temperatures, and practical research findings are used to describe these processes [4 – 6].

In particular, binary and ternary phase diagrams have been widely applied to describe the boriding process and the properties of boronized layers [7 – 9]. These diagrams refine the concentrations of compounds and solid solutions, define phase transformation temperatures, and reveal new compounds. A key finding is the confirmed existence of iron borocarbide [8; 9], which has the formula $\text{Fe}_{23}(\text{C}, \text{B})_6$. In other complex carbides found in steels, alloying elements typically substitute for iron.

It has been established that at 1000 °C, up to 80 % of the carbon in cementite can be replaced by boron, modifying the formula to $\text{Fe}_3\text{C}_{0.2}\text{B}_{0.8}$. This substitution alters the crystal lattice parameters, leading to compression along the a and c axes and expansion along the b axis of the orthorhombic lattice. Additionally, as boron content increases, the saturation magnetization and Curie temperature also rise. This phenomenon is crucial in explaining the properties of borided components, where borocarbide inclusions form beneath the boride layer [10; 11].

Study [8] demonstrated that borocarbide $\text{Fe}_{23}(\text{C}, \text{B})_6$ is isomorphic to cubic chromium carbide Cr_{23}C_6 (structure type $d84$). As the composition shifts from carbon-enriched to boron-enriched, the lattice parameter a increases from 1.0594 to 1.0628 nm. When heated to 800 °C $\text{Fe}_{23}(\text{C}, \text{B})_6$ melts congruently. Isothermal sections at 700, 800, 900, and 1000 °C indicate that the $\text{Fe}_{23}(\text{C}, \text{B})_6$ phase has a composition corresponding to $\text{Fe}_{23}(\text{C}_{0.73}\text{B}_{0.27})_6$ and is in equilibrium with borocementite $\text{Fe}_3(\text{C}, \text{B})$ and Fe_α . The phase $\text{Fe}_{23}(\text{C}_{0.44}\text{B}_{0.56})_6$ is in equilibrium with Fe_2B and $\text{Fe}_3(\text{C}, \text{B})$. An analysis of the section at 800 °C shows that $\text{Fe}_{23}(\text{C}, \text{B})_6$

exists over a wider range of carbon and boron concentrations, between $\text{Fe}_{23}(\text{C}_{0.38}\text{B}_{0.62})_6$ and $\text{Fe}_{23}(\text{C}_{0.77}\text{B}_{0.23})_6$, and is in equilibrium with Fe_γ and $\text{Fe}_3(\text{C}, \text{B})$. It has been determined that $\text{Fe}_{23}(\text{C}, \text{B})_6$ remains stable up to 965 ± 5 °C [12 – 14]. These findings refine the phase composition of phase diagram regions and the properties of borided layers, as borocarbide inclusions exhibit high hardness [15 – 17].

In the study of multicomponent phase diagrams ($n > 3$), the thermodynamic method, which incorporates the characteristics of binary phase diagrams, has been widely used [18]. Specifically, a four-component Fe–Mn–Si–C phase diagram was developed by calculating thermodynamic constants at the phase transformation temperatures of compounds, followed by triangulation of the system and its subsystems. This resulted in a tetrahedral phase diagram consisting of 16 elementary tetrahedra containing congruently and incongruently melting compounds [19].

The Bukke-Schout method [20] represents the system's composition or state as a tetrad on a plane, though it is derived from a four-dimensional figure. However, the systems described in studies [21; 22] create geometric representations of multicomponent compositions in two dimensions, making them less suitable for practical applications. The refinements of the general approach discussed in studies [23; 24] do not produce practical working diagrams but instead generate planar projection systems after double projection, which are also difficult to use as working schematics in technological process development.

To determine the temperatures of eutectic reactions and the compositions of eutectic alloys, differential scanning calorimetry [25; 26], metallographic studies [27; 28], and X-ray diffraction analysis [29] have traditionally been used. These methods, however, are labor-intensive, leading to the increasing use of analytical and statistical approaches for predictive calculations of these characteristics.

A statistical method has been proposed for calculating eutectic temperatures and concentrations in metallic multicomponent systems ($n > 3$), where the only input data are the melting temperatures of the components forming the eutectic or the calculated eutectic melting temperatures resulting from their interaction. In this context, a temperature rule for eutectic reactions has been formulated [30; 32].

The methodology proposed in study [32], based on a developed database incorporating calculation programs and a recursive algorithm, is applicable to simple systems. However, it does not account for the formation of chemi-

cal compounds in multicomponent systems, the presence of multiple eutectics in binary systems, or the formation of solid solutions. A more advanced method that considers atomic electric charges and their interactions [33] also has these limitations, while further complicating theoretical justification and calculations.

Another approach involves calculating eutectic and peritectic temperatures and compositions in binary systems using approximation techniques to model the relationships between these characteristics. These calculations are performed using fractional-linear and power functions, relying only on the melting temperatures of the components [34], or by applying linear geometry to determine the eutectic composition of a binary system based on the known melting temperatures of its components and eutectic [35].

One method for constructing schemes of multicomponent ($n > 3$) phase diagrams in traditional *temperature – concentration* coordinates is the approach proposed in studies [36–38]. This method uses the *Krukovich divergent coordinate grid* to determine the distribution of alloying elements over the diagram's base area – a concentration n -gon, where the number of vertices corresponds to the number of chemical elements in the alloy. The sides of the polyhedral prism represent binary phase diagrams. These phase diagrams, referred to as diagram schemes, omit certain combinations of alloying elements in the concentration polyhedron. Specifically, alloys with equal proportions of three elements are absent in a four-component system, four elements in a five-component system, and so on. Nevertheless, these schemes provide a highly illustrative representation and can serve as a technological reference diagram for analyzing alloy states.

Thus, this study aims to construct the liquidus surface for the multicomponent Fe–B–Mn–C–Cr system, following the recommendations from [36–38] to determine saturation temperatures and explain the structural formation processes that occur during boriding in different aggregate states of treated surfaces.

RESULTS AND DISCUSSION

A wide range of steel grades and alloys, including (AISI) C1020, 5140, L6, D3, 430, SCSiMn2 (Japanese), W 1-0.8 C EXTRA, and others, undergo boriding to enhance wear resistance. Many structural steels are characterized by a combination of Fe–Mn–C–Cr elements. Components made from these steels are borided in both the solid state and the liquid state within casting molds, as well as through partial remelting of the hardened surfaces (in the presence of both liquid and solid phases) when using concentrated heat sources. In such cases, knowledge of melting temperatures involving boron is essential, leading to a system represented as Fe–Cr–Mn–C–B, where the sequence of elements is chosen arbitrarily.

The construction of the liquidus surface for the five-component Fe–B–Mn–C–Cr phase diagram, with the selected sequence of elements, was carried out by analyzing the structural formation of binary phase diagrams of alloys. This process incorporated experimental critical points of several alloys in the system, as well as calculated temperatures and concentrations of eutectic interactions. In particular, when determining boriding conditions for alloy steels and alloys, both binary and ternary phase diagrams containing iron were analyzed, along with binary diagrams that included only alloying elements and boron. To predict the type of borides and their degree of alloying, the isomorphism of boride crystal lattices and the solubility of borides within each other were considered. It can be assumed that the formation of a particular primary boride during alloy saturation with boron depends on the affinity of the elements for boron and the amount of the base element in the alloy. Therefore, in this case, the shape of the liquidus surface is determined by the concentration distribution of boron.

Fe–Cr–B system: at 1000 °C, the phases in equilibrium with γ -Fe include α -Fe and Fe_2B , while those in equilibrium with the α -phase include γ -Fe, Fe_2B , Cr_2B , and Cr_4B . The Fe_2B and, particularly, Cr_2B phases form extensive regions of solid solutions [36]. It has been established that within the boriding temperature range of 700–1250 °C, no ternary phases are formed in this system.

Cr–Mn–B system: at 800 °C, an unlimited series of solid solutions $(\text{Cr}, \text{Mn})\text{B}_2$, $(\text{Cr}, \text{Mn})_3\text{B}_4$, and between Cr_2B and Mn_4B borides has been identified [36]. The degree of mutual solubility of borides is as follows: Cr_5B_3 dissolves 0.08 mass fractions of Mn_5B_3 boride, while CrB dissolves 0.20 mass fractions of MnB; MnB dissolves 0.4 mass fractions of CrB.

An alternative interpretation of the binary phase diagram for the Mn–B system suggests the existence of an unlimited series of solid solutions $(\text{Cr}, \text{Mn})_2\text{B}$ instead of the Cr_2B – Mn_4B system at 1025 °C. Study [39] determined the compositions of solid solutions of chromium and manganese monoborides: $\text{Cr}_{0.46}\text{Mn}_{0.54}\text{B}$ and $\text{Mn}_{0.60}\text{Cr}_{0.40}\text{B}$. The region between the solid solutions based on CrB and MnB corresponds to the $\text{Cr}_x\text{Mn}_{1-x}\text{B}$ boride.

It should also be noted that isomorphic borides of Fe and Mn (FeB and MnB , Fe_2B and Mn_2B) exhibit unlimited mutual solubility.

According to the selected technique for constructing schemes of multicomponent phase diagrams, each element of the system is distributed within the volume of the pentahedral prism from two faces and across the base area (a pentagon) from two sides. For example, carbon is distributed from the C–Cr and C–Mn sides (Fig. 1). The concentration distribution of any element across the pentagon's surface, calculated using the divergent coordinate grid, is non-uniform. The divergence angle of each coordinate line was determined by the formula

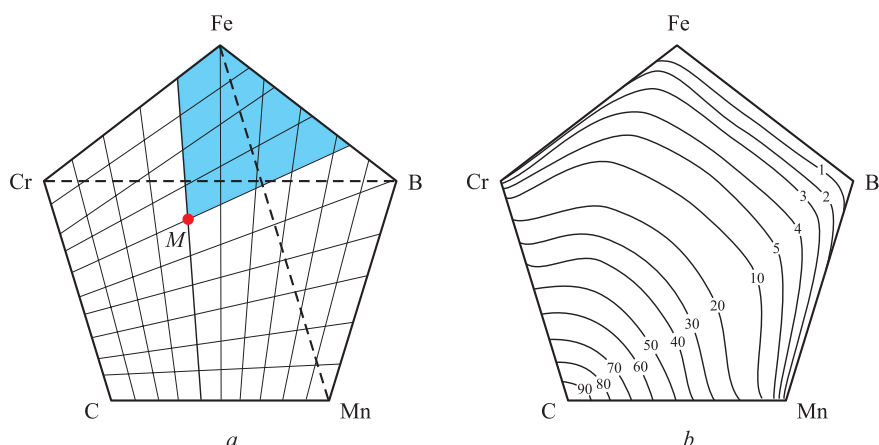


Fig. 1. Basis of the five-component phase diagram with a divergent coordinate grid (a) and concentration distribution of carbon in wt. % (b) (distribution stencil for any element)

Рис. 1. Основание схемы пятикомпонентной диаграммы состояний с дивергентной сеткой координат (a) и концентрационное распределение углерода, мас. % (b) (трафарет распределения для любого элемента)

$$\alpha = \left(1 - \frac{4}{n}\right) \frac{180}{c},$$

where n is the number of components in the system (i.e., the number of polygon sides), and c is the number of divisions on the uniform concentration scale.

In this case, the divergence angle of each coordinate line from the previous one is 3.6° for $c = 10$. The shaded area enclosed by the coordinate lines (Fig. 1) represents the carbon content at point M , expressed as a percentage of the pentagon's total area. This area was determined geometrically. The calculated concentrations at multiple points allowed for the construction of iso-concentration lines across the base of the pentahedral prism, collectively forming a stencil for element distribution.

To determine the concentration of another element at point M (e.g., boron), the stencil is rotated so that 100 % aligns with vertex B (boron). The intersection of point M

with the corresponding iso-concentration line indicates the boron content (Fig. 2), which, in this case, is 10 wt. %.

The liquidus surface for the selected element arrangement is formed by a set of critical points, including the onset of crystallization of chemical elements and solid solutions, the melting temperatures of congruently melting phases, the melting points of binary eutectics from phase diagrams of alloys, and their interactions leading to the formation of new multicomponent eutectics. The two observed peaks correspond to the formation of alloyed chromium borides $(\text{Cr, Fe, Mn})\text{B}$ ($\sim 2100^\circ\text{C}$) and $(\text{Cr, Fe, Mn})\text{B}_2$ ($\sim 2200^\circ\text{C}$) at these boron and chromium concentrations (Fig. 3).

At high boron concentrations, high-temperature eutectics from the Fe–B and Mn–B binary phase diagrams

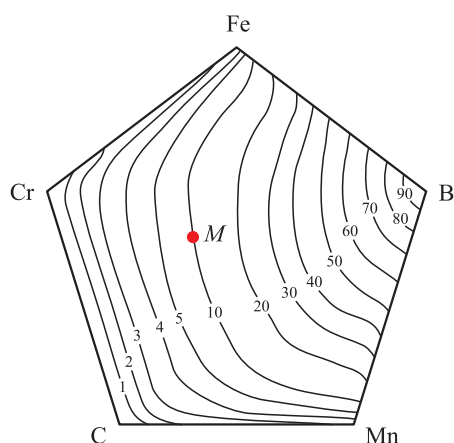


Fig. 2. Determination of boron content at point M

Рис. 2. Определение содержания бора в точке M

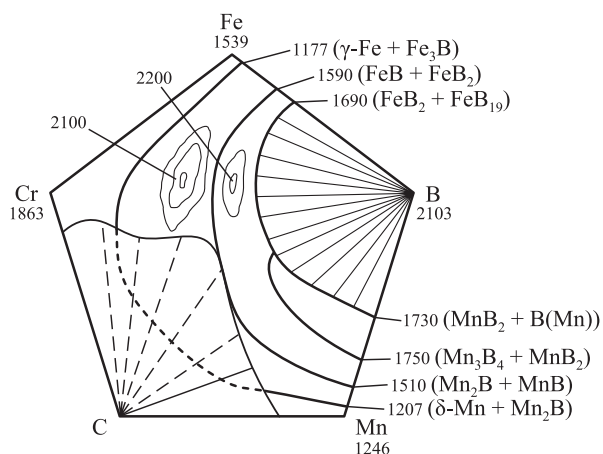


Fig. 3. Liquidus surface of the Fe–B–Mn–C–Cr system with indicated temperatures, phase composition of eutectics and lines of their interaction (top view)

Рис. 3. Поверхность ликвидус системы Fe–B–Mn–C–Cr с обозначенными температурами, фазовым составом эвтектик и линиями их взаимодействия (вид сверху)

interact, forming a new eutectic mixture $\text{FeB}_2 + \text{FeB}_{19} + \text{Mn}_3\text{B}_4 + \text{MnB}_2 + \text{B}(\text{Mn})$ with a calculated melting temperature of 1571 °C. In the presence of a sufficient amount of chromium and a boron concentration in the range of 27.92 – 90.0 wt. %, the formation of a eutectic containing $(\text{Fe}, \text{Mn})\text{B}_2 + \text{FeB}_{19} + \text{Mn}_3\text{B}_4 + \text{B}(\text{CrMn}) + \text{CrB}_2$ possible, with a calculated melting temperature of 1394 °C.

At boron concentrations between 16.25 and 27.92 wt. %, the interaction of $\text{FeB} + \text{FeB}_2$ and $\text{Mn}_2\text{B} + \text{C}$ eutectics results in the formation of a eutectic mixture $(\text{Fe}, \text{Mn})\text{B} + \text{FeB}_2 + \text{Mn}_2\text{B}$ with a calculated melting temperature of 1451 °C.

At boron concentrations between 0.01 and 10 wt. %, the interaction of the $\gamma\text{-Fe} - \text{Fe}_3\text{B}$ and $\delta\text{-Mn} + \text{Mn}_2\text{B}$ eutectics leads to the formation of a new eutectic mixture $\gamma\text{-Fe} + \text{Fe}_3\text{B} + \delta\text{-Mn} + \text{Mn}_2\text{B}$ a calculated melting temperature of 1105 °C. At chromium concentrations above 40 wt. %, another eutectic may form $(\gamma\text{-Fe} + \text{Fe}_3\text{B} + \delta\text{-Mn} + \text{Mn}_2\text{B}) + \text{Cr}(\text{B}) + \text{Cr}_2\text{B}$ with a melting temperature of 978 °C. The phase compositions resulting from eutectic interactions are presented without considering the mutual solubility of borides.

The melting temperatures of congruently melting borides FeB , FeB_2 , Mn_2B , Mn_3B_4 , MnB , Mn_3B_4 , MnB_2 and their interactions are not included in the liquidus surface visualization for clarity. The temperature of the liquidus surface is crucial for boriding castings in molds coated with a boriding mixture, as well as for predicting the phase composition of the boronized layer.

The calculated melting temperatures of new eutectics represent the lowest temperatures at which alloy melting begins, i.e., the solidus surface temperature. This temperature defines the boundary for the formation of boronized layers through a diffusion mechanism in the solid state of treated surfaces and a diffusion-crystallization mechanism in the solidifying state of surfaces.

Eutectic temperatures were calculated in accordance with Krukovich's eutectic reaction rule [17; 30; 31; 36 – 38; 40] using the following formulas:

– for an even number of eutectic components ($2n$)

$$T_{\text{eut}} = K_{\text{eut}}^{n/2} \sum_{i=1}^n T_i;$$

– for an odd number of eutectic components ($2n + 1$)

$$T_{\text{eut}} = K_{\text{eut}}^{\frac{n+1}{2}} \sum_{i=1}^{n-1} T_i + K_{\text{eut}} T_n;$$

$$K_{\text{eut}} = 0.497 \exp(-0.2657X);$$

$$X = \frac{\sum_{1 \leq i \leq j \leq n} |T_i - T_j|}{\left(\sum_{i=1}^n T_i \right)^{0.74}},$$

where T represents the melting temperatures of eutectic phases or the melting temperatures of binary (or ternary) eutectic interactions, which form the components of a new eutectic mixture, K ; K_{eut} is the eutectic temperature coefficient, and X is a temperature scaling parameter.

According to the eutectic reaction rule, when calculating the eutectic temperature of a new eutectic, the melting temperatures of binary eutectics or previously calculated eutectics (whose components also form part of the new eutectic mixture) were used.

The phase composition, structural morphology, and properties of boronized layers depend on the content of alloying elements in the steel, the saturation temperature, and the saturation potential of the environment. Specifically, during the boriding of 5140 steel (AISI), which contains 0.36 – 0.44 % C, 0.17 – 0.27 % Si, 0.5 – 0.8 % Mn, and 0.8 – 1.1 % Cr, at a saturation temperature of 950 °C in a boriding mixture ensuring a boron concentration of ~17 %, layers based on alloyed borides $(\text{Fe}, \text{Cr})\text{B} + (\text{Fe}, \text{Cr}, \text{Mn})_2\text{B}$ are formed. When the melting temperature is exceeded, heterogeneous layers develop, where dispersed alloyed borides are embedded in an α -solid solution.

CONCLUSIONS

The divergent coordinate grid was used to determine the element distribution within the volume of the pentahedral prism by constructing a concentration stencil.

Using the eutectic reaction rule, eutectic temperatures were calculated, and the phase composition of interacting eutectics in the Fe–B–Mn–C–Cr system was determined.

To analyze the structural formation mechanisms during boriding in the liquid, crystallizing, or solid states of treated surfaces, it is recommended to use the constructed liquidus surface of the five-component phase diagram scheme for the Fe–B–Mn–C–Cr system, along with the calculated eutectic melting temperatures, which define the solidus surface of the system.

REFERENCES / СПИСОК ЛИТЕРАТУРЫ

1. Lakhtin Yu.M., Leont'eva V.P. Materials Science. Moscow: Mashinostroenie; 1990:528. (In Russ.).
Лахтин Ю.М., Леонтьева В.П. Материаловедение: Учебник для вузов. Москва: Машиностроение; 1990:528.
2. Zakharov A.M. Phase Diagrams of Binary and Ternary Systems. Moscow: Metallurgiya; 1990:240. (In Russ.).
Захаров А.М. Диаграммы состояния двойных и тройных систем: Учебное пособие для вузов. Москва: Металлургия; 1990:240.
3. Campbell F.C. Phase Diagrams – Understanding the Basics. Materials Park, Ohio: ASM International; 2012:470.

4. Vozdvizhenskii V.M. Prediction of Binary State Diagrams. Moscow: Metallurgiya; 1975:224. (In Russ.).
Воздвиженский В.М. Прогноз двойных диаграмм состояния. Москва: Metallurgiya; 1975:224.
5. Massalski T.B. Binary Alloy. Phase Diagrams. 2nd ed. Vol. 3. ASM International; 1990:525.
6. Baker H. Introduction to Alloy Phase Diagrams: ASM Handbook. Vol. 3. ASM International; 1992:490.
7. Busby P.E., Warga M.E., Wells C. Diffusion and solubility of boron in iron and steel. *JOM*. 1953;(5):1463–1468.
<https://doi.org/10.1007/BF03397637>
8. Carroll K.G., Darken L.S., Filer E.W., Zwilling L. A new iron borocarbide. *Nature*. 1954;174:978–979.
<https://doi.org/10.1038/174978a0>
9. Grange R.A. Boron, Calcium, Columbium, and Zirconium in Iron and Steel. New York: Wiley; London: Chapman and Hall; 1957:533.
Бор, кальций, ниобий и цирконий в чугунах и сталях / Пер. с англ. В.А. Мчедlishvili и В.В. Ховрина; под ред. С.М. Винарова. Москва: Metallurgizdat; 1961:459.
10. Voroshnin L.G., Lyakhovich L.S., Panich G.G., Protasevich G.F. Structure of alloys of the Fe-B system. *Metallovedenie i termicheskaya obrabotka metallov*. 1970;(9):14–17. (In Russ.).
Ворошнин Л.Г., Ляхович Л.С., Панич Г.Г., Протасевич Г.Ф. Структура сплавов системы Fe–B. *Металловедение и термическая обработка металлов*. 1970;(9):14–17.
11. Koifman I.S., etc. X-ray analysis of boron cementite. *Metallovedenie i termicheskaya obrabotka metallov*. 1969;(2):59–60. (In Russ.).
Койфман И.С. и др. Рентгенографический анализ борцементита. *Металловедение и термическая обработка металлов*. 1969;(2):59–60.
12. Stadelmaier H.H., Gregg R.A. Die Ternare Phase Fe₂₃C₃B₃ im Dreistoffsystem Eisen-Kohlenstoff-Bor. *Metall*. 1963; 17(5):412–414. (In Germ.).
13. Cameron T.B., Morral J.E. The solubility of carbon in iron. *Metallurgical Translations A*. 1986;17(8):1481–1483.
<https://doi.org/10.1007/bf02650132>
14. Borlora Lucco M., Pradelli G. Iron-boron-carbon ratio system. *La Metallurgia Italiana*. 1967;59(11):907–916.
15. Samsonov G.V., Umanskii L.S. Solid Compounds of Refractory Metals. Moscow: Metallurgizdat; 1957:265. (In Russ.).
Самсонов Г.В., Уманский Л.С. Твердые соединения тугоплавких металлов. Москва: Metallurgizdat; 1957:265.
16. Villars P., Prince A., Okamoto H. Handbook of Ternary Alloy Phase Diagrams. ASM International; 1994:1500.
17. Krukovich M.G., Prusakov B.A., Sizov I.G. Plasticity of Boronized Layers. Springer Series in Materials Science. Vol. 237. Springer International Publishing Switzerland; 2016:364. <https://doi.org/10.1007/978-3-319-40012-9>
18. Protsyuk A.P., Karapet'yants M.Kh. On the thermodynamic study of processes in multicomponent systems. *Zhurnal prikladnoi khimii*. 1977;50(1):169–171. (In Russ.).
Процюк А.П., Карапетьянц М.Х. О термодинамическом исследовании процессов в многокомпонентных системах. *Журнал прикладной химии*. 1977;50(1):169–171.
19. Gabdulin S.T., Baisanov S., Toleukadyr R.T. Constructing a phase diagram of the Fe – Mn – Si – C system to determine the phase composition of manganese ferroalloys. *Proceedings of the University: Karaganda State University*. Karaganda; 2020;(1(78)):38–43. (In Russ.).
Габдулин С.Т., Байсанов С., Толеукадыр Р.Т. Построение диаграммы состояния системы Fe – Mn – Si – C для определения фазового состава марганцевых ферросплавов. *Труды университета: Сборник трудов Карагандинского государственного университета*. Караганда; 2020;(1(78)):38–43.
20. Anosov V.Ya., Ozerova M.I., Fialkov Yu.Ya. Fundamentals of Physicochemical Analysis. Moscow: Nauka; 1976:503. (In Russ.).
Аносов В.Я., Озерова М.И., Фиалков Ю.Я. Основы физико-химического анализа. Москва: Наука; 1976:503.
21. Lodochnikov V.N. The simplest methods for representation multicomponent systems. *Izvestiya instituta fiziko-khimicheskogo analiza*. 1924;2(2):255–351. (In Russ.).
Лодочников В.Н. Простейшие методы изображения многокомпонентных систем. *Известия института физико-химического анализа*. 1924;2(2):255–351.
22. Radishchev V.P. Method for depicting multicomponent systems. *Izvestiya sektora fiziko-khimicheskogo analiza AN SSSR*. 1936;(9):203–219. (In Russ.).
Радищев В.П. Метод изображения многокомпонентных систем. *Известия сектора физико-химического анализа АН СССР*. 1936;(9):203–219.
23. Radishchev V.P. Methods for displaying multi-component diagrams. *Izvestiya sektora fiziko-khimicheskogo analiza AN SSSR*. 1938;(11):5–20. (In Russ.).
Радищев В.П. Методы изображения многокомпонентных диаграмм. *Известия сектора физико-химического анализа АН СССР*. 1938;(11):5–20.
24. Petrov D.A. State diagram of a five-component eutectic system in the coordinates of three-dimensional pentatopic projection. In: *State Diagrams of Metal Systems*. Moscow: Nauka; 1981:35–45. (In Russ.).
Петров Д.А. Диаграмма состояния пятикомпонентной эвтектической системы в координатах трехмерной проекции пентатопа. В кн.: *Диаграммы состояния металлических систем: Сборник трудов*. Москва: Наука; 1981: 35–45.
25. Ding M.X.U.K., Jow T. Phase diagram of EC-DMC binary system and enthalpic determination of its eutectic composition. *Journal of Thermal Analysis and Calorimetry*. 2000;61(1):177–186.
<https://doi.org/10.1023/A:1010175114578>
26. Ramkumer K.L., Saxena M.K., Deb S.B. Experimental evaluation of procedures for heat capacity measurements by differential scanning calorimetry. *Journal of Thermal Analysis and Calorimetry*. 2001;66(2):387–397.
<https://doi.org/10.1023/A:1013126414406>
27. Li S.-P., Zhao S.-X., Pan M.-X., Zhao D.-Q., Chen X.-C., Barabash O.M. Eutectic reaction and microstructural characteristics of Al(Li)–Mg₂Si alloys. *Journal of Materials Science*. 2001;36(6):1569–1575.
<https://doi.org/10.1023/A:1017525520066>
28. Lewis D., Allen S., Notis M., Scotch A. Determination of the eutectic structure in the Al–Cu–Sn system. *Journal of Electronic Material*. 2002;31(2):161–167.
<https://doi.org/10.1007/s11664-002-0163-y>

29. Luo Ch.H., Martin M. Investigation of the phase diagram and the defect structure of non stoichiometric Li – Mn – O spiral. In: *Proceedings of the European Material Research Society Spring Meeting, May 24 – 28. Strasbourg. 2004*:28–32.
30. Krukovich M.G. Calculation of eutectic temperature and concentration in multicomponent systems. Moscow State University of Railway Engineering. Deposited in the All-Russian Institute of Scientific and Technical Information. Moscow; 1993;(3078-V95):10. (In Russ.).
Крукович М.Г. Расчет эвтектической температуры и концентрации в многокомпонентных системах. Московский государственный университет путей сообщения. Депонирована в Всероссийском институте научной и технической информации, 15.12.93, № 3078 – В95. Москва; 1993:10.
31. Krukovich M.G. Calculation of eutectic temperature and concentration in multicomponent systems. *Metallovedenie i termicheskaya obrabotka metallov*. 2005;(10):9–17. (In Russ.).
Крукович М.Г. Расчет эвтектических концентраций и температуры в двух- и многокомпонентных системах. *Металловедение и термическая обработка металлов*. 2005;(10):9–17.
32. Ganiev A.A., Khalikov A.R., Kabirov R.R. The development of calculation methods of concentrations and state diagram temperatures. *Mashinostroyeniye. Metallovedenie i termicheskaya obrabotka metallov. Vestnik Ufmskogo gosudarstvennogo aviationsionnogo universiteta*. 2008;11(2):116–122. (In Russ.).
Ганиев А.А., Халиков А.Р., Кабиров Р.Р. Разработка методики расчета эвтектических концентраций и температур диаграмм состояния. *Машиностроение. Металловедение и термическая обработка металлов. Вестник Уфимского государственного авиационного университета*. 2008;11(2):116–122.
33. Khalikov A.R. Modelling of eutectic concentrations of multicomponent constitution diagrams. *Mashinostroyeniye. Vestnik Ufmskogo gosudarstvennogo aviationsionnogo universiteta*. 2010;14(2):188–194. (In Russ.).
Халиков А.Р. Моделирование эвтектических концентраций многокомпонентных диаграмм состояния. *Машиностроение. Вестник Уфимского государственного авиационного университета*. 2010;14(2):188–194.
34. Egorova G.F., Afanas'eva O.S., Kaidalova L.V. Calculation of the composition and temperatures of peritectics of two-component systems using known melting temperatures. In: *Mathematical Modeling and Boundary Value Problems. Materials of the XI All-Russ. Sci. Conf. (May 27–30, 2019, Samara, Russian Federation). Vol. 1. Samara: SamSTU; 2019*:264–270. (In Russ.).
Егорова Г.Ф., Афанасьева О.С., Кайдалова Л.В. Расчет состава и температур перитектик двухкомпонентных систем по известным температурам плавления. В кн.: *Математическое моделирование и краевые задачи. Материалы XI Всероссийской научной конференции (27–30 мая 2019 г., Самара, РФ). Т. 1. Самара: СамГТУ; 2019*:264–270.
35. Amuda M.O.H., Akabekwa R.O. Estimating the eutectic composition of simple binary alloy system using linear geometry. *Leonardo Journal of Sciences*. 2008;12:232–242.
36. Krukovich M.G., Prusakov B.A., Sizov I.G. Plasticity of Boronized Layers. Moscow: FIZMATLIT; 2010:384. (In Russ.).
Крукович М.Г., Прусаков Б.А., Сизов И.Г. Пластичность борированных слоев. Москва: ФИЗМАТЛИТ; 2010:384.
37. Krukovich M.G. Technology to improve the performance properties of heterogeneous boronized layers. *Materials Performance and Characterization*. 2020;9(3):329–338.
<https://doi.org/10.1520/MPC20190091>
38. Krukovich M.G., Baderko E.A., Kazakevich G.A. Modeling the patterns of growth of borated layers when heated by high-frequency current. In: *New Materials and Technologies in Mechanical Engineering: Proceedings. 2023*;38:41–45. (In Russ.).
Крукович М.Г., Бадерко Е.А., Казакевич Г.А. Моделирование закономерностей роста борированных слоев при нагреве ТВЧ. *Новые материалы и технологии в машиностроении: Сборник трудов*. 2023;38:41–45.
39. Pradelli G., Gianoglio C. Equilibri allo stato solido nel sistema cromo-manganese-boro. *La Metallurgia Italiana*. 1976;68(4):191–194. (In It.).
40. Krukovich M.G. Computation of eutectic concentrations and temperature in two-component and multicomponent systems. *Metal Science and Heat Treatment*. 2005;47:447–454.
<https://doi.org/10.1007/s11041-006-0009-y>

Information about the Authors

Сведения об авторах

Grigori A. Kazakevich, Postgraduate of the Chair “Technology of Transport Engineering and Repair of Rolling Stock”, Russian University of Transport

ORCID: 0009-0007-1542-979X

E-mail: KazakevichG@mail.ru

Aleksei Yu. Popov, Cand. Sci. (Eng.), Assist. Prof. of the Chair “Technology of Transport Engineering and Repair of Rolling Stock”, Russian University of Transport

ORCID: 0000-0002-3397-9484

E-mail: madrat@inbox.ru

Григорий Алексеевич Казакевич, аспирант кафедры «Технология транспортного машиностроения и ремонта подвижного состава», Российский университет транспорта

ORCID: 0009-0007-1542-979X

E-mail: KazakevichG@mail.ru

Алексей Юрьевич Попов, к.т.н., доцент кафедры «Технология транспортного машиностроения и ремонта подвижного состава», Российский университет транспорта

ORCID: 0000-0002-3397-9484

E-mail: madrat@inbox.ru

Received 09.07.2024

Revised 02.09.2024

Accepted 29.10.2024

Поступила в редакцию 09.07.2024

После доработки 02.09.2024

Принята к публикации 29.10.2024



UDC 669.046.58

DOI 10.17073/0368-0797-2025-1-76-83



Original article

Оригинальная статья

DEVELOPMENT OF RESEARCH ON THE PHYSICO-CHEMICAL PROPERTIES
OF OXIDE AND METAL MELTSO. Yu. Sheshukov^{1, 2}, V. N. Nevidimov¹, I. V. Nekrasov¹,
A. A. Metelkin¹, V. S. Tsepelev¹¹ Ural Federal University named after the first President of Russia B.N. Yeltsin (19 Mira Str., Yekaterinburg 620002, Russian Federation)² Institute of Metallurgy, Ural Branch of the Russian Academy of Sciences (101 Amundsena Str., Yekaterinburg 620016, Russian Federation)

✉ o.j.sheshukov@urfu.ru

Abstract. The paper considers the historical development of scientific views on the structure of oxide and metal melts. The authors, using the research of the Ural Scientific School and their own works as examples, examine the evolution of approaches based on the polymer (ionic) theory of oxide melts and the cluster theory of liquid metals. The possibility of using a polymer model to determine the boundary of slag transition from a homogeneous state to a heterogeneous one and conditions for the formation of a homogeneous slag with maximum refining properties is shown. Al_2O_3 can exhibit both basic and acidic properties. It was found that with Al_2O_3 content of up to 16 % in oxide melts corresponding to the slags formed in ladle furnace unit, alumina exhibits basic properties, and when its content exceeds more than 16 %, it begins to exhibit acidic properties. Additional information on activities of the oxide melt components allows us to determine the parameters of the slag with the best properties for non-metallic inclusions absorption. Metal melt is characterized by a “critical” temperature at which the melt during heating transitions from hereditary cluster-type disequilibrium to a state of thermodynamic equilibrium, i.e., the melt “homogenizes”. Nonequilibrium melts temporarily retain elements of the structures of the initial phases. Overheating of the metal above the “critical” temperature during thermal-time treatment makes it possible to improve and stabilize the quality of products. Modification of the melt leads to a significant decrease in the amount of necessary overheating and acceleration of the homogeneous melt formation. Fundamental studies of the properties and structure of metal liquids showed the development of a new applied direction under the general name “thermal-time treatment”.

Keywords: polymer model, oxide melt, refining properties, cluster, liquid metal, thermal-time treatment

For citation: Sheshukov O.Yu., Nevidimov V.N., Nekrasov I.V., Metelkin A.A., Tsepelev V.S. Development of research on the physico-chemical properties of oxide and metal melts. *Izvestiya. Ferrous Metallurgy*. 2025;68(1):76–83. <https://doi.org/10.17073/0368-0797-2025-1-76-83>

РАЗВИТИЕ ИССЛЕДОВАНИЙ ФИЗИКО-ХИМИЧЕСКИХ СВОЙСТВ
ОКСИДНЫХ И МЕТАЛЛИЧЕСКИХ РАСПЛАВОВО. Ю. Шешуков^{1, 2}, В. Н. Невидимов¹, И. В. Некрасов¹,
А. А. Метелкин¹, В. С. Цепелев¹¹ Уральский федеральный университет имени первого Президента России Б.Н. Ельцина (Россия, 620002, Екатеринбург, ул. Мира, 19)² Институт металлургии Уральского отделения РАН (Россия, 620016, Екатеринбург, ул. Амундсена, 101)

✉ o.j.sheshukov@urfu.ru

Аннотация. В работе сделана попытка анализа исторического развития научных взглядов на строение оксидных и металлических расплавов. Авторы на примере работ Уральской научной школы и собственных исследований рассматривают эволюцию подходов на основе полимерной (ионной) теории оксидных расплавов и кластерной теории жидких металлов. Показана возможность применения полимерной модели для определения границы перехода шлака из гомогенного состояния в гетерогенное и условий формирования гомогенного шлака, обладающего максимальными рафинирующими свойствами. В рассматриваемых условиях оксид Al_2O_3 может проявлять как основные, так и кислотные свойства. При содержании Al_2O_3 до 16 % в оксидных расплавах, соответствующих шлакам, формируемым в агрегате ковш – печь, глинозем проявляет основные свойства, а при содержании более 16 % он начинает проявлять кислотные свойства. Дополни-

тельно информация об активностях компонентов оксидного расплава позволяет определить параметры шлака, обладающего оптимальными свойствами для поглощения неметаллических включений. Металлический расплав характеризуется «критической» температурой, при которой он в ходе нагрева переходит от наследственной неравновесности кластерного типа в состояние термодинамического равновесия, т.е. происходит гомогенизация расплава. Неравновесные расплавы временно сохраняют в себе элементы структур исходных фаз. Перегрев металла выше «критической» температуры в ходе термовременной обработки позволяет добиться повышения и стабилизации качества продукции. Модифицирование расплава приводит к существенному снижению необходимого перегрева и ускорению процесса формирования гомогенного расплава. На примере исследования свойств и строения металлических жидкостей показано развитие нового прикладного направления под общим названием «термовременная обработка».

Ключевые слова: полимерная модель, оксидный расплав, рафинирующие свойства, кластер, жидкий металл, термовременная обработка

Для цитирования: Шешуков О.Ю., Невидимов В.Н., Некрасов И.В., Метелкин А.А., Цепелев В.С. Развитие исследований физико-химических свойств оксидных и металлических расплавов. *Известия вузов. Черная металлургия*. 2025;68(1):76–83.

<https://doi.org/10.17073/0368-0797-2025-1-76-83>

INTRODUCTION

The ongoing advancement of steelmaking processes remains a pressing necessity. However, the development of new, more efficient technologies is only possible through a thorough analysis of experimental data and a deep understanding of their physico-chemical nature. Further progress in various scientific schools and research directions must be based on refining the theoretical foundations of metallurgical processes.

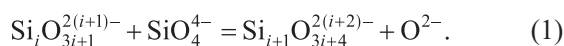
Metallurgical enterprises and research centers in the Ural region have traditionally played a key role in the development of the country's industrial sectors. This study aims to analyze the historical development of research on the physico-chemical properties of oxide and metal melts.

RESEARCH MATERIALS AND METHODS

The structure of oxide melts, which form the basis of steelmaking slags, can be studied both through experimental methods and by evaluating the practical applicability of different theoretical models. When considering existing models of slag melt structure, we believe particular attention should be given to the polymer model.

The idea that oxide melts exhibit polymeric behavior was first proposed by Professor O.A. Esin in 1946 [1]. Based on the ionic nature of these melts, Esin suggested that oxide melts contain silicate-oxygen anions of varying complexity, which are in chemical equilibrium with each other and with “free” oxygen ions.

In general, this equilibrium can be expressed as



Over time, this assumption became the foundation for various polymer models of silicate melts. Some models (non-structural) do not explicitly account for the structure of anions, whereas others (structural) focus primarily on the arrangement of complex anions.

Pioneering studies in this field were conducted by G.V Toop and C.S. Samis in 1962 [2], as well as

by C.R. Masson in 1965 [3]. Within the framework of the non-structural model, they were the first to provide a quantitative assessment of the distribution of “free”, terminal, and bridging oxygen atoms in binary silicate melts and formulated the equilibrium constant for the polymerization reaction (1) as follows:

$$K_p = \frac{n_{\text{O}^{2-}} n_{\text{O}^0}}{n_{\text{O}^-}^2}, \quad (2)$$

where $n_{\text{O}^{2-}}$, n_{O^-} and n_{O^0} represent the number of moles of O^{2-} , O^- and O^0 , per mole of binary silicate melt.

In studies [3 – 6], a structural model was proposed. This model assumes that, in addition to Me^{n+} cations, “free” O^{2-} oxygen ions, and monomers SiO_4^{4-} the binary silicate melt contains only chain-like anions of type $\text{Si}_i\text{O}_{3i+1}^{2(i+1)-}$, which may be either linear or branched. The formation of ring and network structures is excluded, meaning that the model applies to binary silicate melt compositions in the $\text{MeO}-\text{SiO}_2$ system within the range $0 \leq x_{\text{SiO}_2} \leq 0.5$.

The approach of C.R. Masson, I.B. Smith, and S.G. Whiteway was examined across the entire composition range in studies [7; 8] and compared with previous research [4 – 6]. The developed mathematical framework demonstrated strong convergence between calculated and experimental data throughout the investigated composition range.

A considerable number of studies in the literature have focused on extending polymer models of binary silicate melts to multicomponent systems. For example, in [9], the model equations were generalized for ternary systems $\text{Me}'\text{O}-\text{Me}''\text{O}-\text{SiO}_2$, with the assumption that Me'^{n+} and Me''^{n+} cations are randomly distributed and that the degree of melt polymerization is a function of the polymerization constants in binary silicate melts.

Alongside the development of theoretical models describing the structure of silicate melts, experimental studies have been conducted using modern physico-chemical methods.

The application of the analytical method of trimethylsilylation in combination with gas chromatography [10] and paper chromatography [11], as well as ultrasonic investigations [12], confirms the presence of both complex silicate-oxygen structures $(\text{SiO}_2)_i$, which represent the ultimate form of complex anions $\text{Si}_i\text{O}_{3i+1-c}^{2(i+1-c)-}$ (with a self-closing number $c = 1$ for planar rings), and only the simplest silicate anions: monomers SiO_4^{4-} , short linear chains $\text{Si}_2\text{O}_7^{6-}$ and $\text{Si}_3\text{O}_{10}^{8-}$, as well as planar rings.

It is important to note that no isomeric forms of anions, such as branched chains, have been identified in crystalline, glassy, or liquid silicates.

The findings from these studies contributed to the development of a refined version of the polymer model that accounts for the variable functionality of the monomer [13]. According to this model, the monomer SiO_4^{4-} is bifunctional ($f = 2$) in chain-like anions, meaning that only two of the four terminal oxygen atoms in the silicate-oxygen tetrahedron participate in reactions. In cyclic ions, however, the monomer SiO_4^{4-} is tetrafunctional ($f = 4$). The polymer model suggests that the average functionality of the monomer varies from two (in a fully depolymerized melt) to four (in pure SiO_2), increasing progressively as the degree of polymerization rises. Based on this model, equations were derived to quantitatively describe the structural units and component activities in binary silicate melts. These equations were further applied to develop a theoretical framework for calculating the activity of multicomponent oxide melts containing different complex-forming elements.

In steelmaking, the theory of oxide melts is widely used to evaluate the refining properties of slags, the for-

mation of slag crust, and the generation of oxide-based non-metallic inclusions (NMI).

One example of this application is the use of the polymer model to analyze the characteristics of slag melts used in ladle treatment of steel and the formation of oxide-based NMI. To understand how the chemical composition of slag melts (wt. %) influences the thermodynamic activity of components, the melt with a fixed content of magnesium and silicon oxides (11.11 % MgO; 16.67 % SiO_2) was studied, where a portion of lime was replaced with an alumina-based flux. The content of CaO varied from 33.33 to 55.56 %, while Al_2O_3 ranged from 16.76 to 38.89 %, meaning that CaO was progressively substituted with Al_2O_3 .

Using the polymer model, it is possible to calculate the activity of CaO and MgO in the melt, as well as their saturation activity (saturation limits) depending on the CaO/ Al_2O_3 ratio (Fig. 1).

These data on the activity of CaO and MgO oxides are particularly important for analyzing the refining properties of slags [14] and understanding the mechanisms behind the formation of calcium- and magnesium-containing aluminate NMI in steel [15].

A significant increase in CaO concentration causes basic oxides to transition into the solid phase. Thus, the polymer model helps determine the boundary at which slags shift from a homogeneous to a heterogeneous state, ensuring the formation of exclusively homogeneous slags (Fig. 1) with maximum desulfurization capacity and an enhanced ability to absorb NMI.

While the behavior of CaO, MgO, and SiO_2 oxides is well understood, as they act as basic and acidic components, Al_2O_3 is an amphoteric compound that can exhibit both basic and acidic properties. It has been established that in oxide melts – corresponding to slags formed in ladle furnace units and secondary steel refining systems – alumina exhibits basic properties when its content does not exceed 16 %. However, once its concentration surpasses 16 %, it begins to display acidic characteristics [16].

Information on activity values allows for the determination of the parameters of slag melts with the highest capacity for NMI absorption. In particular, the activity values of Al_2O_3 and SiO_2 play a key role in evaluating the slag's ability to absorb and dissolve aluminate and silicate NMIs. Based on the model describing the transfer of NMIs into slag [17], it can be concluded that the dissolution of NMIs in slag is a critical stage in the steel refining process. To analyze this process, the approach, that traditionally employed to describe the dissolution of refractory particles in slag, is applicable [18]:

$$Q = \frac{D}{\Delta} S(C_{\text{sat}} - C), \quad (3)$$

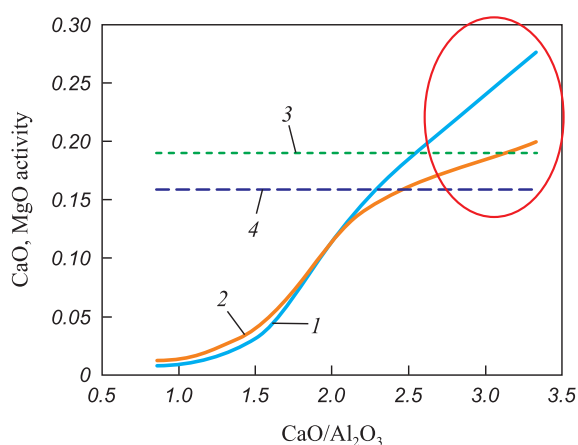


Fig. 1. Activities of CaO and MgO oxides in the melt for slag formation and their saturation activities depending on CaO/ Al_2O_3 ratio:

1 – activity of CaO; 2 – activity of MgO;

3 – saturation activity of CaO; 4 – saturation activity of MgO

Рис. 1. Активности оксидов CaO и MgO в расплаве

для шлакообразования, а также их активности насыщения

в зависимости от отношения CaO/ Al_2O_3 :

1 – активность CaO; 2 – активность MgO;

3 – активность насыщения CaO; 4 – активность насыщения MgO

where Q is the dissolution rate of the solid phase (refractory material or NMI) in the slag, D is the diffusion coefficient of the solid-phase material in the slag, S is the contact area between the solid phase and the slag, Δ is the thickness of the diffusion layer, C_{sat} is the saturation concentration of the slag with the solid-phase material, C is the current concentration of the solid-phase material in the slag.

If the parameters D and Δ in equation (3) are expressed in terms of their known dependencies on slag viscosity, it becomes possible to determine the dissolution rate of non-metallic inclusions

$$Q \sim \frac{C_{\text{sat}} - C}{\left(\frac{\eta}{\rho}\right)^{\frac{5}{6}}}. \quad (4)$$

Al_2O_3 and SiO_2 oxides are the largest and least mobile components of the slag, forming the primary physical mass of silicate and/or aluminate NMI. As a result, these components are expected to control the flow behavior, diffusion mechanism, and dissolution processes of the slag components. The slag's saturation with NMI material should be assessed based on its proximity to saturation with SiO_2 and Al_2O_3 . The corresponding calculated data are presented in Fig. 2.

A comparison of the calculated data suggests that the method of oxide melt formation plays a decisive role in determining its characteristics. This conclusion helps explain the discrepancies observed in practical recommendations regarding the optimal slag composition and the type of deoxidizers used to achieve the desired steel purity [18; 19].

Possible applications of experimental data in research on the ionic theory of slags include determining optimal slag compositions with optimal parameters, such as maximum sulfide capacity and enhanced ability to absorb non-metallic inclusions, as well as identifying the optimal slag compositions at various stages of the steelmaking process.

One of the key research areas developed by the Ural Scientific School is the study of the characteristics of metal melts. This research has been actively pursued since the 1950s at the Ural Polytechnic Institute named after S.M. Kirov, within the Department of Physics under the leadership of Pavel Vladimirovich Geld [20; 21].

According to modern concepts, the liquid state of matter occupies an intermediate position between the crystalline and gaseous states on the temperature scale. From a metallurgical perspective, this task is somewhat simplified, as the liquid state of metals is typically considered within the temperature range from the melting point T_m to approximately $1.25T_m$. This range is close to the melting and crystallization points and is often referred to as

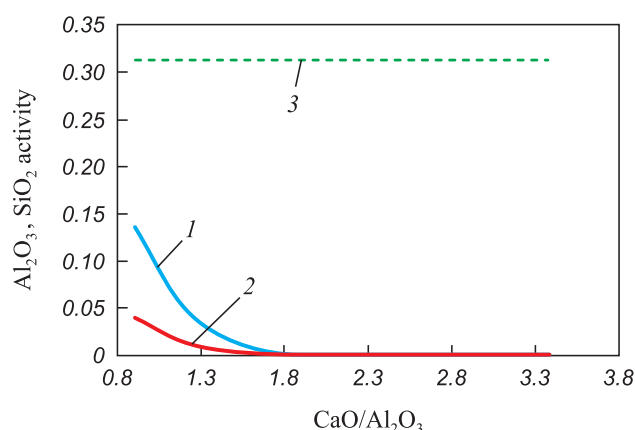


Fig. 2. Activities of Al_2O_3 and SiO_2 oxides in the melt for slag formation and saturation activity of Al_2O_3 (saturation activity of SiO_2 was not detected due to a high value of ~ 0.99) depending on $\text{CaO}/\text{Al}_2\text{O}_3$ ratio: 1 – activity of Al_2O_3 ; 2 – activity of SiO_2 ; 3 – saturation activity of Al_2O_3

Рис. 2. Активности оксидов Al_2O_3 и SiO_2 в расплаве при шлакообразовании, активность насыщения Al_2O_3 (активность насыщения SiO_2 не отображена из-за высокого значения ~ 0.99) в зависимости от отношения $\text{CaO}/\text{Al}_2\text{O}_3$: 1 – активность Al_2O_3 ; 2 – активность SiO_2 ; 3 – активность насыщения Al_2O_3

the melt. Both the crystalline and liquid states are condensed phases in which interatomic attractive forces play a dominant role, unlike in the gaseous phase. By definition, the gas phase is characterized by chaos, the condensed phase – by order, in crystals it is distant, and in the melt it is near.

Experimental data were confirmed through studies of the fundamental properties of metal melts, such as density and electrical resistivity, using differential thermal analysis and X-ray analysis [21; 22]. The results indicate that the decrease in density upon melting of normal and transition metals ranges from 1 to 3 %, primarily due to the formation of “voids” and cavities within the structure. X-ray studies conducted by E.Z. Spektor and A.V. Romanova, later supported by other researchers, demonstrated that during melting, the most probable nearest interatomic distances do not increase – in fact, they may even decrease (including in iron). This suggests that attractive forces cause the atoms of the melt to cluster into aggregates or sibotaxies, with free volume distributed between clusters, containing individual atoms of the heated melt.

To refine this concept further, clusters can be understood as structures formed by the specific attractive forces characteristic of a given type of atom. As a result, each cluster retains a distinctive structure similar to that of its precursor, the crystal. Meanwhile, interatomic interactions and the intensity of thermal motion increase by a factor of $K\Delta T$, where $K = 1.38 \cdot 10^{-23}$ J/K, and ΔT is the absolute temperature increment. It is evident that

quasi-crystalline order within a cluster becomes blurred due to thermal motion, particularly at boundaries where cavities and free volume are present. Consequently, clusters lack sharply defined boundaries, gradually transitioning into a disordered zone, the proportion of which increases with temperature and becomes significant at temperatures above $1.5T_m$.

As a result, the transition from a pure metal to a multi-component melt further complicates its structure. Various interactions within the cluster – metallic, covalent, resonant, or other specific types of bonding – determine its internal arrangement and stability over time. Indirect insights into these and other characteristics can be obtained through physico-chemical analysis methods, particularly by studying the temperature and concentration dependencies of the physical properties of melts.

One of the most significant findings is that a melt, even if it matches the specified chemical composition, is not always ready for casting. Over time, dangerous defects may appear in finished products made from such a melt, including rails, pipes, and machine components, ultimately leading to structural failure. This thermodynamic system is far from equilibrium, and the influence of inherited phase components from the charge material is quite pronounced. These components transfer their numerous local atomic arrangements, as well as chemical and physical microinhomogeneities, to the melt. Convective mixing and bubbling caused by rising carbon monoxide or argon gas bubbles can only partially equalize these inhomogeneities on a microscopic level. The most effective way to eliminate inherited non-equilibrium atomic groupings is to heat the melt to its critical temperature (t_c), at which the average thermal energy of a particle becomes comparable to the activation energy required for it to break away from its parent associate.

According to the obtained data, the term “critical temperature” (t_c) is used to designate specific points on the temperature scale at which a system transitions into a single-phase equilibrium state. These include the critical temperature of equilibrium coexistence between liquid and vapor, the critical temperature of mutual unlimited solubility in liquid mixtures, and the critical temperature associated with the loss of superconductivity or superfluidity.

It is believed that t_c represents the temperature at which a melt, upon heating, transitions from a hereditary cluster-type nonequilibrium state into a thermodynamically equilibrium state. However, if a melt transitions from a multiphase state (such as a suspension or emulsion) to a single-phase state, the term “melt homogenization” is more appropriate than t_c .

A reliable and convenient instrumental method for determining t_c is based on melt viscometry. This approach involves detecting discrepancies in viscosity values

between heating and cooling cycles (Fig. 3). Such discrepancies appear only at a certain overheating level above the liquidus temperature [21]. The position of the reverse viscosity curve (obtained during cooling) depends on the relationship between the maximum heating temperature of the studied metal sample and the temperature at which polytherm branching begins. If the maximum heating temperature does not reach the anomaly temperature, hysteresis (branching) does not occur; it only manifests when t_c is exceeded.

Hysteresis in melt properties reflects hysteresis in its structure. This is why comprehensive studies of melt properties provide insights into its structure, and the obtained results remain independent of the sample volume, as the observed processes occur at a kinetic scale on the microlevel. The value of t_c depends on the steel grade, the phase composition of the charge, and the melting conditions. Heating the melt to t_c is a method of bringing the system into equilibrium. However, excessive overheating beyond t_c can be technologically more detrimental than underheating, as it significantly increases gas saturation in the metal and intensifies interactions with the refractory lining, among other effects.

Thus, nonequilibrium melts temporarily retain structural elements of their initial phases. In contrast, the structure and properties of equilibrium, and therefore maximally homogeneous, systems are determined not by their history but by their chemical composition and

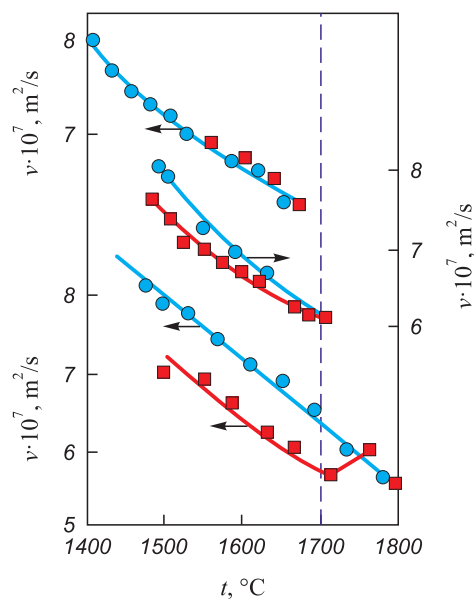


Fig. 3. Viscosity of Fe – 30 % Ni melt depending on the maximum heating temperature of its sample during the experiment:
● – during heating; ■ – during cooling;
dashed line – temperature t_c

Рис. 3. Вязкость расплава Fe – 30 % Ni в зависимости от максимальной температуры нагрева его образца во время опыта:
● – во время нагрева; ■ – во время охлаждения;
штриховая линия – температура t_c

temperature. Casting an equilibrium melt ensures a stable crystallization process from one heat to another, resulting in optimal ingot and casting structures and consistently high product quality [21].

Fundamental studies on the properties and structure of liquid metals have led to the emergence of a new applied field – technologies for transitioning multicomponent metal melts into an equilibrium state to improve and stabilize product quality. This approach has become known as “thermal-time treatment” [21].

Further research in this field has demonstrated the possibility of improving classical thermal-time treatment. It has been established that the required overheating can be significantly reduced, and the formation of a micro-homogeneous melt can be accelerated through modification. For example, introducing an optimal amount of a calcium-containing modifier into steel has been shown to lower t_c from 1780 – 1800 to 1630 – 1640 °C, making it technologically achievable (Fig. 4).

These findings have significant industrial implications, enabling the development of technological solutions for controlling the properties of steel in both its liquid and solid states.

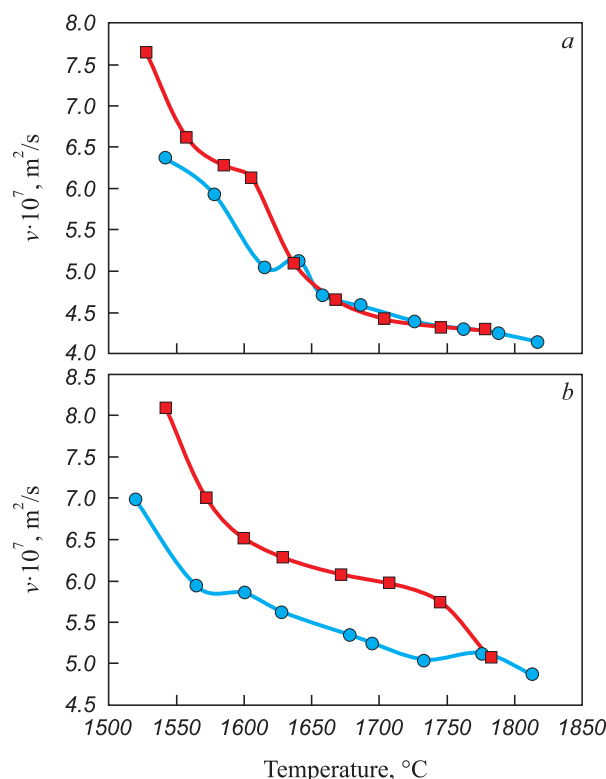


Fig. 4. Polytherms of kinematic viscosity of the melt of 20tr steel: *a* – with SK15A7 treatment; *b* – without treatment; ● – heating; ■ – cooling

Рис. 4. Политермы кинематической вязкости расплава стали марки 20тр: *a* – с обработкой СК15А7; *b* – без обработки; ● – нагрев; ■ – охлаждение

CONCLUSION

Building on the work of the Ural Scientific School and the authors' own research, an attempt has been made to analyze the historical development of scientific concepts regarding the structure of oxides and molten iron. The study explores the emergence of methods based on the polymer (ionic) theory of oxide dissolution and the theory of liquid-metal clusters. The potential applications of the polymer model for determining the transition boundary of slag from a homogeneous to a heterogeneous state and the conditions for forming a homogeneous slag with high refining properties are also presented. The research confirms that under ideal conditions, Al_2O_3 oxide can exhibit both basic and acidic properties. When its concentration in an oxide melt reaches 16 %, alumina acts as a basic component. However, when its content exceeds 16 %, it begins to exhibit acidic properties.

REFERENCES / СПИСОК ЛИТЕРАТУРЫ

1. Esin O.A. The Electrolytic Nature of Liquid Slags. Sverdlovsk: Ural Industrial Institute; 1946:41. (In Russ.).
Есин О.А. Электролитическая природа жидких шлаков. Свердловск: Уральский индустриальный институт; 1946:41.
2. Toop G.V., Samis C.S. Activities of ions in silicate melts. *Transactions of Metallurgical Society AIME*. 1962;224(5): 878–887.
3. Masson C.R. An approach to the problem of ionic distribution in liquid silicates. *Proceedings of the Royal Society A*. 1965;287(1409):201–221.
<https://doi.org/10.1098/rspa.1965.0176>
4. Whiteway S.G., Smith I.B., Masson C.R. Theory of molecular size distribution in multichain polymers. *Canadian Journal of Chemistry*. 1970;48(1):33–45.
<https://doi.org/10.1139/v70-006>
5. Masson C.R., Smith I.B., Whiteway S.G. Molecular size distribution in multichain polymers: application of polymer theory to silicate melts. *Canadian Journal of Chemistry*. 1970;48(1):201–202. <http://doi.org/10.1139/v70-033>
6. Masson C.R., Smith I.B., Whiteway S.G. Activities and ionic distribution in liquid silicates: application of polymer theory. *Canadian Journal of Chemistry*. 1970;48(9):1456–1464.
<https://doi.org/10.1139/v70-238>
7. Esin O.A. Application of polymer theory to molten slags. In: *Physico-Chemical Studies of Metallurgical Processes: Interuniversity Proceedings*. Sverdlovsk: UPI; 1973;1:5–17. (In Russ.).
Есин О.А. Применение теории полимеров к расплавленному шлаку. В кн.: *Физико-химические исследования металлургических процессов: Межвуз. сб.* Свердловск: УПИ; 1973;1:5–17.
8. Esin O.A. On application of a polymer model, taking into account isomeric forms, to molten silicates. In: *Physico-Chemical Studies of Metallurgical Processes: Interuniversity Proceedings*. Sverdlovsk: UPI; 1976;4:17–27. (In Russ.).
Есин О.А. О применении полимерной модели, учитывающей изомерные формы, к расплавленным силика-

- там. В кн.: *Физико-химические исследования металлургических процессов: Межвуз. сб.* Свердловск: УПИ; 1976;4:17–27.
9. Yokokawa T., Niwa K. Free energy and basicity of molten silicate solution. *Transactions of the Japan Institute of Metals*. 1969;10(2):81–84.
<https://doi.org/10.2320/matertrans1960.10.81>
 10. Smart R.M., Glasser F.P. Silicate anion constitution of lead silicate glasses and crystals. *Physics and Chemistry of Glasses*. 1978;19(5):95–102.
 11. Wiekert W., Hoeßel D., Götz J. Die Anionenverteilung in Silikatgläsern und ihre Bedeutung für die Glasbildung. *Wissenschaftliche Zeitschrift Friedrich-Schiller-Universität*. 1979;28(2-3):277–285. (In Germ.)
 12. Baidov V.V. Ultraacoustic studies and microstructure of silicate melts. In: *Properties and Structure of Slag Melts*. Moscow: Nauka; 1970:23–38. (In Russ.).
Байдов В.В. Ультразвуковые исследования и микроструктура силикатных расплавов. В кн.: *Свойства и структура шлаковых расплавов*. Москва: Наука; 1970:23–38.
 13. Novikov V.K., Nevidimov V.N. Polymeric Nature of Molten Slags. Yekaterinburg: USTU–UPI; 2006:62. (In Russ.).
Новиков В.К., Невидимов В.Н. Полимерная природа расплавленных шлаков. Екатеринбург: УГТУ–УПИ; 2006:62.
 14. Sheshukov O.Yu., Nekrasov I.V., Metelkin A.A., Lozovaya E.Yu., Shevchenko O.I., Savel'ev M.V. Modern Steel: Theory and Technology. Yekaterinburg: UrFU; 2020:400. (In Russ.).
Шешуков О.Ю., Некрасов И.В., Метелкин А.А., Лозовая Е.Ю., Шевченко О.И., Савельев М.В. Современная сталь: теория и технология. Екатеринбург: Изд-во УрФУ; 2020:400.
 15. Khoroshilov A.D. Analysis and development of technology for ladle processing of ultra-low carbon steels in order to improve the surface quality of rolled steel. Extended abstract of Cand. Sci. Diss. Moscow; 2022:19. (In Russ.).
Хорошилов А.Д. Анализ и разработка технологии ковшевой обработки сверхнизкоуглеродистых сталей с целью повышения качества поверхности автолитового проката: автореф. дисс. канд. техн. наук. Москва; 2022:19.
 16. Sheshukov O.Yu., Mikheenkova M.A., Nekrasov I.V., Egiazar'yan D.K., Metelkin A.A., Shevchenko O.I. Issues of Utilization of Refining Slags of Steelmaking Production. Nizhny Tagil: NTI (Branch) UrFU; 2017:208. (In Russ.).
Шешуков О.Ю., Михеенков М.А., Некрасов И.В., Егизарьян Д.К., Метелкин А.А., Шевченко О.И. Вопросы утилизации рафинировочных шлаков сталеплавильного производства. Нижний Тагил: НТИ (филиал) УрФУ; 2017:208.
 17. Deryabin V.A., Deryabin A.A. Thermodynamic features of transition of solid nonmetallic inclusions from metal to slag. *Izvestiya. Ferrous Metallurgy*. 1990;33(10):8–9. (In Russ.).
Дерябин В.А., Дерябин А.А. Термодинамические особенности перехода твердых неметаллических включений из металла в шлак. *Известия вузов. Черная металлургия*. 1990;33(10):8–9.
 18. Nekrasov I.V., Sheshukov O.Yu., Nevidimov V.N., etc. Assessment of slag aggressiveness to non-metallic inclusions. In: *Structure and Properties of Metal and Slag Melts. Proceedings of the XIII Russ. Conf.* Yekaterinburg: UB RAS; 2011:16–19. (In Russ.).
Некрасов И.В., Шешуков О.Ю., Невидимов В.Н. и др. Оценка агрессивности шлака к неметаллическим включениям. В кн.: *Строение и свойства металлических и шлаковых расплавов. Труды XIII российской конференции*. Екатеринбург: Изд-во УрО РАН; 2011:16–19.
 19. Sheshukov O.Yu., Nekrasov I.V., Mikheenkova M.A., Egiazar'yan D.K., Ermakova V.P., Smirnova V.G., Chashchin A.A., Kalimullin E.V. Slag mode of a ladle furnace unit and modification efficiency. *Ferrous Metallurgy. Bulletin of Scientific, Technical and Economic Information*. 2015;(9(1389)):38–43. (In Russ.).
Шешуков О.Ю., Некрасов И.В., Михеенков М.А., Егизарьян Д.К., Ермакова В.П., Смирнова В.Г., Чашчин А.А., Калимуллин Э.В. Шлаковый режим УКП и эффективность модифицирования. *Черная металлургия. Бюллетень научно-технической и экономической информации*. 2015;(9(1389)):38–43.
 20. Sheshukov O.Yu., Nekrasov I.V., Bonar' S.N., Egiazar'yan D.K., Tsymbalist M.M., Sivtsov A.V. Sulfide capacity of alumina slags of ladle-furnace steel treatment and activity of oxygen anions. *Ferrous Metallurgy. Bulletin of Scientific, Technical and Economic Information*. 2017;(2(1406)):30–33. (In Russ.).
Шешуков О.Ю., Некрасов И.В., Бонарь С.Н., Егизарьян Д.К., Цымбалист М.М., Сивцов А.В. Сульфидная емкость глиноземистых шлаков внепечной обработки стали и активность анионов кислорода. *Черная металлургия. Бюллетень научно-технической и экономической информации*. 2017;(2(1406)):30–33.
 21. Gel'd P.V., Baum B.A., Petrushevskii M.S. Ferroalloy Melts as Liquid Alloys of Transition Metals with Silicon and Carbon. Moscow: Metallurgiya; 1973:288. (In Russ.).
Гельд П.В., Баум Б.А., Петрушевский М.С. Расплавы ферросплавного производства – жидкие сплавы переходных металлов с кремнием и углеродом. Москва: Металлургия; 1973:288.
 22. Baum B.A., Khasin G.A., Tyagunov G.V., etc. Liquid Steel. Moscow: Metallurgiya; 1984:208. (In Russ.).
Баум Б.А., Хасин Г.А., Тягунов Г.В. и др. Жидкая сталь. Москва: Металлургия; 1984:208.
 23. Sheshukov O.Yu., Nekrasov I.V., Ermakova V.P., Marshuk L.A., Egiazar'yan D.K., Lapin M.V., Shamanov A.N., Kovrizhnykh A.V., Akchibash A.O., Shvedov D.P., Tokarev A.S. Method of ladle-furnace treatment of steel with calcium. Pat. RF 2535428 C1. *Byulleten' izobretenii*. 2014;12. (In Russ.).
Пат. RU 2535428 C1. Способ внепечной обработки стали кальцием / О.Ю. Шешуков, И.В. Некрасов, В.П. Ермакова, Л.А. Маршук, Д.К. Егизарьян, М.В. Лапин, А.Н. Шаманов, А.В. Коврижных, А.О. Акчибаш, Д.П. Шведов, А.С. Токарев; заявл. 10.04.2013; опубл. 10.12.2014.
 24. Nekrasov I.V., Sheshukov O.Yu., Tsepelev V.S. Structure of iron melts and promising technologies. In: *Proceedings of Int. Sci. Conf. "Physico-Chemical Foundations*

of Metallurgical Processes” named after Academician A.M. Samarin. Vyksa: Vyksunskii metallurgicheskii zavod; 2022:131–135. (In Russ.).

Некрасов И.В., Шешуков О.Ю., Цепелев В.С. Структура расплавов железа и перспективные технологии. В кн.: Сборник трудов Международной научной конференции «Физико-химические основы металлургических процессов» имени академика А.М. Самарина. Выкса: АО «Выксунский металлургический завод»; 2022:131–135.

25. Sheshukov O.Yu., Nekrasov I.V., Konashkov V.V., Egiazar'yan D.K. Structure-sensitive properties of steel melt: Efficiency evaluation of steel treatment with modifiers and fining clinkers. *Elektrometallurgiya*. 2019;(2):2–12. (In Russ.).

Шешуков О.Ю., Некрасов И.В., Конашков В.В., Егизарьян Д.К. Структурно-чувствительные свойства расплава стали: оценка эффективности ее обработки модификаторами и рафинирующими шлаками. *Электromеталлургия*. 2019;(2):2–12.

Сведения об авторах

Information about the Authors

Олег Юрьевич Шешуков, д.т.н., профессор, директор Института новых материалов и технологий, Уральский федеральный университет имени первого Президента России Б.Н. Ельцина, главный научный сотрудник, Институт металлургии УрО РАН

ORCID: 0000-0002-2452-826X

E-mail: o.j.sheshukov@urfu.ru

Владимир Николаевич Невидимов, к.т.н., доцент кафедры теории металлургических процессов Института новых материалов и технологий, Уральский федеральный университет им. первого Президента России Б.Н. Ельцина

E-mail: v.n.nevidimov@urfu.ru

Илья Владимирович Некрасов, к.т.н., доцент кафедры металлургии железа и сплавов Института новых материалов и технологий, Уральский федеральный университет им. первого Президента России Б.Н. Ельцина

E-mail: ivn84@bk.ru

Анатолий Алексеевич Метелкин, д.т.н., доцент кафедры металлургии железа и сплавов, института новых материалов и технологий, Уральский федеральный университет им. первого Президента России Б.Н. Ельцина

E-mail: anatoliy82@list.ru

Владимир Степанович Цепелев, д.т.н., доцент, профессор кафедры безопасности жизнедеятельности в техносфере, директор Исследовательского центра физики металлических жидкостей, Уральский федеральный университет им. первого Президента России Б.Н. Ельцина

ORCID: 0000-0003-4195-9042

E-mail: v.s.tsepelev@urfu.ru

Oleg Yu. Sheshukov, Dr. Sci. (Eng.), Prof., Director of the Institute of New Materials and Technologies, Ural Federal University named after the first President of Russia B.N. Yeltsin, Chief Researcher, Institute of Metallurgy, Ural Branch of the Russian Academy of Sciences

ORCID: 0000-0002-2452-826X

E-mail: o.j.sheshukov@urfu.ru

Vladimir N. Nevidimov, Cand. Sci. (Eng.), Assist. Prof. of the Chair of Theory of Metallurgical Processes of the Institute of New Materials and Technologies, Ural Federal University named after the first President of Russia B.N. Yeltsin

E-mail: v.n.nevidimov@urfu.ru

Il'ya V. Nekrasov, Cand. Sci. (Eng.), Assist. Prof. of the Chair of Metallurgy of Iron and Alloys of the Institute of New Materials and Technologies, Ural Federal University named after the first President of Russia B.N. Yeltsin

E-mail: ivn84@bk.ru

Anatolii A. Metelkin, Dr. Sci. (Eng.), Assist. Prof. of the Chair of Metallurgy of Iron and Alloys of the Institute of New Materials and Technologies, Ural Federal University named after the first President of Russia B.N. Yeltsin

E-mail: anatoliy82@list.ru

Vladimir S. Tsepelev, Dr. Sci. (Eng.), Assist. Prof., Prof. of the Chair of Life Safety in the Technosphere, Director of the Research Center for Physics of Metallic Liquids, Ural Federal University named after the first President of Russia B.N. Yeltsin

ORCID: 0000-0003-4195-9042

E-mail: v.s.tsepelev@urfu.ru

Вклад авторов

Contribution of the Authors

О. Ю. Шешуков – постановка задачи исследований, корректировка и редактирование статьи.

В. Н. Невидимов – проведение лабораторных опытов, написание статьи.

И. В. Некрасов – постановка задачи исследований, проведение лабораторных опытов, написание статьи.

А. А. Метелкин – обсуждение полученных результатов, редактирование статьи.

В. С. Цепелев – постановка задачи исследований, корректировка и редактирование статьи.

O. Yu. Sheshukov – setting the research task, correcting and editing the article.

V. N. Nevidimov – conducting laboratory experiments, writing the article.

I. V. Nekrasov – setting the research task, conducting laboratory experiments, writing the article.

A. A. Metelkin – discussion of the results, editing the article.

V. S. Tsepelev – setting the research task, correcting and editing the article.

Поступила в редакцию 18.03.2024

После доработки 20.09.2024

Принята к публикации 25.12.2024

Received 18.03.2024

Revised 20.09.2024

Accepted 25.12.2024

ECONOMIC EFFICIENCY
OF METALLURGICAL PRODUCTION

ЭКОНОМИЧЕСКАЯ ЭФФЕКТИВНОСТЬ
МЕТАЛЛУРГИЧЕСКОГО ПРОИЗВОДСТВА



UDC 621.771:658.53

DOI 10.17073/0368-0797-2025-1-84-89



Short report

Краткое сообщение

DEVELOPMENT OF MODELS FOR FUNCTIONING OF DRAWING EQUIPMENT FOR MULTI-MILL SERVICING

A. R. Fastyskovskii¹, A. I. Musatova¹, N. V. Martyushev²

¹ Siberian State Industrial University (42 Kirova Str., Novokuznetsk, Kemerovo Region – Kuzbass 654007, Russian Federation)

² National Research Tomsk Polytechnic University (30 Lenina Ave., Tomsk 634050, Russian Federation)

✉ omd@sibsiu.ru

Abstract. The great demand for products of the drawing industry causes the need to increase the productivity of existing equipment. There are two ways to solve this issue: creation of new designs of drawing equipment and search for hidden organizational reserves. Increasing productivity through organizational measures requires less time and material costs for implementation. The paper considers the possibility and prospects of multi-mill servicing. Normative models of drawing equipment operation for multi-mill servicing were developed. The prospects of using the developed models are shown on the example of the existing production. Analysis of the drawing equipment operation made it possible to justify the processing modes for multi-mill servicing and thereby increase productivity by 1.35 times and reduce the cost of finished products by 2 %.

Keywords: drawing equipment, standard models, multi-mill servicing

For citation: Fastyskovskii A.R., Musatova A.I., Martyushev N.V. Development of models for functioning of drawing equipment for multi-mill servicing. *Izvestiya. Ferrous Metallurgy*. 2025;68(1):84–89. <https://doi.org/10.17073/0368-0797-2025-1-84-89>

РАЗРАБОТКА МОДЕЛЕЙ ФУНКЦИОНИРОВАНИЯ ВОЛОЧИЛЬНОГО ОБОРУДОВАНИЯ ПРИ МНОГОСТАНОВОМ ОБСЛУЖИВАНИИ

А. Р. Фастыковский¹, А. И. Мусатова¹, Н. В. Мартюшев²

¹ Сибирский государственный индустриальный университет (Россия, 654007, Кемеровская обл. – Кузбасс, Новокузнецк, ул. Кирова, 42)

² Национальный исследовательский Томский политехнический университет (Россия, 634050, Томск, пр. Ленина, 30)

✉ omd@sibsiu.ru

Аннотация. Большая потребность в продукции волочильного производства вызывает необходимость увеличения производительности действующего оборудования. Это можно решить двумя способами: созданием новых конструкций волочильного оборудования и поиском скрытых организационных резервов. Повышение производительности за счет организационных мероприятий требует меньше времени и материальных затрат на реализацию. Авторы рассматривают возможность и перспективы многостанового обслуживания. При многостановом обслуживании разрабатывают нормативные модели функционирования волочильного оборудования. На примере действующего производства показаны перспективы применения разработанных моделей. Проведенный анализ работы волочильного оборудования позволяет обосновать режимы обработки при многостановом обслуживании и за счет этого увеличить производительность в 1,35 раза, снизить себестоимость готовой продукции на 2 %.

Ключевые слова: волочильное оборудование, нормативные модели, многостановое обслуживание

Для цитирования: Фастыковский А.Р., Мусатова А.И., Мартюшев Н.В. Разработка моделей функционирования волочильного оборудования при многостановом обслуживании. *Известия вузов. Черная металлургия*. 2025;68(1):84–89. <https://doi.org/10.17073/0368-0797-2025-1-84-89>

INTRODUCTION

The analysis of the established regulatory framework for performance indicators within the drawing mill–wire drawer system, which includes the duration of operations (machine-based, machine-assisted manual, and manual), situational operational cycles of the mills, their utilization factors, downtime, and system productivity, has enabled the optimization of the number of drawing mills that a single operator can effectively service [1–3].

To achieve this, a standard model for the operation of the human-technical system in a multi-mill servicing mode was developed [4–6]. Initially, drawing mills operating in rough, intermediate, and fine wire drawing sections (over 50 units in total) were grouped according to the degree of drawing reduction (ranging from single-pass to seven-pass processes), the diameters of the drawn wire, and the final drum size (750, 650, 550, or 350 mm). In single-pass drawing mills, the process involves a single die, with the wire undergoing one reduction in cross-section. In multi-pass drawing mills of the magazine-type, block machines are installed, consisting of multiple blocks with individual drive mechanisms for each drum, where the wire stock sequentially passes through multiple dies. Each mill is equipped with pay-off and take-up devices, an overhead crane, welding and pointing machines.

Rough and intermediate (single-pass and multi-pass) drawing mills are designed to produce wire with diameters ranging from 8 to 2 mm, wound into small bundles (*SB*) weighing 100–250 kg, heavy bundles (*HB*) weighing 1.0 or 1.5 tons, or coils (*C*) weighing 1.0 ton, depending on the type of mill. The initial stock wire for these mills consists of rod coils (*RC*) with diameters ranging from 10 to 5 mm. Fine (seven-pass) drawing mills (7/350) are used for producing wire with diameters from 2.0 to 0.8 mm, either in bundles (60 kg) or coils (1.0 ton), depending on the intended application.

Each group of drawing mills was classified based on the following criteria: type of pay-off device (horizontal or vertical); type of take-up device (for forming wire onto coils or heavy bundles); method of small bundle removal (cantilever rotating crane or continuous removal installation); form of the initial stock wire (rod coil or coil); type and weight of finished products (small and heavy bundles, coils); diameter and regulatory standard (GOST) of the finished wire; spatial arrangement of drawing mills, including distances between them and their control panels.

To determine the feasibility of a single wire drawer servicing two or more mills, comprehensive studies were conducted on the drawing mill–wire drawer system using time-lapse photography and chronometric observations over the course of 30 work shifts.

DEVELOPMENT OF A STANDARD MODEL

FOR SYSTEM OPERATION

The standard model for determining the feasibility of an operator servicing multiple drawing mills includes the following parameters [7–9].

1. Time spent by the operator servicing a single drawing mill:

$$\tau_{wN}^s(i) = \sum_{n=1}^{n^*} \tau_{m,n}^s(i) + \sum_{z=1}^{z^*} \tau_{ov,z}^s(i) + \tau_{aN}^s(i); \quad (1)$$

$$\tau_{m,n}^s(i) = \frac{\tau_{m,n}^{mp}(i)}{k_{m,n}^s(i)}; \quad \tau_{ov,z}^s(i) = \frac{\tau_{ov,z}^{mp}(i)}{k_{ov,z}^s(i)}; \quad (2)$$

$$\tau_{aN}^s(i) = t_{mN}^s(i) k_a; \quad t_{mN}^s(i) = \frac{t_{mN}^{mp}(i)}{k_o^s(i)}, \quad (3)$$

where $\tau_{m,n}^s(i)$ and $\tau_{m,n}^{mp}(i)$ – the standard and minimum possible time required for the operator to perform the n -th cyclic operation (or its elements) when manufacturing one unit of the i -th product, not overlapped by machine drawing time, h; $\tau_{ov,z}^s(i)$ and $\tau_{ov,z}^{mp}(i)$ – the standard and minimum possible time required for the operator to perform the n -th cyclic operation (or its elements) when manufacturing one unit of the i -th product, overlapped by machine drawing time, h; $k_{m,n}^s(i)$ and $k_{ov,z}^s(i)$ – the standard instability coefficients for manual operations and their elements, considering both overlapped and non-overlapped machine drawing times; $\tau_{aN}^s(i)$ – the standard time for active observation of the drawing process by the operator, h; $t_{mN}^s(i)$ and $t_{mN}^{mp}(i)$ – the standard and technically possible machine time for drawing wire of the i -th diameter at the N -th drawing speed, h; k_a – the regulated active observation coefficient ($k_a = 0.1 \div 0.2$); k_o^s – the standard equipment (mill) utilization coefficient.

2. Planned machine-free idle time of the operator:

$$t_{mfN}^s(i) = t_{mN}^s(i) - \left[\sum_{z=1}^{z^*} \tau_{ov,z}^s(i) + \tau_a^s(i) \right]. \quad (4)$$

3. Planned operator workload time when servicing S identical drawing mills:

$$\tau_{wN}^s(S, i) = \tau_{wN}^s(i) + \tau_{tx}^s(S, i); \quad (5)$$

$$\tau_{tx}^s(S, i) = \frac{\tau_{tx}^{mp}(S, i)}{k_{ins}^s(S, i)}, \quad (6)$$

where $\tau_{tx}^s(S, i)$ and $\tau_{tx}^{mp}(S, i)$ – the standard and minimum possible duration of the operator's transition from one mill to another, h; $k_{ins}^s(S, i)$ – the standard coefficient accounting for instability in the operator's transition route.

4. Standard transition time for the operator moving between mills, determined through simulation modeling

of operator actions while servicing S mills, considering optimal routing and the number of transitions depending on the weight and type of products.

5. Planned operator idle time during the drawing process when servicing S mills

$$t_{mfN}^s(S, i) = t_{mfN}^s(i) - \tau_{tx}^s(S, i). \quad (7)$$

6. Planned operational time of the operator

$$t_{op,N}^s(S, i) = t_{mfN}^s(i) + \tau_{wN}^s(S, i). \quad (8)$$

7. Operator workload coefficient

$$k_{w,N}(S, i) = \frac{\tau_{wN}^s(S, i)}{t_{op,N}^s(S, i)} \leq k_w^*(i); k_w^*(i) \in (0.4 \div 0.7). \quad (9)$$

8. Planned number of drawing mills to be serviced by a single operator

$$S_N(i) = \left[\frac{t_{mfN}^s(S, i)}{\tau_{wN}^s(S, i)} + 1 \right] k^s, \quad (10)$$

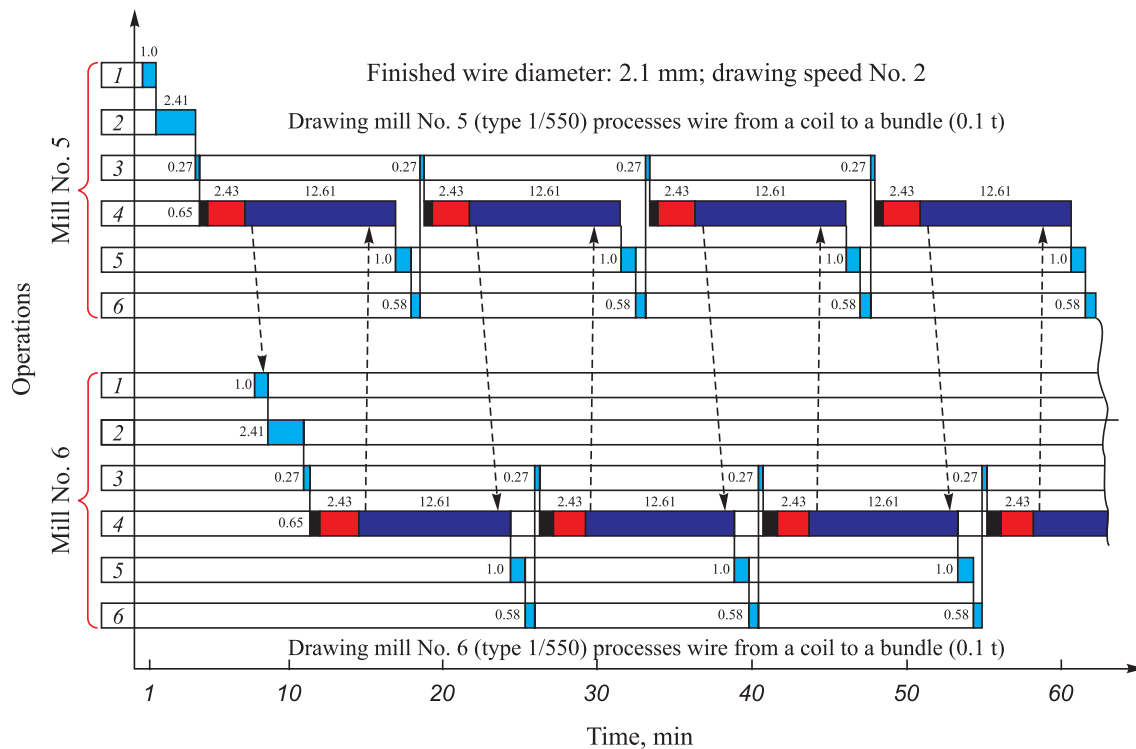
where k^s is the overall coefficient accounting for downtime in multi-mill servicing with S mills.

9. Operator's production rate in multi-mill servicing

$$H_{hts,N}^s(S, i) = P_{hts,N}^s(i) \times S_N^s(i) \Phi B_{hts,sh}^s(S, i), \text{ t/shift}; \quad (11)$$

$$\Phi B_{hts}^s(S, i) = KB_{sh} - \left[\sum_{m=1}^m t_{reg} + t_{tec}^s(i) + t_{tch}^s(i) + t_{cns}^s(i) + t_{org}^s(i) \right], \quad (12)$$

where $P_{hts,N}^s(i)$ – the standard productivity of an identical human-technical system, t/h; $\Phi B_{hts,sh}^s(S, i)$ – the standard working time fund of the human-technical system, considering regulated operator breaks $\sum_{m=1}^m t_{reg}$ standard downtimes due to coinciding manual operations t_{cns}^s while servicing S mills, standard downtimes due to technical t_{tec}^s , technological t_{tch}^s and organizational t_{org}^s reasons, h/shift; S_N^s – the standard (assigned) number of mills at the N -th drawing speed.



Graphical model of the production process during servicing by the operator of two mills (fragment):

1 – installation of coil; 2 – welding of wire ends; 3 – filling wire onto drum; 4 – wire drawing;

5 – removal of the finished wire coil; 6 – transfer of wire drawer to refueling;

■ – time that is not covered by machine time; ■ – time overlapped by machine time; ■ – machine-free dragging time;

■ – time of active observation; → – transition of wire drawer from mill to mill

Графическая модель производственного процесса при обслуживании оператором двух станов (фрагмент):

1 – установка катушки; 2 – сварка концов проволоки; 3 – заправка проволоки на барабан; 4 – волочение проволоки;

5 – сьем мотка готовой проволоки; 6 – переход волочильщика к заправке;

■ – время, не перекрываемое машинным; ■ – время, перекрываемое машинным; ■ – машинно-свободное время волочения;

■ – время активного наблюдения; → – переход волочильщика от стана к стану

Results of modeling the human-technical system in a multi-mill servicing mode

Результаты моделирования человеко-технической системы в режиме многостанового обслуживания

Wire diameter, mm	Standard time, min			Operational time, min	Coefficients		Number of mills per operator		P_{hts}^s , t/h	Standard work time per shift, h/shift	Production rate per shift, t/shift
	τ_a^s	τ_w^s	τ_{mf}^s		k_w	k^s					
							calculated	accepted			
Mills 1/350 process wire from a coil to a bundle (0.06 t)											
1.4	2.72	13.62	48.83	62.45	0.22	0.60	3.0	2	0.039	6.08	0.474
1.4	2.08	12.98	36.78	49.77	0.26	0.65	2.5	2	0.049	6.08	0.596
1.4	1.35	12.25	22.88	35.13	0.35	0.60	1.7	1	0.070	–	–
Mills 2/550 process wire from a rod coil to a coil (1.0 t)											
5.0	2.74	9.44	24.20	3.64	0.28	0.88	3.1	2	1.592	6.50	20.70
5.0	1.99	8.69	17.48	26.17	0.33	0.88	2.6	2	2.042	6.50	26.55
5.0	1.48	8.18	12.83	21.01	0.39	0.87	2.4	2	2.538	6.50	33.02
Mills 3/350 process wire from a rod coil to a bundle (1.5 t)											
3.5	7.84	21.10	68.41	89.51	0.24	0.77	3.3	2	0.875	6.67	11.67
3.5	5.63	18.89	48.53	67.42	0.28	0.77	2.7	2	1.150	6.67	15.34
3.5	4.04	17.30	34.18	51.48	0.34	0.76	2.3	2	1.515	6.67	20.27
Mills 7/350 process wire from a coil to a coil (1.0 t)											
1.6	13.30	16.70	119.21	135.91	0.12	0.82	6.7	3	0.377	7.0	7.92
1.6	9.61	13.01	86.07	99.08	0.13	0.82	6.3	3	0.518	7.0	10.88
1.6	7.72	11.12	68.97	80.09	0.14	0.82	5.9	3	0.641	7.0	13.46

The standard duration of downtime (stoppages) caused by overlapping operations at adjacent mills was evaluated based on empirically observed patterns: the longer the equipment operates and the fewer manual operations are required, the lower the probability of mill stoppages due to overlapping manual operations.

A graphical model of the production process for an operator servicing two drawing mills is schematically presented in the figure. The table provides fragmentary results of system modeling for multi-mill servicing.

The calculations, substantiating the number of drawing mills that can be simultaneously serviced by a single operator, were presented to the management of the wire product manufacturing plant. These calculations demonstrated the feasibility and advantages of multi-mill servicing for certain types of mills, with computations conducted for each finished wire diameter, mass, and product form at the second, third, and fourth drawing speeds.

The modeling results for the human-technical system showed that two drawing mills can be operated by a single wire drawer in specific configurations:

1. Mills 6/550, 5/550, 4/550, 3/550 – processing from a rod coil to a coil (or bundle) weighing 1 t;
2. Mills 1/550 – processing from a coil to a bundle (0.1 t) for finished wire diameters of 2.3 – 1.6 mm; mills

1/350 – processing from a coil to a bundle (0.06 t) at the second and third drawing speeds.

The methodology for transitioning from the calculated number of simultaneously serviced mills to the standardized number was developed based on an analysis of technical, organizational, ergonomic, and economic factors [10 – 12].

A standardized approach was established to determine time norms and wire drawer productivity under multi-mill servicing conditions, considering drawing speed, finished wire diameter and type, and the hourly productivity standards for each mill type.

Based on the developed models, measures were proposed for implementing two-mill servicing in the steel wire drawing shop, resulting in notable improvements in technical and economic performance, including a reduction in personnel, a 1.35-fold increase in labor productivity, and a 2 % decrease in production costs.

REFERENCES / СПИСОК ЛИТЕРАТУРЫ

1. Turaev T.T., Batirov Ya.A., Tozhiev B.A. Modernization of the wire product drawing process. *Universum: Tekhnicheskie nauki: elektron. nauchn. zhurn.* 2019;3(60). Available at URL: <http://7universum.com/ru/tech/archive/item/7049> (Accessed: 12.12.2024). (In Russ.).

- Тураев Т.Т., Батиров Я.А., Тожиев Б.А. Модернизация процесса волочения проволоочного изделия. *Universum: Технические науки: электрон. научн. журн.* 2019;3(60). URL: <http://7universum.com/ru/tech/archive/item/7049> (дата обращения: 12.12.2024).
2. Baek H.M., Jin Y.G., Hwang S.K., Im Y.-T., Son I.-H., Lee D.-L. Numerical study on the evolution of surface defects in wire drawing. *Journal of Materials Processing Technology*. 2012;212(4):776–785. <https://doi.org/10.1016/j.jmatprotec.2011.10.028>
 3. Kharitonov V.A., Usanov M.Yu. Improving the methodology for calculating drawing routes for high-carbon steels. *Ferrous Metallurgy. Bulletin of Scientific, Technical and Economic Information*. 2017;(8):92–95. (In Russ.).
Харитонов В.А., Усанов М.Ю. Совершенствование методики расчета маршрутов волочения для высокоуглеродистых сталей. *Черная металлургия. Бюллетень научно-технической и экономической информации*. 2017;(8):92–95.
 4. Fastyskovskii A.R., Chinokalov E.V. Long coiled reinforcement produced by drawing. *Steel in Translation*. 2019;49(7):481–483. <https://doi.org/10.3103/S0967091219070052>
 5. Fastyskovskii A.R., Martyushev N.V., Musatova A.I., Savchenko I.A., Karlina A.I. Substantiation of normative productivity models of the sheet-rolling shop. Message 1. *Chernye metally*. 2024;(1):9–16. (In Russ.). <https://doi.org/10.17580/chm.2024.01.02>
Фастыковский А.Р., Мартюшев Н.В., Мусатова А.И., Савченко И.А., Карлина А.И. Обоснование нормативных моделей производительности листопрокатного цеха. Сообщение 1. *Черные металлы*. 2024;(1):9–16. <https://doi.org/10.17580/chm.2024.01.02>
 6. Weingartshofer T., Bischof B., Kugi A. Optimization-based path planning framework for industrial manufacturing processes with complex continuous paths. *Robotics and Computer-Integrated Manufacturing*. 2023;82:102516. <https://doi.org/10.1016/j.rcim.2022.102516>
 7. Loginov Yu.N., Grekhov S.K. Generation of residual stresses in drawing low-carbon steel wire. *Stal'*. 2021;(5):25–28. (In Russ.)
Логинов Ю.Н., Грехов С.К. Формирование остаточных напряжений при волочении низкоуглеродистой проволоки. *Сталь*. 2021;(5):25–28.
 8. Kuznetsov S.A., Skorodumov I.S., Skorodumova E.A. Dynamic modeling of coarse-medium direct-flow wire drawing on a drawing mill with an automobile transmission as a drive. *Globus*. 2020;4(50):31–40. (In Russ.). <https://doi.org/10.31618/2658-5197-2020-50-4-6>
Кузнецов С.А., Скородумов И.С., Скородумова Е.А. Динамическое моделирование грубо-среднего прямооточного волочения проволоки на волочильном стане с автомобильной трансмиссией в качестве привода. *Глобус*. 2020;4(50):31–40. <https://doi.org/10.31618/2658-5197-2020-50-4-6>
 9. Volokitina I., Volokitin A., Panin E., Fedorova T., Lawrinuk D., Kolesnikov A., Yerzhanov A., Gelmanova Z., Liseitsev Y. Improvement of strength and performance properties of copper wire during severe plastic deformation and drawing process. *Case Studies in Construction Materials*. 2023;19:e02609. <https://doi.org/10.1016/j.cscm.2023.e02609>
 10. Fung K.H., Khairuddin M.H.B., Shamsudin M.F., Ali W.F.F.W., Salleh M.S. Numerical simulation and prediction of stress distribution in multi-pass drawing process of steel rod. *AIP Conference Proceedings*. 2024;2925(1):020054. <https://doi.org/10.1063/5.0185776>
 11. Emel'yanov A.A., Shil'nikova O.V., Emel'yanova N.Z. Optimization of production programs based on simulation results. *Prikladnaya informatika*. 2015;10(3(57)):109–121. (In Russ.).
Емельянов А.А., Шильникова О.В., Емельянова Н.З. Оптимизация производственных программ на основе результатов имитационного моделирования. *Прикладная информатика*. 2015;10(3(57)):109–121.
 12. Goloviznin S.M., Petrov I.M., Ivantsov A.B. Optimization of wet drawing according to the ratio of breaking stress to draw stress. *Izvestiya. Ferrous Metallurgy*. 2022;65(9):609–614. (In Russ.). <https://doi.org/10.17073/0368-0797-2022-9-609-614>
Головизнин С.М., Петров И.М., Иванцов А.Б. Оптимизация процесса мокрого волочения по критерию запаса прочности. *Известия вузов. Черная металлургия*. 2022;65(9):609–614. <https://doi.org/10.17073/0368-0797-2022-9-609-614>

Information about the Authors

Сведения об авторах

Andrei R. Fastyskovskii, Dr. Sci. (Eng.), Assist. Prof., Prof. of the Chair of Metal Forming and Metal Science. OJSC "EVRAZ ZSMK", Siberian State Industrial University

ORCID: 0000-0001-9259-9038

E-mail: omd@sibsiu.ru

Aleksandra I. Musatova, Senior Lecturer of the Chair "Management and Branch Economy", Siberian State Industrial University

ORCID: 0000-0002-0171-5177

E-mail: musatova-ai@yandex.ru

Nikita V. Martyushev, Cand. Sci. (Eng.), Assist. Prof. of Department of Information Technology, Tomsk Polytechnic University

ORCID: 0000-0003-0620-9561

E-mail: martjushev@tpu.ru

Андрей Ростиславович Фастыковский, д.т.н., доцент, профессор кафедры «Обработка металлов давлением и металловедение. ЕВРАЗ ЗСМК», Сибирский государственный индустриальный университет

ORCID: 0000-0001-9259-9038

E-mail: omd@sibsiu.ru

Александра Ильинична Мусатова, старший преподаватель кафедры «Менеджмент и отраслевая экономика», Сибирский государственный индустриальный университет

ORCID: 0000-0002-0171-5177

E-mail: musatova-ai@yandex.ru

Никита Владимирович Мартюшев, к.т.н., доцент отделения информационных технологий, Национальный исследовательский Томский политехнический университет

ORCID: 0000-0003-0620-9561

E-mail: martjushev@tpu.ru

Contribution of the Authors

Вклад авторов

A. R. Fastykovskii – conceptualization, scientific guidance, formulation of conclusions.

A. I. Musatova – development of normative models of the system functioning, modeling of the human–technical system of multi-mill servicing.

N. V. Martyushev – discussion of results, text correction.

А. Р. Фастыковский – формирование основной концепции, научное руководство, формулирование выводов.

А. И. Мусатова – разработка нормативных моделей функционирования системы, моделирование человеко-технической системы многостанового обслуживания.

Н. В. Мартюшев – обсуждение результатов работы, корректирование текста.

Received 24.04.2024

Revised 15.07.2024

Accepted 15.11.2024

Поступила в редакцию 24.04.2024

После доработки 15.07.2024

Принята к публикации 15.11.2024

ECONOMIC EFFICIENCY
OF METALLURGICAL PRODUCTIONЭКОНОМИЧЕСКАЯ ЭФФЕКТИВНОСТЬ
МЕТАЛЛУРГИЧЕСКОГО ПРОИЗВОДСТВА

UDC 338.2

DOI 10.17073/0368-0797-2025-1-90-97



Original article

Оригинальная статья

DIRECTIONS OF DECARBONIZATION
OF RUSSIAN FERROUS METALLURGYO. P. Chernikova[✉], O. V. Afanas'eva, E. G. Afanas'ev

■ Siberian State Industrial University (42 Kirova Str., Novokuznetsk, Kemerovo Region – Kuzbass 654007, Russian Federation)

✉ chernikovaop@yandex.ru

Abstract. Ferrous metallurgy is a colossal industry with a huge number of industrial facilities and equipment built for centuries. It accounts for approximately 8 % of current global anthropogenic emissions of CO₂ oxides. The future of decarbonization of these assets depends on investments by major market players in the development and implementation of breakthrough steel production technologies and operation of the carbon units market. With careful and responsible management of companies' climate agenda, even against the backdrop of ever-growing demand for steel, metallurgy has every chance of reducing greenhouse gas emissions by 2.5 times in 25 years. At the same time, the implementation of industrial and environmental innovations at enterprises requires an integrated approach. As part of the research, we studied the regulatory documents of the Government of the Russian Federation regulating reduction of carbon intensity of products, growth of energy conservation and reduction of the impact on climate of the metallurgical industry. Criteria for sustainable (including green) development projects for steel producers were identified. The analysis of EVRAZ Group's climate initiatives, carried out as part of the implementation of the company's decarbonization strategy, was conducted. The identified climatic projects of the Russian industrialists were developed with the aim of producing and selling coal units. The formulated key directions of decarbonization of domestic ferrous metallurgy include operational methods for reducing direct and indirect greenhouse gas emissions, transition to environmentally friendly technologies, the use of low-carbon energy sources, introduction of closed crude cycles of ferrous metals, and optimization of the total carbon intensity of the asset portfolio. The implementation of environmental and climate projects will ensure the sustainable development of the metallurgical industry, optimize integrated efficiency indicators, and identify a niche in the competitive business environment.

Keywords: ferrous metallurgy, carbon intensity of steel, energy efficiency, climate project, decarbonization of metallurgy, greenhouse gas emissions, climate agenda

For citation: Chernikova O.P., Afanas'eva O.V., Afanas'ev E.G. Directions of decarbonization of Russian ferrous metallurgy. *Izvestiya. Ferrous Metallurgy*. 2025;68(1):90–97. <https://doi.org/10.17073/0368-0797-2025-1-90-97>

НАПРАВЛЕНИЯ ДЕКАРБОНИЗАЦИИ
РОССИЙСКОЙ ЧЕРНОЙ МЕТАЛЛУРГИИО. П. Черникова[✉], О. В. Афанасьева, Е. Г. Афанасьев

■ Сибирский государственный индустриальный университет (Россия, 654007, Кемеровская обл. – Кузбасс, Новокузнецк, ул. Кирова, 42)

✉ chernikovaop@yandex.ru

Аннотация. Черная металлургия – колоссальная отрасль с большим количеством промышленных объектов и оборудования, построенных на века. На нее приходится примерно 8 % текущих глобальных антропогенных выбросов оксида углерода CO₂. Будущее декарбонизации этих активов зависит от инвестиций крупных игроков рынка в разработку и внедрение прорывных технологий производства стали и от работы рынка углеродных единиц. При грамотном и ответственном управлении климатической повесткой компаний даже на фоне постоянно растущего спроса на сталь у металлургии есть все шансы снизить выбросы парниковых газов в 2,5 раза уже через 25 лет. При этом реализация производственно-экологических инноваций на предприятиях требует комплексного подхода. В рамках проведенного исследования изучали нормативные документы Правительства РФ, регламентирующие снижение углеродоемкости продукции, рост энергосбережения и уменьшение воздействия на климат металлургической отрасли. Выявлены критерии проектов устойчивого (в том числе зеленого) развития для производителей стали. Проведен анализ климатических инициатив EVRAZ Group, проводимых в рамках реализации принятой в компании стратегии декарбонизации. Определены климатические проекты российских промышленников, разработанных с целью выпуска и продажи углеродных единиц. Сформулированные ключевые направления декарбонизации отечественной черной металлургии включают операционные методы снижения прямых и косвенных выбросов парниковых газов, переход к экологи-

чески чистым технологиям, применение низкоуглеродных энергетических источников, внедрение замкнутых сырьевых циклов черных металлов, оптимизацию суммарной углеродоемкости портфеля активов. Реализация экологических и климатических проектов обеспечит устойчивое развитие металлургической отрасли, оптимизацию показателей комплексной эффективности, а также определит занимаемую нишу в конкурентной бизнес-среде.

Ключевые слова: черная металлургия, углеродоемкость стали, энергоэффективность, климатический проект, декарбонизация металлургии, выбросы парниковых газов, климатическая повестка

Для цитирования: Черникова О.П., Афанасьева О.В., Афанасьев Е.Г. Направления декарбонизации Российской черной металлургии. *Известия вузов. Черная металлургия*. 2025;68(1):90–97. <https://doi.org/10.17073/0368-0797-2025-1-90-97>

INTRODUCTION

The global metallurgical industry is a consolidated sector that produces semi-finished products for other areas of the economy, operates with a high level of material processing, and requires extremely high temperatures to sustain technological processes [1–3]. It is a large-scale socio-technical system, employing over six million people directly and generating an additional 40 million indirect jobs throughout the supply chain [4]. The industry's global revenue is estimated at approximately \$2.5 trillion, accounting for 3 % of the world's GDP [5]. Due to the increasing returns to scale in production, the majority of pig iron and steel output is concentrated among a few major players (countries) [6–8].

According to the 2023 World Steel Association rankings, Russia ranked among the top five steel-producing nations, with an output of 76 million tons (4 % of global production, totaling 1,888 million tons). Russia was surpassed by China (54 %, 1,019 million tons), India (7 %, 140 million tons), Japan (5 %, 87 million tons), and the United States (4 %, 81 million tons)¹. Approximately 40 % of Russia's ferrous metallurgy output was exported, primarily as semi-finished products intended for further processing into sheet metal, rolled products, and other materials.

The challenge of climate change is driving global efforts toward carbon neutrality and industrial decarbonization. Given its energy- and carbon-intensive nature, the ferrous metallurgy sector has become a focal point for researchers in various countries, including China [9; 10], Japan [11], the United Kingdom [12; 13], Thailand [14], Sweden [15; 16], Russia [17–20], Ukraine [21], South Korea [22], and others.

At the end of 2022, the Russian government approved the *Strategy for the Development of the Metallurgical Industry of the Russian Federation until 2030*. The strategy outlines a transition toward decarbonization through the advancement of low-carbon technologies, modernization of production facilities, and government support for the development and implementation of breakthrough technologies [23].

Ferrous metallurgy primarily supplies industrial consumers, including machine building, metalworking, construction, and railway transport. Consequently, decarbonization of the metallurgical sector holds significant potential for reducing indirect emissions across other industries [24].

RESEARCH MATERIALS AND METHODS

The study is based on a general scientific methodology, employing methods of scientific abstraction, dialectical development, abstract logic, comparative analysis, and synthesis of information obtained from various recent domestic and international publications.

RESEARCH RESULTS AND DISCUSSION

Over the past four years, Russia has adopted a series of regulatory documents aimed at reducing the carbon intensity of production, increasing energy efficiency, and mitigating climate impact. These include the *Strategy for the Socio-Economic Development of the Russian Federation with Low Greenhouse Gas Emissions until 2050*; the federal law *On Conducting an Experiment to Limit Greenhouse Gas Emissions in Certain Regions of the Russian Federation*; Government Decree No. 455 of March 24, 2022, *On the Approval of the Rules for Verifying the Results of Climate Projects*; Government Decree No. 449 of March 24, 2022, *On the Approval of the Rules for Assessing the Achievement of Target Indicators for Reducing Greenhouse Gas Emissions*; and others.

On March 11, 2023, the Government of the Russian Federation issued Decree No. 373, amending Decree No. 1587 of September 21, 2021. This amendment established criteria for sustainable (including green) development projects for steel producers, including:

- compliance with the lower threshold of specific greenhouse gas emissions for various metallurgical production stages, in accordance with the Best Available Techniques reference guide;
- reduction of actual pollutant emissions and discharges by 10 % or more;
- improvement in resource and energy efficiency by at least 10 %;

¹ World Steel in Figures 2023. – URL: <https://worldsteel.org/data/world-steel-in-figures-2023/> (accessed on 10.01.2025).

- implementation of a closed water circulation system without industrial wastewater discharge;
- production of carbon steel and high-alloy steel;
- adoption of advanced technologies;
- utilization of carbon capture and storage (CCS) technologies.

In response to the growing emphasis on carbon reduction, EVRAZ Group has developed a decarbonization strategy spanning 2020 to 2060. The strategy is structured into three phases: short-term (until 2027), medium-term (2030 – 2045), and long-term (until 2060).

During the short-term phase, initiatives focus on CO₂ emission reductions through energy efficiency projects. The program is planned for the next two years, followed by an annual emission reduction target of 1 %. A roadmap for decarbonization measures in the near future is presented in Fig. 1.

In the medium-term phase, initiatives aim to reduce CO₂ content in “intermediate solutions”. A list of technologies is currently being evaluated for potential implementation at the Ural and Siberia divisions, including syngas utilization, cold briquetting, and replacing sintered ore with pellets.

For long-term sustainability, the most viable production model by 2050 is projected to be electric arc steel-making combined with cold-briquetted iron (CBI) and direct reduced iron (DRI) production. The key considerations for these solutions include technological feasibility, investment volume, and operational costs.

At EVRAZ United West Siberian Metallurgical Plant (EVRAZ ZSMK), Russia’s first Green Rails pilot project has been implemented. The term “green rails” refers to products manufactured with four times lower CO₂ emissions compared to traditional blast furnace-basic oxygen furnace steelmaking. The carbon intensity of the steel used for rail production is approximately 0.5 t CO_{2-eq.} per ton. This reduction is achieved through electric steelmaking, renewable energy sources, and an optimized process with a higher proportion of steel scrap in the charge.

Research is underway to implement an innovative technology for reducing the carbon footprint using direct reduced iron (DRI). DRI is obtained by directly reducing iron ore (lumps, pellets, or fines) using a gas containing elemental carbon or hydrogen. Fig. 2 presents the technological process of cold briquetting.

The key advantages of DRI include: uniform chemical composition; low levels of harmful impurities; energy-efficient and environmentally friendly production; no seasonal dependence on raw material supplies; ease of transportation and use.

To enhance transparency and justify production-ecological decisions, EVRAZ Group calculates carbon inten-

sity and carbon footprint for its products. This includes processing client requests for steel, vanadium, and coke-chemical products and developing methodologies for calculating supply chain emissions.

The company collaborates with the Russian Union of Industrialists and Entrepreneurs (RSPP) and the Russian Steel Association to mitigate carbon regulation risks and advocate for the ferrous metallurgy sector. An industry-wide benchmarking of CO₂ emissions among association members was conducted to develop a unified methodology for assessing steel production’s carbon intensity. This initiative aims to establish a common industry stance on the potential risks of carbon pricing mechanisms.

Companies can assess their compliance with regulated entity status under Government Decree No. 355 of March 14, 2022, which defines criteria for classifying legal entities and individual entrepreneurs as regulated organizations. This assessment, based on Federal Law No. 296-FZ of July 2, 2021 (On Limiting Greenhouse Gas Emissions), is available on the State Information System for Energy Saving and Energy Efficiency Improvement. The CO₂ emissions calculator for ferrous metallurgy enterprises includes indicators listed in Table 1.

The Siberia Division is currently implementing a greenhouse gas emissions automation project to facilitate mandatory reporting, particularly for the *Carbon Border Adjustment Mechanism* (CBAM). Additionally, efforts are underway to automate data collection for Scope 3 emissions calculations, including developing technical specifications and conducting investment evaluations.

The experience gained will later be applied to enterprises in the Ural region.

EVRAZ Group is committed to reducing its carbon footprint, integrating climate impact and sustainability considerations into its regularly updated documentation:

- Comprehensive Environmental Permit – from 2024, all reports must include greenhouse gas emissions data;
- mandatory government reporting – starting January 1, 2025, all enterprises with emissions exceeding 50,000 tons of CO₂ must submit annual reports via the State Information System for Energy Efficiency);
- quarterly CBAM reports – detailing emissions from imported goods;
- annual corporate sustainability report.

Russian companies from various industries are actively developing climate projects. Examples of the largest projects by the volume of issued carbon units are listed in Table 2. Among all projects listed in the Russian Carbon Unit Registry, the metallurgical sector is represented only by business entities of the aluminum company RUSAL. There are no projects from ferrous metallurgy companies

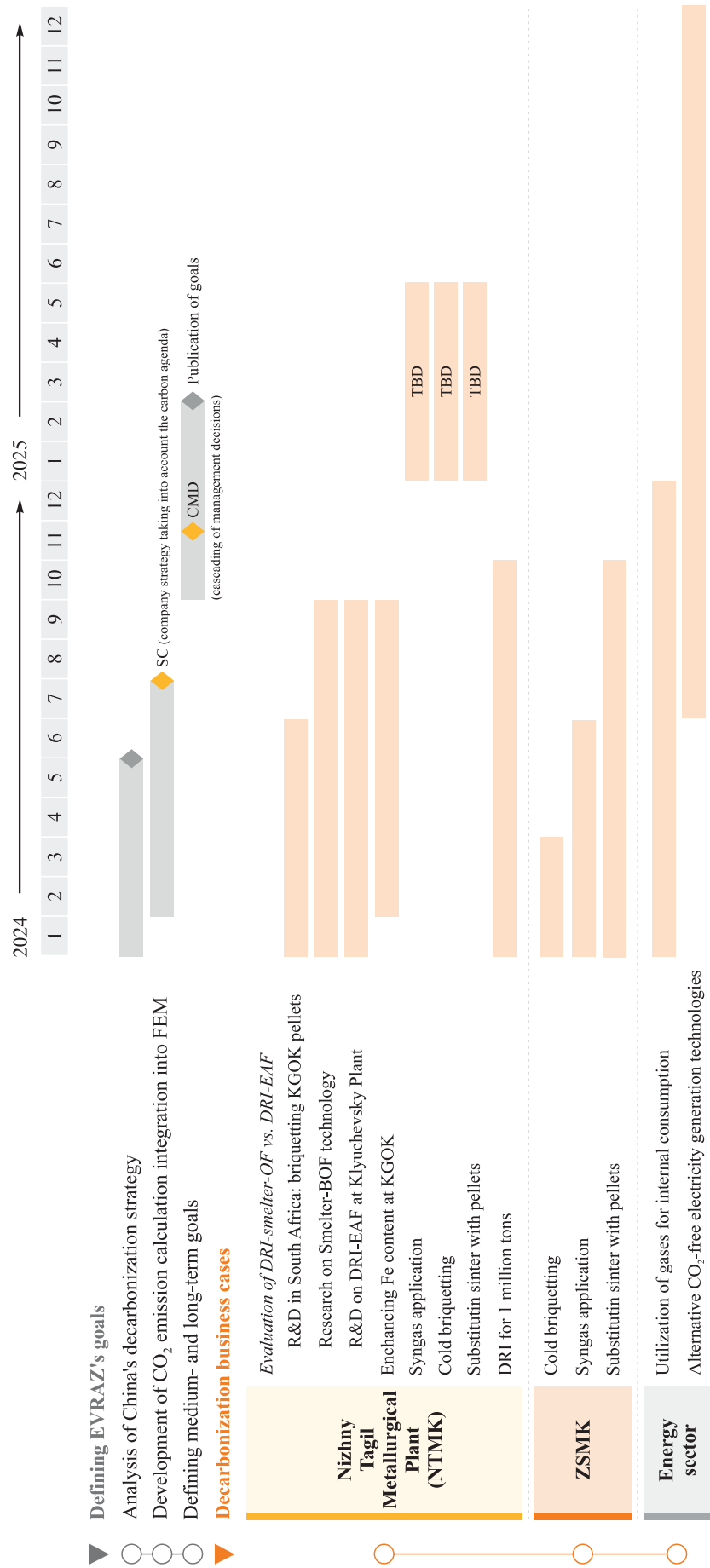


Fig. 1. Schedule for working out decarbonization measures for EVRAZ Group

Рис. 1. План-график проработки мер по декарбонизации производства EVRAZ Group

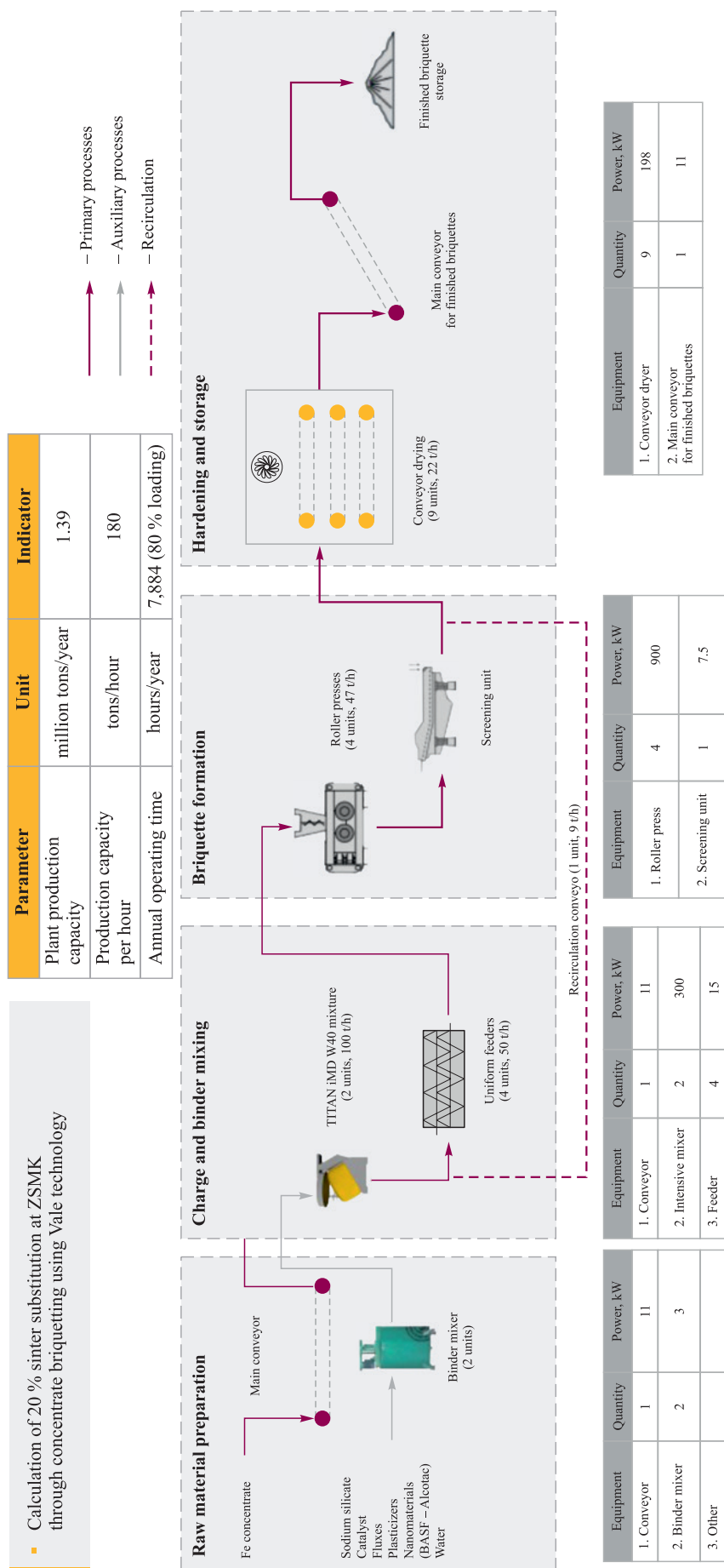


Fig. 2. Diagram of technological process of cold briquetting

Рис. 2. Схема технологического процесса холодного брикетирования

Table 1. Indicators of production processes of ferrous metallurgy enterprises

Таблица 1. Показатели производственных процессов предприятий черной металлургии

Production process	Greenhouse gases emitted during production	CO ₂ -equivalent mass per unit of production process indicator (conversion factor), thousand tons	Total greenhouse gas emissions in CO ₂ -equivalent, thousand tons
Coke production	CO ₂ , CH ₄	0.56	Estimated value
Sinter production	CO ₂ , CH ₄	0.20	Estimated value
Iron ore pellet production	CO ₂	0.03	Estimated value
Direct reduced iron production	CO ₂ , CH ₄	0.53	Estimated value
Pig iron production	CO ₂	1.50	Estimated value
Basic oxygen and open-hearth steel production	CO ₂	0.13	Estimated value
Electric steel production	CO ₂	0.05	Estimated value
Ferrochrome production	CO ₂	1.30	Estimated value
Metallic silicon production	CO ₂ , CH ₄	5.03	Estimated value
Ferrosilicon production	CO ₂ , CH ₄	4.83	Estimated value
Silicomanganese production	CO ₂	1.40	Estimated value

in the registry; however, carbon units (CUs) are available for metallurgical enterprises, with 80,824,742 CUs planned for issuance upon the completion of 31 climate projects.

CONCLUSIONS

The study identifies the following key directions for decarbonizing the ferrous metallurgy sector:

1. Operational decarbonization methods, including improvements in operational efficiency, enhanced energy efficiency in production processes, and reduction of indirect emissions from raw material and component manufacturing (Scope 3).

2. Transition to environmentally clean technologies, such as: *Direct Reduced Iron* (DRI) – the reduction of iron ore or pellets using gases (CO, H₂, NH₃) and solid

Table 2. Climate projects of the Russian companies

Таблица 2. Климатические проекты российских компаний

Company	Climate project	Carbon Units Issued (CU)	Implementation period
JSC RUSAL Krasnoyarsk	Aerial fire protection of a forest area in the Nizhne-Yeniseiskoye forestry, Symskoye district forestry, Yartsevo settlement, Krasnoyarsk Krai, Russia	5,152,843	19.07.2019 – 19.10.2033
PJSC Nizhnekamskneftekhim	Energy-efficient re-equipment at PJSC Nizhnekamskneftekhim	5,647,684	01.11.2022 – 31.10.2032
JSC RUSAL Ural	Improving energy efficiency in thermal energy production at the Krasnogorsk CHP plant of the Ural Aluminum Plant	800,152	08.06.2023 – 31.12.2036
LLC Gazprom MKS	Prevention of GHG (methane) emissions using mobile compressor stations during the preparation of main pipelines for repair work	49,928,002	01.10.2019 – 31.12.2029
JSC Polyus Krasnoyarsk	Replacing electricity generation from coal and oil-fired power plants at JSC Polyus Krasnoyarsk	4,122,439	01.05.2018 – 30.04.2028
PJSC Tatneft named after V.D. Shashin	Reconstruction of a cryogenic unit for deep processing of dry de-hexanized gas with the production of new products, Tatneftegazpererabotka Division, PJSC Tatneft	1,963,434	01.01.2021 – 31.12.2034
JSC Delfin Group	Reduction of greenhouse gas emissions through the use of used lubricating oil regeneration technology	6,187,316	01.03.2024 – 28.02.2039

carbon; Green H₂ DRI-EAF – the use of environmentally friendly hydrogen as a reducing agent for iron ore; *Carbon Capture, Use and Storage* (CCUS) – technologies for capturing, storing, and utilizing carbon, among others.

3. Adoption of low-carbon energy sources, including natural gas, hydrogen, biofuels, and renewable resources.

4. Implementation of circular economy principles, such as the reuse and recycling of material and secondary energy resources, waste processing, and a shift toward secondary raw materials (scrap metal).

5. Optimization of total carbon intensity within asset portfolios, which may involve divesting carbon-intensive operations, establishing carbon farms, and acquiring carbon units.

When forming investment portfolios, companies should prioritize projects that have the potential to be classified as climate projects, provided they meet the additionality criteria.

The ongoing decarbonization processes in ferrous metallurgy contribute to increased energy efficiency, modernization of steel production in electric arc furnaces (EAFs), greater utilization of recycled metal, and advancements in hydrogen technologies and direct CO₂ capture. The implementation of such projects drives the sustainable development of the metallurgical industry, enhances efficiency dynamics, and strengthens its niche in the competitive business environment.

REFERENCES / СПИСОК ЛИТЕРАТУРЫ

- Worldsteel Association, World Steel in Figures 2019. Brussels; 2019:30.
 - Donskoi E., Poliakov A., Manuel J.R. Automated optical image analysis of natural and sintered iron ore. In: *Iron Ore*. Woodhead Publishing; 2015:101–159.
<https://doi.org/10.1016/B978-1-78242-156-6.00004-6>
 - Carpenter A. CO₂ Abatement in the Iron and Steel Industry. IEA Clean Coal Cent; 2012:119.
 - Gleich A., Ayres R.U., Gossling-Reisemann S. Sustainable Metals Management: Securing Our Future-steps Towards a Closed Loop Economy 19. Springer Science & Business Media; 2007:395.
<https://doi.org/10.1007/1-4020-4539-5>
 - IEA, Iron and Steel Technology Roadmap. Paris; 2020:187.
 - Industrial Decarbonisation and Energy Efficiency Roadmaps to 2050 – Iron and Steel. Montreal; 2015:106.
 - Crompton P., Lesourd J.-B. Economies of scale in global iron-making. *Resources Policy*. 2008;33(2):74–82.
<https://doi.org/10.1016/j.resourpol.2007.10.005>
 - 2020 World Steel in Figures. Brussels: Worldsteel Association, 2020:30.
 - Xu W., Wan B., Zhu T., Shao M. CO₂ emissions from China's iron and steel industry. *Journal of Cleaner Production*. 2016;139:1504–1511.
<https://doi.org/10.1016/j.jclepro.2016.08.107>
 - Jing R., Yasir M.W., Qian J., Zhang Z. Assessments of greenhouse gas (GHG) emissions from stainless steel production in China using two evaluation approaches. *Environment Progress & Sustainable Energy*. 2019;38(1):47–55.
<https://doi.org/10.1002/ep.13125>
 - Kuramochi T. Assessment of midterm CO₂ emissions reduction potential in the iron and steel industry: a case of Japan. *Journal of Cleaner Production*. 2016;132:81–97.
<https://doi.org/10.1016/j.jclepro.2015.02.055>
 - Griffin P.W., Hammond G.P. Analysis of the potential for energy demand and carbon emissions reduction in the iron and steel sector. *Energy Procedia*. 2019;158:3915–3922.
<https://doi.org/10.1016/j.egypro.2019.01.852>
 - Griffin P.W., Hammond G.P. Industrial energy use and carbon emissions reduction in the iron and steel sector: A UK perspective. *Applied Energy*. 2019;249:109–125.
<https://doi.org/10.1016/j.apenergy.2019.04.148>
 - Juntueng S., Towprayoon S., Chiarakorn S. Energy and carbon dioxide intensity of Thailand's steel industry and greenhouse gas emission projection toward the year 2050. *Resources, Conservation and Recycling*. 2014;87:46–56.
<https://doi.org/10.1016/j.resconrec.2014.03.014>
 - Larsson M., Dahl J. Reduction of the specific energy use in an integrated steel plant – The effect of an optimisation model. *ISIJ International*. 2003;43(10):1664–1673.
<https://doi.org/10.2355/isijinternational.43.1664>
 - Wang Ch., Ryman Ch., Dahl J. Potential CO₂ emission reduction for BF – BOF steelmaking based on optimised use of ferrous burden materials. *International Journal of Greenhouse Gas Control*. 2009;3(1):29–38.
<https://doi.org/10.1016/j.ijggc.2008.06.005>
 - Glushakova O.V., Chernikova O.P. Institutionalization of ESG principles at the international level and in the Russian Federation, their impact on the activities of ferrous metallurgy enterprises. Part 1. *Izvestiya. Ferrous Metallurgy*. 2023;66(2):253–264. (In Russ.).
<https://doi.org/10.17073/0368-0797-2023-2-253-264>
- Глушакова О.В., Черникова О.П. Институционализация ESG-принципов на международном уровне и в Российской Федерации, их влияние на деятельность предприятий черной металлургии. Часть 1. *Известия вузов. Черная металлургия*. 2023;66(2):253–264.
<https://doi.org/10.17073/0368-0797-2023-2-253-264>
- Butorina I.V., Butorina M.V., Vlasov A.A., Semench A.V. Assessment of the possibility of ferrous metallurgy decarbonization. *Chernye metally*. 2022;(3):71–77. (In Russ.).
<https://doi.org/10.17580/chm.2022.03.13>
- Буторина И.В., Буторина М.В., Власов А.А., Семенча А.В. Оценка возможности декарбонизации черной металлургии. *Черные металлы*. 2022;(3):71–77.
<https://doi.org/10.17580/chm.2022.03.13>
- Klimenko A.V., Tereshin A.G., Prun O.E. Ways to reduce greenhouse gas emissions in the ferrous metallurgy of Russia. *Promyshlennaya energetika*. 2023;(9):8–19. (In Russ.).
<https://doi.org/10.34831/EP.2023.67.59.002>
- Клименко А.В., Терешин А.Г., Прун О.Е. Пути снижения выбросов парниковых газов в черной металлургии России. *Промышленная энергетика*. 2023;(9):8–19.
<https://doi.org/10.34831/EP.2023.67.59.002>
- Chernikova O.P., Zlatitskaya Yu.A. Resource efficiency of metallurgical production. *Izvestiya. Ferrous Metallurgy*.

2022;65(6):390–398. (In Russ.).

<https://doi.org/10.17073/0368-0797-2022-6-390-398>

Черникова О.П., Златицкая Ю.А. Ресурсоэффективность металлургического производства. *Известия вузов. Черная металлургия*. 2022;65(6):390–398.

<https://doi.org/10.17073/0368-0797-2022-6-390-398>

21. Glushchenko A.M. Decarbonization of the steel industry: The role of state economic policy. *The Problems of Economy*. 2020;(1(43)):340–347.

<https://doi.org/10.32983/2222-0712-2020-1-340-347>

22. Yoon Y., Kim Y.-K., Kim J. Embodied CO₂ emission changes in manufacturing trade: Structural decomposition analysis of China, Japan, and Korea. *Atmosphere*. 2020;11(6):597.

<https://doi.org/10.3390/atmos11060597>

23. The strategy for the development of the metallurgical industry of the Russian Federation for the period up to 2030, approved by Decree of the Government of the Russian Federation No. 4260-r dated December 28, 2022.

Стратегия развития металлургической промышленности Российской Федерации на период до 2030 года утверждена распоряжением Правительства РФ от 28 декабря 2022 г. № 4260-р. URL: <http://publication.pravo.gov.ru/Document/View/0001202212300019> (дата обращения 10.01.2025).

24. Skelton A.C.H., Allwood J.M. The incentives for supply chain collaboration to improve material efficiency in the use of steel: An analysis using input output techniques. *Ecological Economics*. 2013;89:33–42.

<https://doi.org/10.1016/j.ecolecon.2013.01.021>

Information about the Authors

Oksana P. Chernikova, Cand. Sci. (Economics), Assist. Prof., Head of the Chair of Economics, Accounting and Finance, Siberian State Industrial University

ORCID: 0000-0002-5410-6623

E-mail: chernikovaop@yandex.ru

Ol'ga V. Afanas'eva, MA Student, Siberian State Industrial University

E-mail: ova-75@mail.ru

Evgenii G. Afanas'ev, MA Student, Siberian State Industrial University

E-mail: evggen2475@gmail.com

Сведения об авторах

Оксана Петровна Черникова, к.э.н., доцент, заведующий кафедрой экономики, учета и финансов, Сибирский государственный индустриальный университет

ORCID: 0000-0002-5410-6623

E-mail: chernikovaop@yandex.ru

Ольга Владимировна Афанасьева, магистрант, Сибирский государственный индустриальный университет

E-mail: ova-75@mail.ru

Евгений Геннадьевич Афанасьев, магистрант, Сибирский государственный индустриальный университет

E-mail: evggen2475@gmail.com

Contribution of the Authors

O. P. Chernikova – conceptualization, analysis of results, writing the article.

O. V. Afanas'eva – literature review, writing the article.

E. G. Afanas'ev – literature review, writing the article.

Вклад авторов

О. П. Черникова – концепция работы, анализ результатов, написание статьи.

О. В. Афанасьева – обзор литературы, написание статьи.

Е. Г. Афанасьев – обзор литературы, написание статьи.

Received 12.08.2024

Revised 26.08.2024

Accepted 28.10.2024

Поступила в редакцию 12.08.2024

После доработки 26.08.2024

Принята к публикации 28.10.2024



UDC 62-932.2

DOI 10.17073/0368-0797-2025-1-98-105



Original article

Оригинальная статья

DEVELOPMENT OF A CONTINUOUS EXTRA-FURNACE STEEL PROCESSING UNIT

V. A. Murashov[✉], K. V. Strogonov, A. K. Bastynets, D. D. Lvov

■ Moscow Power Engineering Institute (14 Krasnokazarmennaya Str., Moscow 111250, Russian Federation)

✉ MurashovViacA@mpei.ru

Abstract. The increase in consumption of high-quality steel dictates the need for more steel undergoing the vacuum process, since processing the steel melt under vacuum improves its properties by reducing gas and non-metallic inclusions in it. However, rising fuel prices and the desire to transition to carbon-free metallurgy require the industry to reduce energy intensity and, as a consequence, reduce energy consumption. This can be achieved by switching to continuous production, reducing the period of technological downtime of high-temperature equipment, the temperature of which must be maintained to increase the lining service life and improve the final product quality. But the transition to continuous steelmaking requires the development of a number of new technological units capable of functioning within the framework of the continuous steelmaking unit, including the extra-furnace processing unit for the melt. The propose of the work was development of a theoretical basis for extra-furnace processing unit of molten steel with a continuous degasser. A unit for extra-furnace processing of steel melt with a continuous U-shaped vacuum degasser is presented, which is part of a unit for continuous liquid-phase iron reduction with a capacity of 10 tons per hour for production of St3 steel. The authors studied the influence of residual pressure in a vacuum chamber on the rate of degassing and the time of a gas bubble ascent. Dimensions of the vacuum degasser were determined taking into account the productivity of the iron reduction unit. A multilayer lining was selected, and losses to the environment were assessed, taking into account convective and radiant heat transfer.

Keywords: energy efficiency, continuous degassing, steel, melt, vacuum, continuous steel making unit, extra-furnace processing, nonblast-furnace iron reduction

Acknowledgements: The research was supported by the Russian Science Foundation, grant no. 24-29-00421, <https://rscf.ru/project/24-29-0042>.

For citation: Murashov V.A., Strogonov K.V., Bastynets A.K., Lvov D.D. Development of a continuous extra-furnace steel processing unit. *Izvestiya. Ferrous Metallurgy*. 2025;68(1):98–105. <https://doi.org/10.17073/0368-0797-2025-1-98-105>

РАЗРАБОТКА АГРЕГАТА ВНЕПЕЧНОЙ ОБРАБОТКИ СТАЛИ НЕПРЕРЫВНОГО ДЕЙСТВИЯ*

В. А. Мурашов[✉], К. В. Строгонов, А. К. Бастынец, Д. Д. Львов

■ Национальный исследовательский университет «МЭИ» (Россия, 111250, Москва, Красноказарменная ул., 14)

✉ MurashovViacA@mpei.ru

Аннотация. Рост потребления качественной стали диктует необходимость увеличения количества стали, проходящей процесс вакуумирования, так как обработка стального расплава под вакуумом улучшает ее свойства за счет уменьшения в ней газовых и неметаллических включений. Однако рост цен на топливо и стремление к переходу на безуглеродную металлургию требуют снижения энергоемкости и, как следствие, сокращения потребления энергоресурсов. Достичь этого можно переходом на непрерывное производство, сокращая период технологического простоя высокотемпературного оборудования, температура которого должна поддерживаться для увеличения срока службы футеровки и повышения качества конечного продукта. Однако для перехода на непрерывное сталеплавильное производство требуется разработка ряда новых технологических узлов, способных функционировать в рамках сталеплавильного агрегата непрерывного действия, в том числе и агрегата внепечной обработки расплава. Целью работы является разработка теоретических основ для узла внепечной обработки стального расплава, включающего в себя вакууматор непрерывного действия. В работе представлен узел внепечной обработки стального расплава с вакууматором непрерывного действия П-образного типа, являющийся частью агрегата непрерывного жидкофазного восстановления железа производительностью 10 т/ч для получения стали Ст3. Изучено влияние остаточного давления в вакуум-камере на скорость дегазации и время всплытия пузырька газа. Габариты вакууматора определены с учетом производительности агрегата восстановления железа. Авторы произвели подбор многослойной футеровки, а также провели оценку потерь в окружающую среду с учетом конвективного и лучистого теплообмена.

* В связи с наличием различных мнений рецензентов, как отрицательных, так и положительных, главным редактором принято решение опубликовать эту статью как дискуссионную.

Ключевые слова: энергоэффективность, непрерывное вакуумирование, сталь, расплав, разрежение, сталеплавильный агрегат непрерывного действия, внепечная обработка, внедоменное восстановление железа

Благодарности: Исследование выполнено за счет гранта Российского научного фонда № 24-29-00421, <https://rscf.ru/project/24-29-00421>.

Для цитирования: Мурашов В.А., Строгонов К.В., Бастынец А.К., Львов Д.Д. Разработка агрегата внепечной обработки стали непрерывного действия. *Известия вузов. Черная металлургия*. 2025;68(1):98–105. <https://doi.org/10.17073/0368-0797-2025-1-98-105>

INTRODUCTION

The continuous growth of industrialization and the global population leads to an increase in steel consumption. Over the past 22 years (from 2000 to 2022), global steel production has increased annually by an average of 4 %. Despite a reduction in global steel production in 2023, Russia saw a 5.6 % rise in steel output. In 2023, global steel production reached 1,888 million tons¹. With increased production comes increased fuel consumption and environmental emissions, particularly greenhouse gases such as CO₂. The high concentration of CO₂ is one of the factors contributing to the rise in average surface temperatures on Earth [1; 2]. Therefore, it is important to reduce the energy intensity of steel products, including improving the energy efficiency of steel production.

The transition to continuous production processes, specifically through continuous steelmaking units (CSUs), can reduce specific energy consumption and harmful emissions compared to traditional steel production technologies [3 – 5]. However, the transition to continuous processes requires the development of new components and units capable of operating continuously, including extra-furnace steel processing units.

Extra-furnace steel processing refers to a set of technological operations aimed at producing liquid steel of the required quality, traditionally carried out outside of the steelmaking unit in conventional metallurgy. These processes take place outside the primary unit, thus increasing the productivity of the entire technological chain.

Extra-furnace processing of steel improves the quality of steel, particularly its mechanical properties, corrosion resistance, and other parameters, which is crucial in the production of high-quality steels [6; 7].

The scientific novelty of this work lies in the development of a continuous extra-furnace steel processing unit operating within a CSU, incorporating an alloying zone and a continuous U-shaped vacuum degasser [3]. The study also involves determining the time of gas bubble ascent through analytical and computational methods. The practical significance is focused on reducing the energy intensity of steel during extra-furnace

processing, particularly in the vacuum degassing process, improving lining durability by reducing the number of thermal cycles associated with technological downtimes [8], and reducing harmful emissions by lowering exhaust gas output.

OBJECTS AND METHODS OF RESEARCH

The object of development is the extra-furnace steel processing zone, operating within a continuous steelmaking unit (CSU) with a capacity of 10 tons of steel per hour. It consists of two main sections: the deoxidation and alloying zone and the degassing zone.

The deoxidation and alloying processes are essential for achieving the required composition and quality of steel with the necessary strength properties. During extra-furnace processing, elements are introduced in a sequence from weakly oxidizing to strongly oxidizing, considering their affinity for oxygen, which helps to reduce their oxidation losses. For example, manganese oxidation loss can range from 10 to 35 %, silicon from 15 to 25 %, and aluminum from 60 to 90 %.

Based on the state of the elements being introduced, alloying can be categorized into the following: alloying with solid ferroalloys, alloying with liquid ferroalloys, and alloying with exothermic ferroalloys.

To determine the list and quantity of elements, it is essential to know the steel grade being produced. The most common steel grade is St3, so the alloying system will be developed for the production of St3.

According to GOST 380–2005 [9] St3 must have the following chemical composition:

- carbon content: 0.14 to 0.22 %;
- manganese content: 0.40 to 0.65 %;
- silicon content: 0.15 to 0.30 %.

Since the vacuum degasser being developed is of continuous operation, a liquid-phase iron reduction unit using natural gas [10] with a reduced capacity of 10 tons per hour can be used as the source of reduced iron. This choice is justified by the existing continuous metal casting system using roll-casting methods. The liquid metal exiting the liquid-phase reduction reactor contains 99.9 % iron [10]. Therefore, for the production of St3, taking into account the affinity of elements for oxygen, the following ferroalloy feeding scheme is proposed: initially, ferromanganese is introduced into the stream of liquid

¹ World Steel in Figures 2022. Available at URL: <https://worldsteel.org/steel-topics/statistics/world-steel-in-figures-2022/> (Accessed: 09.09.2024).

metal exiting the reduction unit, followed by the introduction of ferrosilicon during degassing. Based on experience in alloying in traditional metallurgy and the continuous nature of the process, the additives are proposed to be introduced in solid powder form in an argon stream under pressure, similar to calcium.

The reactions taking place are endothermic, so to accelerate the degassing process of the melt, it is recommended to increase the temperature of the liquid steel to approximately 1600 °C before degassing, either by overheating in the reduction reactor or using electrodes installed in the ferromanganese introduction zone.

The amount of alloying component required can be determined using the formula

$$G_l = \frac{100G_m(E_e - E_m)}{E_l(100 - U_e)}, \quad (1)$$

where G_l is the mass flow of the alloying component, kg/s; G_m is the mass flow of the metal, kg/s; U_e is the oxidation loss of the alloying components, %; E_e , E_m and E_l are the alloying component fractions at the end of the process, the beginning of the process, and in the alloying components, respectively.

The oxidation loss of the alloying components is assumed to be around 25 %, and it is proposed to introduce ferromanganese FeMn78(B) and ferrosilicon FeSi90.

After the deoxidation and alloying processes, the steel is transferred to a continuous U-shaped vacuum degasser [11].

For the developed unit, the internal length of the vacuum chamber was set at 1200 mm, considering the expected lining thickness and the need for a constriction.

Based on the unit's capacity of 10 tons per hour and the vacuum chamber length, the width of the vacuum chamber can be calculated. To do this, the degassing time of the melt must be known. One of the factors determining degassing time is the ascent time of the gas bubble, which depends on its ascent velocity and the height of the melt layer. The bubble ascent velocity in Stokes' mode (Reynolds number $Re < 1$) can be determined by the formula (2). For Reynolds numbers from 10 to 1000, it is described by Malenkov's equation

$$U = \frac{2\alpha g \rho R^2}{9\mu}; \quad (2)$$

$$U = \alpha \sqrt{\beta \frac{2\sigma}{D\rho} + \frac{gD}{2}}, \quad (3)$$

where α and β are numerical constants equal to one in the theoretical derivation; $\rho = 7800 \text{ kg/m}^3$ is the density of the liquid metal at 1400 °C; R is the radius of the gas

bubble; $\mu = 0.0064 \text{ Pa}\cdot\text{s}$ is the viscosity of the steel melt; D is the diameter of the gas bubble; and $\sigma = 1.25$ is the surface tension coefficient.

Let us assume a characteristic bubble diameter of 1 mm.

Inside the vacuum chamber, a vacuum is created, which will affect the size of the ascending bubble. The change in diameter depending on the vacuum above the melt surface can be determined by the formula

$$D = D_0 \sqrt[3]{\frac{P_0}{P_{\text{abs}}}}, \quad (4)$$

where $D_0 = 0.001 \text{ m}$ is the characteristic bubble diameter; $P_0 = 101.3 \text{ kPa}$ is the atmospheric pressure above the melt; and P_{abs} is the absolute pressure above the melt surface.

Once the flow mode is determined, the bubble ascent time can be calculated, taking into account the melt thickness:

$$\tau = \frac{h}{U}, \quad (5)$$

where $h = 0.4 \text{ m}$ is the height of the melt layer, assumed based on methodological recommendations.

According to studies [12; 13], three stages of bubble removal can be distinguished during degassing: gas bubble formation, bubble ascent, and bubble removal from the melt surface.

The degassing time of the liquid metal can be determined using the equation [12 – 14]

$$\tau = -\frac{1}{K_H} \ln \left(\frac{[\% H_k] - [\% H_{\text{eq}}]}{[\% H_n] - [\% H_{\text{eq}}]} \right), \quad (6)$$

where $K_H = 0.13 \text{ min}^{-1}$ is the hydrogen removal rate constant; $[\% H_k] = 1.5 \text{ ppm}$ is the final hydrogen concentration (based on industrial practice); $[\% H_n] = 6 \text{ ppm}$ is the initial hydrogen concentration (based on literature data); and $[\% H_{\text{eq}}] = 0.8 \text{ ppm}$ is the equilibrium hydrogen concentration (Table 1).

Fig. 1 shows the graph of the dependence of the extra-furnace steel processing time (degassing) on the absolute pressure in the vacuum chamber, constructed according to equation (6) and data from Table 1.

The width of the vacuum chamber can be determined using the following formula

$$b = \frac{G}{Lh\rho} \tau. \quad (7)$$

To ensure a uniform melt flow rate in the degasser and the reduction unit, it is necessary to balance the pres-

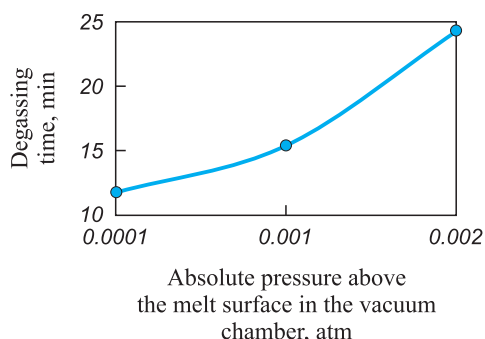


Fig. 1. Dependence of degassing time on pressure above the melt surface

Рис. 1. Зависимость времени дегазации от давления над поверхностью расплава

Table 1. Equilibrium hydrogen content depending on the absolute pressure in the vacuum chamber

Таблица 1. Равновесное содержание водорода в зависимости от абсолютного давления в вакуум-камере

P_H , atm	1.0	0.1	0.01	0.001
[H], ppm	25.6	8.1	2.6	0.8

sure at points on the same level in the extra-furnace processing zone and at the entrance of the riser pipe in the vacuum chamber. To achieve this, the pressure in the riser pipe must be created by the melt layer. Taking this into account, the height of the riser pipes should be approximately 1.3 m, which is comparable to the dimensions of circulation degasser [15].

Additionally, there should be a clearance between the melt surface and the roof since large bubbles formed during degassing can carry melt droplets, which may damage the lining of the roof.

For ease of maintenance and replacement, the vacuum chamber should be a quick-release component of the extra-furnace processing unit, and it should be equipped with nozzles for introducing alloying elements and inert gas, which are integrated into the riser pipe.

In cases of emergency shutdowns of the steelmaking unit, the design of the degasser must allow for easy drain-

age of the melt inside the vacuum chamber, which is why the vacuum chamber must have a slope of at least 3°.

To ensure uniform rarefaction in the degasser, it is proposed to have at least two nozzles connected to the vacuum generation system.

Since the developed degasser has a relatively low capacity of about 10 tons per hour, the most efficient solution is to use a vacuum generation system based on mechanical pumps. According to studies [16; 17], using mechanical pumps instead of steam ejector pumps reduces operational costs (variable costs) by at least 80 %. At the same time, capital costs for low-tonnage installations remain at the same level as for systems with steam ejector pumps.

The selection of thermal insulation materials was carried out in accordance with the recommendations from the handbook authored by I.D. Kasheev [18] as well as lining manufacturers² and drawings of existing RH-degassers.

Table 2 presents the structure of the vacuum degasser's fencing elements, including the number of layers, layer thickness, and material. The layers are listed from the inside to the outside.

The general design scheme of the fencing structure is shown in Fig. 2.

Taking into account Fig. 2, the integral equation that allows for the determination of the specific heat flux through the fencing structure is as follows:

$$\frac{1}{\delta_0} \int_{t_1}^{t_{in}} \lambda_0(t) dt = \frac{1}{\delta_1} \int_{t_2}^{t_1} \lambda_1(t) dt = \frac{1}{\delta_2} \int_{t_{out}}^{t_2} \lambda_2(t) dt = \alpha_{sum} (t_{out} - t_{core}), \quad (8)$$

where α_{sum} is the total heat transfer coefficient, considering both convective and radiative heat and mass transfer, measured in $W/(m^2 \cdot ^\circ C)$, and determined by equation (9); λ is the thermal conductivity of the lining material, measured in $W/(m \cdot ^\circ C)$, and determined by equation (10);

² RHI Magnesita. The driving force of the refractory industry. Available at URL: <https://www.rhimagnesita.com/> (Accessed: 09.09.2024).

Table 2. Design of vacuum degasser fencing elements

Таблица 2. Конструкция элементов ограждения вакууматора

Fencing element	Number of layers	Layer characteristics: material – thickness (mm)		
		1	2	3
Roof	3	PKhPP – 150	ShL-1.0 – 100	ShVP-350 – 100
Wall	3	PKhPP – 250	ShL-1.0 – 100	ShVP-350 – 100
Floor	1	PKhPP – 500	–	–

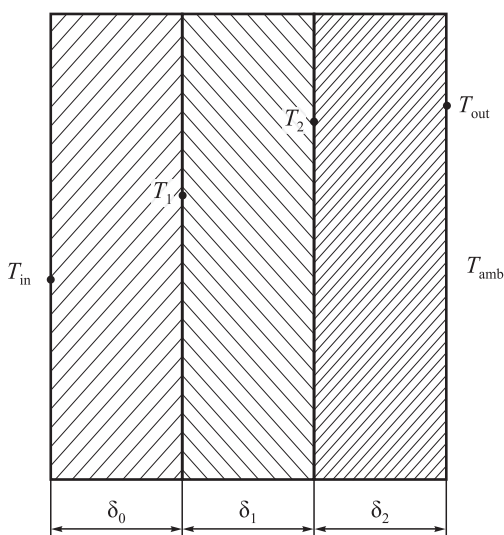


Fig. 2. Calculation of vacuum degasser lining:

T_{in} , T_{out} – temperature on the inner and outer surfaces of the fence, respectively;

T_{amb} – ambient temperature;

T_1 – temperature between the inner and middle layer of the lining;

T_2 – temperature between the middle and outer layer of the lining;

δ_0 , δ_1 , δ_2 – thickness of the inner, middle and outer layer of the lining

Рис. 2. Расчетная схема футеровки вакууматора:

T_{in} , T_{out} – температура на внутренней и наружной поверхности ограждения соответственно;

T_{amb} – температура окружающей среды; T_1 – температура между внутренним и средним слоем футеровки;

T_2 – температура между средним и наружным слоем футеровки;

δ_0 , δ_1 , δ_2 – толщина внутреннего, среднего и наружного слоя футеровки

δ is the thickness of the lining layer, measured in meters; and t is the temperature, °C.

$$\alpha_{sum} = n_0 + n_1(t_{out} - 20)^{n_2}; \quad (9)$$

$$\lambda = k_0 + k_1 t. \quad (10)$$

The coefficients for the equations are presented in Tables 3 and 4.

RESULTS AND DISCUSSION

According to formula (1), in order to produce steel of the required grade, considering an oxidation loss of alloying elements of approximately 25 %, the following amounts need to be added:

- ferromanganese FeMn78(B) – 11.5 kg/ton;
- ferrosilicon FeSi90 – 2.9 kg/ton.

The manganese content in the steel will be 0.64 %, and the silicon content will be 0.25 %, which meets the requirements for St3 according to GOST [10].

The bubble ascent velocity, calculated using equations (2) and (3) as a function of bubble diameter, is presented in Fig. 3.

Table 3. Approximation coefficients n_i

Таблица 3. Коэффициенты аппроксимации n_i

Fencing element	n_0	n_1	n_2
Roof	7.09	0.68	0.562
Side wall	7.20	0.56	0.592
Floor	7.20	0.485	0.614

Table 4. Properties of fencing materials

Таблица 4. Свойства материалов ограждения

Material	Thermal conductivity coefficient, W/(m·°C)
PKhPP	2.5
ShL-1.0	$0.35 + 35 \cdot 10^{-5}t$
ShVP-350	$0.115 + 9.6 \cdot 10^{-5}t$

From the graph, it follows that the critical gas bubble diameter, which satisfies Stokes' ascent, is 0.1 mm. The refore, the velocity of a bubble with a characteristic size of 1 mm is described by equation (3). Substituting this into equation (4) and using it together with equation (5), we determine that the bubble ascent time is 1.3 s. From this, we can conclude that the gas bubble ascent velocity is not the determining factor in steel degassing. Consequently, according to equation (6) and Fig. 1, the degassing time of the liquid metal will be approximately 15.5 min.

Based on the process time and the capacity of 10 tons per hour, we calculate the width of the vacuum chamber using formula (7), which is 0.7 m.

The specific heat fluxes through various parts of the fencing elements, along with the surface temperature of the vacuum degasser, calculated using formulas (8) – (10), are presented in Table 5.

The obtained values of the specific heat flux are comparable to those for existing RH-degassers, taking

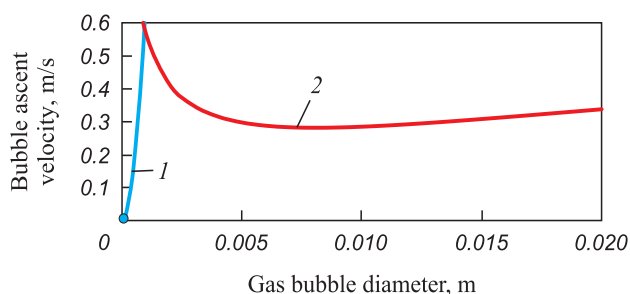
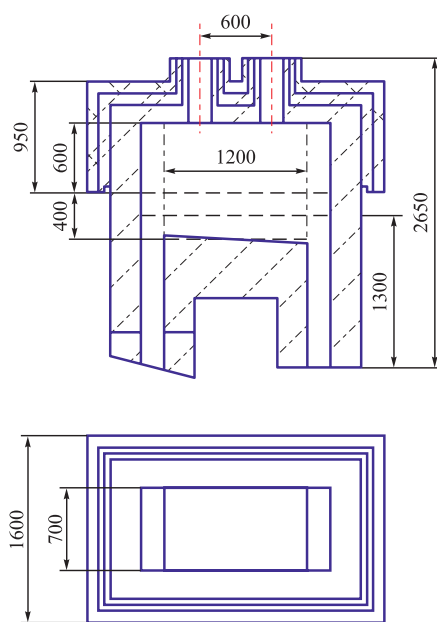


Fig. 3. Dependence of bubble ascent velocity on diameter under different ascent modes: 1 – Stokes mode; 2 – Malenkov's equation

Рис. 3. Зависимость скорости всплытия пузырька от диаметра при различных режимах всплытия: 1 – стоксовый режим; 2 – формула Маленкова

Table 5. Specific heat flux for fencing elements**Таблица 5. Удельный тепловой поток для элементов ограждения**

Fencing element	Specific heat flux, kW/m ²	Surface temperature, °C
Roof	1662	122
Side wall	1561	119

**Fig. 4.** Schematic drawing of a vacuum chamber (side cut and bottom view)**Рис. 4.** Эскизный чертеж вакуум-камеры (разрез сбоку и вид снизу)

into account radiative heat exchange. The specific heat flux for the floor of the vacuum chamber was not determined, as the vacuum chamber floor does not directly contact the surrounding environment.

A schematic drawing of the vacuum chamber, considering the previously determined internal dimensions and lining thickness, is shown in Fig. 4.

According to Fig. 4, the external surface area of the roof will be 3.6 m², and the surface area of the side walls in contact with the surrounding environment will be 7.8 m². The refore, the heat loss to the environment will be around 18.2 kW.

A schematic drawing of the extra-furnace processing unit for continuous steel melt degassing is shown in Fig. 5.

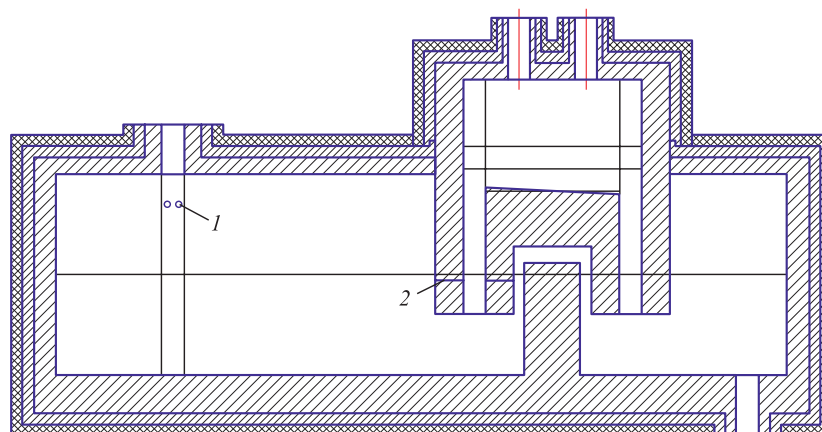
The schematic drawings include a system for introducing alloying elements in an argon stream under pressure into the melt stream *1* and a system for blowing inert gas during degassing *2*.

CONCLUSIONS

Given the annual increase in steel production, including degassed steel, the industry faces the task of improving production efficiency and reducing fuel consumption. Transitioning to continuous processes, as noted in sources [19 – 21] allows for reduced energy consumption in processes and lowers the energy intensity of the final product.

This paper presents a continuous extra-furnace steel processing unit with a capacity of 10 tons of melt per hour, including a U-shaped continuous vacuum degasser. The introduction of alloying elements for St3 steel was considered: ferromanganese is introduced as a powder under pressure into the melt stream during the transfer from the iron reduction zone to the extra-furnace processing zone, and ferrosilicon is introduced into the vacuum degasser together with an inert gas for blowing. The alloying consumption for producing St3 steel from liquid-phase reduced iron will be:

- ferromanganese FeMn78(B) – 11.5 kg/ton;
- ferrosilicon FeSi90 – 2.9 kg/ton.

**Fig. 5.** Schematic drawing of an extra-furnace melt processing unit**Рис. 5.** Эскизный чертеж агрегата внепечной обработки расплава

It is proposed to create a vacuum in the vacuum chamber using mechanical vacuum pumps, as compared to steam ejector systems, capital and operating costs, including energy resource consumption, will be lower.

The degassing time of the melt will be about 15.5 min with a melt layer height of 0.4 m, and the internal width and length of the vacuum chamber will be 0.7 and 1.2 m, respectively. The total heat loss to the environment through the roof and side walls, considering the multilayer lining, will be 18.2 kW, with no losses accounted for through the floor, as it does not contact the surrounding environment. The external surface temperature of the roof will be 122 °C, and the side walls will be 119 °C.

REFERENCES / СПИСОК ЛИТЕРАТУРЫ

1. Ekwurzel B., Boneham J., Dalton M., Heede R., Mera R., Allen M., Frumhoff P. The rise in global atmospheric CO₂, surface temperature, and sea level from emissions traced to major carbon producers. *Climatic Change*. 2017;144(4): 579–590. <https://doi.org/10.1007/s10584-017-1978-0>
2. Gordon Y., Kumar S., Freislich M., Yaroshenko Yu. Comparative evaluation of energy efficiency and GHG emissions for alternate iron-and steelmaking process technologies. In: *Creative Legacy of V.E. Grum-Grzhimailo: History, Modern State, Future*. Yekaterinburg: UrFU; 2014;1:50–59. (In Russ.).
Gordon Y., Kumar S., Freislich M., Yaroshenko Yu. Comparative evaluation of energy efficiency and GHG emissions for alternate iron-and steelmaking process technologies. *Творческое наследие В.Е. Грум-Гржимайло: история, современное состояние, будущее*. Екатеринбург: Уральский федеральный университет; 2014;1:50–59.
3. Ivantsov G.P., Vasilivitskii A.V., Smirnov V.I. Continuous Steelmaking. Moscow: Metallurgiya; 1967:147 (In Russ.).
Иванцов Г.П., Василивицкий А.В., Смирнов В.И. Непрерывный сталеплавильный процесс. Москва: Металлургия; 1967:147.
4. Strogonov K., Kornilova L., Popov A., Zdarov A. Continuous steelmaking unit of bubbling type. In: *Proceedings of the Int. Symp. on Sustainable Energy and Power Engineering 2021*. Singapore: Springer Nature Singapore; 2022:63–72.
5. Strogonov K., Borisov A., Murashov V., Lvov D. Calculation of individual elements of enclosing structures of a continuous steelmaking unit. In: *5th Int. Youth Conf. on Radio Electronics, Electrical and Power Engineering (REEPE)*. IEEE; 2023;(5):1–6.
6. De Paula Lopes B., de Castro J.A., Demuner L.M. A predictive model for hydrogen content in steel in non-degassed heats. *Tecnologia em Metalurgia, Materiais e Mineração*. 2021;18:e2519. <http://dx.doi.org/10.4322/2176-1523.20212519>
7. Toirov O., Tursunov N., Alimukhamedov S., Kuchkorov L. Improvement of the out-of-furnace steel treatment for improving its mechanical properties. *E3S Web of Conferences*. 2023;(365):05002. <https://doi.org/10.1051/e3sconf/202336505002>
8. Protasov A.V. Domestic developments of equipment and technologies of steel in-line degassing in the process of continuous casting. *Ferrous Metallurgy. Bulletin of Scientific, Technical and Economic Information*. 2020;76(10): 1004–1012. (In Russ.). <https://doi.org/10.32339/0135-5910-2020-10-1004-1012>
Протасов А.В. Отечественные разработки оборудования и технологии поточного вакуумирования стали в процессе непрерывной разливки. *Черная металлургия. Бюллетень научно-технической и экономической информации*. 2020;76(10):1004–1012. <https://doi.org/10.32339/0135-5910-2020-10-1004-1012>
9. GOST 380-2005. Carbon steel of ordinary quality. Moscow, Interstate Council for Standardization, Metrology and Certification. 2005:16. (In Russ.).
ГОСТ 380-2005. Сталь углеродистая обыкновенного качества. Москва: Межгосударственный совет по стандартизации, метрологии и сертификации. 2005:16.
10. Strogonov K.V., Petelin A.L., Terekhova A.Yu., L'vov D.D., Murashov V.A., Borisov A.A. Liquid-phase reduction of iron ores with a carbon-hydrogen mixture and hydrogen. *Pro-myshlennaya ehnergetika*. 2023;(8):43–49. (In Russ.). <https://doi.org/10.34831/EP.2023.43.83.006>
Строгонов К.В., Петелин А.Л., Терехова А.Ю., Львов Д.Д., Мурашов В.А., Борисов А.А. Жидкофазное восстановление железных руд углеродводородной смесью и водородом. *Промышленная энергетика*. 2023;(8):43–49. <https://doi.org/10.34831/EP.2023.43.83.006>
11. Strogonov K.V., Murashov V.A. Continuous steel vacuuming unit. Patent RF no. 2806948. MPK C21C 7/10. *Bulleten' izobretenii*. 2023;(31). (In Russ.).
Пат. 2806948 RU. Агрегат непрерывного вакуумирования стали / Строгонов К.В., Мурашов В.А.; заявл. 05.04.2023; опубл. 08.11.2023. Бюл. № 31.
12. Metelkin A.A., Sheshukov O.Yu., Nekrasov I.V., Shevchenko O.I., Korogodskii A.Yu. About hydrogen removal from metal in circular type degasser. *Teoriya i tekhnologiya metallurgicheskogo proizvodstva*. 2016;(1(18)):29–33. (In Russ.).
Метелкин А.А., Шешуков О.Ю., Некрасов И.В., Шевченко О.И., Корогодский А.Ю. К вопросу удаления водорода из металла в вакууматоре циркуляционного типа. *Теория и технология металлургического производства*. 2016;(1(18)):29–33.
13. Korneev S.V. Modern approaches to the removal of hydrogen from steel. In: *Metallurgy: Republican Interdepartmental Collection of Scientific Papers*. 2018;(39):3–11. (In Russ.).
Корнеев С.В. Современные подходы к удалению водорода из стали. *Металлургия: республиканский межведомственный сборник научных трудов*. 2018;(39):3–11.
14. Selivanov V.N., Budanov B.A., Alankin D.V. Kinetic model of hydrogen removal during circulating degassing of steel. *Teoriya i tekhnologiya metallurgicheskogo proizvodstva*. 2013;(1(13)):31–33. (In Russ.).
Селиванов В.Н., Буданов Б.А., Аланкин Д.В. Кинетическая модель удаления водорода при циркуляционном вакуумировании стали. *Теория и технология металлургического производства*. 2013;(1(13)):31–33.
15. Dong W., Xu A., Liu B., Zhou H., Ji C., Wang S., Li H., Wang T. Mechanism and model of nitrogen absorption of molten steel during N₂ injection process in RH vacuum.

- Metallurgical and Materials Transactions B.* 2024;55(1): 72–82. <https://doi.org/10.1007/s11663-023-02937-8>
16. Dorstevits F., Tembergen D. Vacuum pump systems for secondary metallurgical processes. *Chernye metally.* 2013;(9): 37–45. (In Russ.).
Дорштейн Ф., Темберген Д. Критерии выбора вакуумных насосов для агрегатов внепечной обработки стали. *Черные металлы.* 2013;(9):37–45.
 17. Burgmann V., Davenet J. The cost structure of steel vacuuming, taking into account the processing in the bucket-furnace unit. *Chernye metally.* 2012;(11):41–49. (In Russ.).
Бургман В., Давене Ж. Структура затрат на вакуумирование стали с учетом обработки в агрегате ковш-печь. *Черные металлы.* 2012;(11):41–49.
 18. Kashcheev I.D. Properties and Application of Refractories. Moscow: Teplotekhnika; 2004:352. (In Russ.).
Кашеев И.Д. Свойства и применение огнеупоров. Москва: Теплотехник; 2004:352.
 19. LIN CS. Analysis of Temperature Dropping of Molten Steel in Ladle for Steelmaking. *China Steel Technical Report.* 2022;(35):7–12.
 20. Polulyakh L.A., Evseev E.G., Savostyanov A.V., Boche-rikov R.E. Study of the behavior of phosphorus in the production of manganese alloys using ores with a low manganese content. *Metallurgist.* 2023;67(10):469–475.
<https://doi.org/10.1007/s11015-023-01532-1>
Полулях Л.А., Евсеев Е.Г., Савостьянов А.В., Бочери-ков Р.Е. Исследование поведения фосфора при производстве марганцевых сплавов с использованием руд с низким содержанием марганца. *Металлург.* 2023;(4):58–62.
https://doi.org/10.52351/00260827_2023_04_58
 21. Nurzhanov O.S., Petelin A.L., Nurzhanov A.S., Polu-lyakh L.A. Analysis of the propagation zone and calculation of concentration fields in the atmosphere of emissions of fine dust from blast furnace No. 4 (PJSC NLMK). *Chernye metally.* 2022;(9):76–81. (In Russ.).
<https://doi.org/10.17580/chm.2022.09.12>
Нуржанов О.С., Петелин А.Л., Нуржанов А.С., Полу-лях Л.А. Анализ зоны распространения и расчет полей кон-центраций в атмосфере выбросов мелкодисперсной пыли доменной печи № 4 ОАО «НЛМК». *Черные металлы.* 2022;(9):76–81. <https://doi.org/10.17580/chm.2022.09.12>

Information about the Authors

Сведения об авторах

Viacheslav A. Murashov, Engineer, Moscow Power Engineering Institute

ORCID: 0009-0007-9576-8539

E-mail: MurashovViacA@mpei.ru

Konstantin V. Strogonov, Cand. Sci. (Eng.), Assist. Prof. of the Chair of Innovative Technologies of Knowledge-Intensive Industries, Moscow Power Engineering Institute

ORCID: 0000-0003-3276-4403

E-mail: StrogonovKV@mpei.ru

Andrey K. Bastynets, Student, Moscow Power Engineering Institute

E-mail: BastynetsAK@mpei.ru

Dmitry D. Lvov, Postgraduate, Moscow Power Engineering Institute

ORCID: 0000-0002-3808-2094

E-mail: LvovDD@mpei.ru

Вячеслав Андреевич Мурашов, инженер, Национальный исследова-тельский университет «МЭИ»

ORCID: 0009-0007-9576-8539

E-mail: MurashovViacA@mpei.ru

Константин Владимирович Строгонов, к.т.н., доцент кафедры инновационных технологий наукоемких отраслей, Национальный исследовательский университет «МЭИ»

ORCID: 0000-0003-3276-4403

E-mail: StrogonovKV@mpei.ru

Андрей Константинович Бастынец, студент, Национальный исследовательский университет «МЭИ»

E-mail: BastynetsAK@mpei.ru

Дмитрий Дмитриевич Львов, аспирант, Национальный исследова-тельский университет «МЭИ»

ORCID: 0000-0002-3808-2094

E-mail: LvovDD@mpei.ru

Contribution of the Authors

Вклад авторов

V. A. Murashov – literary analysis, performing calculations, develop-ment of a continuous vacuum degasser, analysis of results, writing the text.

K. V. Strogonov – scientific guidance, development of a continuous vacuum degasser and a zone for nonblast-furnace liquid-phase iron reduction, discussion of experimental results, writing the text.

A. K. Bastynets – literary analysis, verification of calculations, analysis of results, writing the text.

D. D. Lvov – literary analysis, verification of calculations, development of a zone for nonblast-furnace liquid-phase iron reduction, analysis of results, writing the text.

В. А. Мурашов – анализ литературных данных, выполнение рас-четов, разработка вакууматора непрерывного действия, анализ результатов, написание статьи.

К. В. Строгонов – научное руководство, разработка вакууматора непрерывного действия и зоны внедоменного жидкофазного восстановления железа, обсуждение результатов экспериментов, написание статьи.

А. К. Бастынец – анализ литературных данных, проверка расче-тов, анализ результатов, написание статьи.

Д. Д. Львов – анализ литературных данных, проверка расчетов, разработка зоны внедоменного жидкофазного восстановления железа, анализ результатов, написание статьи.

Received 10.07.2024

Revised 31.07.2024

Accepted 22.08.2024

Поступила в редакцию 10.07.2024

После доработки 31.07.2024

Принята к публикации 22.08.2024

Над номером работали:

Л.И. Леонтьев, *главный редактор*

Е.В. Протопопов, *заместитель главного редактора*

Е.А. Ивани, *ответственный секретарь*

Л.П. Бащенко, *заместитель ответственного секретаря*

Е.Ю. Потапова, *заместитель главного редактора по развитию*

О.А. Долицкая, *научный редактор*

Е.М. Запольская, *ведущий редактор*

В.В. Расенец, *верстка, иллюстрации*

Г.Ю. Острогорская, *менеджер по работе с клиентами*

Подписано в печать 20.02.2025. Формат 60×90 ¹/₈. Бум. офсетная № 1.
Печать цифровая. Усл. печ. л. 13,0. Заказ 21562. Цена свободная.

Отпечатано в типографии Издательского Дома МИСИС.
119049, Москва, Ленинский пр-кт, д. 4, стр. 1.
Тел./факс: +7 (499) 236-76-17



Development of profile pipes production technology, providing higher accuracy of geometric parameters compared to foreign manufactures

Stiffness modulus of stands in finishing group of continuous wide-strip hot rolling mill

Tensile fracture of tempered martensitic steel

Influence of inclined electric field on decay of a liquid jet during heat treatment and surfacing

Anthology of rails produced by JSC EVRAZ United West Siberian Metallurgical Plant in the 21st century

Influence of heat treatment modes on the properties of 56DGNKh (Cu20Ni20Mn2Cr) alloy

Development of a continuous extra-furnace steel processing unit

Effect of thermal cycles on formation of pearlitic heat-resistant steel structure under wire arc additive manufacturing

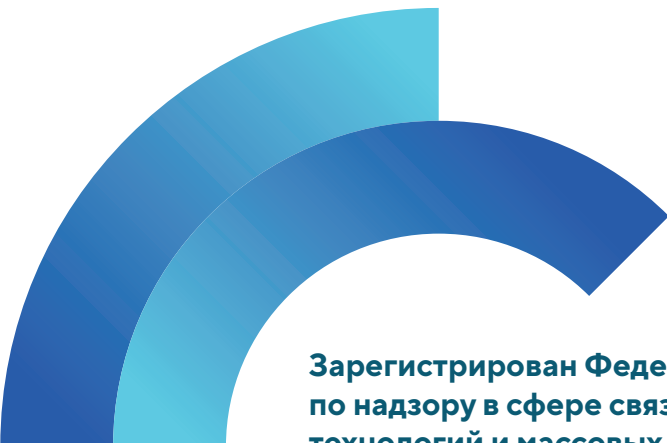
Development of research on the physico-chemical properties of oxide and metal melts

Influence of heat treatment on structure, phase composition, hardness and electrical conductivity of VZhL14N-VI nickel superalloy

Directions of decarbonization of Russian ferrous metallurgy

Construction of liquidus surface of Fe – B – Mn – C – Cr five-component diagram

Development of models for functioning of drawing equipment for multi-mill servicing



**Зарегистрирован Федеральной службой
по надзору в сфере связи, информационных
технологий и массовых коммуникаций.
Свидетельство о регистрации
ПИ № ФС77-35456.**

Подписной индекс 70383.

